QUANTUM LIQUIDS AND QUANTUM CRYSTALS

Relaxation of concentration and temperature in superfluid mixtures ^{3}He–^{4}He at low temperatures

K. È. Nemchenko

Kharkov State University, 310077 Kharkov, Ukraine*
(Submitted January 3, 1997; revised March 7, 1997)
Fiz. Nizk. Temp. **23**, 799–802 (August 1997)

It is shown on the basis of the solution of the kinetic equation for the gas of impurity excitations of superfluid mixtures ^{3}He–^{4}He that the relaxation of concentration and temperature occurs due to two modes (acoustic and dissipative). The parameters characterizing these modes are determined. The obtained results show that the relaxation of concentration and temperature of impuritons is completely determined by the thermal conductivity of the mixture and by the acoustic mode (second sound). © *1997 American Institute of Physics.*
[S1063-777X(97)00108-4]

Superfluid solutions ^{3}He–^{4}He possess a number of unique properties, including the existence of two essentially different mechanisms of concentration and temperature relaxation,[1–3] viz., second sound[4] and dissipative diffusive mode.[5] This distinguishes superfluid solutions from pure helium in which temperature stabilization occurs due to second sound[1] as well as from normal solutions in which the temperature and concentration relaxation is determined only by dissipative processes (thermal and diffusive waves).[6]

The existence of two modes responsible for equilibrium stabilization of concentration and temperature in superfluid solutions necessitates their simultaneous inclusion in an analysis of various kinetic processes. One of such processes attracting attention of experimenters[7–9] as well as theoretical physicists[10–13] is the phase separation of supersaturated superfluid solutions ^{3}He–^{4}He.

In the publications[7,11,14] that laid the basis of the kinetic theory of phase separation of metastable solutions ^{3}He–^{4}He, either dissipative processes were not taken into account altogether,[14] or it was assumed, in analogy with normal solutions, that diffusion is the main process responsible for the motion of impurities.[7,11] However, subsequent experimental[9] and theoretical[10] investigations proved that second sound should also be taken into account in the description of phase separation of supersaturated solutions ^{3}He–^{4}He.[12] The effect of second sound on the growth of a new phase was analyzed in Ref. 13, but dissipative processes were only partially taken into consideration. This research aims at an analysis of temperature and concentration relaxation in superfluid solutions ^{3}He–^{4}He at low temperatures, for which the contribution of thermal excitations in He II can be neglected, and the transport properties of the solution are determined only by impurity quasiparticles.

An analysis of hydrodynamic modes in the impuriton gas is based on the kinetic equation for the impuriton distribution function f_i[15]:

$$\frac{\partial f_i}{\partial t} + (\mathbf{v}_i \cdot \nabla) f_i = J_{ii}(f_i). \tag{1}$$

Here $\mathbf{v}_i = \partial \varepsilon_i / \partial \mathbf{p}_i$ is the impuriton velocity and J_{ii} the collision integral for impuritons. In addition, the case of low concentrations is considered, when it can be assumed that the superfluid background remains in equilibrium.

In order to derive the dispersion equation characterizing small oscillations in the solution, we must linearize Eq. (1). This leads to the following equation for the Fourier component of the function δf_i describing the deviation from equilibrium:

$$(\omega - \mathbf{k} \cdot \mathbf{v}_i) \delta f_i = i I_{ii}(\delta f_i). \tag{2}$$

Here I_{ii} is the linearized collision integral depending on δf_i; ω the frequency and $\mathbf{k}$ the wave vector.

We shall seek the solution of Eq. (2) in the form

$$\delta f = -f_i' g_i, \tag{3}$$

where f_i' is the derivative of the function f_i with respect to energy. This leads to the following equation for the unknown function g_i:

$$(\omega - \mathbf{k} \cdot \mathbf{v}_i - i I_{ii}) g_i = 0. \tag{4}$$

The problem of determining the energy-momentum relations $\omega = \omega(\mathbf{k})$ describing hydrodynamic modes is equivalent to determining the resolvent poles R_i of Eq. (4)

$$R_i = (\omega - \mathbf{k} \cdot \mathbf{v}_i - i I_{ii})^{-1} \tag{5}$$

in the subspace of impuriton collision invariants. For this purpose, we introduce operators projecting onto the subspace of collision invariants for the number of particles, energy, and momentum of impuritons:

$$|J_N\rangle = \frac{|1\rangle}{\langle 1|1\rangle^{1/2}}; \quad |J_\varepsilon\rangle = \frac{|\widetilde{\varepsilon}_i\rangle}{\langle \widetilde{\varepsilon}_i|\widetilde{\varepsilon}_i\rangle^{1/2}};$$

$$|J_{p_z}\rangle = \frac{|p_{iz}\rangle}{\langle p_{iz}|p_{iz}\rangle^{1/2}}, \tag{6}$$

where $\widetilde{\varepsilon}_i = \varepsilon_i - \langle \varepsilon_i|1\rangle/\langle 1|1\rangle$. The vectors $|J_{p_x}\rangle$, $|J_{p_y}\rangle$ can be omitted since the z-axis is chosen along the vector $\mathbf{k}$. In

expressions (6), we have introduced the one-dimensional vectors in the space of impuriton momenta and defined the scalar product

$$\langle \psi_i | \chi_i \rangle = - \int \psi_i^*(\mathbf{p}_i) \chi_i(\mathbf{p}_i) f_i' d\Gamma_i . \tag{7}$$

We project expression (5) onto the subspace of collision invariants:

$$P_{ic} R_i P_{ic} = P_{ic}(\omega - P_{ic}\Omega_i P_{ic})^{-1} P_{ic} , \tag{8}$$

where

$$\Omega_i = \mathbf{k}\cdot\mathbf{v}_i + \mathbf{k}\cdot\mathbf{v}_i P_{in}(\omega - P_{in}\mathbf{k}\cdot\mathbf{v}_i P_{in} - i P_{in}I_{ii}P_{in})^{-1} P_{in}\mathbf{k}\cdot\mathbf{v}_i . \tag{9}$$

Here, we have introduced the operator projecting on the subspace of invariants

$$P_{ic} = |J_N\rangle\langle J_N| + |J_\varepsilon\rangle\langle J_\varepsilon| + |J_{p_z}\rangle\langle J_{p_z}| \tag{10}$$

as well as the subspace orthogonal to it:

$$P_{in} = 1 - P_{ic} . \tag{11}$$

For calculating the matrix elements in (8) and (9), we shall use the correct τ-approximation[16] according to which $P_{in}I_{ii}P_{in}$ can be replaced by $-P_{in}/\tau_{ii}$, where τ_{ii} is the characteristic time of impuriton collisions. Since $\omega\tau_{ii}\ll 1$ and $kv_i\tau_{ii}\ll 1$ in the hydrodynamic approximation being considered, we can calculate the matrix elements of the operator $\omega - P_{ic}\Omega_i P_{ic}$ in the basis P_{ic} and equate to zero the determinant of the obtained matrix. This leads to the following dispersion equation:

$$\omega(\omega^2 - k^2 u_i^2) + i k^2 \omega^2 \left(\frac{\kappa_i}{C_i} + \frac{4}{3} \frac{\eta_i}{\rho_{in}} \right) - i u_{iN}^2 k^4 \frac{\kappa_i}{C_i} = 0. \tag{12}$$

Here

$$u_i^2 = u_{iN}^2 + u_{i\varepsilon}^2,$$

$$u_{iN}^2 = \frac{1}{m_i}\left(\frac{\partial P_f}{\partial n_i}\right)_T, \qquad u_{i\varepsilon}^2 = \frac{T\overline{S}^2}{\rho_{in}C_i}$$

are the squares of characteristic velocities in the gas of impuritons, $\overline{S}_i = S_i - (\partial S_i/\partial n_i)_T n_i$; $P_f, S_i, C_i, \rho_i = m_i n_i$ are the osmotic pressure, entropy, heat capacity, and normal density of impuriton gas, κ_i is the thermal conductivity, and η_i the first (shear) viscosity of impuritons. The latter quantities can be expressed in the standard form[17] in terms of the time τ_{ii} of impuriton collisions:

$$\eta_i = \langle \varphi_{\eta i} | \varphi_{\eta i} \rangle \tau_{ii} , \tag{13}$$

$$\kappa_i = \langle \varphi_{\kappa i} | \varphi_{\kappa i} \rangle \tau_{ii} , \tag{14}$$

where the vectors are defined as follows:

$$|\varphi_{\eta i}\rangle = \frac{1}{2\sqrt{3}} |3 p_{iz} v_{iz} - p_i v_i\rangle, \tag{15}$$

$$|\varphi_{\kappa i}\rangle = \frac{1}{\sqrt{T}} |\tilde{\varepsilon}_i v_{iz} - (\overline{S}T/\rho_{in}) p_{iz}\rangle. \tag{16}$$

Calculations based on formulas (13) and (14) lead to the following expressions for dissipative coefficients:

$$\eta_i = P_f \tau_{ii} ; \tag{17}$$

$$\kappa_i = C_i \frac{v_F^2}{3} \tau_{ii} , \quad (T\ll T_F); \tag{18}$$

$$\kappa_i = \frac{5}{2} \frac{n_i T}{m_i} \tau_{ii} , \quad (T\gg T_F).$$

Here $T_F = m_i v_F^2/2$ is the Fermi temperature of impuritons.

In the hydrodynamic approximation used here, the dispersion equations for two collective modes can be determined from (12).

The first mode is the acoustic mode ($\omega \sim k$) with the energy–momentum relation

$$\omega^2 = k^2 u_i^2 \left\{ 1 - i \frac{\omega}{u_i^2} \left[\frac{4}{3} \frac{\eta_i}{\rho_i} + \frac{u_{i\varepsilon}^2}{u_i^2} \frac{\kappa_i}{C_i} \right] \right\}. \tag{19}$$

The obtained result has a simple physical meaning: when the properties of solutions are determined by impuritons alone, sound propagates in the impuriton gas ("impuriton second sound") at a velocity u_i coinciding with the velocity of sound in an ideal gas of particles of mass m_i. The second and third terms in (19) describe attenuation of impuriton second sound due to viscosity and thermal conductivity respectively.

The second collective mode is dissipative ($\omega \sim k^2$) and has the energy–momentum relation

$$\omega = - i k^2 D_{\text{eff}}, \tag{20}$$

where

$$D_{\text{eff}} = \frac{\kappa_i}{C_i} \frac{u_{iN}^2}{u_i^2} \tag{21}$$

is the dissipative coefficient describing this mode.

The obtained mode corresponds to a thermal wave in ordinary liquids, which describes dissipative relaxation of temperature and number density of particles to the equilibrium state. In superfluid solutions, this collective mode is associated with the relaxation of ³He concentration, and hence determines in fact the diffusion of impurities. According to (21), the effective diffusion coefficient in this case is determined by the thermal conductivity of the impuriton gas.

As regards the actual diffusion processes, it follows from (19) and (21) that the dissipative impurity diffusion does not exist as such at such low temperatures, and as a result, the mass, thermal and pressure diffusion coefficients are equal to zero, This is due to the fact that in the absence of thermal excitations, the impuriton system in the situation under investigation is effectively a one-component system, and diffusion processes do not occur in it. On the other hand, dissipative relaxation occurs, like in one-component gases, through the thermal mode in which density relaxation at a constant partial pressure [$\nabla P(n,T) = 0$] takes place simultaneously with temperature relaxation by virtue of the relation

$$(\partial P/\partial n)_T \nabla n = -(\partial P/\partial T)_n \nabla T$$

and is determined by the thermal conductivity of the gas.

600   Low Temp. Phys. 23 (8), August 1997

K. È. Nemchenko   600

Thus, the above analysis shows that superfluid solutions ^{3}He–^{4}He exhibit a peculiar two-stage relaxation of initial deviations of temperature and concentration from equilibrium. At the first stage, a nonequilibrium state without an impuriton partial pressure gradient ($\nabla P_f = 0$) sets in virtually at the velocity of second sound. However, the number density of impuritons and temperature may have gradients which are connected through the relation

$$\nabla n_i = -\frac{(\partial P_f/\partial T)_{n_i}}{(\partial P_f/\partial n_i)_T}\,\nabla T. \tag{22}$$

At the second stage, the existence of a temperature gradient leads to a dissipative heat flow determined by the thermal conductivity of the solution, which blurs the deviation of temperature from its equilibrium value. In this case, nondissipative motion of impuritons in the second sound wave ensures the fulfillment of equality (22) everywhere, and thus the density gradient sort of ''follows'' the temperature gradient, both gradients tending to zero simultaneously with the same characteristic dissipative coefficient (21).

Relation (22) makes it possible to determine the mechanism (dissipative or acoustic) responsible for relaxation of concentration and temperature under specific experimental conditions. We confine our analysis to the temperature range $T < 0.25$ K and concentrations $x > 0.5\%$, for which the contribution of thermal excitations in He II can be neglected, and the gas of quasiparticles (impuritons) can be regarded as a one- component system. In this case, for low concentrations ($x \sim 1\%$) and not very low temperatures ($T \sim 0.2$ K), relaxation of perturbations of concentration and temperature is determined by both modes to the same extent. For higher concentrations ($x \sim 10\%$) and at quite low temperatures ($T \sim 10$ mK), the main part (exceeding 99.9%) of concentration perturbation relaxes to the second sound wave, propagating through the solution at the velocity U_i. The remaining purely temperature excitation relaxes to equilibrium slowly and dissipatively due to thermal conductivity of the impuriton gas.

Thus, in an analysis of various kinetic properties in superfluid solutions ^{3}He–^{4}He at low temperatures, we must take into account both hydrodynamic modes, viz., acoustic (19) and dissipative (20) modes, as well as the absence of dissipative diffusion processes in the one-component gas of impuritons.

*E-mail: berezhnoy@pem.kharkov.ua

[1] I. M. Khalatnikov, *Theory of Superfluidity* [in Russian], Nauka, Moscow (1971).

[2] L. V. Gor'kov and L. P. Pitaevskii, Zh. Éksp. Teor. Fiz. **33**, 634 (1957) [Sov. Phys. JETP **6**, 406 (1957)].

[3] A. Griffin, Can. J. Phys. **47**, 426 (1969).

[4] I. Ya. Pomeranchuk, Zh. Éksp. Teor. Fiz. **19**, 42 (1949).

[5] J. Ferzinger and H. Kaper, *Mathematical Theory of Transport Processes in Gases*, North Holland, Amsterdam (1972).

[6] L. D. Landau and E. M. Lifshitz, *Hydrodynamics* 2nd ed. Pergamon 1987.

[7] J. Bodensohn, S. Klesy, and P. Leiderer, Europhys. Lett. **8(1)**, 59 (1989).

[8] V. A. Maidanov, V. A. Mikheev, N. P. Mikhin *et al.*, Fiz. Nizk. Temp. **18**, 943 (1992) [Sov. J. Low Temp. Phys. **18**, 663 (1992)].

[9] T. Satoh, M. Marushita, S. Katoh, *et al.*, Physica **B197**, 397 (1994).

[10] I. N. Adamenko, O. E. Gusev, K. È. Nemchenko, and V. I. Tsyganok, Fiz. Nizk. Temp. **18**, 1085 (1992) [Sov. J. Low Temp. Phys. **18**, 760 (1992)].

[11] S. N. Burmistrov, L. B. Dubovskii, and V. L. Tsymbalenko, J. Low Temp. Phys. **90**, 363 (1992).

[12] I. N. Adamenko, V. K. Chagovets, A. I. Chernanyov *et al.*, J. Low Temp. Phys. **96**, 295 (1994).

[13] S. N. Burmistrov and T. Satoh, Phys. Rev. **B52**, 12867 (1995).

[14] I. M. Lifshits, V. N. Polesskii, and V. A. Khokhlov, Zh. Éksp. Teor. Fiz. **74**, 268 (1978) [Sov. Phys. JETP **47**, 137 (1978)].

[15] I. N. Adamenko and V. I. Tsyganok, Zh. Éksp. Teor. Fiz. **87**, 865 (1984) [Sov. Phys. JETP **60**, 491 (1984)].

[16] I. N. Adamenko and V. I. Tsyganok, Zh. Éksp. Teor. Fiz. **88**, 1641 (1985) [Sov. Phys. JETP **61**, 978 (1985)].

[17] I. N. Adamenko, K. E. Nemchenko, and V. I. Tsyganok, J. Low Temp. Phys. **88**, 15 (1992).

Translated by R. S. Wadhwa

Small-amplitude oscillations of magnetization accompanying long-lived spin-precession in ³He-*B*

G. A. Kharadze, N. G. Suramlishvili, and G. E. Vachnadze

Institute of Physics of the Georgian Academy of Sciences, 6 Tamarashvili st., Tbilisi GE-380077, Georgia[*]

Frequency spectrum of small-amplitude oscillations of magnetization against the background of coherently precessing (phase-correlated) spin modes in superfluid ³He placed in a strong magnetic field depends on the magnitude of spin polarization S and spin-orbit structure of dynamical ordered states. Spectrum of these oscillations is calculated for unconventional precessing modes in ³He-*B* characterized by $S = S_0/2$, where S_0 is the value of S at equilibrium. © *1997 American Institute of Physics.* [S1063-777X(97)00208-9]

The coherent dipole-dipole interaction between nuclear magnetic moments in the superfluid phases of liquid ³He defines (along with other symmetry-breaking terms) the spin-orbit structure of the equilibrium and dynamic (time-dependent) ordered states of ³He-*A* and ³He-*B*.

In the presence of a static magnetic field $\mathbf{H}_0 = H_0\hat{z}$ and a low-amplitude transverse rf field of frequency ω the stable and metastable (long-lived) spin-orbit configurations are realized at the minima of the thermodynamic potential

$$F' = F + \omega \mathbf{S}, \qquad (1)$$

which is constructed in the coordinate frame rotating with an angular velocity $\omega = \omega\hat{z}$ ($\mathbf{S}$ denotes the spin-density). In Eq. (1) F is the sum of the Zeeman and the dipole-dipole energies, so that

$$F = -\omega_0\mathbf{S} + U_D, \qquad (2)$$

where $\omega_0 = \omega_0\hat{z}$ with the Larmor frequency $\omega_0 = gH_0$. Since

$$F' = (\omega - \omega_0)S_z + U_D, \qquad (3)$$

in the absence of the first (spectroscopic) term (at the Larmor resonance $\omega = \omega_0$) the stationary spin-orbit configurations (in the rotating coordinate frame) are defined by the minima of U_D.

For ³He-*B*

$$U_D = \frac{2}{15}\chi_B(\Omega_B/g)^2(\mathrm{Tr}\,\hat{R} - 1/2)^2, \qquad (4)$$

where χ_B is the magnetic susceptibility; Ω_B is the frequency of the longitudinal NMR; and the orthogonal matrix $\hat{R}$ describes the relative rotations of the spin and orbital spaces:

$$\hat{R} = \hat{R}^{(S)}\hat{R}^{(L)-1}. \qquad (5)$$

Here $\hat{R}^{(S)}$ and $\hat{R}^{(L)}$ are the matrices of $3D$ rotations of the spin and orbital degrees of freedom, respectively. Parametrizing these rotations by the triples of Euler angles $(\alpha_S, \beta_S, \gamma_S)$ and $(\alpha_L, \beta_L, \gamma_L)$, we find

$$\mathrm{Tr}\,\hat{R} = s_z l_z + \frac{1}{2}(1+s_z)(1+l_z)\cos(\alpha+\gamma) + \frac{1}{2}(1-s_z)(1-l_z)\cos(\alpha-\gamma) + \sqrt{(1-s_z^2)(1-l_z^2)}(\cos\alpha + \cos\gamma), \qquad (6)$$

where $s_z = \cos\beta_S$, $l_z = \cos\beta_L$, $\alpha = \alpha_S - \alpha_L$, and $\gamma = \gamma_S - \gamma_L$.

The absolute minimum of (4) is realized at $\mathrm{Tr}\,\hat{R} = 1/2$. It occurs, in particular, for the nonprecessing states with $s_z = 1$ and $-1/4 < l_z < 1$. The dynamic counterpart (a mirror image $l_z \leftrightarrow s_z$) of this set of equilibrium states is the Brinkman–Smith (BS) spin-precessing mode with $l_z = 1$ and $-1/4 < s_z < 1$. In the BS mode the magnetization is precessing exactly at the Larmor frequency ω_0 and the Leggett–Takagi (LT) relaxation mechanism is completely switched off ($S_z = \mathrm{const}$).

At $\omega \neq \omega_0$, where in the rotating coordinate frame the action of the static magnetic field is eliminated only partly, a new hierarchy of the long-lived spin-processing states is stabilized in ³He-*B*. These states do not correspond to the absolute minimum of U_D and the LT relaxation mechanism is operative. Among them the most thoroughly explored is the HPD state[1,2] generated at $\omega > \omega_0$. In this situation the spectroscopic term in (3) pushes the left boundary $s_z = -1/4$ of the BS state farther to the left, and the spin-precessing states with $l_z = 1$ and $-1 < s_z < -1/4$ are formed at the balance of the dipole-dipole and spectroscopic forces. For the case where ω exceeds ω_0 only slightly the spin-precession takes place at $s_z \simeq -1/4$ and the LT relaxation is rather slow. Due to the presence of the spectroscopic term, the HPD transforms to the precessing two-domain configuration in the presence of the magnetic field gradient.

An effective way of analyzing other possible long-lived spin-precessing states in ³He-*B* is to consider the case of a strong magnetic field with $\omega_0 \gg \Omega_B$. In this situation the dynamic variables α and γ, which appear in expression (4) for the dipole-dipole potential, are naturally arranged as the fast and slow linear combinations (on the long time scale $1/\Omega_B$). As a good starting approximation one can discard the rapidly oscillating terms in U_D and deal with the average potential $\bar{U}_D$ that contains only slow variables: s_z and l_z and possibly some slow combination of α and γ. In this way, it is easy to construct a proper first-order solution for the coherently precessing spin-states and then to explore small-amplitude oscillations of magnetization [proportional to $(\Omega_B/\omega_0)^2 \ll 1$], superimposed on the ''mean-field'' solution.

When constructing the above-described ''mean-field''

(average) picture, it should be realized that the answer for $\bar{U}_D$ depends crucially on the magnitude $S=|\mathbf{S}|$ of the spin-density of a particular precessing state. For the conventional case of S close to its equilibrium value $S_0=(\chi_B/g)H_0$ a slow angular variable surviving the averaging procedure is $\varphi=\alpha+\gamma$ and corresponding expression for $\bar{U}_D$ was extensively used in Ref. 3. The series of homogeneously precessing, metastable states different from HPD were established as a result of establishing a balance between $\bar{U}_D$, the spectroscopic term, and the action of the finite-amplitude transverse rf field.

The new metastable spin-precessing states were found in Ref. 4 for unconventional situations with $S=S_0/2$ (the HS state) and $S=2S_0$ (the DS state). In these cases (again for $\omega_0\gg\Omega_B$)

$$\bar{U}_D=\frac{1}{10}\chi_B(\Omega_B/g)^2\left[1+2s_z^2l_z^2+(l-s_z^2)(1-l_z^2)\right.$$
$$\left.+\frac{2}{3}\sqrt{(1-s_z^2)(1-l_z^2)}(1+l_z)(1+l_z)\cos\tilde{\varphi}\right], \quad (7)$$

where the slow angular variable $\tilde{\varphi}=\alpha+2\gamma(2\alpha+\gamma)$ for the HS(DS) state. Considering the case of an exact Larmor resonance ($\omega=\omega_0$) and noticing that the stationary value $\tilde{\varphi}_{\mathrm{st}}=\pi$, we see that there are two degenerate spin-orbit configurations: ($s_z\simeq0.75$, $l_z\simeq0.3$), and $s_z\leftrightarrow l_z$. These metastable, coherently precessing, spin states are at the minima of $\bar{U}_D$, not at the true minimum of an exact dipole-dipole potential U_D. For this reason the HS(DS) states, as well as all metastable precessing states considered in Ref. 3, are characterized by the small-amplitude oscillations of the magnetization against the background of the ''mean-field'' dynamics. These oscillations are driven by the dipole-dipole torque, which is nonzero for the metastable dynamic states. For them the LT relaxation is also operative (as mentioned above, only for the HPD at $\omega\simeq\omega_0$ it is anomalously slow because of the closeness to the BS mode). In what follows we study the frequency spectrum of the small-amplitude oscillations of the magnetization, accompanying the long-lived (metastable) spin-precessing state in ^{3}He-B with $S=S_0/2$ (HS mode). This question was explored recently by means of the computer simulation.[5] Here we describe the results of an analytic approach based on the self-consistent separation of the fast and slow spin-dynamics appropriate to the strong field case[6] ($\omega_0\gg\Omega_B$).

Using two pairs of canonically conjugate variables (α,P) and (φ,S) with $\varphi=\alpha+2\gamma$ and $P=S_z-1/2\,S$, we write the Leggett equations in a dimensionless form

$$\dot{\alpha}=-1+\varepsilon\frac{\partial f}{\partial P}, \quad \dot{P}=-\varepsilon\frac{\partial f}{\partial\alpha},$$
$$\dot{\varphi}=2\left[(S-1/2)+\varepsilon\frac{\partial f}{\partial S}\right], \quad \dot{S}=-2\varepsilon\frac{\partial f}{\partial\varphi}, \quad (8)$$

where the time is measured in units of $1/\omega_0$, (P,S) is measured in units of S_0, and $\varepsilon f=U_D/\omega_0 S_0$ with $\varepsilon=2/15(\Omega_B/\omega_0)^2\ll1$. In order to solve the system of equations (8) to the first order in ε, we use a new set of variables $\bar{\alpha}$, $\bar{P}$, $\bar{\varphi}$, and $\bar{S}$ according to the transformation

$$\alpha=\bar{\alpha}+\varepsilon u_\alpha(\bar{P},\bar{S},\bar{\varphi}|\bar{\alpha}),$$
$$P=\bar{P}+\varepsilon u_p(\bar{P},\bar{S},\bar{\varphi}|\bar{\alpha}),$$
$$\varphi=\bar{\varphi}+\varepsilon u_\varphi, \quad S=\bar{S}+\varepsilon u_s \quad (9)$$

with yet unknown functions u_i of slow ($\bar{P},\bar{S},\bar{\varphi}$) and fast ($\bar{\alpha}$) variables. In what follows $\bar{\varphi}$ is a slow variable (along with $\bar{P}$ and $\bar{S}$) since we consider a ''resonating'' regime with $S=1/2+\varepsilon\sigma$.

Implying that $\bar{\alpha}$, $\bar{P}$, $\bar{S}$, and $\bar{\varphi}$ satisfy a set of equations

$$\dot{\bar{\alpha}}=-1+\varepsilon A_\alpha(\bar{P},\bar{S},\bar{\varphi}), \quad \dot{\bar{P}}=\varepsilon A_p(\bar{P},\bar{S},\bar{\varphi}),$$
$$\dot{\bar{\varphi}}=\varepsilon(2\sigma+A_\varphi(\bar{P},\bar{S},\bar{\varphi})), \quad \dot{\bar{S}}=\varepsilon A_s(\bar{P},\bar{S},\bar{\varphi}), \quad (10)$$

we can easily obtain a set of equations for u_i

$$\dot{u}_\alpha=\frac{\partial f}{\partial\bar{P}}-A_\alpha, \quad \dot{u}_p=-\frac{\partial f}{\partial\bar{\alpha}}-A_p,$$
$$\dot{u}_\varphi=2\left(\frac{\partial f}{\partial\bar{S}}+u_s\right)-A_\varphi, \quad \dot{u}_s=-2\frac{\partial f}{\partial\bar{\varphi}}-A_s. \quad (11)$$

Here the functions A_i of the slow variables $\bar{P}$, $\bar{S}$, and $\bar{\varphi}$ are found according to the condition for the absence of secular terms in the solution of Eqs. (11) ($\lim_{\bar{\alpha}\to\infty}|u_i|<\infty$). In this way it can be established that

$$A_\alpha=\frac{\partial\bar{f}}{\partial\bar{P}}, \quad A_p=-\frac{\partial\bar{f}}{\partial\bar{\alpha}},$$
$$A_\varphi=2\left(\frac{\partial\bar{f}}{\partial\bar{S}}+\bar{u}_s\right), \quad A_s=-2\frac{\partial\bar{f}}{\partial\bar{\varphi}}, \quad (12)$$

where $\bar{f}$ and $\bar{u}_s$ denote time-averaged parts of the corresponding functions of the fast variable $\bar{\alpha}$ (without loss of generality it can be assumed that all $\bar{u}_i=0$). Isolating a rapidly oscillating part of the dipole-dipole energy $\tilde{f}=f-\bar{f}$ and noticing that $\dot{u}_i\simeq(\partial u_i/\partial\bar{\alpha})\dot{\bar{\alpha}}=-\partial u_i/\partial\bar{\alpha}$, from Eqs. (11) we find that

$$u_\alpha(\bar{P},\bar{S},\bar{\varphi}|\bar{\alpha})=-\int\frac{\partial\tilde{f}}{\partial\bar{P}}d\bar{\alpha},$$
$$u_p(\bar{P},\bar{S},\bar{\varphi}|\bar{\alpha})=\int\frac{\partial\tilde{f}}{\partial\bar{\alpha}}d\bar{\alpha}, \quad (13)$$
$$u_s(\bar{P},\bar{S},\bar{\varphi}|\bar{\alpha})=2\int\frac{\partial\tilde{f}}{\partial\bar{\varphi}}d\bar{\alpha}.$$

Stationary values of the variables $\bar{P}$, $\bar{S}$, and $\bar{\varphi}$ are found according to the equations

$$\frac{\partial\bar{f}}{\partial\bar{\alpha}}=0, \quad \frac{\partial\bar{f}}{\partial\bar{\varphi}}=0, \quad \frac{\partial\bar{f}}{\partial\bar{S}}=-\sigma. \quad (14)$$

The first of these equations is satisfied identically since $\bar{f}$ is independent of $\bar{\alpha}$. The second one shows that the stationary value $\bar{\varphi}_{\mathrm{st}}=\pi$ and from the last one we see that

$$\overline{S}_{\text{st}} = \frac{1}{2} - \varepsilon \frac{\partial \overline{f}}{\partial \overline{S}}. \tag{15}$$

From the relation $S_z = P + 1/2\, S$ we conclude that the low-amplitude high-frequency oscillations of S_z and $S_\perp$ are given by

$$\delta S_z = S_z - \overline{S}_z = \varepsilon u_z(\overline{\alpha}),$$

$$\delta S_\perp = S_\perp - \overline{S}_\perp = \varepsilon u_\perp(\overline{\alpha}), \tag{16}$$

where

$$u_z(\overline{\alpha}) = u_p(\overline{\alpha}) + \frac{1}{2} u_s(\overline{\alpha}),$$

$$u_\perp(\overline{\alpha}) = \frac{1}{\sqrt{1 - s_z^2}} (u_s(\overline{\alpha}) - u_z(\overline{\alpha}) s_z). \tag{17}$$

Now we can easily pass to S_x and S_y components:

$$S_x = \overline{S}_\perp \cos \overline{\alpha} + \varepsilon (u_\perp(\overline{\alpha}) \cos \overline{\alpha} - \overline{S}_\perp u_\alpha(\overline{\alpha}) \sin \overline{\alpha}),$$

$$S_y = \overline{S}_\perp \sin \overline{\alpha} + \varepsilon (u_\perp(\overline{\alpha}) \sin \overline{\alpha} + \overline{S}_\perp u_\alpha(\overline{\alpha}) \cos \overline{\alpha}). \tag{18}$$

In order to obtain the final results for δS_z, δS_x, and δS_y we must construct, according to Eqs. (13), the oscillatory contributions $u_\alpha(\overline{\alpha})$, $u_p(\overline{\alpha})$, and $u_s(\overline{\alpha})$. After some algebra, from Eqs. (4), (6), and (7) it can be shown that

$$\widetilde{f}(\alpha) = \frac{1}{8} \left[(1 + s_z)^2 (1 + l_z)^2 \cos(\alpha + \varphi) \right.$$

$$+ (1 - s_z)^2 (1 - l_z)^2 \cos(3\alpha - \varphi) \Big]$$

$$+ \frac{1}{2} \sqrt{(1 - s_z^2)(1 - l_z^2)} \left[(1 + s_z)(1 + l_z) \left(\cos \alpha \right. \right.$$

$$+ \cos \frac{\alpha - \varphi}{2} + \cos \frac{3\alpha + \varphi}{2} \right) + (1 - s_z)(1 - l_z) \left(\cos \alpha \right.$$

$$+ \cos \frac{\alpha - \varphi}{2} + \cos(2\alpha - \varphi) + \cos \frac{5\alpha - \varphi}{2} \Big) \Big] + \frac{3}{4} (1$$

$$- s_z^2)(1 - l_z^2) \left[\cos 2\alpha + \cos(\alpha - \varphi) + \frac{4}{3} \cos \frac{\alpha + \varphi}{2} \right.$$

$$+ \frac{4}{3} \cos \frac{3\alpha - \varphi}{2} \right] + (s_z l_z - 1/2) \Big[(1 + s_z)(1$$

$$+ l_z) \cos \frac{\alpha + \varphi}{2} + (1 - s_z)(1 - l_z) \cos \frac{3\alpha - \varphi}{2}$$

$$+ 2 \sqrt{(1 - s_z^2)(1 - l_z^2)} \left(\cos \alpha + \cos \frac{\alpha - \varphi}{2} \right) \Big] \Big]. \tag{19}$$

Using this expression, after some lengthy calculations, we find

$$u_z(\overline{\alpha}) = \sum_{n=1}^{3} [a_n(s_z, l_z) \cos n\overline{\alpha} + a_{n-1/2}(s_z, l_z) \sin(n$$

$$- 1/2)\overline{\alpha}], \tag{20}$$

$$u_\perp(\overline{\alpha}) = \sum_{n=1}^{3} [b_n(s_z, l_z) \cos n\overline{\alpha} + b_{n-1/2}(s_z, l_z) \sin(n$$

$$- 1/2)\overline{\alpha}], \tag{21}$$

and

$$u_\alpha(\overline{\alpha}) = \frac{1}{\sqrt{1 - s_z^2}} \sum_{n=1}^{3} [c_n(s_z, l_z) \sin n\overline{\alpha}$$

$$+ c_{n-1/2}(s_z, l_z) \cos(n - 1/2)\overline{\alpha}], \tag{22}$$

where the coefficients a, b, and c are given in the Appendix.

According to Eqs. (16) and (18) we finally arrive to the following answer for the small-amplitude oscillating components δS_z, δS_x, and δS_y:

$$\delta S_z(t) = \varepsilon \sum_{n=1}^{3} [a_n \cos n\overline{\alpha} + a_{n-1/2} \sin(n - 1/2)\overline{\alpha}], \tag{23}$$

$$\delta S_x(t) = \frac{1}{2} \varepsilon \sum_{n=1}^{3} [d_n^{(+)} \cos(n+1)\overline{\alpha} + d_n^{(-)} \cos(n-1)\overline{\alpha}$$

$$+ d_{n-1/2}^{(-)} \sin(n + 1/2)\overline{\alpha} + d_{n-1/2}^{(+)} \sin(n$$

$$- 3/2)\overline{\alpha}], \tag{24}$$

$$\delta S_y(t) = \frac{1}{2} \varepsilon \sum_{n=1}^{3} [d_n^{(+)} \sin(n+1)\overline{\alpha} - d_n^{(-)} \sin(n-1)\overline{\alpha}$$

$$+ d_{n-1/2}^{(+)} \cos(n - 3/2)\overline{\alpha} - d_{n-1/2}^{(-)} \cos(n$$

$$+ 1/2)\overline{\alpha}], \tag{25}$$

where $d^{(\pm)} = b \pm 1/2\, c$.

Inspection of Eq. (23) shows that the spectrum of longitudinal oscillations of magnetization superimposed on the HS precessing mode comprises high-frequency harmonics with $\widetilde{\omega} \simeq \omega_0$, $2\omega_0$, $3\omega_0$, $1/2\,\omega_0$, $3/2\,\omega_0$, and $5/2\,\omega_0$. The same set of harmonics governs the small-amplitude oscillations of transversal components of the precessing magnetization [see Eqs. (24) and (25), keeping in mind that $d_3^{(+)} = d_{5/2}^{(-)} = 0$].

It should be stressed that the coefficients $a(s_z, l_z)$ are symmetric with respect to the interchange $s_z \leftrightarrow l_z$ (see the Appendix), so that the ''mirror'' precessing HS states found in Ref. 4 for the case of a Larmor resonance ($\omega = \omega_0$) are characterized by identical longitudinal oscillations. In contrast to this observation, the coefficients entering the expressions for δS_x and δS_y have no spin-orbit symmetry and measurement of the spectrum of transverse small-amplitude oscillations in the case of HS mode at $\omega = \omega_0$ can discriminate between the two above-mentioned degenerate spin-orbit states. It can be checked that in the case of the precessing mode I ($s_z \simeq 0.75$, $l_z \simeq 0.3$) the oscillations with $\widetilde{\omega} = 3/2\,\omega_0$ have the largest amplitude. Next are contributions of $\widetilde{\omega} = (1/2\,\omega_0, \omega_0)$, which have about four times smaller amplitudes. In the case of the precessing mode II ($s_z \simeq 0.3$, $l_z \simeq 0.75$) the oscillations with $\widetilde{\omega} = 3/2\,\omega_0$ are again the strongest, but now contributions of comparable amplitudes come from $\widetilde{\omega} = (1/2\,\omega_0, 2\omega_0)$.

604   Low Temp. Phys. **23** (8), August 1997

Kharadze *et al.*   604

Away from the Larmor resonance ($\omega \neq \omega_0$) the states I and II are displaced from their initial positions. In particular, as has been demonstrated in Ref. 7, in the presence of sufficiently large negative spectroscopic term ($\omega < \omega_0$) the state I moves toward a spin-orbit configuration $s_z \simeq 1$, $l_z \simeq 0$, while the state II loses its stability. Expressions for δS_z, δS_x, and δS_y are especially simple for this HS precessing state:

$$\delta S_z(t) = -\varepsilon(\cos\bar\alpha - 2\sin\bar\alpha/2),$$

$$\delta S_x(t) = \frac{2}{3}\varepsilon\sin\bar\alpha/2, \tag{26}$$

$$\delta S_y(t) = \frac{2}{3}\varepsilon\cos\bar\alpha/2.$$

The HS coherently precessing mode in the spin-orbit configuration $s_z \simeq 1$, $l_z \simeq 0$ was recently observed experimentally.[8] It has been identified by means of application of a transverse 90° rf pulse, after which the measurement of the amplitude of an induction signal has allowed to establish the magnitude of the spin polarization of the precessing state. It is certainly the most direct way to identify a spin-precessing mode with $S = S_0/2$ and $s_z \simeq 1$. At the same time, the spectroscopy of small-amplitude oscillations of magnetization accompaning phase-correlated spin-precessing states could serve as an additional source of information about their spin-orbit structure.

We would like to thank Prof. V. Dmitriev for providing us with his recent experimental results prior to publication.

APPENDIX

We give here the expressions for the coefficients appearing in Eqs. (23)–(25). We introduce the transverse components $s_\perp = \sqrt{1 - s_z^2}$ and $l_\perp = \sqrt{1 - l_z^2}$:

$$a_1 = 3s_z s_\perp l_z l_\perp - \frac{1}{4}(1 + s_z)^2(1 + l_z)^2,$$

$$a_2 = \frac{1}{4}[3(s_\perp l_\perp)^2 - s_\perp(1 - s_z)l_\perp(1 - l_z)],$$

$$a_3 = -\frac{1}{12}(s_\perp l_\perp)^2,$$

$$a_{1/2} = -4(1 + s_z)(1/2 - s_z)(1 + l_z)(1/2 - l_z),$$

$$a_{3/2} = -\frac{2}{3}[s_\perp(1 + s_z)l_\perp(l + l_z) - 2(1 - s_z)(1/2 + s_z)(1 - l_z)(1/2 + l_z)],$$

$$a_{5/2} = \frac{2}{5}s_\perp(1 - l_z)l_\perp(1 - l_z). \tag{A1}$$

These coefficients have spin-orbit symmetry (they are invariant at $s_z \leftrightarrow l_z$). On the other hand, the coefficients b and c have no such symmetry:

$$b_1 = \frac{1}{2}s_\perp\left[3l_\perp^2 - \frac{1}{2}(1 + s_z)(1 + l_z)^2\right] - 3s_z^2 l_\perp l_z,$$

$$b_2 = \frac{1}{4}[(2 + s_z)(1 - s_z)l_\perp(1 - l_z) - 3s_\perp s_z l_\perp^2],$$

$$b_3 = \frac{1}{12}s_\perp(1 - s_z)(1 - l_z)^2,$$

$$b_{1/2} = -2[3s_z l_\perp l_z + 2s_\perp(1/2 - s_z)(1 + l_z)(1/2 - l_z)],$$

$$b_{3/2} = -\frac{2}{3}[(1 + s_z)(1/2 - s_z)l_\perp(1 + l_z) + 2s_\perp(1/2 + s_z) \\ \times (1 - l_z)(1/2 + l_z)],$$

$$b_{5/2} = -\frac{2}{5}(1 - s_z)(1/2 + s_z)(1 - l_z)l_\perp; \tag{A2}$$

$$c_1 = s_\perp\left[\frac{1}{2}(1 + s_z)(1 + l_z)^2 - 3s_z l_\perp^2\right] - 6(1 - 2s_z^2)l_\perp l_z,$$

$$c_2 = \frac{3}{2}s_\perp s_z l_\perp^2 - (1 - s_z)(1/2 + s_z)l_\perp(1 - l_z),$$

$$c_3 = -2b_3,$$

$$c_{1/2} = 4[3(1 - 2s_z^2)l_\perp l_z + s_\perp(1 + 4s_z)(1 + l_z)(1/2 - l_z)],$$

$$c_{3/2} = \frac{4}{3}[s_\perp(1 - 4s_z)(1 - l_z)(1/2 + l_z) - (1 + s_z)(1/2 \\ - s_z)(l_\perp(1 + l_z)],$$

$$c_{5/2} = 2b_{5/2}. \tag{A3}$$

*E-mail: khar@physics.iberiapac.ge

[1] Yu. M. Bunkov, in *Progress in Low Temperature Physics*, V. 24, W. P. Halperin (Ed.), Elsevier Science (1995), p. 69.
[2] I. A. Fomin, in *Modern Problems of Condensed Matter* Sciences, V. 26: *Helium Three*, W. P. Halperin and L. P. Pitaevskii (Eds.), North Holland, Amsterdam (1990), p. 610.
[3] G. E. Volovik, J. Phys.: Condens. Matt. **5**, 1759 (1993).
[4] G. Kharadze and G. Vachnadze, JETP Lett. **56**, 458 (1992).
[5] V. V. Dmitriev, private communication.
[6] I. A. Fomin, JETP **50**, 144 (1979).
[7] G. E. Vachnadze and N. G. Suramlishvili, Low Temp. Phys. **22**, 545 (1996).
[8] V. V. Dmitriev et al., Phys. Rev. Lett. **7**, 86 (1997).

605   Low Temp. Phys. 23 (8), August 1997

Kharadze *et al.*   605

SUPERCONDUCTIVITY, HIGH-TEMPERATURE SUPERCONDUCTIVITY

Scaling of critical current in granular HTS materials

N. A. Bogoliubov

Institute of Inorganic Chemistry, Siberian Branch of Russian Academy of Sciences, 630090 Novosibirsk, Russia*

The temperature and size dependences of critical current of three bismuth-based and one yttrium-based ceramic samples of rectangular cross sections in zero magnetic field are studied by a contactless method. It is shown that the critical current in ceramic HTS can be presented as the product of temperature- and size-dependent factors. The temperature-dependent factor describes the individual properties of Josephson net for each sample, while the size-dependent factor is a universal homogeneous function whose index is independent of the ratio of the sides of the cross section, temperature, and individual properties of the HTS sample. © *1997 American Institute of Physics.* [S1063-777X(97)00308-3]

INTRODUCTION

A granular high-temperature superconductor is a system of granules forming a three-dimensional Josephson network of weak bonds.[1] In a strong applied field, most of these bonds are ruptured, and such a superconductor can be regarded as an ensemble of noninteracting granules.[2] In the case of weak fields smaller than the lower critical field of the grains, the properties of the granular system can be described in the framework of weak-field electrodynamics of HTS materials.[3–5] However, the experimental study of the effect of such fields (of a few oersteds) on the critical current in a ceramic sample is complicated since the contribution from the field created by the transport current itself becomes significant. Different regions of a spatially homogeneous sample are in fields of different intensities during the passage of current, since each intergranular junction is in the overall field created by currents passing through other branches of the Josephson network. Consequently, the only method of control for this field is probably the variation of the sample cross section. However, most of authors investigated the so-called size effect, viz., the dependence of the critical current I_c and its average density on the size of the cross section of a ceramic HTS sample in zero field for various sample cross sections.[3,6–17] It was found[10] that the change in the height and width of the sample of rectangular cross section leads to different changes in the magnitude of critical current. The size effect is associated with the magnetic field created on the sample surface by the critical current passing through it.[10,14,16]

In this paper, we analyze the dependence of critical current on the temperature and size of the rectangular cross section of some HTS samples in zero external magnetic field. It is shown that the functional dependence of critical current can be presented in the form of the product of two factors. The size factor is a homogeneous Euler function,[18] i.e., the critical current of an HTS ceramic obeys the similitude principle. We will not use these or other empirical dependences of critical current on magnetic field in analyzing the result

since these dependences cannot be regarded as reliably substantiated in the general case.

OBJECTS AND METHODS OF INVESTIGATIONS

We analyzed the dependence of the critical current of four ceramic HTS samples on the size of rectangular cross section (samples 1–4) and on temperature (sample 1) in zero external field. All the samples were prepared by using solid-phase synthesis. Sample 1 ($Bi_{1.8}Pb_{0.3}Sr_{1.9}Ca_2Cu_3O_x$) had the density 4.75 g/cm^3 and the superconducting transition temperature $T_c = 106.3$ K, sample 2 (Y–123) had the parameters 4.97 g/cm^3 and $T_c = 91.2$ K, sample 3 ($Bi_{1.6}Pb_{0.4}Sr_2Ca_2Cu_3O_x$) had the density 4.71 g/cm^3 and $T_c = 109.1$ K, while sample 4 ($Bi_{1.8}Pb_{0.3}Sr_{1.9}Ca_{2.6}Cu_{3.3}O_x$) had the density 4.87 g/cm^3 and $T_c = 108.6$ K. The x-ray phase analysis did not reveal the presence of the Bi-2212 phase in samples 1, 3, and 4, but $CaCuO_3$ was present in sample 3 in the form of the impurity phase.

The critical current was measured by the contactless transformer technique, which is widely used for studying HTS objects.[10,16,19] The sample in the shape of a ring having a rectangular cross section was placed inside a ferrite case-type magnetic core together with the primary and the measuring winding of a transformer. When ac current was passed through the primary, a current of the opposite direction was induced in the superconducting ring so that the magnetic flux accumulated by the central kernel of the case-type core and passing through the hole in the ring and through remaining windings remained unchanged. When the current amplitude in the ring approaches the value of the critical current and exceeds it, a signal in the form of a sharp peak is induced in the measuring winding. The magnitude of critical current is recorded at the moment of emergence of the signal and calculated from the relation $I_c = n_1 I_1$, where n_1 and I_1 are the number of turns and the amplitude of the current in the primary. The values of I_c were measured at frequency 20 Hz. The electric field in the sample at the instant of I_c recording amounts to $\sim 10^{-2}$ μV/cm. At each fixed temperature,
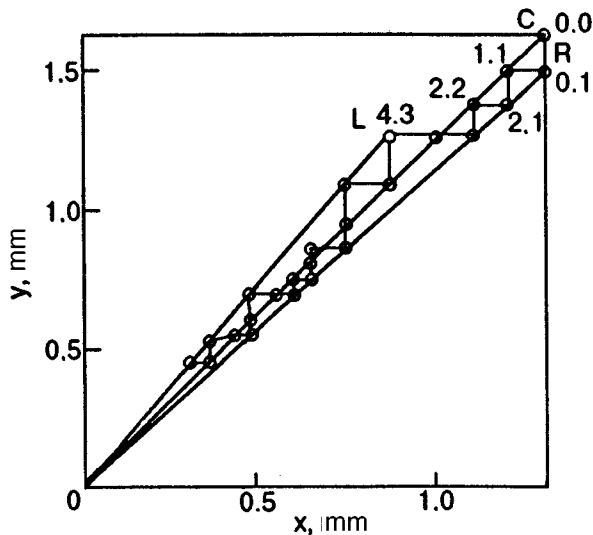
FIG. 1. Diagram illustrating the variation of cross section of sample 3. The indices of the points are indicated only for initial cross sections.

FIG. 2. Temperature dependence of critical current in sample 1 for various cross sections (in mm): 1.140×1.542, ($\bigcirc$) 0.955×1.283, ($\square$) 0.855×1.150, ($\triangle$) 0.693×0.831, ($\diamondsuit$) and 0.554×0.748; ($*$) I_T is the normalized dependence of the critical current in this sample: $I_T = I_c(x,y,T)/I_c(x,y,77.3 \text{ K})$.

10–20 measurements were made. The spread in the values of I_c obtained in this way did not exceed a few thousandth and amounted to 1% only in rare cases. The size of the samples was measured with the help of a clock-type indicator. Then the sample was cooled, and the values of I_c were measured at liquid nitrogen temperature (samples 2, 3, and 4) or in the temperature range from T_c to 77.3 K (sample 1). After this, the sample was heated, its size was measured, and the measuring cycle was repeated. Such a sequence of procedures could lead to a change in the superconducting parameters of the sample. For this reason, the value of T_c of the sample was measured every time during heating and cooling. The critical current of the first sample was measured at liquid nitrogen temperature immediately after cooling as well as before the extraction of the sample from the cryostat at the end of the experiments. If the sample was extracted in a day or two after the main measurements, the values of I_c were measured repeatedly for all the samples at 77.3 K. The constancy of the parameters being measured indicated that the superconducting properties of the sample remained unchanged.

The width x and height y of sample 1 were varied in proportion, and hence all the seven sizes of the cross section (from 1.140×1.542 to 0.554×0.746 mm^2) were similar. The size of the cross section of sample 2 changed according to a similar regularity. The values of I_c were measured for six similar cross sections from 1.945×2.768 to 1.122×1.333 mm. The variation of cross section of sample 3 followed a more complex regularity shown by the step line in Fig. 1. For this purpose, three families of similar cross sections of the sample were obtained. The first family contained five similar cross sections associated with the diagonal OL in Fig. 1 (from 0.855×1.245 to 0.302×0.447 mm). The second family included 12 cross sections pertaining to diagonal OC. The third family associated with the straight line OR was formed by seven cross sections from 1.310×1.147 to 0.483×0.550 mm. The critical current of the fourth sample was measured for two families of similar cross sec-
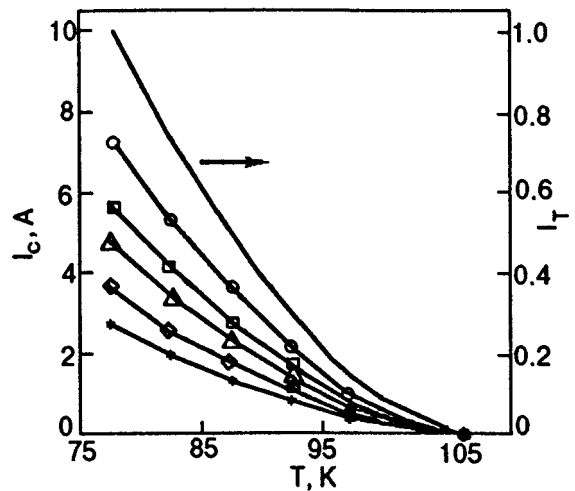
tions (from 1.280×1.280 to 0.645×0.645 mm and from 1.280×1.100 to 0.748×0.645 mm). As a result, we obtained a set of results for seven families of similar cross sections with values of tan α varying from 1.43 to 0.859 (α is the angle formed by the diagonal of the rectangular cross section with the x-axis).

DISCUSSION OF RESULTS

We start from an analysis of data obtained for the first sample. The temperature dependence of critical current for five different cross sections is shown in Fig. 2. For each cross section, we obtain the dependences presented by the upper curve I_T in Fig. 2 by dividing the experimentally determined value of critical current by the value of current at liquid nitrogen temperature. The values of I_T obtained for different cross sections are so close that the corresponding points in Fig. 2 cannot be distinguished on the adopted scale, and hence only the curve connecting these points is presented. If we carry out such a normalization for another sample, we obtain a different temperature dependence of I_T since each sample is characterized by its own superconducting transition temperature, and the normalized dependences will pass through zero at different values of T_c.[16] Thus, we can draw the conclusion that such a dependence of critical current is a characteristic of the ceramic sample material and is completely determined by the temperature:

$$I_T(T) = I_c(x,y,T)/I_c(x,y,T_0). \tag{1}$$

The form of this dependence remains unchanged for any other choice of the value of T_0.

Figure 3 shows the dependence of critical current through sample 1 on the length of the diagonal of its cross section at various temperatures. It can be seen that the critical current decreases nonlinearly upon a decrease in the sample size. Since all intermediate cross sections are similar, it would be interesting to find the ratio of the critical currents
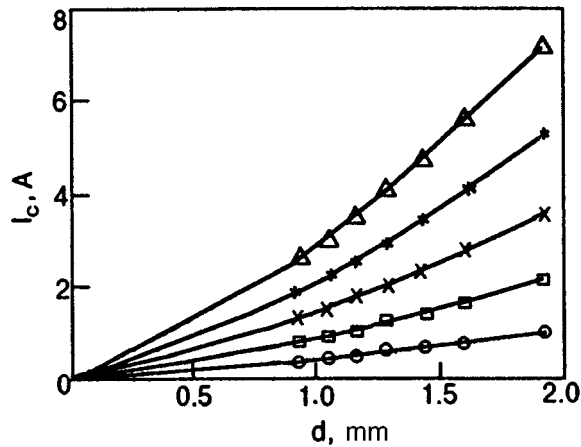
FIG. 3. Dependence of the critical current in sample 1 on the length of the diagonal of its cross section for various temperatures, K: 97.1 (○), 92.45 (□), 87.55 (×), 82.5 (*), and 77.3 (△).

corresponding to these cross sections, i.e., we are interested in the dependence of the quantity $I_G = I_c(x_i, y_i, T)/I_c(x_0, y_0, T)$ on k_i, where $k_i = x_i/x_0 = y_i/y_0$ according to the model used in our experiments. In view of inevitable errors, a rigorous equality of the ratios of the sided for the cross sections under investigation cannot be obtained. For this reason, the quantity k_i was defined as $k_i = 0.5(x_i/x_0 + y_i/y_0)$. Figure 4 shows the dependence of I_G on k for five temperature values on the log–log scale. The quantities corresponding to the fourth cross section of the sample (counting from the initial cross section) are used as normalization values. The same figure shows the results of measurements for sample 2 normalized to the values corresponding to the third cross section of the sample as well as the results of measurements for sample 3 normalized to the
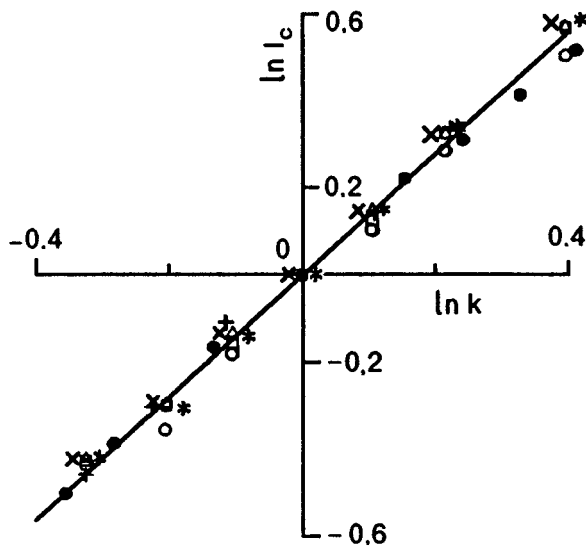

FIG. 4. Dependence of the relative current in sample 1 on the relative size of the sample (notation is the same as in Fig. 3) for different temperatures and in samples 2 (+) and 3 (●) at 77.3 K. The results obtained at 87.55 K (×) are displaced to the left, and at 82.5 K (*) to the right along the axis $\ln k$ by 0.014.

results corresponding to the point x_4, y_4 (see Fig. 1). It can be seen that all the points fit into the universal linear dependence

$$\ln I_G = p \ln k. \tag{2}$$

If we plot the points obtained for another choice of normalization values, we obtain a continuation of the obtained curve (these points are not shown in Fig. 4 to avoid complication of the diagram), i.e., the relation $I_G(k)$ does not depend on the choice of normalization values. Consequently, we can write

$$I_c(kx, ky) = k^p I_c(x, y), \tag{3}$$

i.e., the critical current of a granular HTS sample in zero external field, which is regarded as a function of the size of the rectangular cross sections, is a homogeneous Euler function with exponent p. The value of p can be determined with the help of the least squares technique by using the static model (2) which does not contain a free term since the critical current should not change upon an identity transformation of the space into itself (i.e., for $k=1$). Evaluating the exponent p for sample 1 in each temperature series of the results of measurements, we obtain a set of values coinciding within confidence intervals, i.e., these values can be averaged. Moreover, the verification confirms the validity of zero-point hypothesis concerning the equality of general mean values (for confidential probability of 0.95).[20] Consequently, having determined the mean value, we ultimately obtain $p = 1.40 \pm 0.03$. Here and below, confidence intervals are determined by using quantiles of the Student distribution with a confidential probability of 0.95. Thus, the exponent of the Euler function does not depend on temperature, and hence the relative current I_G does not depend on T and is determined only by the geometrical parameters:

$$I_G(x, y) = I_c(x, y, T)/I_c(x_0, y_0, T). \tag{4}$$

Let us prove that the value of the index p does not depend on the properties of a specific Josephson network existing in the sample or on the ratio of the sides of the rectangular cross section of the sample. We use the experimental results obtained at 77 K for samples 2, 3, and 4. Figure 5 shows the dependence of I_G on k on the log–log scale for three families of similar cross sections of sample 3 and two families for sample 4. The values corresponding to the initial sample cross sections are used for normalization. It can be seen that all the points fit into the same linear dependence, i.e., the results of measurements made for samples 3 and 4 satisfy the definition of a homogeneous function. The values of p obtained separately for each family of similar cross sections of sample 3 coincide to within confidence intervals. The criterion confirming the validity of the hypothesis concerning the equality of mean values is satisfied, i.e., the values of exponents obtained for three families of cross sections for sample 3 can be averaged. Finally, we obtain $p = 1.36 \pm 0.07$. The same refers to the results obtained for sample 4. In this case, $p = 1.42 \pm 0.04$. For sample 2, we obtain $p = 1.36 \pm 0.05$, i.e., the fact that the point in Fig. 4 corresponding to the results of measurements for three sample fit into the universal dependence is not accidental. In
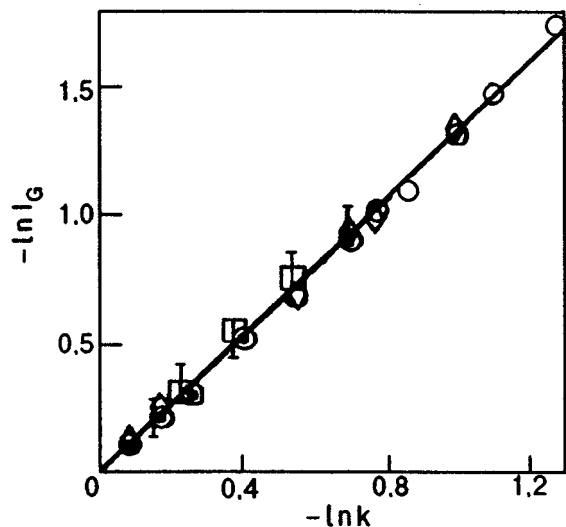
FIG. 5. Dependence of the relative current I_G in samples 3 and 4 on the ratio of the corresponding sides of similar cross sections: the results obtained for the central, left, and right diagonals are marked by $\bigcirc$, $\bullet$, and $\diamondsuit$, respectively (see Fig. 1), I and $\square$ mark the points corresponding to cross sections of sample 4 of square and rectangular shape, respectively.

FIG. 7. Correspondence of experimental results obtained for sample 3 to Euler's theorem. The symbols $\bigcirc$, $\bullet$, and $\diamondsuit$ indicate the values obtained for points lying on the diagonals OC, OL, and OR, respectively (see Fig. 1).

Fig. 6, the values of the ratios of sides for seven families of similar cross sections of the four samples under investigation are laid along the abscissa axis, while the values of exponents for the corresponding cross sections with confidence intervals are plotted along the ordinate axis. It can be seen that no dependence of the exponent on the value of $\tan \alpha$ can be traced. Calculating the weight-average value, we obtain $p = 1.39 \pm 0.02$. Thus, the exponent does not depend on temperature, or on the type of the sample, or on the ratio of the sides of its rectangular cross section. In other words, the dimensionless current $I_G(k)$ is a universal function. The same result, i.e., relations (1) and (4), was obtained by us earlier,[16] but in contrast to this research, we measured only the sample width at a constant height, and successive cross sections were not similar. The dependence $I_G(x, y_0)$ was more complicated, but was universal, i.e., independent of sample material and temperature.
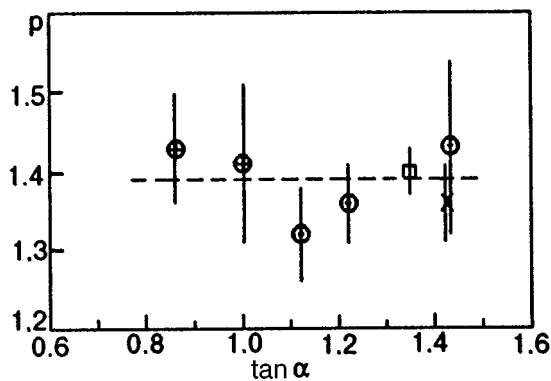

FIG. 6. Values of the exponent of the homogeneous function, obtained for cross sections of the samples with different ratios of sides. Symbols $\square$, $\times$, $\odot$, and $\oplus$ correspond to samples 1, 2, 3, and 4, respectively. Vertical lines indicate confidence intervals. The dashed line corresponds to the average value of the exponent p.
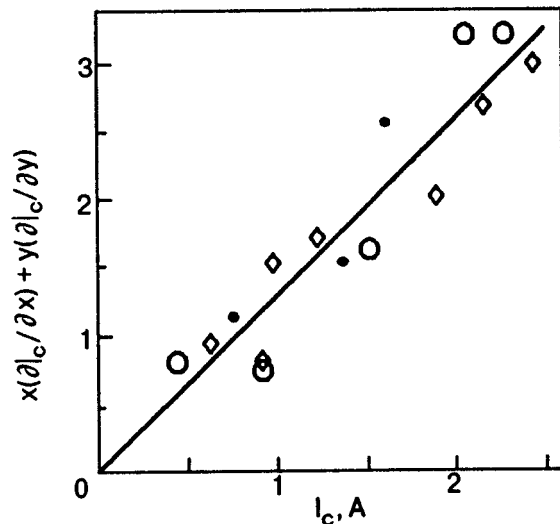
We arrive at the conclusion that experimental data can be presented in the form of the dimensionless currents $I_T(T)$ and $I_G(x,y)$ irrespective of the way in which the sample dimensions are varied. According to the experimental facts (1) and (4), the critical current of a granular HTS material in zero external field has the form

$$I(x,y,T) = G(x,y)f(T), \tag{5}$$

where $G(x,y)$ is a function depending only on the sample size and $f(T)$ the individual characteristic of the material of the specific sample. Equation (5) shows that it is $G(x,y)$ that is a homogeneous Euler's function:

$$G(kx,ky) = k^p G(x,y). \tag{6}$$

Let us prove that the critical current in a granular superconductor not only corresponds to the definition of a homogeneous function, but also possesses all the properties of such a function. Above all, Euler's theorem[18] must be satisfied:

$$x(\partial I_c / \partial x) + y(\partial I_c / \partial y) = pI_c, \tag{7}$$

i.e., the combination of derivatives on the left-hand side is proportional to critical current, and the proportionality factor must coincide with the value obtained earlier. The experimental data obtained for sample 3 make it possible to determine the required derivatives by using the difference method. Figure 7 shows that the dependence under consideration is linear indeed, i.e., Euler's theorem is valid. Approximating the obtained results by Eq. (7), we obtain the value of exponent $p = 1.3 \pm 0.2$, which coincides with the one obtained earlier. The larger confidence interval is associated with the errors emerging in the evaluation of derivatives. Since the number of points at which the derivatives can be evaluated is small, we do not divide them into groups associated with a certain family of similar cross sections during approximation, but different symbols are used in Fig. 7 for denoting points forming such groups.
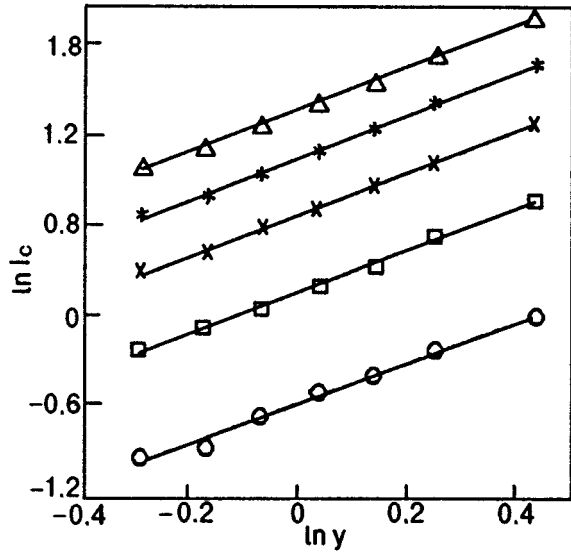
FIG. 8. Correspondence of experimental results obtained for sample 1 to relation (5) at different temperatures (notation is the same as in Fig. 3).

For the critical current $I_c(x,y,t)$ to be a homogeneous function of the variables x and y, it is necessary and sufficient that it can be represented in the form[18]

$$I_c(x,y) = x^p F_1(y/x) f(T). \qquad (8)$$

Since the coordinates x and y are equivalent, the condition

$$I_c(x,y) = y^p F_2(x/y) f(T). \qquad (9)$$

is satisfied simultaneously. Such a representation of experimental data for similar cross sections can be satisfied easily since the ratio of the sides x and y remains unchanged, and hence the functions $F_1(y/x)$ and $F_2(x/y)$ are constants, while I_c depends only on x or only on y. Figure 8 shows the dependence of the critical current in the first sample in double logarithmic coordinates at five temperatures. The curves are displaced relative to one another due to the presence of the factor $f(T)$ in Eq. (9), which has different values at different temperatures. If the results for sample 3 are presented in such coordinates, we obtain three straight lines that are displaced relative to one another. In this case, the shift is caused by the factor $F_2(x/y)$ in (9), which assumes different values for different families of identical cross-sections of sample 3. Going over to new variables in Eq. (3), viz., the length d of the cross-sectional diagonal and angle α, and putting $k = 1/d$, we obtain $I_c(d,\alpha,T) = d^p \varphi(\alpha,T)$. For samples with identical cross sections, the critical current depends only on d. This dependence is shown by solid curves in Fig. 3. Thus the critical current in a granular superconductor satisfies the definition of a homogeneous function and possesses all its properties. Note that the dependence of critical current on temperature and cross-section may change in the vicinity of T_c. We shall show that formulas (5) and (6) are valid at least for $\tau > 0.085 [\tau = (T_c - T)/T_c]$.

Formula (5) leads to the similitude law which is obeyed by the critical current in a ceramic superconductors in zero fields. Indeed, introducing the relative current I_G with the help of formula (5), we eliminate the individual properties of the sample material:

$$I_G = G(x,y)/G(x_0,y_0). \qquad (10)$$

In view of this relation, any set of ceramic samples has the same size dependence of the relative current. The size of the rectangular transverse cross-section of the samples being compared must vary according to the same law. Let us consider a few examples. If an arbitrary cross-section of a sample is identical to its preceding and succeeding cross-sections, we obtain the relation $I_G = k^p$ from (10) with the help of (6). In this case, the cross-sections of different samples need not be identical. This situation is illustrated by the straight line in Fig. 5. If, for example, only the width x of the samples changes while their height y_0 remains unchanged for all samples as in Ref. 16, the curve describing the law of similitude will reflect the behavior of the function $F_2(x/y_0)$ in (9): $I_G = F_2(x/y_0)/F_2(x_0/y_0)$. If two samples have identical cross sections, the ratio of their critical currents will be defined in terms of their temperature factors:

$$I_1/I_2 = (x_1/x_2)^p f_1(T)/f_2(T).$$

It can be naturally assumed that the obtained results are valid not only for samples with rectangular cross sections. This raises the question about the magnitude of the index for samples with other types of cross section. It has been shown in numerous investigations that the critical current of ceramic superconductors depends significantly on the magnetic field. In our experiments, the external magnetic field was equal to zero, and the sample was subjected only to the magnetic field produced by the current flowing in it. Such a field depends on the sample shape, and hence it can be expected that the index p will also depend on the shape of the cross section. For a circular sample, the function G depends only on its radius R. Putting $k = 1/R$, we obtain from (5) and (6)

$$I_c(R,T) = CR^p f(T),$$

where C is a constant. On the other hand, the current in such a sample and the field produced by it must be connected through a relation that is obeyed for all currents, including the critical current: $I_c = c/2\,RH_f$, where H_f is the field produced by the critical current at the sample surface. The similarity of these two expressions leads to the conclusion that $p = 1$ and $f(T)$ coincides with H_f but for a constant factor, i.e., $f(T)$ has the meaning of the magnetic field produced by the critical current at the sample surface and transforming the sample to the critical state.

Most of the works devoted to the critical current investigations of HTS objects contain data on the average critical current density $j_c = I_c/S$ (S is the sample cross-sectional area). Using (3), we determine the average critical current density of the sample whose rectangular cross-sectional dimensions are changed by a factor of k:

$$j_c(kx,ky) = k^{p-2} j_c(x,y).$$

Thus, the average critical current density is also a homogeneous Euler function albeit with a different index $p_j = p - 2$. Since $p = 1.38$, we find that $p_j < 0$ and j_c increases upon a

gradual reduction of the sample size. However, the divergence of j_c is not observed, since the nature of the $j_c(x,y)$ dependence changes as soon as the cross section becomes comparable with the size of the HTS grains (or a block of grains).

Let us consider the dependence of I_c and j_c on the cross-sectional area. Using (8) and (9), we obtain

$$I_c = S^{p/2}\Psi(x,y), \quad j_c = S^{p/2-1}\Psi(x,y).$$

It can be seen that a decrease in the cross-sectional area leads to a decrease in the critical current and an increase in j_c. However, it was stated above that this increase cannot be indefinite. Several authors have endeavored to express the variation of j_c as a power function of S. The values $-1/2$, $-1/3$, and -1 of exponents were obtained in Refs. 3, 8, 12 respectively. Nevertheless, it follows from what has been stated above that the nature of variation of j_c depends on the sample shape as well as the manner in which the shape is varied. For example, if the size of a sample having a rectangular cross section is varied in proportion, the exponent of S will be approximately equal to -0.3, which is close to the result obtained in Ref. 8.

CONCLUSIONS

An analysis of the obtained results shows that the critical current in HTS ceramic samples of rectangular cross section in zero external magnetic field can be presented as the form of the product of a factor determined by the sample geometry and a temperature-dependent factor reflecting individual properties of the Josephson network of the sample: $I_c(x,y,T) = G(x,y)f(T)$, where $G(x,y)$ is a homogeneous function of power p: $G(kx,ky) = k^p G(x,y)$, $p = 1.39 \pm 0.02$. It is shown that the exponent of the homogeneous function depends neither on temperature, nor on the material of the HTS sample, nor on the ratio of the sides of its cross section. In all probability, the index p for a sample of another shape will have a different value. The above properties of critical current imply that it must obey the similitude law, and the average density of critical current is a homogeneous function of degree $p-2$.

*E-mail: mart@casper.che.nsk.su

[1] J. R. Clem, Physica **C153−155**, 50 (1988).
[2] V. V. Val'kov and B. P. Khrustalev, Zh. Éksp. Teor. Fiz. **107**, 1221 (1995) [JETP **80**, 680 (1995)].
[3] H. Dearch and G. Blatter, Phys. Rev. **B38**, 11391 (1988).
[4] S. L. Ginzburg, G. Yu. Logvinova, I. D. Luzyanin *et al.*, Zh. Éksp. Teor. Fiz. **100**, 532 (1991) [Sov. Phys. JETP **73**, 292 (1991)].
[5] K.-H. Müller, Physica **C159**, 717 (1989).
[6] A. A. Zhukov, D. A. Komarkov, V. V. Moshchalkov *et al.*, Physica **C162−164**, 1623 (1989).
[7] L. U. Grant, Mat. Lett. **8**, 346 (1989).
[8] S. I. Zakharchenko, V. Mityushin, N. A. Podlevskikh, and L. M. Fisher, Sverkhprovodimost': Fiz. Khim., Tekh. **2**, 136 (1989).
[9] A. A. Zhukov, D. A. Komarkov, V. V. Moshchalkov *et al.*, Sverkhprovodimost': Fiz. Khim., Tekh. **3**, 1234 (1990).
[10] G. P. Meisner and C. A. Taylor, Physica **C169**, 303 (1990).
[11] C.-W. Cheng, A. C. Rose-Innes, N. McAlford, and T. W. Button, Supercond. Sci. Technol. **3**, 90 (1990).
[12] A. A. Zhukov, V. V. Moshchalkov, D. A. Komarkov *et al.*, Jpn. J. Appl. Phys. **29**, L760 (1990).
[13] B. H. Kliem, A. Wegers, and J. Lutzner, J. Appl. Phys. **69**, 1534 (1991).
[14] C. A. D'ovido, J. E. Fiscina, and D. A. Esparza, J. Appl. Phys. **69**, 8265 (1991).
[15] E. Babic, M. Prester, D. Drobac *et al.*, Phys. Rev. **B45**, 913 (1992).
[16] N. A. Bogoliubov, Sverkhprovodimost': Fiz. Khim., Tekh. **7**, 294 (1994).
[17] C. R. H. Grovenor, S. Fix, and J. C. Mare, Physica **C257**, 332 (1996).
[18] J. Aczel, *Lectures on Functional Equations and Their Applications*, Academic Press, New York–London (1966).
[19] E. A. Harris, J. E. L. Bishop, R. L. Havill, and P. J. Ward, J. Phys. **C21**, L673 (1988).
[20] E. I. Pustyl'nik, *Statistical Methods of Analysis and Observation Data Processing* [in Russian], Nauka, Moscow (1968).

Translated by R. S. Wadhwa

On peculiarities of superconducting state formation in $2D$ metallic systems

V. P. Gusynin, V. M. Loktev, and S. G. Sharapov

N. N. Bogoliubov Institute of Theoretical Physics, National Academy of Sciences of the Ukraine, 252143 Kiev, Ukraine[*]

It is shown that the phase diagram of a $2D$ metal with a varying charge carrier density consists of normal phase regions in which the modulus of the order parameter is zero, the so-called anomalously normal phase in which it differs from zero but has a random phase, and the Berezinskii–Kosterlitz–Thouless phase. The characteristic temperatures of transitions between these phases are determined as well as the behavior of the chemical potential as a function of the fermion density and temperature. An attempt is made to compare qualitatively the obtained phase diagram with the observed peculiarities in the behavior of underdoped high-T_c superconducting compounds above their critical temperature. © *1997 American Institute of Physics.* [S1063-777X(97)00408-8]

1. Peculiarities of the crossover region bounded by the limiting cases of superconductivity of condensate of Cooper pairs on one side and the superfluidity of compound bosons on the other hand have attracted the attention of scientists for a long time in connection with a more general problem of description of high-T_c superconductors (HTS materials) (see, for example, Ref. 1). The situation for $3D$ systems at zero and finite temperatures is more or less clear,[2] the crossover in quasi-$2D$ systems has also been studied (although incompletely),[3] while for $2D$ systems, only the case $T=0$ has been in fact investigated.[2,4] The latter circumstance is due to the fact that phase fluctuations of the charged complex order parameter in $2D$ systems are so strong that the establishment of the long-rage order in such systems is ruled out for any finite T (the Hohenberg theorem). The description of the formation of a nonhomogeneous condensate with an exponential decrease of correlations, including superconducting ones (the so-called Berezinskii–Kosterlitz–Thouless (BKT) phase), involves certain complications of mathematical origin. Nevertheless, certain advances have been made in this direction also. For example, the BKT transition in the relativistic field theory 2 + 1 was studied by MacKenzie *et al.*,[5] while a crossover in the value of charge carried density n_f from superconductivity to superfluidity was analyzed by Drechsler and Zwerger.[6] However, the method used in Ref. 6 for obtaining the BKT transition temperature T_{BKT} has a number of drawbacks. For example, the equation for T_{BKT} was derived without taking into account the existence of a neutral order parameter ρ whose nonzero value is associated with the violation of discrete symmetry alone, and hence does not contradict the Hohenberg theorem. It will be shown below that the inclusion of this parameter leads to the emergence of a finite region with $\rho \neq 0$ on the phase diagram, which separates the conventional normal phase (NP) and the BKT phase. In spite of the exponential decrease in correlations in this new (nonsuperconducting) region, it can possess peculiar properties since the quantity ρ appears in the expression for observables in the same way as the energy gap Δ in the theory of traditional superconductors. In other words, the electron spectrum of the new phase differs considerably from

the spectrum of metals in their NP. The existence of this phase (which is also normal in a certain sense) will probably explain the anomalous behavior sometimes observed for the normal state of HTS materials, namely, the temperature dependences of spin susceptibility, resistance, heat capacity, photoemission and optical spectra, etc.,[7,8] which are being interpreted by using widely the concept of pseudogap (as well as the spin gap) formed at a certain temperature exceeding T_c considerably in some cases. Sometimes, even two or three such temperatures corresponding to the emergence of certain anomalies are used.

This communication aims at obtaining an n_f vs. T phase diagram of a $2D$ metal with attraction between charge carriers and calculating the values of T_{BKT} and T_ρ bounding the region of ''anomalously normal'' phase (ANP) as functions of n_f (T_ρ is the temperature at which ρ vanishes).

2. The density of the simplest Hamiltonian describing $2D$ fermions in volume v has the form

$$H_{(x)} = \psi_\sigma^+(x)\left[-\frac{\nabla^2}{2m} - \mu \right]\psi_\sigma(x)$$
$$- V\psi_\uparrow^+(x)\psi_\downarrow^+(x)\psi_\downarrow(x)\psi_\uparrow(x), \tag{1}$$

where $x \equiv \mathbf{r}, \tau; \psi_\sigma(x)$ is the Fermi field, m and σ are the effective mass and spin of fermions, μ is their chemical potential, V the attraction constant, and $\hbar = k_B = 1$.

In order to calculate the required phase diagram, we use the Hubbard–Stratonovich method (see, for example, Ref. 4) which has become a standard approach for solving such problems. In this method, the partition function $Z(v, \mu, T)$ is a functional integral over Fermi fields (Nambu spinors) as well as the auxiliary field $\Phi = V\psi_\uparrow^+\psi_\downarrow^+$. In contrast to the generally accepted method of calculating Z in the variables Φ and Φ^*, in our case it is expedient, following Aitchison *et al.*,[9] to go over to the modulus–phase variables in the corresponding integral, i.e., to use the parametrization $\Phi(x) = \rho(x)\exp[-i2\theta(x)]$, carrying out the obvious substitution $\psi_\sigma(x) = \chi_\sigma(x)\exp[i\theta(x)]$. This gives

$$Z = \int \rho D\rho D\theta \, \exp[-\beta\Omega(\rho,\partial\theta)],$$

where

$$\Omega(\rho,\partial\theta) = \frac{T}{V}\int_0^\beta d\tau \int d\mathbf{r}\rho^2 - T \, \mathrm{Tr} \, \mathrm{Ln} \, \mathscr{G}^{-1} \quad (2)$$

is the effective thermodynamic potential of the system and $\mathscr{G}$ is its Green's function, so that

$$\mathscr{G}^{-1} = -\hat{I}\partial_\tau + \tau_3\left(\frac{\nabla^2}{2m}+\mu\right) + \tau_1\rho - \tau_3\left(i\partial_\tau\theta + \frac{(\nabla\theta)^2}{2m}\right)$$

$$+ \hat{I}\left(\frac{i\nabla^2\theta}{2m} + \frac{i\nabla\theta\nabla}{2m}\right) \equiv G^{-1}(\rho) - \Sigma(\partial\theta); \quad (3)$$

In formula (2), the trace (Tr) is taken over space, imaginary time $\tau(\leqslant\beta\equiv1/T)$ and the Nambu indices appearing in the Pauli matrices τ_j. It should be noted that the smallness or low rate of variation of the phase $\theta(x)$ is not assumed anywhere at this stage since we have in fact only carried out a transition to new variables.

The low-energy dynamics in the region where $\rho \neq 0$ is determined by phase fluctuations, and hence we can confine the analysis to expansions of $\Omega(\rho,\partial\theta)$ only in derivatives of θ:

$$\Omega(\rho,\partial\theta) = \Omega_{\mathrm{kin}}(\rho,\partial\theta) + \Omega_{\mathrm{pot}}(\rho);$$

$$\Omega_{\mathrm{kin}}(\rho,\partial\theta) = T \, \mathrm{Tr} \sum_{n=1}^\infty \frac{1}{n}(G\Sigma)^n\bigg|_{\rho=\mathrm{const}};$$

$$\Omega_{\mathrm{pot}}(\rho) = \frac{1}{V}\int d\mathbf{r}\rho^2 - T \, \mathrm{Tr} \, \mathrm{Ln} \, G^{-1}\bigg|_{\rho=\mathrm{const}}. \quad (4)$$

3. In the expansion of Ω_{kin} up to terms $\sim(\nabla\theta)^2$ in (4), it is sufficient to retain the terms only with $n=1,2$. The computation procedure is similar to that used by Schakel[10] who analyzed only the case of high densities n_f at $T=0$ and gives[1] (see Appendix)

$$\Omega_{\mathrm{kin}} = \frac{T}{2}\int_0^\beta d\tau \int d\mathbf{r}[J[\mu,T,\rho(\mu,T)](\nabla\theta)^2$$

$$+ K[\mu,T,\rho(\mu,T)](\partial_\tau\theta)^2], \quad (5)$$

where

$$J(\mu,T,\rho) = \frac{1}{m}n_F(\mu,T,\rho)$$

$$- \frac{T}{\pi}\int_{-\mu/2T}^\infty dx \frac{x+\mu/2T}{\cosh^2[x^2+\rho^2/(4T^2)]^{1/2}} \quad (6)$$

and

$$K(\mu,T,\rho) = \frac{m}{2\pi}\left\{1 + \frac{\mu}{(\mu^2+\rho^2)^{1/2}}\tanh\frac{(\mu^2+\rho^2)^{1/2}}{2T}\right\}, \quad (7)$$

and the quantity

$$n_F(\mu,T,\rho) = \frac{m}{2\pi}\left\{(\mu^2+\rho^2)^{1/2}+\mu+2T\ln\left[1+\exp\left(-\frac{(\mu^2+\rho^2)^{1/2}}{T}\right)\right]\right\} \quad (8)$$

has the meaning of number density of Fermi particles (for $\rho=0$, expression (8) describes the density of free fermions). Direct comparison of expression (5) with the Hamiltonian of the XY model[11] enables us to write the following equation for T_{BKT}:

$$\frac{\pi}{2}J[\mu,T_{BKT},\rho(\mu,T_{BKT})] = T_{BKT}. \quad (9)$$

However, in order to determine T_{BKT} self-consistently as a function of n_f, we must supplement this equation with equations for ρ and μ. (It should be recalled that the chemical potential in the BCS theory is normally equated to the Fermi energy, and hence the self-consistent approach is not required.)

4. The effective potential Ω_{pot} defined in (4) has the form

$$\Omega_{\mathrm{pot}} = v\left[\frac{\rho^2}{V} - \int\frac{d\mathbf{k}}{(2\pi)^2}\left\{2T\ln\cosh\frac{[\xi^2(\mathbf{k})+\rho^2]^{1/2}}{2T}\right.\right.$$

$$\left.\left. - \xi(\mathbf{k})\right\}\right], \quad (10)$$

where $\xi(\mathbf{k}) = \mathbf{k}^2/2m - \mu$. In this case, the missing equations are the condition $\partial\Omega_{\mathrm{pot}}/\partial\rho=0$ of the minimum of (10) and the equality $v^{-1}\partial\Omega_{\mathrm{pot}}/\partial\mu = -n_f$ defining n_f:

$$\frac{1}{V} = \int\frac{d\mathbf{k}}{(2\pi)^2}\frac{1}{2[\xi^2(\mathbf{k})+\rho^2]^{1/2}}\tanh\frac{[\xi^2(\mathbf{k})+\rho^2]^{1/2}}{2T}, \quad (11)$$

$$n_F(\mu,T,\rho) = n_f. \quad (12)$$

Thus, equations (11) and (12) form the sought system for self-consistent determination of the modulus of the order parameter ρ and the chemical potential μ for given values of T and n_f.[2] It was mentioned above that the same equation lead to the initial values of ρ and μ required for calculating T_{BKT}.

If we put $\rho=0$ in (11) and (12), we arrive at equations for the critical temperature $T_\rho(=T_c^{MF})$ and the value of μ corresponding to it in the self-consistent field approximation[3]:

$$\ln\frac{|\varepsilon_b|}{T_\rho}\frac{\gamma}{\pi} = -\int_0^{\mu/2T_\rho}du\frac{\tanh u}{u} \quad (\gamma=1.781), \quad (13)$$

$$T_\rho\ln\left[1+\exp\left(\frac{\mu}{T_\rho}\right)\right] = \epsilon_F. \quad (14)$$

Here $\varepsilon_b = -2W\exp(-4\pi/mV)$ is the energy of two-particle coupled states, where W is the conduction band width, $\epsilon_F = \pi n_f/m$ the Fermi energy, and a transition to ε_b indicates a transition to the limit $W\to\infty$ and $V\to0$. It is much more convenient to use the parameter ε_b than the four-fermion constant V. For example, Eq. (11) acquires after such a transition the form
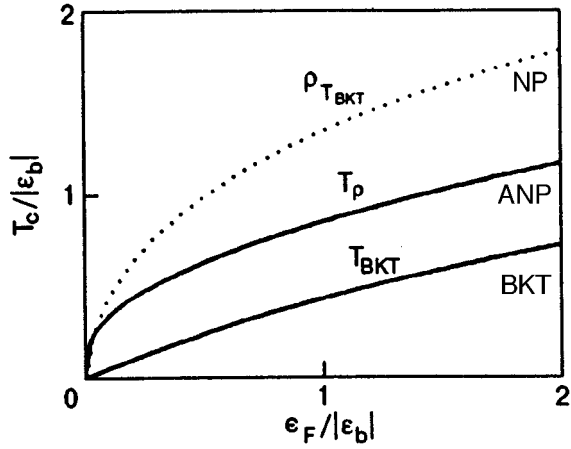
FIG. 1. Dependences $T_{BKT}(\epsilon_F)$ and $T_\rho(\epsilon_F)$. The dotted curve illustrates the behavior of $\rho(\epsilon_F)$ at $T=T_{BKT}$. The regions of NP, ANP, and BKT phase are indicated.

$$\ln \frac{|\varepsilon_b|}{(\mu^2+\rho^2)^{1/2}-\mu}$$

$$=2\int_{-\mu/T}^{\infty} du \, \frac{1}{(u^2+(\rho/T)^2)^{1/2}[\exp\{u^2+(\rho/T)^2\}^{1/2}+1]}, \tag{15}$$

and we can easily verify that the system of equations (12), (15) has the exact solution $\rho=(2|\varepsilon_b|\epsilon_F)^{1/2}$ and $\mu=-|\varepsilon_b|/2+\epsilon_F$ at $T=0$,[2,4] which means that the relation between ϵ_F and $|\varepsilon_b|$ determines not only the magnitude, but also the sign of μ. It should also be noted that the quantity (6) vanishes on (and above) the mean-field critical line demarcating the NP and ANP.

5. An analysis of the system of equations (9), (12), (15) and (13), (14) was carried out numerically and led to the following most interesting results presented graphically.

(a) The ANP region (see Fig. 1) turns out to be commensurate with the BKT region.

(b) For small $\epsilon_F(\ll|\varepsilon_b|)$, the $T_{BKT}(\epsilon_F)$ dependence is linear, which is also confirmed by the analytic solution of the system of equations (9), (12), and (15) leading to $T_{BKT}=\epsilon_F/2$. It should be noted that the temperature of formation of a uniform order parameter is of the order of $T_c=\epsilon_F/(2\alpha)$ (where $\alpha\gg1$) for the quasi-2D model[3] in the limit of small n_f also. This means that weak three-dimensionalization can preserve both the ANP region, and the BKT phase (at least, for small n_f), which is observed, for example, in the relativistic quasi-2D model,[14] although the concentration dependence was not analyzed in it. On the other hand, an increase in the three-dimensionalization parameter can and must lead to the disappearance of the BKT phase, i.e., to its ''replacement'' by an ordinary superconducting phase with a uniform order parameter.

(c) Figure 2 demonstrates graphically the relations between ϵ_F and $|\varepsilon_b|$ for which the quantity μ differs considerably from ϵ_F. In other words, the Landau theory of Fermi liquid is not quite suitable for describing such metals with a low fermion density ($\epsilon_F\sim|\varepsilon_b|$). The kink on the μ at $T=T_\rho$ observed in the experiments considered in Ref. 12 and ex-
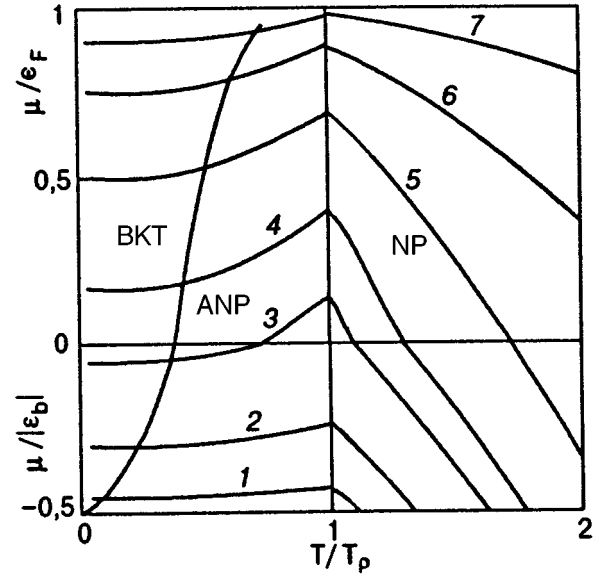

FIG. 2. Temperature dependence of μ for various values of $\epsilon_F/|\varepsilon_b|$: 0.05 (curve 1), 0.2 (curve 2), 0.45 (curve 3), 0.6 (curve 4), 1 (curve 5), 2 (curve 6), and 5 (curve 7). (Relative values for $\mu>0$ and $\mu<0$ were obtained with the help of ϵ_F and $|\varepsilon_b|$, respectively.) Cold lines demarcate the regions of the BKT phase, ANP, and NP.

plained in the case of a 123 cuprate[13] becomes less and less noticeable with increasing ϵ_F as expected. However, it is important that the kink is observed at the NP–ANP interface, i.e., prior to the actual emergence of superconductivity. For this reason, additional experiments clarifying the $\mu(T)$ dependence, especially for strongly anisotropic (quasi-2D) and relatively underdoped cuprates will undoubtedly be of considerable importance.

(d) Curve 3 in Fig. 2 shows that a transition from local pairs to Cooper pairs (sign reversal of μ) is possible not only as a result of an increase in ϵ_F (which is more of less evident), but also upon an increase in T (for a certain choice of n_f).

(e) Finally, according to calculations, the ratio $2\Delta/T_{BKT}>4.4$ (Fig 3) in all cases, which is in accord with experimental data for HTS materials; in this case, the value
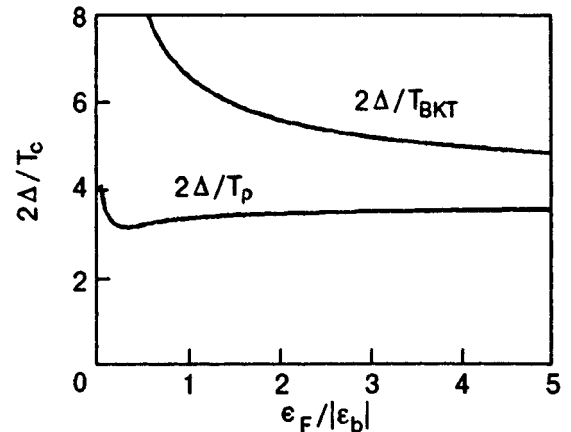

FIG. 3. Dependences $2\Delta/T_{BKT}$ and $2\Delta/T_\rho$ on ϵ_F (we assume that $\Delta=(\mu^2+\rho^2)^{1/2}$ for $\mu<0$ and $\Delta=\rho$ for $\mu>0$.)

of $2\Delta/T_\rho(=2\Delta/T_c^{MF})$ is smaller and attains (for $\epsilon_F \gg |\varepsilon_b|$) the limit of the BCS theory equal to 3.52 as expected. The nonmonotonic dependence $2\Delta(\epsilon_F)/T_\rho(\epsilon_F)$ is due to the above-mentioned difference between the quantities Δ and ρ for $\mu < 0$ (see footnote 2) on p. 616).

6. Although the phase diagram was obtained under simplifying assumptions (for example, only the fluctuations of the order parameter phase were taken into account consistently), it demonstrates the sensitivity of the parameters of its critical curves to the value of n_f. At the same time, it should be borne in mind that, in contrast to a $3D$ transition at $\rho=0$, the BKT transition occurs in the state in which $\rho \neq 0$, and hence the fluctuations of the modulus of the order parameter are less significant in this case, although they lead to the above-mentioned decrease in T_ρ relative to T_c^{MF}. The inclusion of these fluctuations would hardly affect the qualitative pattern, but it would be undoubtedly interesting to estimate separately the role of each of corresponding contributions of fluctuations of ρ and θ separately. It should be borne in mind that the parametrization used by us is convenient and physically justified only in regions where $\rho \neq 0$.

It can be stated with confidence that correlated and non-correlated pairs whose presence in HTS materials is being discussed extensively (see reviews in Refs. 7 and 8) correspond to regions on the theoretical phase diagram: in the NP $(T > T_\rho)$, only the fluctuations of the order parameter are present; in the $2D$ case, these fluctuations are so strong that anomalies associated with the presence of virtual pairs[15] can be manifested in the behavior of the system even in this phase. If we compare again the situation with the XY model in which, however, the modulus of spin is also the required quantity (which is usually neglected), the normal phase of a $2D$ metal corresponds to the paramagnetic phase in this model with zero (on the average) spin at a lattice site. In the ANP region $(T_{BKT} < T \leqslant T_\rho)$, the modulus of the order parameter becomes finite, indicating the existence of a finite number of stable pairs (which, however, are still incoherent). In such an XY model, the corresponding temperature region is the region of existence of two-component spins at lattice site, whose temperature-dependent moduli are identical, and the directions are random and not correlated. Finally, coherence between pairs emerges below T_{BKT} (and/or T_c in the quasi-2D case), while in the spin model, spins are somehow ordered (nonuniformly of uniformly) in the real space.

The phase diagram obtained above can be considered with a certain degree of authenticity, while the phase transition between the NP and ANP, in which a neutral order parameter can appear, required separate analysis (this question will not be considered here in detail). On one hand (see, for example, Ref. 5), such a transition is undoubtedly a phase transition if we formally use the Landau theory of phase transitions: a certain physical parameter (the modulus of the order parameter in our case) is equal to zero above a certain temperature T_ρ and differs from zero below this temperature. It can easily be seen, however, that the value of ρ itself does not appear in thermodynamic quantities, and the calculation of an observable of a certain correlator is always accompanied with the emergence of a cofactor depending on the correlation function of the order parameter phase. In the low-

dimensional case, fluctuations are especially strong and can blur the corresponding phase transition to such an extent that no temperature peculiarities of thermodynamic quantities are observed in the vicinity of the transition. It is appropriate to note that HTS materials indeed exhibit a behavior close to the predicted mode, although a literal comparison of the simple model under investigation with complex objects like HTS materials would be naive.

On the other hand, considering superconducting systems, it should be emphasized that certain changes occur in them (see above). For example, the electron spectrum acquired features of a forthcoming gap since the density of states in the ANP under investigation near ϵ_F (for $\mu > 0$) decreases rapidly (upon an increase in ρ), but does not vanish anywhere. In other words, T_ρ, viz., the temperature at which a pseudogap is formed, is an observable and measurable parameter of $2D$ or strongly anisotropic $3D$ superconductors. An obvious reason behind the absence of a true gap in these superconductors in a certain temperature range can be associated with the scattering of neutral (uncharged) fermions [Green's function $G(\rho)$ in (3) corresponds to such particles] at phase fluctuations.

However, required investigations (e.g., the determination of one-particle Green's function of the initial charged fermions) have not been carried out even for the simple model under investigation. Besides, such investigations can be regarded as very important since the type and the properties of a transition involving the ''ordering'' of only the modulus of a complex order parameter remain unclear.

7. Thus, our calculations revealed the two-stage formation of the superconducting state in a $2D$ metal, occurring through an ANP emerging between the NP and the BKT phase. We proved only the existence of the ANP and calculated its boundaries, while its physical properties, and above all the spectrum, require further investigations.

In conclusion, let us briefly consider why the anomalies in the behavior of physical properties of HTS materials are manifested most clearly just in underdoped samples. At the qualitative level, we can state that an increase in the carrier concentration in quasi-2D systems (including HTS materials) necessitates a suppression of the effect of fluctuations. As the role of the latter becomes smaller, $T_c \rightarrow T_c^{MF}$,[16] otherwise, the ANP region in real system would in all probability contract upon an increase in the hole concentration. As regards the $2D$ model considered above, it explains the origin of the ANP and the role of the critical temperature corresponding to the emergence of the modulus of the order parameter, but does not allow us to attain the convergence of the corresponding temperatures T_ρ and T_{BKT} (or T_c in the quasi-2D case). In this connection, it is necessary to analyze the quasi-2D model which permits in principle the existence of a uniform order parameter also.

raised the important question concerning the physical meaning and observability of the temperature T_ρ.

APPENDIX A

Let us derive the kinetic component (5) of the effective action Ω. For this purpose, we must determine the first two terms of the series (4), which are formally presented in the form $\Omega_{\text{kin}}^{(1)} = T \, \text{Tr}(G\Sigma)$ and $\Omega_{\text{kin}}^{(2)} = (1/2)T \, \text{Tr}(G\Sigma G\Sigma)$.

Direct calculations of $\Omega_{\text{kin}}^{(1)}$ gives

$$\Omega_{\text{kin}}^{(1)} = T \int_0^\beta d\tau \int d\mathbf{r} \, \frac{T}{(2\pi)^2} \sum_{n=-\infty}^{\infty} \int d\mathbf{k} \, \text{Tr}[G(i\omega_n,\mathbf{k})\tau_3]$$
$$\times \left(i\partial_\tau \theta + \frac{(\nabla\theta)^2}{2m} \right), \tag{A1}$$

where

$$G(i\omega_n,\mathbf{k}) = -\frac{i\omega_n\hat{I} + \tau_3\xi(\mathbf{k}) - \tau_1\rho}{\omega_n^2 + \xi^2(\mathbf{k}) + \rho^2} \tag{A2}$$

is Green's function for neutral fermions in the frequency–momentum representation. Carrying out summation in (A1) over Matsubara frequencies $\omega_n = \pi(2n+1)T$ and integration with respect to momenta $\mathbf{k}$, we obtain

$$\Omega_{\text{kin}}^{(1)} = T \int_0^\beta d\tau \int d\mathbf{r} \, n_F(\mu,T,\rho)\left(i\partial_\tau\theta + \frac{(\nabla\theta)^2}{2m} \right), \tag{A3}$$

where $n_F(\mu,T,\rho)$ is defined by formula (8). It should be noted that, according to (3), the quantity Σ has the structure

$$\Sigma = \tau_3 O_1 + \hat{I} O_2,$$

where O_1 and O_2 are differential operators. It can easily be verified, however, that the component of Σ proportional to the unit matrix $\hat{I}$ makes no contribution to $\Omega_{\text{kin}}^{(1)}$.

In the case of $T=0$, when the imaginary time τ is replaced by the real time t, it follows necessarily from the Galilean invariance of the theory that the coefficient of $\partial_t\theta$ is uniquely connected with the coefficient of $(\nabla\theta)^2$ so that the latter cannot be generated by $\Omega_{\text{kin}}^{(2)}$.[9,10] At $T\neq 0$, such arguments become inapplicable, and hence the value of $\Omega_{\text{kin}}^{(2)}$ must also be calculated explicitly. In this case, the term containing O_1 leads to the expression

$$\Omega_{\text{kin}}^{(2)}(O_1) = \frac{T}{2} \int_0^\beta d\tau \int d\mathbf{r} \, \frac{T}{(2\pi)^2}$$
$$\times \sum_{n=-\infty}^{\infty} \int d\mathbf{k} \, \text{Tr}[G(i\omega_n,\mathbf{k})\tau_3 G(i\omega_n,\mathbf{k})\tau_3]$$
$$\times \left(i\partial_\tau\theta + \frac{(\nabla\theta)^2}{2m} \right)^2, \tag{A4}$$

Summation and integration of this expression leads to

$$\Omega_{\text{kin}}^{(2)}(O_1) = -\frac{T}{2} \int_0^\beta d\tau \int d\mathbf{r} \, K(\mu,T,\rho)$$
$$\times \left(i\partial_\tau\theta + \frac{(\nabla\theta)^2}{2m} \right)^2, \tag{A5}$$

where the quantity $K(\mu,T,\rho)$ was defined in (7). It can be seen that the obtained expression does not change the coefficient of $(\nabla\theta)^2$. It can easily be verified that the cross term including the product of O_1 and O_2 in $\Omega_{\text{kin}}^{(2)}$ is missing.

Finally, the calculation of the contribution from O_2 in $\Omega_{\text{kin}}^{(2)}$ leads to[4]

$$\Omega_{\text{kin}}^{(2)}(O_2) = \frac{T}{2} \int_0^\beta d\tau \int d\mathbf{r} \, \frac{T}{(2\pi)^2}$$
$$\times \sum_{n=-\infty}^{\infty} \int d\mathbf{k} \, \mathbf{k}^2 \, \text{Tr}[G(i\omega_n,\mathbf{k})\hat{I}G(i\omega_n,\mathbf{k})\hat{I}]$$
$$\times \frac{(\nabla\theta)^2}{4m^2}. \tag{A6}$$

Subsequent summation over Matsubara frequencies ultimately gives

$$\Omega_{\text{kin}}^{(2)}(O_2) = -\int_0^\beta d\tau \int d\mathbf{r} \, \frac{1}{32\pi^2 m^2} \int d\mathbf{k}$$
$$\times \frac{\mathbf{k}^2}{\cosh^2[\{\xi^2(\mathbf{k}) + \rho^2\}^{1/2}/2T]} (\nabla\theta)^2. \tag{A7}$$

The last expression tends to zero as $T\to 0$ as expected, but remains comparable to (A3) at $T\neq 0$. Combining (A3), (A5), and (A7), we arrive at (5).

[*]E-mail: vloktev@gluk.apc.org

[1])The total derivative with respect to τ is omitted.

[2])It should be borne in mind that, in the mode of local pairs, when $\mu<0$, the gap Δ in the quasiparticle excitation spectrum is equal not to ρ (as for $\mu>0$), but $\sqrt{\mu^2+\rho^2}$ (see Ref. 2 and the literature cited therein).

[3])In a certain sense, the temperature T_ρ is the pairing temperature (i.e., the temperature of formation of local or Cooper pairs), which is often denoted by T_P in the $3D$ case.[2] It should be borne in mind, however, that in view of the discrete nature of symmetry violation for $\rho \neq 0$ noted above, the value of t_ρ remains finite even in the case when fluctuations of the order parameter modulus are taken into account. Naturally, the value of T_ρ, which is slightly smaller than the critical temperature T_c^{MF} in the mean-field approximation, remains finite in the $2D$ case also. This distinguishes it basically from the latter temperature which immediately drops to zero when fluctuations are taken into account if we treat it as the temperature corresponding to the emergence of complete uniform order parameter (and not its modulus!).

[4])Higher-order derivatives have not been determined.

[1] V. M. Loktev, Fiz. Nizk. Temp. **22**, 490 (1996) [Low Temp. Phys. **22**, 376 (1996)].

[2] M. Randeria, in *Bose–Einstein Condensation* (ed. by A. Griffin, D. W. Snoke, and S. Stringari), Cambridge U. P., New York (1995).

[3] E. V. Gorbar, V. M. Loktev, and S. G. Sharapov, Physica **C257**, 355 (1996).

[4] E. V. Gorbar, V. P. Gusynin, and V. M. Loktev, Sverkhprovodimost': Fiz., Khim., Tekhnol. **6**, 483 (1992); Fiz. Nizk. Temp. **19**, 1171 (1993) [Low Temp. Phys. **19**, 832 (1993); Preprint ITP-92-54E (1992).

[5] R. MacKenzie, P. K. Panigrahi, and S. Sakhi, Int. J. Mod. Phys. **A9**, 3603 (1994).

[6] M. Drechsler and W. Zwerger, Ann. Phys. (Germany) **1**, 15 (1992).

[7] B. G. Levi, Physics Today **49**, 17 (1996).

[8] H. Ding, T. Yokoya, I. C. Campuzano et al., Nature **382**, 51 (1996).

[9] I. J. R. Aitchison, P. Ao, D. J. Thouless, and X.-M. Zhu, Phys. Rev. **B51**, 6531 (1995).

[10] A. M. J. Schakel. Mod. Phys. Lett. **B4**, 927 (1990).

616   Low Temp. Phys. **23** (8), August 1997

Gusynin et al.   616

[11] Yu. A. Izyumov and Yu. N. Skryabin, *Statistical Mechanics of Magnetically Ordered Systems* [in Russian], Nauka, Moscow (1987).

[12] D. van der Marel, Physics **C165**, 35 (1990).

[13] A. V. Dotsenko and O. P. Sushkov, Preprint cond-mat/9601031.

[14] H. Yamamoto and I. Ichinose, Nucl. Phys. **B370**, 695 (1992).

[15] V. M. Loktev and S. G. Sharapov, Fiz. Nizk. Temp. **23**, 180 (1997) [Low Temp. Phys. **23**, 132 (1997)].

[16] I. E. Dzyaloshinskii and E. I. Kats, Zh. Éksp. Teor. Fiz. **55**, 2373 (1968) [Sov. Phys. JETP **28**, 1259 (1968)].

Translated by R. S. Wadhwa

Lower critical fields of textured high-T_c superconductors

V. A. Finkel' and V. V. Toryanik

National Science Center "Kharkov Physicotechnical Institute," 310108 Kharkov, Ukraine*

The possibility of studying the anisotropy of lower critical fields in HTS materials during the measurements of critical currents of textured samples subjected to the action of magnetic fields applied in three different directions is explored in the theory of magnetic properties of anisotropic superconductors. The critical fields H_{c1}^{ab} and H_{c1}^{c} of the high-T_c materials YBa$_2$Cu$_3$O$_{7-\delta}$ and DyBa$_2$Cu$_3$O$_{7-\delta}$ are determined at $T = 77.3$ K. It is found that the dependences $H_{c1}^{ab}(m_c/m_{ab})$ and $H_{c1}^{c}(m_c/m_{ab})$ are universal for all the investigated samples. © *1997 American Institute of Physics.* [S1063-777X(97)00508-2]

INTRODUCTION

It is well known that Abrikosov vortices start penetrating type II superconductors including all high-T_c compounds (HTS materials) without any exception in the applied fields $H = H_{c1}$, where H_{c1} is the lower critical field. The values of H_{c1} which play an exceptionally important role in the electrodynamics of type II superconductors are determined frequently by using the "classical" magnetic technique: the critical field H_{c1} at a given temperature T is determined from the kink emerging on the $M(H)$ isotherm obtained under diamagnetic screening of zero-field cooling (ZFC) (M is the magnetic moment of the superconductor; see, for example, Ref. 1). Apparently, the penetration of the magnetic field in a type II superconductor would be accompanied by a decrease in the critical current I_c for $H = H_{c1}$, but the effect observed in HTS ceramics is vanishingly small.[2] The values of H_{c1} for HTS materials can be determined from the anomalies emerging on the dependences $I_c(H_{tr})$ of critical current on the "treatment field" H_{tr} which initiates the magnetic flux trapping, leading to a decrease in the critical current $I_c(0)$ measured in zero magnetic field[1] (see, for example, Refs. 3 and 4).

A number of other methods of measuring lower critical fields in HTS materials are also known. Strictly speaking, none of these methods of determining H_{c1} is "direct," and model concepts should be used for obtaining the values of the field from the results of measurements of certain physical quantities.[5]

For isotropic superconductors with cubic symmetry of the crystal lattice, the magnetic and current methods of measurements of lower critical fields are quite suitable. In the case of strongly anisotropic HTS materials, these methods are applicable, strictly speaking, only when the corresponding measurements are made on single crystals to which a magnetic field is applied along the principal crystallographic axes. For granular HTS ceramics, especially in the presence of preferred orientation in the arrangement of grains (texture), the results of magnetic or current measurements of H_{c1} can apparently lead only to certain averaged values, the form of averaging itself remaining unclear. Obviously, the results of such measurements indicate that the possibility of obtaining reliable information on the anisotropy of lower critical fields H_{c1} is disputable even if we have a complete quantitative description of the HTS texture, i.e., if the grain orientation distribution function (ODP) can be reconstructed from the results of x-ray or neutron diffraction experiments.[6]

The modern theory of magnetic properties of anisotropic type II superconductors,[7] which had been constructed before the discovery of high-temperature superconductivity, makes it possible (see below) to study the anisotropy of the field H_{c1} of an HTS material on the basis of simple experiments on polycrystalline objects. Balatskii *et al.*[7] proved, among other things, that the penetration of magnetic vortices in an type II anisotropic superconductor must start for a certain minimum value of H_{c1}, which, however, depends on the orientation of the applied field **H** relative to the crystal axes a_i. As the applied field increases, the vortex lattice rotates, and the direction of induction **B** coincides with the field **H** only when the field attains the value H^* corresponding to complete penetration (Bean's field). For layered superconductors (all HTS materials belong in first approximation to uniaxial layered superconductors if we neglect a certain anisotropy in the basal plane ab of rhombic crystal lattices), the equations for the lower critical field $H_{c1}(\gamma)$ (γ is the angle between the magnetic anisotropy axis **c** and the external field **H**) and for the angle θ at which the field starts penetrating the crystal for $H_{c1} = H(\gamma)$ were obtained in terms of the Ginzburg–Landau "effective mass tensor" for $m_c \gg m_{ab}$ (m_c and m_{ab} are effective masses of an electron in the directions perpendicular and parallel to the layer, respectively):

$$H_{c1}(\gamma) = H_{c1}^{c}[\cos^2 \gamma + (m_c/m_{ab})\sin^2 \gamma]^{-1/2}, \quad (1)$$

$$\tan \theta = (m_c/m_{ab})\tan \gamma, \quad (2)$$

where H_{c1}^{c} is the lower critical field along the anisotropy axis c.

The idea of the method of determining the anisotropy of lower critical field of HTS materials developed here lies in the following. If we apply a magnetic field **H** to a crystal in three mutually orthogonal directions L, N, and T in the laboratory system of coordinates (Fig. 1), the field forms the angles α, β, and c, respectively, with the magnetic anisotropy axis. The orientational dependence of the critical field
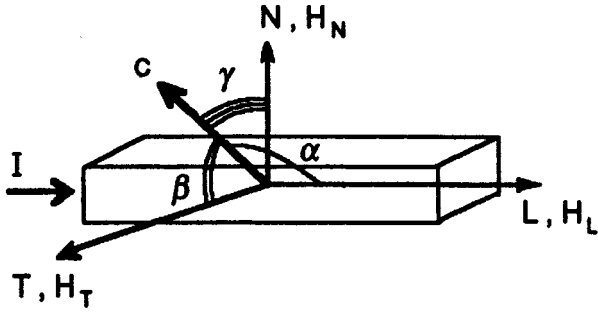
FIG. 1. Schematic diagram of experiment.

H_{c1} for the L, T, and N directions can be described by three equations of type (1). In addition, these equations are supplemented with the fourth equation

$$\cos^2 \alpha + \cos^2 \beta + \cos^2 \gamma = 1. \qquad (3)$$

in view of orthogonality of the axes L, T, and N.

It is well known (see, for example, Refs. 5, 8) that the anisotropy of the lower (H_{c1}) and upper (H_{c2}) critical fields, coherence length ξ, and penetration depth λ are connected with the ratio m_c/m_{ab} through the following simple relation:

$$H_{c1}^c/H_{c1}^{ab} = H_{c2}^{ab}/H_{c2}^c = \xi_{ab}/\xi_c = \lambda_c/\lambda_{ab} = (m_c/m_{ab})^{1/2}. \qquad (4)$$

It follows hence that, from the measurement of the lower critical fields for the three orientations of the magnetic field relative to the axes of the orthogonal laboratory system of coordinates, we can determine five unknowns (the values of H_{c1} along the anisotropy axis of the crystal (H_{c1}^c) and at right angles to this axis (H_{c1}^{ab}) as well as the Euler angles α, β, and γ of the anisotropy axis $\mathbf{c}$ in the laboratory system of coordinates LTN) from the four available equations ''to within'' the effective mass ratio m_c/m_{ab}. The experimental realization of the method requires the measurements of critical currents $I_c(0)$ in a certain direction in the laboratory reference frame (e.g., along the axis L, see Fig. 1) in zero magnetic field on HTS samples as a function of the magnitude and direction of the magnetic field applied preliminarily at the same temperature, i.e., $I_c(0)[H_{tr}]$. Having determined the values of critical fields from the $I_c(0)[H_{tr}]$ curves with the help of objective criteria (see below) for three mutually orthogonal directions of the vector $\mathbf{H}_{tr}$ (longitudinal direction H_{c1}^L relative to the superconducting current, transverse direction H_{c1}^T, and normal direction H_{c1}^N), we can obtain the values of critical fields H_{c1}^{ab} and H_{c1}^c as well as the values of averaged Euler's angles α, β, and γ for the sample under investigation as functions of the ratio m_c/m_{ab}. Obviously, the obtaining of universal dependences $H_{c1}^{ab}(m_c/m_{ab})$ and $H_{c1}^c(m_c/m_{ab})$ on the basis of measurements on samples of the same HTS material with essentially different textures (i.e., set of the angles α, β, and γ) can serve as a criterion of correctness of the method.

EXPERIMENTAL TECHNIQUE

Experiments were made on textured HTS samples of $YBa_2Cu_3O_{7-\delta}$ and $DyBa_2Cu_3O_{7-\delta}$ with $T_c \sim 92$ K. Various types of textures were created by mechanical treatment by pressing[6] or by magnetic treatment at $T < T_c$.[2,9] The last stage of obtaining samples was thermal treatment in an oxidizing medium according to the standard technique,[10] leading to sample fritting and saturation of crystal lattices with oxygen to the oxygen index $7 - \delta \sim 6.90 - 6.95$. Low-resistivity current and potential Ag contacts were deposited on the samples from the vapor phase in vacuum at $T \sim 200°C$.

It was mentioned above that the experiments involved precision measurements of critical currents $I_c(0)$ of HTS materials in zero magnetic field as functions of the magnitude and direction of the ''treatment field'' $\mathbf{H}_{tr}(0 < H_{tr} < 1000$ Oe), i.e., of the magnitude and orientation of the trapped magnetic flux. All the measurements were made at the liquid nitrogen temperature. As a rule, the value of H_{tr} was varied with a small ''step'': $\Delta H_{tr} \sim 1$ Oe.

A special setup was developed of an IBM PC/AT 386 computer for recording current–voltage characteristics and for obtaining the $I_c(0)[H_{tr}]$ dependences.[9] The setup consists of two similar components: the block controlling the current I_{src} of the source for creating the magnetic field $\mathbf{H}_{tr}$ in the form of a solenoid made of copper wire and the block controlling the specimen current I_{spc}. Preliminary calibration of the solenoid with the help of a Hall pickup made it possible to preset the magnetic field H_{tr} to within 0.5 Oe. The specimens were placed in a Dewar flask inserted in the solenoid. The currents I_{src} and I_{spc} as well as the voltage U_{spc} are fed to the computer through the KAMAK interface with the help of digital-analog converters and controlling blocks.

The setup software makes it possible to increase smoothly the transport current I_{spc} for a certain value of current I_{src} through the solenoid corresponding to a preset value of H_{tr}, and to detect the voltage U_{spc} across the specimen. The value of $U_{spc} = 1$ μV was used as a criterion of the critical current I_c. After the attainment of this value, I_c is recorded, the transport current is reduced to zero, and the next value of I_{src} is stabilized (which is taken higher to avoid hysteresis effects). After the completion of a measuring cycle, the results are stored in the hard disk of the computer in the form of the $I_c(0)[H_{tr}]$ dependences.

DISCUSSION OF EXPERIMENTAL RESULTS

The results of measurements of the dependences of the critical current in zero magnetic field on the magnitude and orientation of the field $\mathbf{H}_{tr}$ acting on an HTS $YBa_2Cu_3O_{7-\delta}$ specimen obtained with the help of uniaxial pressing (in this case, relatively weak axial texture in the basal plane is observed)[6] are presented in Fig. 2. The results are normalized to $I_c(0) = I_c(H_{tr} = 0)\{[I_c(H_{tr})/I_c(0)](H_{tr})\}$. Naturally, all the curves are qualitatively similar. The initial horizontal segments of the $[I_c(H_{tr})/I_c(0)](H_{tr})$ curves illustrate the ideal diamagnetic state of the samples. As the field H_{tr} increases, granules trap the magnetic flux, which is reflected in the regions of abrupt decrease on the $[I_c(H_{tr})/I_c(0)](H_{tr})$ curves. A transition to the region of slow decrease in critical currents upon a significant increase in H_{tr} is associated with saturation of residual magnetization of grains.[3]
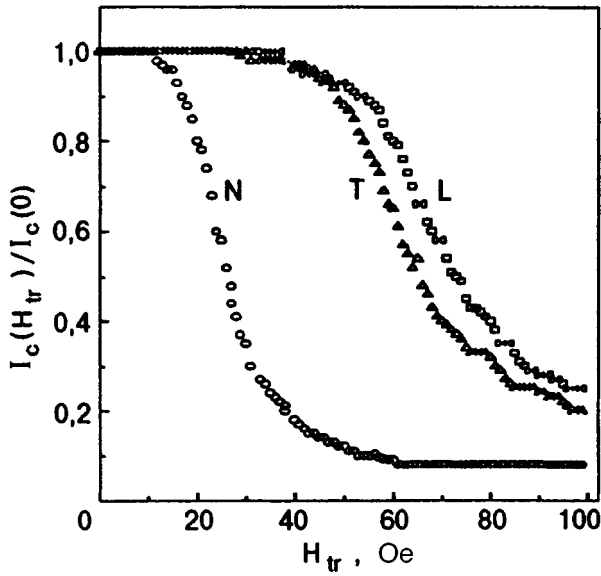
FIG. 2. Critical current of an HTS sample of YBa$_2$Cu$_3$O$_{7-\delta}$ at $T = 77.3$ K as a function of the ''treatment field'' strength $\mathbf{H}_{tr}$ for the longitudinal (L), transverse (T), and normal (N) orientations.

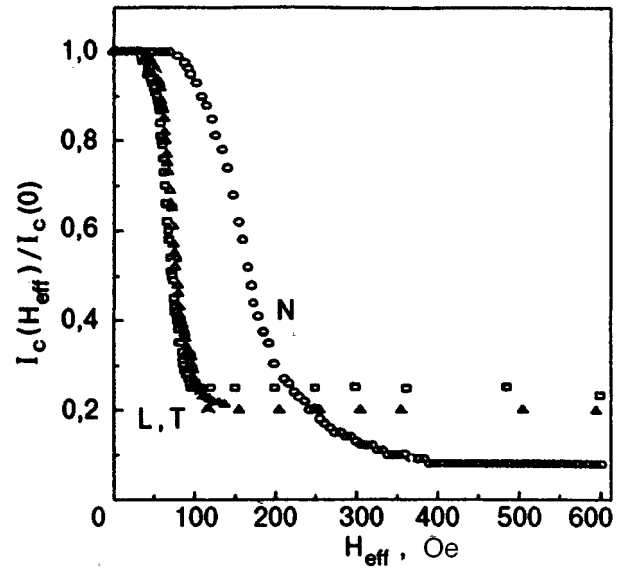FIG. 3. Critical current of an HTS sample of YBa$_2$Cu$_3$O$_{7-\delta}$ at $T = 77.3$ K as a function of the reduced field $\mathbf{H}_{eff}$ for the longitudinal (L), transverse (T), and normal (N) orientations.

Obviously, the processing of the data requires their correction, taking into account the demagnetizing factor D with a view of applying them to analyze the anisotropy of H_{c1}. For a (diamagnetic) superconductor in which the magnetic field does not penetrate ($H < H_{c1}$), the effective value of the field H_{eff} acting on the sample surface under the action of the applied field H_a is[11]

$$H_{eff} = H_a / (1 - D). \tag{5}$$

In order to calculate the demagnetizing factors D_L, D_T, and D_N, taking into account the actual sample geometry for the three orientations of the applied magnetic field (L, T, and N), we used computational formulas and nomograms described in Ref. 12. In contrast to the $[I_c(H_{tr})/I_c(0)](H_{tr})$ curves shown in Fig. 2 and corresponding to the same HTS sample YBa$_2$Cu$_3$O$_{7-\delta}$, the $[I_c(H_{eff})/I_c(0)](H_{eff})$ dependences shown in Fig. 3 reveal significant differences in the positions of various segments of the curve.

In all probability, the presence of segments of abrupt descent on the $[I_c(H_{eff})/I_c(0)](H_{eff})$ curves is due to the presence in the surface layers of the sample of grains oriented at random relative to the field $\mathbf{H}_{tr}$, i.e., possessing different sets of angles α, β, and γ between the anisotropy axis c of the crystal and the fields $\mathbf{H}_{tr}$ oriented along the axes L, T, or N of the laboratory reference frame. This means that the abscissas of all these segments of the $[I_c(H_{eff})/I_c(0)](H_{eff})$ curves contain a complete set of values of $H_{c1}(\alpha, \beta, \gamma)$, and the condition $H_{c1}^{ab} < H_{eff} < H_{c1}^{c}$ must be satisfied for all orientations of the field $\mathbf{H}_{tr}$ in the absence of a texture. Owing to texture which is always present in HTS samples, the ''perfect'' shape of the curves under consideration is not realized: the curves are deformed in accordance with the actual distribution of the angles between the vectors $\mathbf{c}$ and $\mathbf{H}_{tr}$ for a given specimen and a preset orientation of the magnetic field (L, T, or N).

It is also logical to assume that in the case of a not very strong texture, the orientational distribution of granules, and hence the distribution of lower critical fields $H_{c1}(\gamma)$ is Gaussian. Indeed, it can be seen from Fig. 3 that the $[I_c(H_{eff})/I_c(0)](H_{eff})$ curves have a shape close to the normal distribution function for a random quantity (see, for example, Ref. 13). The probability density, i.e., the value of the derivative $d[I_c(H_{eff})/I_c(0)]/dH_{eff}$ as a function of H_{eff} is correctly described by the Gaussian function (Fig. 4):
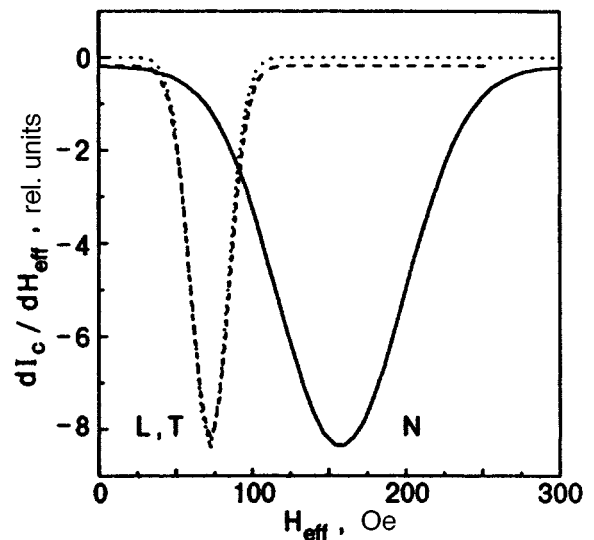

FIG. 4. Derivatives $d[I_c(H_{eff})/I_c(0)]/dH_{eff}$ for an HTS sample of YBa$_2$Cu$_3$O$_{7-\delta}$ as functions of $\mathbf{H}_{eff}$ for the longitudinal (L), transverse (T), and normal (N) orientations.

620   Low Temp. Phys. **23** (8), August 1997

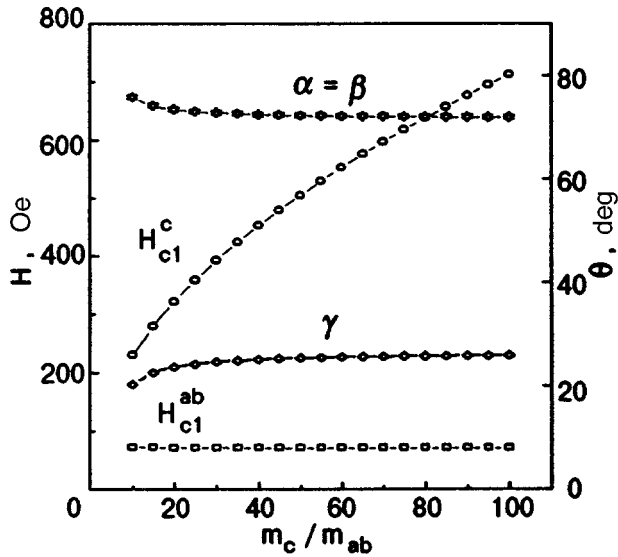V. A. Finkel' and V. V. Toryanik   620

FIG. 5. Critical fields H_{c1}^{ab} and H_{c1}^{c} at $T = 77.3$ K and the Euler angles α, β, and γ of the axis c in the laboratory reference frame LTN as functions of the effective mass ratio m_c/m_{ab} for an HTS sample of YBa$_2$Cu$_3$O$_{7-\delta}$.

$$d[I_c(H_{\text{eff}})/I_c(0)]/dH_{\text{eff}} = \frac{1}{(2\pi)^{1/2}\Delta H_{c1}}$$
$$\times \exp[-(H_{\text{eff}} - H_{c1})^2/(2\Delta H_{c1}^2)].$$
(6)

We can assume that the values of H_{c1}^L, H_{c1}^T, and H_{c1}^N determined in this way give the most reliable values of lower critical fields of the HTS specimen under investigation for the three mutually orthogonal orientations of the vector $\mathbf{H}_{\text{tr}}$.[2] Using these values, we can calculate the lower critical fields in the basal plane ab and along the principal axis c of HTS crystals (H_{c1}^{ab} and H_{c1}^c) as well as the Euler angles of the magnetic anisotropy axis c (α, β, and γ) as functions of the effective mass ratio m_c/m_{ab}. In order to illustrate this statement, Fig. 5 shows the dependences of the quantities H_{c1}^{ab}, H_{c1}^c, α, β, and γ on the effective mass ratio m_c/m_{ab} for the HTS sample YBa$_2$Cu$_3$O$_{7-\delta}$ obtained on the basis of experimental data presented in Figs. 2, 3, and 4.

It was noted in Introduction that the universal dependences $H_{c1}^{ab}(m_c/m_{ab})$ and $H_{c1}^c(m_c/m_{ab})$ obtained from the results of measurements on samples with different textures can serve as a criterion of the correctness of the ideas concerning the possibility of studying the anisotropy of lower critical fields of HTS materials by using current measurements on polycrystalline objects, which are developed here. Indeed, it can be seen from Fig. 6a that the corresponding curves obtained for four HTS samples of YBa$_2$Cu$_3$O$_{7-\delta}$ with different textures of the basal plane coincide to a high degree of accuracy (while the dependences of α, β, and γ on m_c/m_{ab} differ significantly).

The universal nature of the dependences of critical fields is also observed for the HTS ceramics DyBa$_2$Cu$_3$O$_{7-\delta}$ with three different types of texture obtained by magnetic treatment of powders at $T < T_c$ (Fig. 6b).
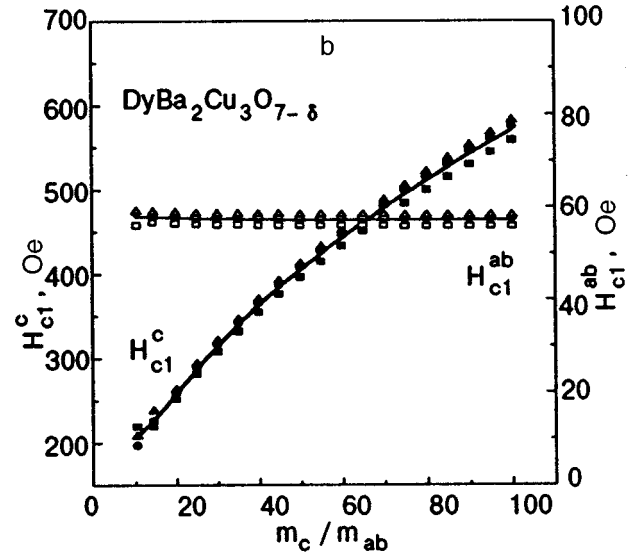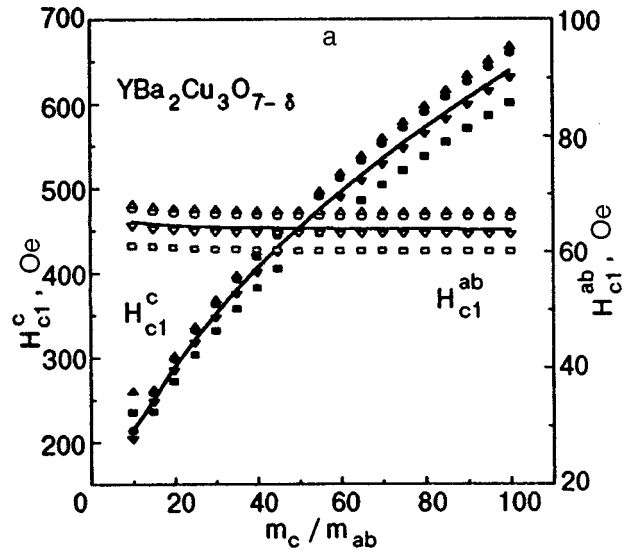

FIG. 6. Critical fields H_{c1}^{ab} and H_{c1}^c at $T = 77.3$ K as functions of the effective mass ratio m_c/m_{ab} for four HTS samples of YBa$_2$Cu$_3$O$_{7-\delta}$ (a) and for three HTS samples of DyBa$_2$Cu$_3$O$_{7-\delta}$ (b) with different textures obtained by uniaxial pressing.

CONCLUSION

The main result of this research is the development of ideas concerning the possibility of studying anisotropy of fundamental superconducting parameters of HTS materials by measuring critical currents of textured material for different orientations of the magnetic field and the experimental implementation of the proposed method. In order to obtain the dependences $H_{c1}^{ab}(m_c/m_{ab})$ and $H_{c1}^c(m_c/m_{ab})$, there is no need to use information on the texture of a material. Moreover, the Euler angles (α, β, and γ) of the "averaged" anisotropy axis c of the HTS material obtained on the basis of measurements of lower critical fields carry sufficient information for describing the texture of the HTS material in the language of polar diagrams or the orientation distribution function for grains (again as a function of the effective mass ratio).

In spite of the fact that the information obtained by using the algorithm described here is semiquantitative (the quantities H_{c1}^{ab}, H_{c1}^{c}, α, β, and γ can be measured only as functions of the effective mass ratio), it is possible to compare different HTS materials on the basis of the degree of anisotropy of their lower critical fields of (see Figs. 5, 6) as well as different samples of the same HTS materials on the basis of the type of texture and its intensity. Naturally, the combination of the method of current measurements in magnetic fields of various orientations developed here with a quantitative texture analysis (it is sufficient to plot only the polar diagram for the basal plane) will make it possible to obtain quantitative information on the magnitudes of lower critical fields of HTS materials in the principal crystallographic directions.

and transverse (T) fields virtually coincide, which is in accord with the uniaxial form of texture created by pressing.

*E-mail: kfti@rocket.kharkov.ua

[1])The critical field H_{c1} can also be determined from the measuring magnetic field H_a opposite to the ''treatment field'' H_{tr} and compensating the trapped magnetic flux.[2]

[2])In this case, the dependences $[I_c(H_{eff})/I_c(0)](H_{eff})$ for the longitudinal (L)

[1] N. N. Efimova, Yu. A. Popkov, M. B. Ustimenkova, and V. A. Finkel', Fiz. Nizk. Temp. **20**, 343 (1994) [Low Temp. Phys. **20**, 273 (1994)].

[2] V. V. Toryanik and V. A. Finkel', Funktsion. Mat. **1**, 5 (1994).

[3] E. Altshuler, S. Garsia, and J. Barroso, Physica **C177**, 61 (1991).

[4] A. A. Zhukov, D. A. Komarkov, G. Karapetov *et al.*, Supercond. Sci. Technol. **5**, 338 (1992).

[5] E. Z. Meilikhov and V. G. Shapiro, Sverkhprovodimost': Fiz., Khim., Tekh. **4**, 1437 (1991).

[6] A. S. Kapcherin, I. I. Papirov, P. I. Stoev *et al.*, Sverkhprovodimost': Fiz., Khim., Tekh. **5**, 113 (1992).

[7] A. V. Balatskii, L. I. Burlachkov, and L. P. Gor'kov, Zh. Éksp. Teor. Fiz. **90**, 1478 (1986) [Sov. Phys. JETP **63**, 866 (1986)].

[8] Y. Iye, Comments Cond. Mat. Res. **16**, 89 (1992).

[9] V. V. Toryanik, V. A. Finkel', and V. V. Derevyanko, Fiz. Khim. Org. Mat. **5**, 55 (1995).

[10] V. M. Arzhavitin, Yu. Yu. Razdovskii, and V. A. Finkel', Sverkhprovodimost': Fiz., Khim., Tekh. **5**, 86 (1992).

[11] U. Yaron and I. Felner, Phys. Rev. **B44**, 12531 (1991).

[12] J. A. Osborn, Phys. Rev. **67**, 351 (1945).

[13] N. Hastings and J. Peacock, *Handbook of Statistical Distributions* [Russian transl.], Statistika, Moscow (1980).

Translated by R. S. Wadhwa

Nonlinear stationary profile waves in spatially disordered magnetic media

E. A. Ivanchenko

National Science Center ''Kharkov Physicotechnical Institute,'' 310108 Kharkov, Ukraine[*]
(Submitted February 27, 1996; revised November 29, 1996)
Fiz. Nizk. Temp. **23**, 830–834 (August 1997)

A nonlinear evolution system of hydrodynamic-type equations describing a three-dimensional multisublattice magnet is investigated. Explicit form of the energy density function for magnetic systems that have an invariant energy density relative to right and left spin rotations is obtained. For quadratic-biquadratic dependence of the energy density (in terms of Cartan's invariant functions), exact solutions are obtained in the one-dimensional case for spin density in the form of stationary profile waves. Solutions for magnon fields that induce such waves are also obtained. © *1997 American Institute of Physics.* [S1063-777X(97)00608-7]

INTRODUCTION

The analysis of spin excitations in spatially disordered media like multisublattice magnets, He^3 in the superfluid state, spin glasses, etc., is based on the hypothesis about spontaneous symmetry violation of the statistical equilibrium state.[1,2] This hypothesis formed the basis of the hydrodynamic approach proposed in Ref. 3 for formulating dynamic equations for magnetic media with a spontaneously violated symmetry relative to spin rotations. Linear dynamic equations were obtained in Refs. 4 and 5. Nonlinear dynamics was taken into account in Refs. 6 and 7 using the method of phenomenological Lagrangians, and in Ref. 8 using the Hamiltonian formalism.

The dynamic variables describing the nonequilibrium state of magnets with a spontaneously violated symmetry include the spin density $s_\alpha(\mathbf{x})(\alpha=x,y,z)$ and the order parameter, i.e., orthogonal matrix of rotations $a_{\alpha\beta}(\mathbf{x})$ $\times(a^T a=1)$, for which the set of Poisson brackets has the form

$$\{s_\alpha(\mathbf{x}),s_\beta(\mathbf{x}')\}=e_{\alpha\beta\gamma}s_\gamma(\mathbf{x})\delta(\mathbf{x}-\mathbf{x}'),$$

$$\{s_\alpha(\mathbf{x}),a_{\beta\gamma}(\mathbf{x}')\}=e_{\alpha\gamma\rho}a_{\beta\rho}(\mathbf{x})\delta(\mathbf{x}-\mathbf{x}'), \qquad (1)$$

$$\{a_{\alpha\beta}(\mathbf{x}),\ a_{\gamma\rho}(\mathbf{x}')\}=0.$$

We shall analyze the dynamics in the longwave limit when spatial inhomogeneities of dynamic variables are small, and take into account possible nonlinear interactions of spin waves by using the concept of spontaneous violation of the $SO(3)$ symmetry of spin rotations relative to which the exchange interactions are invariant. We assume that the energy density is a function of the quantities s,a, and ∇a or, equivalently, a function of the quantities s,a,

$\omega_{\alpha k}(a) = 1/2\, e_{\alpha\beta\gamma}a_{\lambda\gamma}\nabla_k a_{\lambda\beta}$ (Cartan's left form function):

$$\varepsilon(x,s_\alpha(\mathbf{x}'),a(\mathbf{x}'))=\varepsilon(s_\alpha(\mathbf{x}),\quad \omega_{\alpha k}(a),a),\quad k$$
$$=x,y,z. \qquad (2)$$

Since the energy density of exchange interactions is invariant to uniform rotations

$$\{S_\alpha,\varepsilon\}=0, \qquad (3)$$

where

$$S_\alpha=\int d^3x\, s_\alpha(\mathbf{x}),$$

we obtain

$$\varepsilon(s,a,\omega_k)=\varepsilon(bs,ba,b\omega_k)=\varepsilon(\underline{s},\underline{\omega}_k). \qquad (4)$$

Here b is an arbitrary orthogonal matrix, $\underline{s} \equiv as$, and $\underline{\omega}_{\alpha k} = 1/2\, e_{\alpha\beta\gamma}a_{\beta\lambda}\nabla_k a_{\gamma\lambda}$ is Cartan's right form function. Using Poisson's bracket (1), we can write the equation of motion for a spatially disordered magnet in the Hamiltonian form without allowance for the dissipation:

$$\dot{s}_\alpha=\{s_\alpha,H\}=-\nabla_k\partial_{\omega_{\alpha k}}\varepsilon,$$

$$\dot{a}_{\alpha\beta}=\{a_{\alpha\beta},H\}=a_{\alpha\rho}e_{\rho\beta\gamma}\partial_{s_\gamma}\varepsilon, \qquad (5)$$

where

$$H=\int d^3x\,\varepsilon(\mathbf{x})$$

is the Hamiltonian of the system. The dot over symbols indicates partial time derivative.

For the variables $\underline{s}_\alpha \equiv a_{\alpha\beta}s_\beta$, $\underline{\omega}_{\alpha k} \equiv a_{\alpha\beta}\omega_{\beta k}$ the Poisson brackets have the form

$$\{\underline{s}_\alpha(\mathbf{x}),\underline{s}_\beta(\mathbf{x}')\}=-e_{\alpha\beta\gamma}\underline{s}_\gamma(\mathbf{x})\delta(\mathbf{x}-\mathbf{x}'),$$

$$\{\underline{\omega}_{\alpha k}(\mathbf{x}),\underline{\omega}_{\beta l}(\mathbf{x}')\}=0,$$

$$\{\underline{s}_\alpha(\mathbf{x}),\underline{\omega}_{\beta k}(\mathbf{x}')\}=e_{\alpha\upsilon\beta}\underline{\omega}_{\upsilon k}(\mathbf{x})\delta(\mathbf{x}-\mathbf{x}')$$
$$+\delta_{\alpha\beta}\nabla'_k\delta(\mathbf{x}-\mathbf{x}'). \qquad (6)$$

The evolution equations (5) in variables $\underline{s}_\alpha,\underline{\omega}_{\alpha k}$ therefore assume the form of equations with Maurer–Cartan constraints:[8,9]

$$\dot{\underline{s}}_\alpha=-\nabla_k\partial_{\underline{\omega}_{\alpha k}}\varepsilon+e_{\alpha\beta\gamma}(\underline{s}_\beta\partial_{\underline{s}_\gamma}\varepsilon+\underline{\omega}_{\beta k}\partial_{\underline{\omega}_{\gamma k}}\varepsilon),$$

$$\dot{\underline{\omega}}_{\alpha k}=-\nabla_k\partial_{\underline{s}_\alpha}\varepsilon+e_{\alpha\beta\gamma}\underline{\omega}_{\beta k}\partial_{\underline{s}_\gamma}\varepsilon, \qquad (7)$$

$$\nabla_k\underline{\omega}_{\alpha i}-\nabla_i\underline{\omega}_{\alpha k}=e_{\alpha\beta\gamma}\underline{\omega}_{\beta k}\underline{\omega}_{\gamma i}.$$

In these equations, $\underline{\omega}_\alpha = 1/2\, e_{\alpha\beta\gamma}(aa^T)_{\gamma\beta}$ is the right form which is connected with the time derivative, and $\underline{\omega}_\alpha \equiv -\partial_{\underline{s}_\alpha}\varepsilon$. It follows from this system of equations that the energy density ε and the momentum components π_i are conserved locally:

$$\dot{\underline{\varepsilon}} = -\nabla_k \partial_{\underline{s}_\alpha}\varepsilon\, \partial_{\underline{\omega}_{\alpha k}}\varepsilon, \quad \dot{\underline{\pi}}_\alpha = -\nabla_k t_{ik}, \tag{8}$$

where $\pi_i = \underline{s}_\alpha \underline{\omega}_{\alpha i}$, and

$$t_{ik} = -\delta_{ik}(\varepsilon - \underline{s}_\alpha \partial_{\underline{s}_\alpha}\varepsilon) + \underline{\omega}_{\alpha i}\partial_{\underline{\omega}_{\alpha k}}\varepsilon \tag{9}$$

is the momentum flux density tensor.

The general system of equations (7) was analyzed by us earlier.[11] In the present work, we shall derive formulas describing helical spin density waves in an isotropic quasi-one-dimensional magnet, taking into account the biquadratic contributions to the energy density. Ivanov[12] obtained soliton solutions using the Lagrangian approach for quadratic dependence of the energy density (amorphous magnet). Nonlinear dynamics of multisublattice noncollinear antiferromagnets with modulated magnetic structure in an external magnetic field was studied in Ref. 13.

MODEL ENERGY DENSITY

Let us consider a disordered magnet whose energy density is invariant relative to left and right spin rotations. In this case, the energy density function ε satisfies the overdetermined system of partial differential equations:[10]

$$e_{\alpha\beta\gamma}(\underline{s}_\beta \partial_{\underline{s}_\gamma}\varepsilon + \underline{\omega}_{\beta k}\partial_{\underline{\omega}_{\gamma k}}\varepsilon) = 0. \tag{10}$$

The general solution of this system is

$$\varepsilon = G(\underline{s}_\alpha^2, \underline{\omega}_{\alpha x}^2, \underline{\omega}_{\alpha y}^2, \underline{\omega}_{\alpha z}^2, \pi_x, \pi_y, \pi_z), \tag{11}$$

where G is an arbitrary function of the above arguments. Since the system (10) is invariant to the group of transpositions of the index k, it is expedient to go over to symmetric variables, after which the practical calculations can be confined to the following expression for the energy density:

$$\varepsilon = \varepsilon_i + \varepsilon_a,$$

in which

$$\varepsilon_i = \frac{1}{2\chi}\,\underline{s}_\alpha^2 + \frac{\rho}{2}\,\underline{\omega}_{\alpha i}^2 + \frac{q}{2}\,\pi_i^2 \tag{12}$$

is the isotropic part of the energy and

$$\varepsilon_a = \frac{\gamma}{2}\,(\underline{\omega}_{\alpha x}^2\underline{\omega}_{\alpha y}^2 + \underline{\omega}_{\alpha x}^2\underline{\omega}_{\alpha z}^2 + \underline{\omega}_{\alpha y}^2\underline{\omega}_{\alpha z}^2) + \frac{\delta}{2}\,\underline{\omega}_{\alpha x}^2\underline{\omega}_{\alpha y}^2\underline{\omega}_{\alpha z}^2$$
$$+ \frac{\gamma_1}{2}\,(\pi_x^2\pi_y^2 + \pi_x^2\pi_z^2 + \pi_y^2\pi_z^2) + \frac{\delta_1}{2}\,\pi_x^2\pi_y^2\pi_z^2 \tag{13}$$

is the anisotropic part, χ is the magnetic susceptibility, ρ is the rigidity, and q, γ, δ, γ_1, and δ_1 are phenomenological coupling constants.

For an isotropic quadratic-biquadratic dependence of the energy density (12) on variables $\underline{s}_\alpha, \underline{\omega}_{\alpha k}$, we can present one-dimensional spin excitations in terms of the equations

$$\dot{\underline{s}}_\alpha = -\partial_x(\rho\underline{\omega}_{\alpha x} + q\pi\underline{s}_\alpha),$$

$$\dot{\underline{\omega}}_{\alpha x} = -\partial_x\left(\frac{\underline{s}_\alpha}{\chi} + q\pi\underline{\omega}_{\alpha x}\right) + \frac{1}{\chi}\,e_{\alpha\beta\gamma}\underline{\omega}_{\beta x}\underline{s}_\gamma, \tag{14}$$

$$\pi \equiv \underline{s}_\alpha\underline{\omega}_{\alpha x}.$$

SOLUTION OF EQUATIONS

We shall now obtain the exact, nonlinear, stationary profile solutions, i.e., solutions for the case in which the required functions $\underline{s}_\alpha(x,t), \underline{\omega}_{\alpha x}(x,t)$ depend on the self-simulating variable $x + et$ (the parameter e defines the various propagation velocities of perturbations in the system). In this case, the system of equations (14) assumes the form

$$(e\underline{s}_\alpha + \rho\underline{\omega}_{\alpha x} + q\pi\underline{s}_\alpha)' = 0,$$

$$\left(e\underline{\omega}_{\alpha x} + \frac{\underline{s}_\alpha}{\chi} + q\pi\underline{\omega}_{\alpha x}\right)' = \frac{1}{\chi}\,e_{\alpha\beta\gamma}\underline{\omega}_{\beta x}\underline{s}_\gamma, \tag{15}$$

$$f' \equiv \frac{df}{d(x+et)}.$$

It follows directly from this system of equations that

$$e\underline{s}_\alpha + \rho\underline{\omega}_{\alpha x} + q\pi\underline{s}_\alpha = C_\alpha,$$
$$\pi = \frac{C_\alpha\underline{s}_\alpha - e\underline{s}_\alpha^2}{\rho + q\underline{s}_\alpha^2}, \tag{16}$$

where C_α are integration constants. We can use these equations to eliminate the unknown functions $\underline{\omega}_{\alpha x}$. At the first stage, we obtain a system of three ordinary differential equations:

$$(k'\delta_{\alpha\beta} + F_\alpha F_\beta)\underline{s}_\beta' = e_{\alpha\beta\gamma}C_\beta\underline{s}_\gamma, \tag{17}$$

in which the following notation was used:

$$k' = \rho - \chi(e + q\pi)^2,$$
$$F_\alpha = \left(\frac{\chi q}{\rho + q\underline{s}_\alpha^2}\right)^{1/2}\left\{C_\alpha - \frac{2(e\rho + qC_\alpha\underline{s}_\alpha)}{\rho + q\underline{s}_\alpha^2}\,\underline{s}_\alpha\right\}. \tag{18}$$

If we know the explicit form of the derivatives $\underline{s}_\alpha'$, we can easily transform the system of equations (17) into a linear system by multiplying (17) by a matrix reciprocal to the matrix $k'\delta_{\alpha\beta} + F_\alpha F_\beta$:

$$\underline{s}_\alpha' = \frac{1}{k'}\,e_{\alpha\beta\gamma}C_\beta\underline{s}_\gamma, \quad k'^3 + k'^2 F_\alpha^2 \neq 0. \tag{19}$$

It follows from (19) that the quantities $C_\alpha\underline{s}_\alpha$ and $\underline{s}_\alpha^2$ are independent of the variable $x + et$. Carrying out scaling transformation $\xi = (x + et)|C_\alpha|/[\rho - \chi(e + q\pi)^2]$, we obtain the following linear system of Euler equations for the right form $\underline{s}_\alpha$:

$$\frac{d}{d\xi}\,\underline{s}_\alpha = e_{\alpha\beta\gamma}n_\beta\underline{s}_\gamma, \quad n_\alpha \equiv \frac{C_\alpha}{|C_\alpha|}. \tag{20}$$

The solution of this system is

$$\underline{s}_\alpha(\xi) = g_{\alpha\beta}\underline{s}_\beta(\xi_0), \tag{21}$$

where the orthogonal rotation matrix g $(g^T g = 1)$ is defined as

$$g_{\alpha\beta} = \cos\xi\,\delta_{\alpha\beta} + (1-\cos\xi)n_\alpha n_\beta - \sin\xi\,e_{\alpha\beta\gamma}n_\gamma, \quad (22)$$

and $\underline{s}_\beta(\xi_0)$ are integration constants.

The solution (21) for the right form obtained above can be used to define the spin density

$$s_\alpha = a_{\beta\alpha}\underline{s}_\beta. \quad (23)$$

The orthogonal rotational matrix $a_{\alpha\beta}$ satisfies the redefined system of equations

$$\underline{\omega}_\alpha = \frac{1}{2}\,e_{\alpha\beta\gamma}a_{\beta\lambda}\dot{a}_{\gamma\lambda},$$

$$\underline{\omega}_{\alpha x} = \frac{1}{2}\,e_{\alpha\beta\gamma}a_{\beta\lambda}\partial_x a_{\gamma\lambda}. \quad (24)$$

In order to solve this system of equations with respect to the matrix $a_{\alpha\beta}$, we use parametrization with the help of Euler's angles:[14]

$$a = \begin{pmatrix} \cos\psi\cos\varphi - \cos\theta\sin\psi\sin\varphi & \cos\theta\sin\psi\cos\varphi + \cos\psi\sin\varphi & \sin\theta\sin\psi \\ -\sin\psi\cos\varphi - \cos\theta\cos\psi\sin\varphi & \cos\theta\cos\psi\cos\varphi - \sin\psi\sin\varphi & \sin\theta\cos\psi \\ \sin\theta\sin\varphi & -\sin\theta\cos\varphi & \cos\theta \end{pmatrix}. \quad (25)$$

In terms of the variables ψ, θ, and φ, the system (24) assumes the form

$$\underline{\omega}_1 = -\dot\theta\cos\psi - \dot\varphi\sin\theta\sin\psi,$$

$$\underline{\omega}_2 = \dot\theta\sin\psi - \dot\varphi\sin\theta\cos\psi,$$

$$\underline{\omega}_3 = -\dot\psi - \dot\varphi\cos\theta,$$

$$\omega_{1x} = -\theta_x\cos\psi - \varphi_x\sin\theta\sin\psi, \quad (26)$$

$$\underline{\omega}_{2x} = \theta_x\sin\psi - \varphi_x\sin\theta\cos\psi,$$

$$\underline{\omega}_{3x} = -\psi_x - \varphi_x\cos\theta.$$

Let us consider the case in which $\mathbf{n} = (0,0,-1)$, i.e., $C_3 < 0$ and $\underline{s}(\xi_0) = (c_1, 0, c_3)$. The exact solution of the redefined system (26) can be obtained easily for $\varphi = \varphi_0 = \text{const}$. Under the above-mentioned conditions the system (26), with allowance for Eqs. (16) and (21), becomes

$$-\dot\theta\cos\psi = \left(-\frac{1}{\chi} + q\pi z\right)c_1\cos\xi,$$

$$\dot\theta\sin\psi = \left(\frac{1}{\chi} - q\pi z\right)c_1\sin\xi,$$

$$-\dot\psi = -q\pi\frac{C_3}{\rho} + \left(-\frac{1}{\chi} + q\pi z\right)c_3,$$

$$\theta_x\cos\psi = zc_1\cos\xi,$$

$$\theta_x\sin\psi = zc_1\sin\xi,$$

$$\psi_x = -\frac{C_3}{\rho} + zc_3, \quad z \equiv \frac{e + q\pi}{\rho}. \quad (27)$$

The solution for the function $\psi(x,t)$ has the obvious form

$$\psi(x,t) = \left(-\frac{C_3}{\rho} + zc_3\right)x + \left[q\pi\frac{C_3}{\rho} - \left(-\frac{1}{\chi} + q\pi z\right)c_3\right]$$

$$\times t + \psi_0, \quad (28)$$

where ψ_0 is a constant. The redefined differential system (27) with respect to the function $\theta(x,t)$ can be eliminated easily by equating the functions $\xi(x,t)$ and $\psi(x,t)$, i.e., by satisfying the conditions

$$-\frac{C_3}{\rho} + zc_3 = k_1,$$

$$q\pi\frac{C_3}{\rho} - \left(-\frac{1}{\chi} + q\pi z\right)c_3 = k_1 e \equiv \omega_1, \quad (29)$$

$$k_1 \equiv \frac{|C_3|}{\rho - \chi(e + q\pi)^2}.$$

These relations are the redefined system of algebraic equations in parameter e, which is evidently compatible since we can present it in the form

$$z^2 - \frac{C_3}{c_3\rho}z - \frac{1}{\chi\rho} = 0,$$

$$\left(z^2 - \frac{C_3}{c_3\rho}z - \frac{1}{\chi\rho}\right)(\chi q\pi z - 1) = 0. \quad (30)$$

This system has two real solutions for e, and hence for k_1 and ω_1:

$$e_\pm = -\frac{q}{\rho}C_3 c_3 + \left[1 + \frac{q}{\rho}(c_1^2 + c_3^2)\right]$$

$$\times\left[-\frac{|C_3|}{2c_3} \pm \left(\frac{C_3^2}{4c_3^2} + \frac{\rho}{\chi}\right)^{1/2}\right],$$

$$k_1 = \frac{c_3}{\rho}\left[\frac{|C_3|}{2c_3} \pm \left(\frac{C_3^2}{4c_3^2} + \frac{\rho}{\chi}\right)^{1/2}\right],$$

$$\omega_1 = -\frac{|C_3|}{c_3}\left(1 + \frac{q}{\rho}c_1^2\right)k_1 + \frac{\rho}{c_3}\left[1 + \frac{q}{\rho}(c_1^2 + c_3^2)\right]k_1^2. \quad (31)$$

Hence the function $\theta(x,t)$ is linear in x and t on the set $\{x,t : \xi \neq m\pi/2,\ m = 0, \pm 1, \pm 2, \ldots\}$; i.e.,

$$\theta(x,t)=k_2 x+\omega_2 t+\theta_0,$$

$$k_2=\frac{c_1}{c_3}\left(k_1+\frac{C_3}{\rho}\right)=\frac{c_1}{\rho}\left[-\frac{|C_3|}{2c_3}\pm\left(\frac{C_3^2}{4c_3^2}+\frac{\rho}{\chi}\right)^{1/2}\right],$$

$$\omega_2=\frac{c_1}{c_3}\left(\omega_1-q\pi\frac{C_3}{\rho}\right)=\frac{|C_3|}{c_3}\left(1+\frac{q}{\rho}c_3^2\right)k_2+\frac{\rho}{c_1}$$

$$\times\left[1+\frac{q}{\rho}(c_1^2+c_3^2)\right]k_2^2,\tag{32}$$

where θ_0 is a constant. Solutions for the parameters φ, θ, and ψ determine the rotational matrix (25), and the spin density s_α is defined in accordance with Eq. (23) as follows:

$$s_1=c_3\sin\varphi_0\sin\theta+c_1\cos\varphi_0.$$

$$s_2=-c_3\cos\varphi_0\sin\theta+c_1\sin\varphi_0,\tag{33}$$

$$s_3=c_3\cos\theta.$$

The effective magnetic field h_α which forms stationary profile waves with a spin density s_α, is defined by the relation $h_\alpha\equiv\partial_{s_\alpha}\varepsilon$:

$$h_{\alpha\pm}=\frac{1}{\chi}s_\alpha+\left\{\left[\frac{qC_3c_3}{\rho}-\frac{q}{\rho}(c_1^2+c_3^2)\right]\left[-\frac{|C_3|}{2c_3}\pm\left(\frac{C_3^2}{4c_3^2}\right.\right.\right.$$

$$\left.\left.\left.+\frac{\rho}{\chi}\right)^{1/2}\right]\right\}\left\{a_{3\alpha}\frac{C_3}{\rho}-\frac{1}{\rho}\left[-\frac{|C_3|}{2c_3}\right.\right.$$

$$\left.\left.\pm\left(\frac{C_3^2}{4c_3^2}+\frac{\rho}{\chi}\right)^{1/2}\right]s_\alpha\right\}.\tag{34}$$

The spin density s_α induces a field of the same wavelength and frequency. Particular solution for $\theta=\pi/2$, $\underline{s}(\xi_0)=(0,c_2,c_3)$, $\mathbf{n}=(0,0,-1)$ is obtained in the same way as described above:

$$s_1=c_3\sin\varphi,\quad s_2=-c_3\cos\varphi,\quad s_3=c_2,$$

$$\varphi=k_2 x+\omega_2 t\tag{35}$$

by replacing c_1 by c_2 in k_2 and ω_2 in Eqs. (33) and (34).

CONCLUSIONS

A characteristic feature of the Hamiltonian formalism is a stepwise solution of a system of first-order equations. Therefore, the choice of the parametrization (25) at the intermediate stage is determined entirely by the form of the solution (21), which simplifies integration. According to Eqs. (33) and (35), the exact nonlinear solutions for stationary profile waves are helical in the model under consideration. Contribution of biquadratic terms in the energy density (12) increases with increasing density of the initial spin density distribution in the system and decreases rigidity ρ [this follows from Eq. (31) for $e_\pm$ and Eq. (32) for the frequency ω_2]. However, this dependence is exhibited only in frequency ω_2 of the helical spin density wave (33), and the wave vector k_2 does not depend on q.

*E-mail: yevgeny@kipt.kharkov.ua

[1] N. N. Bogoliubov, Physica **26**, 1 (1960).
[2] J. J. Goldstone, J. Nuovo Cimento **19**, 154 (1961).
[3] B. I. Halperin and P. C. Hohenberg, Phys. Rev. **188**, 898 (1969).
[4] B. I. Halperin and W. M. Saslow, Phys. Rev. **B16**, 2154 (1977).
[5] W. M. Saslow, Phys. Rev. **B22**, 1174 (1980).
[6] D. V. Volkov and A. A. Zheltukhin, Izv. Akad. Nauk SSSR, Ser. Fizika **44**, 1487 (1980).
[7] A. F. Andreev and V. I. Marchenko, Usp. Fiz. Nauk **130**, 39 (1980).
[8] I. E. Dzyaloshinskii and G. E. Volovik, Ann. Phys. **125**, 67 (1980).
[9] M. Yu. Kovalevskii, S. V. Peletminskii, and A. L. Shishkin, Ukr. Fiz. Zh. **36**, 245 (1991).
[10] M. Yu. Kovalevskii and S. V. Peletminskii, Teor. Mekh. Fiz. **100**, 59 (1994).
[11] E. A. Ivanchenko, Fiz. Nizk. Temp. **20**, 158 (1994) [Low Temp. Phys. **20**, 127 (1994)].
[12] B. A. Ivanov, Solid State Commun. **34**, 437 (1980).
[13] A. L. Sukstanskii and B. A. Ivanov, Zh. Éksp. Teor. Fiz. **108**, 914 (1995) [JETP **81**, 502 (1995)].
[14] H. Goldstein, *Classical Mechanics* [in Russian], Nauka, Moscow (1975).

Translated by R. S. Wadhwa

Magnetic and galvanomagnetic properties of the ordering Pd₂AuFe alloys

N. I. Kourov

Institute of Metal Physics, Ural Branch of the Russian Academy of Sciences, 620219 Ekaterinburg, Russia*

L. N. Tyulenev

Ural State Engineering University, 620002 Ekaterinburg, Russia

T. Mydlars

International Laboratory of High Magnetic Fields and Low Temperatures, 53–529 Wroclaw, Poland

Magnetic and galvanomagnetic properties of ordering alloys Pd₂AuFe are studied in fields $H \leq 12$ MA/m at $T = 4.2$ K. It is shown that the disappearance of spontaneous magnetization in the region of ferromagnetic–antiferromagnetic phase transition which occurs as a result of atomic ordering of the Pd₂AuFe alloys is accompanied by peaks of paraprocess susceptibility and of the anomalous positive Hall effect. The sign of the normal Hall effect is reversed in this case. It is shown that the peculiarities of galvanomagnetic properties are associated with the rearrangement of the electronic band structure during ordering of the alloys. © *1997 American Institute of Physics.* [S1063-777X(97)00708-1]

In the disordered state, Pd₂AuFe alloys are normal ferromagnets (FM) with $T_c \sim 460$ K.[1–3] Atomic ordering of these alloys by annealing at $T = 720$ K for $\tau \geq 30$ min transforms them into a state close to antiferromagnetic (AFM) with $T_N \sim 130$ K. Such an FM–AFM phase transition is accompanied by the anomalous behavior of magnetic properties as well as electron properties that have been studied earlier.

An increase in the atomic ordering degree η in the alloys under consideration leads to an increase in the average effective magnetic moment μ_{eff} from $\sim 3 \mu_B$/mole for a quenched alloy to $\sim 5.6 \mu_B$/mole for a sample annealed for a period $\tau = 30$ min. This is accompanied by a sharp decrease in the low-temperature heat capacity and an increase in resistivity values $\rho \sim 200 \mu\Omega \cdot$cm, which is unusual for ordered alloys.[2,3] These experimental facts point towards a considerable variation in the degree of localization of atomic magnetic moments upon a transition from FM to AFM state as a result of atomic ordering of Pd₂AuFe alloys, which is associated with the rearrangement of the electronic band structure in the vicinity of the Fermi level E_F. This is confirmed by the results of analysis of optical properties of ordering Pd₂AuFe alloys.[4]

Investigations of the galvanomagnetic properties, viz., magnetoresistance (MR) as well as normal and anomalous components of the Hall effect (HE), can provide additional information about the variation of the electronic band structure and the scattering processes for conduction electrons in the region of transition from FM to AFM state as a result of annealing of the alloys under consideration. The order of localization of magnetic moments can be estimated by comparing the effective moment obtained from paramagnetic susceptibility measurements and the spontaneous moment at $T \sim 0$ K obtained from magnetization curves (from the magnitude of the Rhodes–Wohlfarth parameter μ_{eff}/μ_s).[5] In order to single out the characteristics of alloys that are highly

inhomogeneous in the FM–AFM phase transition region and in which we are interested, we must study the magnetic and galvanomagnetic properties in identical, extremely high magnetic fields (in the paraprocess region).

In the present work, we shall discuss the magnetic and galvanomagnetic properties of ordering Pd₂AuFe alloys. Measurements were made at the International Laboratory of High Magnetic Fields and Low Temperatures, Wroclaw, Poland, at 4.2 K in magnetic fields up to $H \sim 12$ MA/m. The magnetization J was measured with the help of a ballistic galvanometer with an absolute measurement error not exceeding $\sim 3\%$. Galvanomagnetic properties were measured by the conventional four-probe technique with a constant current using instruments whose relative error did not exceed $10^{-4}\%$.

The results of measurements of magnetization and Hall effect for Pd₂AuFe alloys with various atomic orders are presented in Figs. 1 and 2. It can be seen that the magnetization process in atomically disordered state has the conventional form for ferromagnets, i.e. $J(H)$ does not display any hysteresis in the region of technical magnetization (below the saturation field $H_s \sim 1$ MA/m). For $H > H_s$, the magnetization in the paraprocess region can be described by the relation[6]

$$J = J_s + \chi_p H, \tag{1}$$

where J_s is the spontaneous magnetization, and $\chi_p \sim 10^{-6}$ cm³/g is the paraprocess susceptibility.

The field dependence of the Hall resistivity $\rho_H(H)$ for $H > 1$ MA/m is also a linear function and can be represented in the form

$$\rho_H = R_0 B + 4\pi R_s J = R_0^* H + 4\pi R_s^* J_s. \tag{2}$$

Here, R_0 and R_s are the normal and anomalous Hall coefficients respectively; $B = H + (4\pi - N)J$ the inductance in the sample, and N the demagnetizing factor of the sample. Ac-
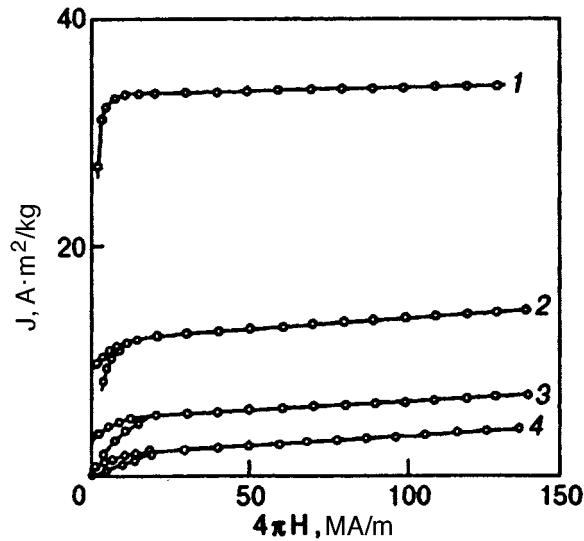
FIG. 1. Magnetization of Pd_2AuFe alloys at $T = 4.2$ K in disordered state (curve *1*) and after annealing of samples at $T = 720$ K over the time $\tau = 10$ (curve *2*), 30 (curve *3*) and 300 min (curve *4*).

cording to Ref. 3, the MR in atomically disordered alloys is associated with the paraprocess starting from even weaker fields ($H \geqslant 0.3$ MA/m, and the familiar Akulov rules (see, for example, Ref. 6) are applicable for its longitudinal and transverse components.

An increase in the value of η in Pd_2AuFe alloys leads to a broadening of the technical magnetization interval, enhancement of hysteresis on $J(H)$ curves in fields $H < H_s$,
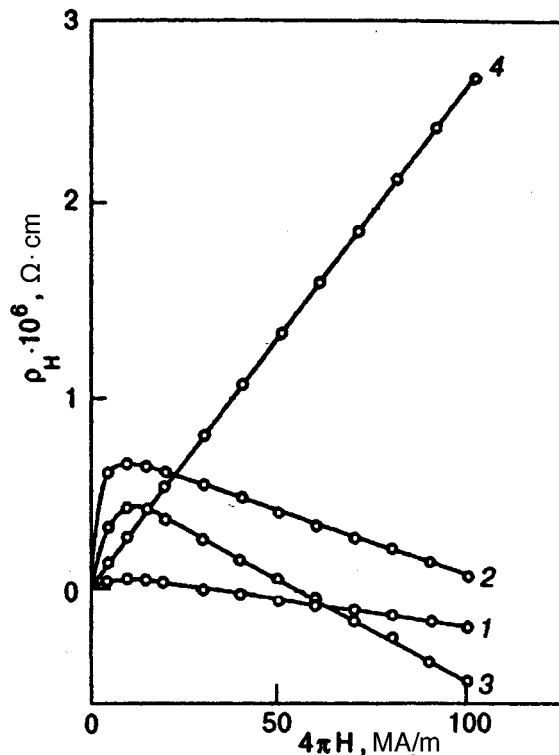

FIG. 2. Hall resistivity of Pd_2AuFe alloys at $T = 4.2$ K in disordered state (curve *1*) and after annealing of samples at $T = 720$ K over the time $\tau = 10$ (curve *2*), 30 (curve *3*) and 300 min (curve *4*).

and to an increase in the paraprocess susceptibility for $H > H_s$. The field below which the nonlinear dependence $\rho_H(H)$ corresponding to technical magnetization is observed increases insignificantly, and the slope of the linear part of the dependence $\rho_H(H)$ reverses its sign in the paraprocess region. In the entire range of investigated fields ($0 \leqslant H < 12$ MA/m, the behavior of MR in partially and completely ordered samples is characteristic for the paraprocess when the longitudinal and transverse effects are equal, negative, and linearly quadratic functions of the external field:[6]

$$\frac{\Delta\rho}{\rho} = \frac{\rho(H) - \rho(0)}{\rho(0)} \sim -(J^2 - J_s^2) \sim (2\chi_p J_s H + \chi_p^2 H^2).$$

It follows from (1) and (2) that together with the magnetic characteristics J_s and χ_p, a mathematical analysis of the obtained linear dependences $J(H)$ and $\rho_H(H)$ for $H > H_s \sim 1$ MA/m leads to the values of effective normal and anomalous Hall coefficients: $R_0^* = R_0 + 4\pi R_s \chi_p$ and $R_s^* = R_s + (1 - N/4\pi)R_0$ respectively. Since the samples have the form of a parallelepiped with $N \sim 4\pi$ in the case under consideration and the paraprocess susceptibility in them does not exceed $\chi_p \sim 10^{-4}$ cm^3/g, the true normal and anomalous Hall coefficients in which we are interested can be assumed to be equal to the experimental values of the effective constants within the measurement errors, i.e., $R_0 \sim R_0^*$ and $R_s \sim R_s^*$.

The main magnetic and galvanomagnetic characteristics of the Pd_2AuFe alloys are presented in Fig. 3 as functions of the degree of atomic ordering (i.e., the annealing time τ). It can be seen that the spontaneous magnetic moment $\mu_s \sim 2.8 \ \mu_B$/mole in the disordered state. The value of this quantity decreases with increasing η due to a transition to the AFM state after annealing of the samples over a period $\tau \geqslant 30$ min. In view of the cluster type of FM–AFM phase transition, the observed decrease in the value of J_s in ordered samples must be attributed to the decrease in the volume of the FM phase. Naturally, the increase in the "paraprocess" susceptibility in this case is caused by the ordering of magnetic inhomogeneities (FM and AFM clusters) arising in the FM–AFM phase transition region. The ordering process for such inhomogeneities in a magnetic field is responsible for nearly identical behavior of longitudinal and transverse MR.

A comparison of the results of magnetization measurements obtained by us (see Figs. 1 and 3) and the paramagnetic susceptibility results published in Ref. 3 shows that disordered Pd_2AuFe alloys belong to the class of Heisenberg magnets in which the magnetic moments are extremely localized at iron atoms. In this case, the Rhodes–Wohlfarth parameter (the ratio μ_{eff}/μ_s) is nearly equal to unity.

According to the experimental results presented in Fig. 3 and Ref. 3, the decrease in the value of μ_s upon an increase in η is accompanied by an increase in the value of μ_{eff}. On one hand, this points towards a decrease in the degree of localization of atomic magnetic moments due to ordering of alloys, since the Rhodes–Wohlfarth parameter defined in the manner proposed in Ref. 5 becomes much larger than unity in this case. On the other hand, however, an increase in the value of μ_{eff} and its closeness to the moments of free iron
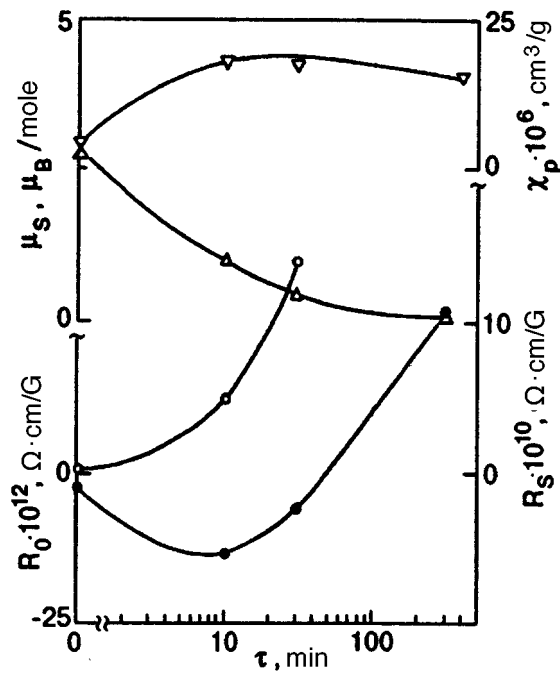
FIG. 3. Spontaneous moment μ_s($\triangle$), susceptibility of paraprocess χ_p(∇), and the normal R_0($\bullet$) and anomalous R_S($\bigcirc$) Hall coefficients at $T = 4.2$ K for Pd$_2$AuFe alloys as functions of annealing time τ at $T = 720$ K.

ions (for frozen orbital angular momentum, the values of $\mu_{Fe_{2+}}$ and $\mu_{Fe_{3+}}$ are 4.9 μ_B and 5.92 μ_B respectively) led us to the conclusion[3] about a decrease in overlapping and hence an increase in the localization of d-states of the main magnetically active iron atoms during ordering of Pd$_2$AuFe alloys.

The above contradiction can be associated with the error in experimental determination of μ_s as a characteristic of the local state of iron atoms in the alloys under investigation. In the region of FM–AFM phase transition, the values of J_s obtained experimentally in accordance with Eq. (1) are computed for the entire volume of the sample although in actual practice they are determined only by its FM component. If the FM–AFM phase transition is treated as a cluster phenomenon, the volume of the FM phase in the alloy decreases with increasing τ and remains practically unknown. Under such conditions, it is not possible to determine the spontaneous moment corresponding to the FM part of the sample by conventional methods for partially ordered Pd$_2$AuFe alloys.

In the FM–AFM phase transition region, for the case when the samples contain two magnetic subsystems, the value of μ_s determined by the above method does not characterize the true moment localized at iron atoms. Hence the Rhodes–Wohlfarth parameter μ_{eff}/μ_s cannot define unambiguously the degree of localization of atomic magnetic moments. In such cases, a more correct information about the blurring of d-wave functions of magnetically active atoms can be obtained by comparing the value of μ_{eff} obtained from the results of measurements of paramagnetic susceptibility with the theoretical values of the magnetic moment of the corresponding free ion. An estimation of the true degree of localization of the magnetic moments in the ordered

Pd$_2$AuFe alloys requires further investigations that would help in obtaining the local spin and charge density distributions.

It can be seen from Fig. 3 that a transition from FM to AFM state in the investigated alloys is accompanied by an anomalous variation of normal as well as anomalous Hall coefficients. In partially ordered samples annealed over a period $\tau \sim 30$ min, when the earlier investigated electronic properties of alloys display singularities and sharp variations are observed in the values of the moments localized at iron atoms,[1–3] a reversal of the sign of the coefficient $R_0(r)$ is observed experimentally.

In the one-band approximation, the reversal of the sign of the normal Hall coefficient indicates a transition from electron to hole type of Hall carriers for an atomic order corresponding to an annealing time $\tau \sim 30$ min. For transition metal alloys, however, the model with one type of carriers is very crude. The use of the two-band approximation, for which

$$R_0 = \frac{n_h \mu_h^2 - n_e \mu_e^2}{(n_h \mu_n + n_e \mu_2)^2},$$

leads to the conclusion that the densities $n_h(n_e)$ as well as mobilities $\mu_h(\mu_e)$ of h and e-type Hall carriers vary sharply upon annealing for $\tau \sim 30$ min. In any case, the results of measurements of the coefficient R_0 are in accord with the conclusions drawn in Refs. 3 and 4 about a considerable rearrangement of the electronic band structure in the vicinity of E_F, which takes place due to a decrease in the overlapping of d-wave functions of Fe atoms upon ordering of Pd$_2$AuFe alloys as a result of transition of the nearest neighbors of analogous Fe atoms from first coordination sphere to the second.

According to Fig. 3, annealing leads to an increase in the anomalous Hall coefficient which is positive for a quenched alloy. The coefficient attains its highest value for annealing times $\tau \sim 30$ min when the FM subsystem in the alloy disappears. For AFM alloys annealed for a period $\tau > 30$ min, anomalous Hall effect is not observed within the limits of measuring error for the technique used, i.e., the coefficient $R_s \sim 0$.

The anomalous Hall effect is usually associated with the asymmetry of scattering of Hall carriers by various perturbations in the metal.[6,7] It would appear that the sharp increase in the coefficient R_s in the immediate vicinity of the FM–AFM transition region of the alloys under investigation indicates the predominance of scattering at magnetic inhomogeneities (FM or AFM clusters) in the anomalous Hall effect. However, MR studies reveal[3] that for any extent of magnetic ordering, the magnetoresistance has nearly the same magnitude and amounts to $\sim(2-3)$% of the total resistivity ρ. It can be seen from Fig. 3 that the high-field magnetic susceptibility also changes insignificantly upon an increase in the annealing time. However, the coefficient R_s increases by more than an order of magnitude upon annealing of a quenched alloy for $\tau \sim 30$ min.

A comparison of the anomalous Hall coefficient determined by us (see Fig. 3) with the resistance data presented in Ref. 3 points towards the correlation of their dependence on

τ in the FM state. This is in accord with the conclusions of the theory of a power relationship between the kinetic properties under consideration.[6,7] However, the absence of anomalous HE in AFM alloys for a large value of ρ that depends weakly on τ indicates that such kinetic properties are probably determined by peculiarities of the electronic band structure in the vicinity of E_F. The scattering of conduction electrons by the magnetic subsystem perturbations is insignificant in this case.

The behavior of magnetic and galvanomagnetic properties observed during annealing of Pd_2AuFe alloys can be explained by taking into account the contribution of interference effects in the anomalous HE, and by assuming that the dominant role in hall conductivity is played by the rearrangement of the electronic band structure near E_F in the FM–AFM transition region. The latter assumption is quite significant if magnetized d-carriers are responsible for Hall conductivity.

It must be remarked that the maximum value of the coefficient R_s is about two orders of magnitude higher than the quantity R_0. Such a situation is quite normal for most FM alloys. The signs of normal and anomalous HE determined by the type of Hall carriers are opposite in the FM state. This is possible in the one-band approximation if the spin–orbit coupling constant λ appearing in the expression for the coefficient R_s is negative.[6,7]

Thus, the obtained results of investigation of magnetic and galvanomagnetic properties of ordering Pd_2AuFe alloys show that

(a) the Rhodes–Wohlfarth parameter obtained as a result of measurement of magnetic properties only is not a true criterion for the degree of localization of atomic magnetic moments of transition metal alloys in the FM–AFM phase transition region when two magnetic subsystems coexist in the samples;

(b) the anomalous Hall coefficient is positive and non-zero only in the FM state of ordering Pd_2AuFe alloys. As the spontaneous magnetization disappears as a result of annealing of samples, the negative normal Hall coefficient passes through zero and becomes positive in AFM alloys;

(c) in the region of phase transition from FM to AFM state, the peculiarities of kinetic properties observed during ordering of Pd_2AuFe alloys are due to a rearrangement of the electronic band structure near E_F.

*E-mail: lowtemp@ifm.e-burg.su

[1] M. A. Borozdina, Yu. G. Karpov, Yu. A. Vereshchagin *et al.*, Fiz. Metal. Metalloved. **55**, 1112 (1983).

[2] N. I. Kourov, M. A. Alekseeva, and Yu. A. Vereshchagin, Fiz. Nizk. Temp. **13**, 173 (1987) [Sov. J. Low Temp. Phys. **13**, 95 (1987)].

[3] A. S. Shcherbakov, N. I. Kourov, Yu. A. Vereshchagin, and M. A. Alekseeva, Fiz. Metal. Metalloved. **76**, 68 (1993).

[4] N. I. Kourov, Yu. V. Knyazev, and L. N. Tyulenev, Fiz. Metal. Metalloved. **80**, 84 (1995).

[5] S. V. Vonsovskii, *Magnetism,* J. Wiley, New York, 1974.

[6] P. Rhodes and E. P. Wohlfarth, Proc. Roy. Soc. **273**, 247 (1963).

[7] A. V. Vedyaev, A. N. Voloshinskii, A. B. Granovskii, and N. V. Ryzhanova, Izv. Vuzov, Fizika **1**, 66 (1987).

Translated by R. S. Wadhwa

Giant magnetoresistance of $La_{0.5}Pb_{0.2}Ca_{0.2}Y_{0.1}MnO_{3-\delta}$ films obtained by magnetron sputtering

S. I. Khartsev, V. N. Krivoruchko, and V. P. Pashchenko

*A. Galkin Physicotechnical Institute, National Academy of Sciences of the Ukraine, 340114 Donetsk, Ukraine**

Magnetoresistive properties of thin $La_{0.5}Pb_{0.2}Ca_{0.2}Y_{0.1}MnO_{3-\delta}$ films obtained by magnetron sputtering technique are studied. A giant decrease in resistance (up to 98%) in magnetic fields $H = 10$ T is observed at a temperature of 175 K. The physical factors responsible for the effect of composition and preparation technique on their magnetotransport properties are discussed. The mechanisms and empirical relations describing the temperature and field dependences of the resistive properties of films are also discussed. © *1997 American Institute of Physics.* [S1063-777X(97)00808-6]

INTRODUCTION

Magnetic semiconductors with a large negative magnetoresistance have a special field of application in microelectronics. Perovskite manganites have been known for quite some time as compounds closely related to the electrical and magnetic properties (see, for example, Refs. 1–4). Following the discovery of giant negative magnetoresistance in systems based on perovskite manganites,[5–9] the interest in these materials has grown enormously in recent years (see review by Nagaev[10]). The need for practical application of manganites in electronics necessitates an increase in the sensitivity of the materials to weak magnetic fields. Naturally, the solution of the problem concerning a weak saturation field requires a deep understanding of the physical mechanisms lying at the root of the magnetoresistance of manganites. These mechanisms are not known at present, but two factors affecting significantly the transport and magnetic properties of manganites have been clearly outlined, viz., (1) the average ionic radius of cations in the A-position[11–13] and (2) the concentration and mobility of charge carriers, determined by the ratio of Mn^{3+} and Mn^{4+} ions (see, for example, Refs. 1, 2, 10, and 14). However, these are obviously not the only physical factors responsible for the formation of the magnetoresistive effect.

The potential practical application of magnetoresistive properties of manganites has also aroused considerable interest in the technology of preparation and properties of thin films of the material which are characterized by a large value of the magnetoresistive effect.[10] Most manganite films were prepared by using the expensive technique of laser sputtering of samples (see, for example, Refs. 7–9). However, the more economical technique of magnetron sputtering was recently applied successfully for preparing high-quality films of $(LaCa)MnO_3$.[15] We used the same technique to obtain thin films of $La_{0.5}Pb_{0.2}Ca_{0.2}Y_{0.1}MnO_{3-\delta}$ films. In this work, we report the results of magnetoresistive studies of such films. Among other things, a giant variation of the film resistance with $-\Delta R/R_0 = [R(H) - R_0]/R_0$ up to 98% in a magnetic field $H = 10$ T was observed at a temperature of 175 K [$(R(H)$ and R_0 are the resistance in a magnetic field and in the absence of a magnetic field, respectively]. The physical factors responsible for the effect of film composition and preparation technique on their magnetic and transport characteristics are indicated. Empirical relations describing temperature and field dependences of film resistance, and the conductivity mechanisms corresponding to these dependences, are discussed.

2. CHOICE OF COMPOSITION, PREPARATION TECHNIQUE, AND INVESTIGATION OF THE SAMPLES

It was mentioned above that the physical nature of the metal–semiconductor and ferromagnetic–antiferromagnetic phase transitions in perovskite manganites is not clear as yet. However, it has ben established that the magnetoresistive effect depends significantly on oxygen nonstoichiometry, ratio of manganese ions of different valencies, and the average radius r_A of cations in the A-position. Resistance variation of more than 50% in a magnetic field was observed only in systems with r_A smaller than 1.23 Å. We took this circumstance into account while selecting the composition of oxide mixtures. The average cation radius in the A-position for $La_{0.5}Pb_{0.2}Ca_{0.2}Y_{0.1}MnO_{3-\delta}$ compounds is 1.19 Å. According to the current theory,[11–13] this should lead to high magnetoresistive characteristics of the material, as well as to high metal-semiconductor transition temperatures. The results of investigations presented in Sec. 3 confirm the accuracy of the assumptions made above.

Thin $La_{0.5}Pb_{0.2}Ca_{0.2}Y_{0.1}MnO_{3-\delta}$ films of thickness ~3500 Å were prepared by reactive magnetron sputtering on the setup VUP–5M. The powder of required composition was synthesized from a mixture of oxides La_2O_3, PbO, MnO_2, Y_2O_3 and calcium carbonate by annealing the mixture $CaCO_3$ for 24 hours at 850 °C in air followed by slow cooling and crushing. Targets for sputtering were obtained by hydrostatic pressing of synthesized powder into pellets and sintering at 1050 °C for six hours. The sputtering of films was carried out on sapphire substrates $Al_2O_3(01\overline{1}2)$, whose temperature was maintained at 800 °C. The pressure of the gaseous mixture $Ar:O_2 = 1:4$ was 50 mTorr and the residual pressure in the chamber was
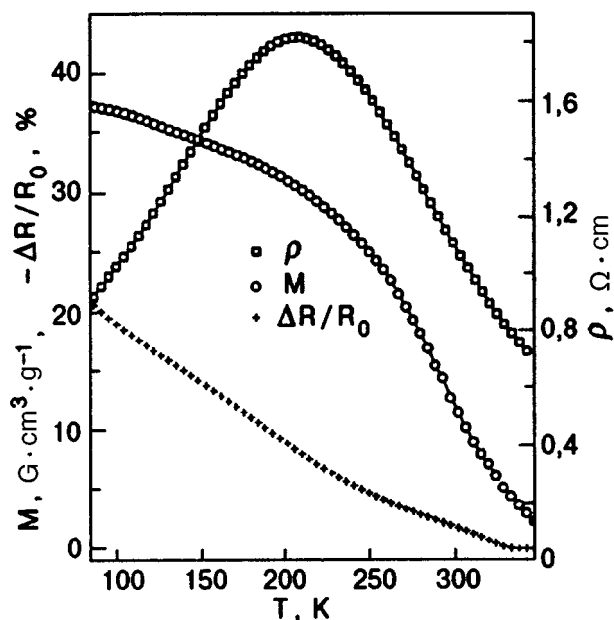
FIG. 1. Temperature dependence of magnetization M, resistivity ρ, and magnetoresistive effect $\Delta R/R_0$ in ceramic samples of $La_{0.5}Pb_{0.2}Ca_{0.2}Y_{0.1}MnO_{3-\delta}$ in a field $H = 1$ T.
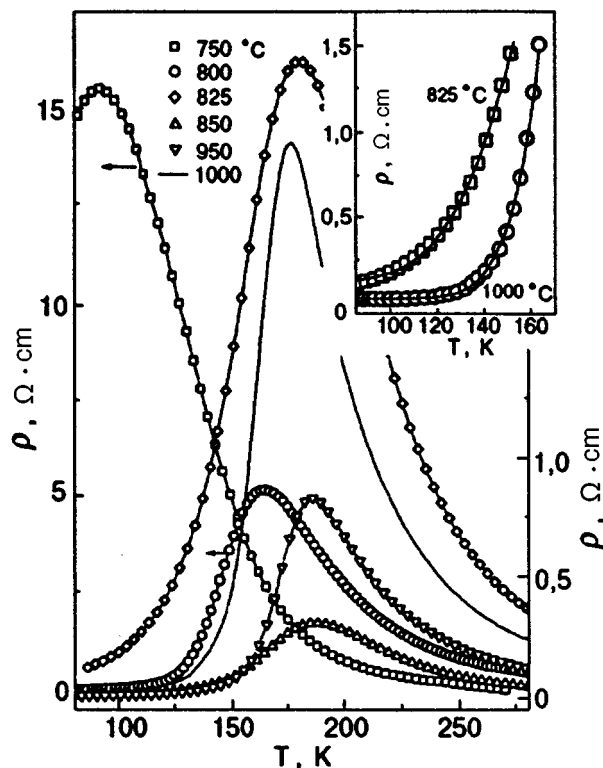

FIG. 2. Temperature dependence of resistivity of $La_{0.5}Pb_{0.2}Ca_{0.2}Y_{0.1}MnO_{3-\delta}$ films annealed in oxygen at various temperatures. The inset shows the accuracy with which the dependence $\rho(T) = \rho_0 + A \exp(-B/T)$ is observed for the resistivity of films annealed at 825 and 1000 °C.

5×10^{-7} Torr. The results of x-ray structural analysis showed that the ceramic and film samples have a single-phase perovskite structure. Texturized structure of films was observed upon a growth of blocks parallel to the (202)−axis of the sapphire substrate. The angle of disorientation of blocks did not exceed 3.5°.

The resistance and magnetoresistance of films were measured as functions of temperature and magnetic field by using the four-probe technique. Magnetic field up to 10 kOe were produced by an electromagnet, and up to 100 kOe by pulse technique in a solenoid. The field was applied parallel to the plane of the film. The magnetoresistance was independent of the mutual orientation of field and current. The temperature dependence of the magnetization of bulk ceramic samples was measured on pendulum balance magnetometer.

We did not carry out direct measurements of the oxygen concentration in as-deposited films. However, thermogravitational data for ceramic samples and several other arguments (including the results of measurements presented below) indicate unambiguously that the films obtained as a result of magnetron sputtering are oxygen-deficient. Change in the oxygen concentration affects significantly the ratio of Mn^{3+} and Mn^{4+} ions as well as the magnetoresistive effect. In order to optimize the ratio $Mn^{3+}:Mn^{4+}$, we subjected the films to supplementary annealing in oxygen flow for a period of 30 min. Different annealing regimes were tried with the annealing temperature varying between 750 and 1000 °C.

3. DISCUSSION OF RESULTS OF MEASUREMENT

The temperature dependence of the resistivity ρ, magnetoresistance $\Delta R/R_0$ (in a field of 1T), and magnetization M of bulk ceramic samples of $La_{0.5}Pb_{0.2}Ca_{0.2}Y_{0.1}MnO_{3-\delta}$, which were later used as targets for obtaining films, are pre-

sented in Fig. 1. It can be seen that the $\rho(T)$ curve has a broad peak in the region of temperature $T_m = 200$ K. The resistance is of semiconductor type ($d\rho/dT < 0$) above T_m and metallic type ($d\rho/dT > 0$) below T_m. This temperature is usually considered as the metal−semiconductor transition temperature T_{MS}. The magnetoresistance increases with decreasing temperature and is reduced to 20% at 77 K in a field $H = 1$ T. It follows from the $M(T)$ dependence that the phase transition from the paramagnetic to ferromagnetic state is quite blurred, and magnetization saturation does not occur even at liquid-nitrogen temperature. This circumstance points towards considerable magnetic defects in ceramic samples.

The $\rho(T)$ dependence obtained for films in a magnetic field at various temperatures of annealing in oxygen atmosphere is shown in Fig. 2. It can be seen that like for the original targets, the resistance attains a peak value ρ_{max} at a certain temperature T_m. The value of T_m increases and the resistance ρ_{max} decreases rapidly upon an increase in the temperature of annealing of films in the interval 750−850 °C, and remains esssentially constant upon a further increase in the annealing temperature. The physical reason behind such a behavior lies in the variation of the ratio $Mn^{3+}:Mn^{4+}$,[1,2,14] and can be described as follows. The stoichiometric $LaMnO_3$ is an antiferromagnet and an insulator. Substitution of bivalent ions (Pb^{2+} and Ca^{2+} in the present case) for La^{3+} and annealing in oxygen lead to the emergence of mobile charge carriers and Mn^{4+} ions. This process, in turn, stimulates the

system to undergo a metal–semiconductor phase transition, which correlates with the magnetic phase transition from the ferromagnetic state to the paramagnetic state. As the number of Mn^{4+} ions increases, the transition temperature T_{MS} increases. The characteristic diffusion temperature for oxygen lies in the region of 850 °C, and any further increase in the annealing temperature does not affect the diffusion rate significantly. However, manganites with all their manganese ions in the tetravalent state are also ferromagnets and insulators. Hence an increase in resistance and a decrease in T_{MS} should be expected for a very large number of Mn^{4+} ions. This is the tendency displayed by the data presented in Fig. 2.

An analysis of the experimental results presented in Fig. 2 shows that the film resistance above T_m is of activation type and can be approximated quite well by the expression $\rho(T) = \rho_0 \exp(E_a/kT)$ with an activation energy E_a of the order of 0.1 eV. This points towards the polar nature of film conductivity for $T > T_m$.[5,9] Note that the exponential temperature dependence of the resistance approaches closer to T_m with decreasing frequency of the metal-semiconductor phase transition. For films annealed at 1000 °C this law is obeyed everywhere in the region $T > T_m$, which suggests a higher degree of perfection of crystal and magnetic structure of films. However, we did not observe any indications of a transition to the charge ordered state in these films.[16,17]

While no special information is available about the mechanism of conductivity of manganites in the paramagnetic phase, the situation is entirely different for the magnetically ordered state. Historically, the first interpretation concerned the properties of manganites in the model of double exchange between Mn^{3+} and Mn^{4+} ions.[18,19] (It is also worthwhile to mention the model based on RKKY interaction.[20]) However, attempts to explain the large magnetoresistive effect in the double exchange model encounter serious difficulties.[21] It is also difficult to explain several results of magnetic measurements[14,22] on the basis of the mechanisms described in Refs. 18 and 19. Earlier, it was proposed by Nagaev[23,24] that a magnetic semiconductor may go over to spatially inhomogeneous state under certain conditions. Giant magnetoresistance is one of the peculiarities of inhomogeneous state.[23,25] These ideas were generalized to perovskite manganites in the review by Nagaev.[10] In our opinion, however, the inhomogeneous state model also has a number of drawbacks, especially in view of recent results concerning the charge-ordered state in manganite single crystals.[16,17] The magnetic-polaron model,[26] which leads to a number of reasonable relations for the resistive properties of a narrow-band semiconductor, may turn out to be useful.

It was mentioned above that the film conductivity is of activation type in the high-temperature region. It is interesting to note that the exponential temperature dependence of resistance was also observed by us at low temperatures. By way of an example, the inset in Fig. 2 shows the dependence of the resistance of films annealed at 825 °C and 1000 °C. It can be seen that the dependence $\rho(T)$ can be described quite accurately by the expression $\rho(T) = \rho_0 + A \exp(-B/T)$. The
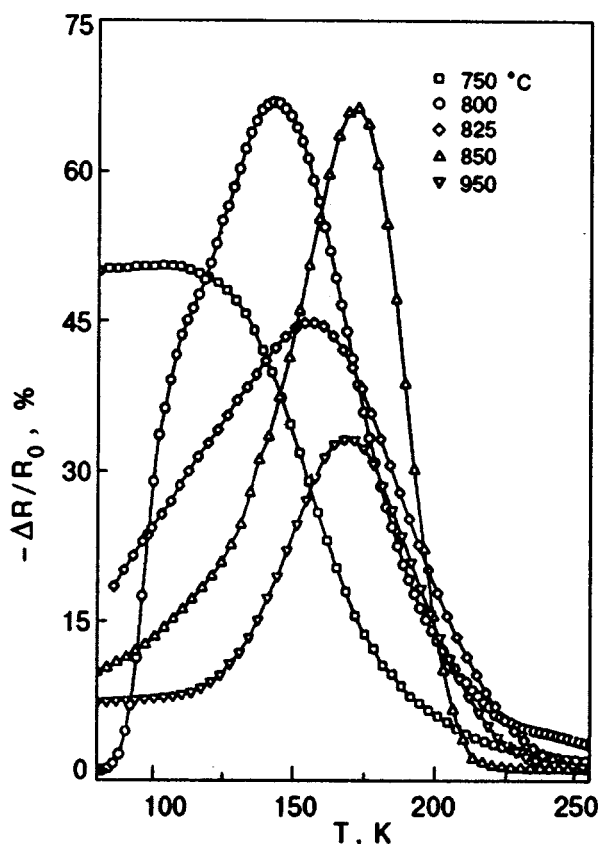

FIG. 3. Temperature dependence of the magnetoresistive effect $\Delta R/R_0$ in a field $H = 1$ T in $La_{0.5}Pb_{0.2}Ca_{0.2}Y_{0.1}MnO_{3-\delta}$ films annealed at various temperatures.

corresponding activation energy is about 1.5–2 times higher than the activation energy obtained for the paramagnetic phase. For comparison, we observe that the double exchange model predicts the $T^{9/2}$-dependence for resistance in the low-temperature region.[27] In several cases, the experimental dependence $\rho(T)$ was approximated by the relation[28] $\rho(T) = \rho_0 + AT^2$ or even the relation[29] $\rho(T) = \rho_0 - CT + BT^2$. Such a spread of empirical relations apparently points towards diverse elastic and inelastic scattering mechanisms for charge carriers in the low-temperature region, each of which can be enhanced or suppressed by an external force.

Figure 3 shows the temperature dependence of the magnetoresistive effect in the 1-T field for films annealed at 750, 800, 850, and 950 °C. It can be seen that the films are highly magnetoresistive with the maximum effect $\sim 65\%$ occurring at 180 K. The complete field–temperature diagram of the magnetoresistive effect $\Delta R(H,T)/R_0$ of a film annealed at 1000 °C is shown in Fig. 4. A 98% decrease in the resistance is observed in a field $H = 10$ T at a temperature of 175 K. The analysis of data presented in this figure shows (see inset in Fig. 4) that the film resistance has a quadratic dependence on the field at all temperatures $T > T_m : \sigma(H) = \sigma_0 + kH^2$. Such a behavior of $\sigma(H)$ corresponds to the quadratic dependence of conductivity on magnetization observed in most cases[13,28,30] for low values of the latter.
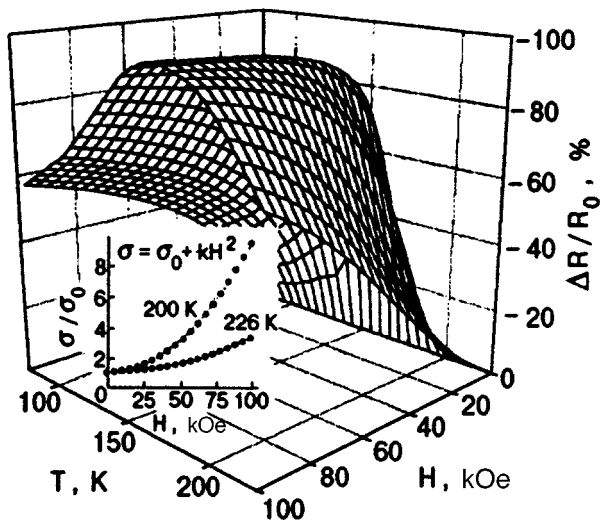
FIG. 4. Temperature and field dependence of the magnetoresistive effect in $La_{0.5}Pb_{0.2}Ca_{0.2}Y_{0.1}MnO_{3-\delta}$ films annealed in oxygen at 1000 °C. The inset shows the accuracy with which the quadratic dependence of the effect on magnetic field is observed at 200 and 226 K.

CONCLUSIONS

We have studied the $La_{0.5}Pb_{0.2}Ca_{0.2}Y_{0.1}MnO_{3-\delta}$ films obtained by using the reactive magnetron sputtering technique. The film resistance decreases by 98% in a field $H = 10$ T in the temperature range 125–175 K, as compared to a decrease of just 10% for bulk ceramic samples. It is shown that the variation of annealing temperature in oxygen atmosphere can effectively vary the ratio of the ions Mn^{3+} and Mn^{4+}, and thus alter the magnetoresistive properties of films. Empirical relations describing the temperature and field dependences of the film resistance are established, and the existing conductivity models for manganites in paramagnetic and ferromagnetic phase are discussed.

We wish to thank G. K. Volkova for carrying out the x-ray structural analysis of films, Yu. V. Medvedev for stimulating discussions and encouragement, and S. V. Tarasenko for drawing our attention to the work of Balbashev et al.[15]

*E-mail: krivoruc@host.dipt.donetsk.ua

[1] J. H. van Santen and G. H. Jonker, Physica **16**, 599 (1950).
[2] E. O. Wollan and W. C. Koehler, Phys. Rev. **100**, 545 (1955).
[3] C. W. Searle and S. T. Wang, Can. J. Phys. **48**, 2023 (1970).
[4] K. P. Belov, E. P. Svirina, O. E. Portugal et al., Fiz. Tverd. Tela (Leningrad) **20**, 3492 (1978) [Sov. Phys. Solid State **20**, 2021 (1978)].
[5] R. M. Kusters, J. Singleton, D. A. Keen et al., Physica **B155**, 362 (1989).
[6] K. Chahara, T. Ohno, M. Kasai, and Y. Kozono, Appl. Phys. Lett **63**, 1990 (1993).
[7] R. von Helmolt, J. Wecker, B. Holzapfer et al., Phys. Rev. Lett. **71**, 2331 (1993).
[8] S. Jin, M. McCormack, T. H. Tiefel, and R. Ramesh, J. Appl. Phys. **76**, 6929 (1994).
[9] H. L. Ju, C. Kwon, Qi Li et al., Appl. Phys. **65**, 2108 (1994).
[10] È. L. Nagaev, Usp. Fiz. Nauk **166**, 833 (1996) [sic.].
[11] R. Mahesh, R. Mahendran, A. K. Raychaudhuri, and C. N. R. Rao, J. Solid State Chem. **120**, 204 (1995).
[12] J. Fontcuberta, B. Martinez, A. Seffar et al., Phys. Rev. Lett. **76**, 1122 (1996).
[13] H. Y. Hwang, S.-W. Cheng, P. G. Radaelli et al., Phys. Rev. Lett. **75**, 914 (1995).
[14] I. O. Troyanchuk, Zh. Éksp. Teor. Fiz. **102**, 251 (1992) [Sov. Phys. JETP **75**, 132 (1992)].
[15] A. M. Balbashev, V. A. Kozlov, A. V. Mozhaev, and Ya. M. Mukovskii, in *Abstracts of Papers to XV All-Russian Seminar-cum-School on New Magnetic Materials in Microelectronics*, Moscow (1996).
[16] Y. Tomioka, A. Asamitsu, Y. Moritomo et al., Phys. Rev. Lett. **74**, 5108 (1995).
[17] Y. Tokura, Y. Tomioka, H. Kuwahara et al., J. Appl. Phys. **79**, 5288 (1996).
[18] C. Zener, Phys. Rev. **81**, 440 (1951).
[19] P. W. Anderson and H. Hasegawa, Phys. Rev. **100**, 675 (1955).
[20] T. M. Perekalina, T. A. Sivokon', S. A. Cherkezyan, and I. E. Lipinski, Fiz. Tverd. Tela (Leningrad) **31**, 87 (1989) [sic.].
[21] A. J. Millis, P. S. Littlewood, and B. I. Shraiman, Phys. Rev. Lett. **74**, 5144 (1994).
[22] M. K. Gubkin, A. V. Zalesskii, V. G. Krivenko, et al., Pis'ma Zh. Éksp. Teor. Fiz. **60**, 56 (1994) [JETP Lett. **60**, 57 (1994)].
[23] V. A. Kashin and È. L. Nagaev, Zh. Éksp. Teor. Fiz. **66**, 2105 (1974) [JETP **39**, 1036 (1974)].
[24] È. L. Nagaev, *Magnetic Semiconductors*, [in Russian], Nauka, Moscow (1979).
[25] V. N. Krivoruchko, Fiz, Nizk, Temp. **22**, 1047 (1996) [Low Temp. Phys. **22**, 798 (1996)].
[26] S. Zhang, J. Appl. Phys. **79**, 4592 (1996).
[27] H. Kubo and N. Ohata, J. Phys. Soc. Jpn. **33**, 21 (1972).
[28] A. Urushibara, Y. Moritomo, T. Arisma et al., Phys. Rev. **B51**, 14103 (1995).
[29] S. E. Lofland, S. M. Bhagat, H. L. Ju et al., Phys. Rev. **B52**, 15058 (1995).
[30] J. Z. Sun, L. Krusin-Elbaum, S. S. P. Parkin, and G. Xiao, Appl. Phys. **67**, 2726 (1995).

Translated by R. S. Wadhwa

Spin structure of antiferromagnetic disclination

B. A. Ivanov, V. E. Kireev, and V. P. Voronov

Institute of Magnetism, National Academy of Sciences of the Ukraine, 252142 Kiev, Ukraine[*]

The spin structure of magnetic disclination, viz., spin inhomogeneity manifested in antiferromagnets in the presence of a dislocation, is analyzed. The analysis is carried out on the basis of the discrete model as well as in the specially constructed generalized continual theory based on the local introduction of the antiferromagnetism vector **l** and taking into account the possibility of a change in the length of this vector. In the solution without singularities constructed for disclination, the modulus of the antiferromagnetism vector vanishes at the center of the disclination. In the discrete model, the disclination energy depends significantly on the arrangement of spins near the core and on the type of their interaction. With the proposed model of spin arrangement, the results of numerical analysis based on the discrete and continual models are in good agreement. It is shown that planar disclinations are stable to the emergence of spins from the easy plane. © *1997 American Institute of Physics.* [S1063-777X(97)00908-0]

1. INTRODUCTION

Antiferromagnets (AFM) have attracted the attention of a large number of researchers for more than fifty years (see reviews in Refs. 1–3). The spin ordering in AFM is usually described for a finite number of magnetic sublattices each of which is ferromagnetically ordered so that the total magnetic moment of the AFM is equal to zero in the exchange approximation. The properties of AFM observed during the last decade cannot be explained by using the simple model of sublattices. It suffices to mention the peculiar quantum properties of low-dimensional AFM (see Ref. 1) and the existence of frustrated AFM whose properties cannot be described in general by the simple sublattice model.

The concept of frustration is usually associated with spin glasses in which ferromagnetic and antiferromagnetic links between nearest neighbors are distributed at random. However, frustration effects can also be observed in magnets with a regular lattice and with the antigferromagnetic interaction. In this connection, we can mention AFM with a triangular lattice[4] or with a more complex *kagomee* lattice.[5] For these AFM, the division of the initial lattice into a finite number of magnetic sublattices taking into account the interaction only between nearest neighbors cannot satisfy the condition of minimum energy for neighboring spins, i.e., the condition of antiparallel orientation. In this case, the problem of the ground state becomes nontrivial even in the classical spin approximation. For example, according to the results of numerical analysis, a 120° three-sublattice structure observed for a triangular sublattice is not unconditionally advantageous, while the exact solution of the problem for a *kagomee* lattice is unknown. The study of frustrated magnets forms an interesting trend in the modern theory of magnetism.

The strong dependence of the properties of AFM on the type of the lattice must lead to a considerable effect of extended lattice defects on antiferromagnetic ordering. According to Dzyaloshinskii[6] and Kovalev and Kosevich,[7] the presence of a dislocation in AFM is responsible for ''distor-tions'' in the sublattices and leads to the formation of macroscopic magnetic defects, viz., domain walls terminating on a special line (disclination). Since a disclination can be regarded as an antiferromagnetic vortex with a semi-integral value of topological charge (vorticity),[2,3] its analysis presents an independent interest in view of growing importance of two-dimensional magnetic solitons and especially vortices. Magnetic vortices are known to make a specific contribution to the response function of magnets[2] and lead to the emergence of localized or quasilocal magnon modes.[8,9] Thus, the emergence of a disclination leads to the observed physical effects whose analysis must be based on the study of the actual spin distribution in the disclination core as well as far away from it.

An analysis of the properties of magnetic vortices can be based on the discrete spin model as well as on the continual approach. The results of these approaches during an analysis of an out-of-plane vortex in a ferromagnet and in AFM are in good agreement even in the case when the length parameter in the macroscopic theory, viz., the radius of the vortex core, is close to the lattice constant a.[8] An analysis of a vortex in discrete models can be carried out only numerically for finite lattices (whose size usually does not exceed 40×40). For this reason, the continual approach which makes it possible to find general regularities for a vortex in an unbounded medium plays a special role. Natural roughness of the continual approach applied to real magnets which contain spins in discrete sites can be controlled by comparing with the results of numerical analysis based of discrete models. In the case of disclination, however, the continual approach based on an analysis of the antiferromagnetism vector as a unit vector leads to singularities near the center of the disclination and requires modification.

Kovalev[10] proposed a one-dimensional continual model for describing the structure and dynamics of complex magnetostructural topological defects predicted in Refs. 6 and 7. In this model, which generalizes the well-known Frenkel–Kontorova model to the case of magnetically ordered media,

no singularity is observed near the center of the dislocation and disclination. However, this model fails to give correct asymptotic forms of field distribution at large distances from the center of the defect in view of its one-dimensional nature.

In this paper, we carry out a detailed analysis of the spin structure of a disclination near its core as well as away from it. The analysis was made on the basis of the discrete model for classical spins as well as in the generalized continual model based on the local introduction of the antiferromagnetism vector **l** taking into account the possibility of the change in the length of this vector.

In the discrete model, the disclination energy depends considerably on the arrangement of atoms near the dislocation core and on the nature of their interaction. It is shown that an anisotropy of the ''easy plane'' type with a planar orientation of spins in this model is stable to the emergence of spins from the ''easy plane.''

In the continual model, a solution without singularities is constructed for a disclination in an AFM near the Néel temperature. In this solution, the modulus of the antiferromagnetism vector vanishes at the center of the disclination. The possibility of application of this solution at low temperatures also is discussed. Among other things, a specific model of spin arrangement is indicated, for which the results of analysis based on the discrete and continuous models are in good agreement.

2. STRUCTURE OF DISCLINATION CORE ON THE BASIS OF LATTICE MODEL

The Heisenberg classical model is often used for a microscopic description of a magnet (see, for example, Refs. 2 and 3). The model used by us here is based on a two-dimensional square lattice with withdrawn half-line of lattice sites (Fig. 1). Each site is put in correspondence with the spin vector S_i of constant length, $S_i^2 = S^2$:

$$H = J\sum (S_{xi}S_{xj} + S_{yi}S_{yj} + \lambda S_{zi}S_{zj}). \tag{1}$$

Here and below, the summation is carried out over pairs of nearest neighbors, $J > 0$ is the exchange integral which is assumed for simplicity to be the same for all links, and λ the constant describing magnetic anisotropy. Assuming that the AFM has an ''easy plane'' type anisotropy, we put $0 \leqslant \lambda \leqslant 1$.

We introduce the following parametrization:

$$S_z = Sm, \quad S_x = S\sqrt{1-m^2}\cos\varphi,$$
$$S_y = S\sqrt{1-m^2}\sin\varphi. \tag{2}$$

Here the values of $|m| \leqslant 1$, and φ is the angle between **S** and a fixed direction in the basal plane. In these variables, we have

$$H = JS^2\sum\left\{\sqrt{1-m_i^2}\sqrt{1-m_j^2}\cos(\varphi_i-\varphi_j)+\lambda m_i m_j\right\}. \tag{3}$$

If, however, all the spins lie in the basal plane (it will be shown below that this assumption is confirmed by numerical calculations), it is sufficient to proceed from the expression
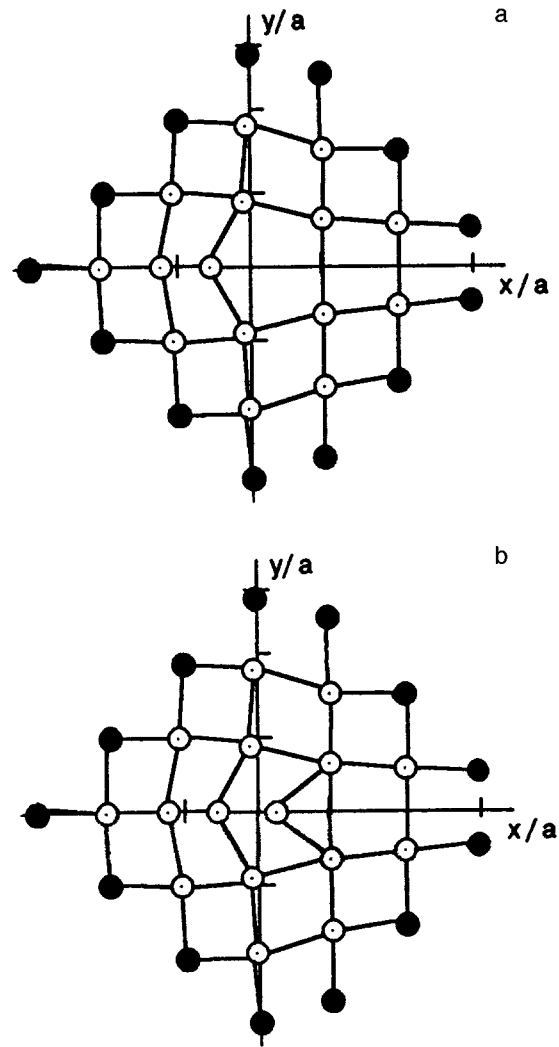

FIG. 1. Lattice fragments used for calculations of the spin structure of a disclination with a pentagon (a) and a triangle (b) of central atoms coupled through the exchange interaction. Segments of straight line indicate exchange bonds. Light circles denote atoms whose spin orientation is determined by energy variation, while dark circles denote atoms whose spins are fixed by the boundary conditions.

$$H = JS^2\sum \cos(\varphi_i-\varphi_j). \tag{4}$$

In the case of an ideal antiferromagnetic ordering, the spins of neighboring magnetic atoms are antiparallel. Such an ideal antiferromagnetic ordering can obviously take place only if the number of atoms in any closed chain of exchange-coupled atoms in the crystal is even. If, however, the magnetic lattice of the crystal contains a closed chain of atoms with an odd number of sites, such a spin ordering cannot exist. Before we analyze the disclination, it would be expedient to consider a model problem on the ground state of a closed chain with an odd number N of sites and with antiferromagnetic interaction.

We take the energy of spin interaction in the form (4), assuming that the summation is carried out over the spins in the chain. For definiteness, we choose an arbitrary site and ascribe to it the number $i = 0$ and $\varphi_i = 0$. The sites will be

numbered in the counterclockwise direction. The system symmetry allows us to write the solution for the angles φ_k, which ensures the minimum of energy E:

$$\varphi_k = (-1)^k \pi + \frac{2\pi k}{N} \nu, \qquad (5)$$

where k is the site number and ν a half-integer such that $-N/2 < \nu < N/2$.

The energy of a chain containing an odd number of sites and measured from the level $-JS^2 N$ is defines as

$$E_n = JS^2 N (1 - \cos[2\pi\nu/N]).$$

The absolute minimum corresponds to $\nu = \pm 1/2$. Stable local minima correspond to $|\nu| < N/4$. The angle between the directions of the vector $\sigma_i = (-1)^i S_i$ at neighboring chain sites is the same for all links and is equal to $2\pi\nu/N$. Such a behavior of σ_i corresponds to the behavior of the director vector $\mathbf{n}$ during circumvention of a disclination in liquid crystals; the number ν corresponds to the Frank index of the disclination. As we move along the chain, the vector σ_i rotates through the angle $2\pi\nu$. This explains the half-integral value of ν.

We arrange the lattice sites at the vertices of a regular N-gon inscribed in a circle of radius R. For the direction of σ which can be specified at each point of the circle in the limit $N \to \infty$, the expression for φ_i can be presented in the form $\varphi = \chi/2$, where χ is the angular coordinate of the given point on the circle. For a large number of sites in the chain, we can easily obtain the following asymptotic form for the ground-state energy: $E = \pi^2 JS^2/2N$.

In a crystal with a square lattice containing a dislocation, the Burgers vector is equal to the lattice constant, and any closed loop drawn through exchange links and embracing the dislocation axis contains an odd number of sites. It was noted above that this leads to the emergence of spin inhomogeneity, viz., disclination. Variation of the Hamiltonian of the magnet along the directions of spins makes it possible to find the spin configuration corresponding to this disclination.

In a numerical analysis of the spin structure, we can use a lattice fragment with a finite number of sites. In order to determine the structure of the core, we can choose a fragment containing approximately 100 lattice sites. Its interaction with the remaining part of the lattice can be taken into account by choosing certain boundary conditions. Usually, we use the so-called fixed boundary conditions, i.e., choose certain directions corresponding to a known asymptotic forms of the solution for spins adjacent to the fragment. In our case, the form of these conditions can be determined by using the analogy between the closed loop in the lattice and a free chain. Considering the closed loop formed by spins adjacent to the fragment and having a nearly circular shape, we assume that the angle formed by σ and a fixed axis is equal to half the value of the polar coordinate of this site, $\varphi = \chi/2$. (It should be noted that the same asymptotic form can also be obtained from the phenomenological theory; see below.) Such an approach (the choice of fixed boundary conditions of the type $\varphi = \chi$) was used for studying magnetic vortices.[8,9] However, the situation with a disclination is somewhat more complicated. Indeed, the symmetry of the

problem implies that the vortex center, which coincides with the origin (pole) of the polar system of coordinates, lies at the center of a unit cell of the magnet. In view of the lower symmetry of the problem on magnetic disclination, the coordinate of the pole in the direction of the withdrawn half-line of atoms (x-axis) is not defined and must be determined independently from the condition of energy minimum. For this reason, we proceed as follows. Solving the equations $\partial H/\partial \mathbf{S}_i = 0$ with a fixed value of $\mathbf{S}$ at the boundary corresponding to a certain position x_0 of the pole, we determine the spin configuration and its energy for the given x_0. Then we find the energy minimum of the fragment in the parameter x_0 by changing the position of the pole.

Let us start from the simple case when all the spins lie in the basal plane (it will be proved below that this configuration is stable and corresponds to the absolute minimum of the disclination energy). The equation for φ_i can be written in the form

$$\tan \varphi_i = \frac{\Sigma \sin \varphi_i}{\Sigma \cos \varphi_i}.$$

The summation is carried out over the nearest neighbors of the ith site. These equations can be solved by the iteration method with the initial approximation chosen in the form $\varphi = \chi/2$. For our calculations, we used fragments of two types depicted in Figs. 1a and b.

The values of φ_i at the boundary sites denoted by dark circles in Fig. 1 were fixed by the condition $\varphi = \chi/2$. Energy minimization for values of φ_i at inner sites was carried out for various positions of the pole, and the energy of the spin configuration was determined. Then the energy minimum was determined from the position of the center of the disclination (pole). The dependence of energy on the position of the disclination center on the symmetry line x_0 is shown in Fig. 2. The minimum is attained at $x_0 = 0.570a$ for the fragment with a triangle of atoms coupled through the exchange interaction at the center (see Fig. 1b) and at $x_0 = 0.611a$ for the fragment with the central pentagon (see Fig. 1a). It is interesting to note that the difference between the values of angles φ and the values of $\chi/2$ is small even for central atoms. For example, the corresponding values of angles for the configuration shown in Fig. 1a are 0, $\pm 69.75°$, and $\pm 148.72°$. This is quite close to the asymptotic values ± 72 and $\pm 144°$. The difference between these values decreases rapidly as we move away from the center, while an increase in the fragment size virtually does not affect the spin orientation at the central sites.

The analysis of the planar distribution of spins should be supplemented with the analysis of the possibility of spin emergence from the basal plane. Indeed, according to the analysis carried out in Refs. 6, 7, a structure of the type of a domain wall emerging from the center of the dislocation is formed in the case of an easy-axis AFM for which $\lambda > 1$, and the spin distribution is not planar. This means that for an easy-plane AFM with $1 > \lambda > 0$, there can exist in principle such a $\lambda_c > 0$ that the planar distribution of spins is violated for $\lambda \geq \lambda_c$ at least in a certain region. In the case of a magnetic vortex, this problem was analyzed by Wysin,[9] and the
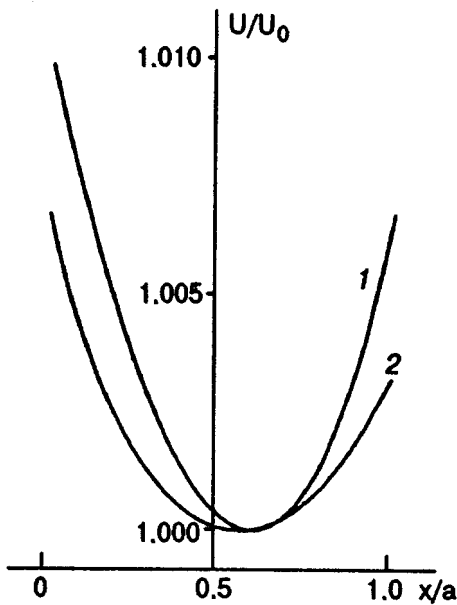
FIG. 2. Spin distribution energy for various positions of the pole (disclination center) as a function of the pole coordinate x. Curves 1 and 2 correspond to two versions of arrangement of exchange bonds of atoms represented in Fig. 1a and b.

values of λ_c for different lattices were found to be of the order of 0.7–0.9.

Let us analyze the stability of the planar spin configuration relative to the emergence of spins from the basal plane. Following the method developed by Wysin,[9] we linearize the complete system of equations $\partial H/\partial\varphi_i=0$, $\partial H/\partial m_i=0$ relative to m_i. In matrix form, this system can be written as

$$\sum_j\left(-\frac{1}{\lambda}A_i\delta_{ij}+e_{ij}\right)m_j=0,$$

where $e_{ij}=1$ if i and j are nearest neighbors and $e_{ij}=0$ otherwise, and $A_i=\sum_j\cos(\varphi_i-\varphi_j)$ is the sum of energies of the links emerging from the ith site. The value of λ_c is determined by the condition that this system has a nontrivial solution, i.e., $\det(-A_i\delta_{ij}+\lambda_c e_{ij})=0$. Our numerical analysis revealed that this condition does not hold for any $0\leqslant\lambda\leqslant1$. This means that the disclination in the model under investigation is of purely in-plane type for easy-plane and for isotropic AFM (with $\lambda=1$).

We have calculated the ground-state energy of an AFM with a disclination for lattice fragments close to circles with radii $5a$, $6a$, $7a$, and $8a$, where a is the lattice constant. The disclination center was chosen in accordance with the results obtained above at points $x_0=0.570a$ and $0.611a$ for fragments with a triangle and a pentagon of atoms at the center coupled though exchange interaction. An analysis shows that the disclination energy can be approximated quite well by the formula

$$E=\frac{1}{4}\pi JS^2\ln\left(\frac{CR}{a}\right),\qquad(6)$$

where C is a constant whose value depends strongly on the configuration of exchange bonds between atoms at the center

of the dislocation. For the models with a pentagon and a triangle of exchange-coupled atoms at the center, the values of C are 3.15 and 11.84. The logarithmic dependence of energy on the size of the system coincides with the dependence following from the continual approximation [see formula (10) below].

3. PHENOMENOLOGICAL DESCRIPTION OF DISCLINATION NEAR THE NÉEL POINT

It was mentioned above that sublattices cannot be introduced into an AFM with a dislocation so that the spins in each sublattice be parallel, and the division into the sublattices be consistent for the entire crystal. However, sublattices can be introduced with the help of the following procedure. We divide the lattice into several regions that do not contain the dislocation core. In each such region, we can introduce sublattices and define the antiferromagnetism vector $\mathbf{l}$ as the normalized difference between mean values of magnetizations of the sublattices. For intersecting regions, the numeration of the sublattices can be matched.

Let us consider a system of n intersecting regions with an ideal lattice, which form a closed contour embracing the dislocation core. We will match the sublattices moving along this contour. Having returned to region 1 from the side of region n, we note that sublattices have changed places, and the sign of $\mathbf{l}$ has been reversed. Consequently, we can use the phenomenological description of AFM by introducing the vector $\mathbf{l}$ on a plane with a cut emerging from the center of the dislocation and by assuming that $\mathbf{l}$ has opposite signs on the opposite banks of the cut. Thus, the vector $\mathbf{l}$ can be defined locally in any region which does not contain the dislocation center. (This resembles the procedure which is normally used for introducing the deformation field in the description of a crystal with a dislocation in the theory of elasticity.[11]) In the vicinity of the center, the direction of $\mathbf{l}$ is not defined, and hence the model with $|\mathbf{l}|=1$ used for ideal AFM cannot be used directly. A similar difficulty is also encountered in a phenomenological analysis of a Bloch point[12] and can be overcome in the same way by assuming that the length of the vector $\mathbf{l}$ can change and that $|\mathbf{l}|=0$ at the center of the disclination. The contribution of this modification to the system energy can be taken into account by supplementing the energy with terms depending on the length of $\mathbf{l}$.

With such an approach, the gradient of $\mathbf{l}$ near the center of the disclination is not small, which is in contradiction to the traditional assumption $|a(\nabla\mathbf{l})|^2\ll1$ in the phenomenological theory. However, we can indicate an interesting case from the physical point of view, when a transition from the discrete to the continual model can be made easily, and the continual theory describes exactly the structure of singular solitons of the type of a disclination in an AFM. Let us consider the temperature T close to the Néel point T_N of the AFM. In this case, the equilibrium value of $l\propto\sqrt{\tau}$, where $\tau=(T_N-T)/T_N$, and accordingly the characteristic size of spin inhomogeneity is $\Delta=\Delta(T)=\Delta_0/\sqrt{\tau}$, where the value of Δ_0 is of the order of the lattice constant a. The characteristic size of the disclination core is determined by the quantity Δ and increases indefinitely as $T\to T_N$; for this reason, the conditions for the applicability of the continual approxi-

mation are essentially satisfied. It should be noted that we need not consider the critical region in the immediate vicinity of the Néel point: the value of $\Delta(T) \approx 3\Delta_0 \approx 3a$ even for $\tau \sim 0.1$, and in accordance with the results obtained in Ref. 8 the continual and discrete approaches are in good agreement (at any rate, for an analysis of static properties of magnetic inhomogeneities).

While constructing the phenomenological theory, we proceed from the energy of the form

$$W = \frac{1}{2} A \int_\Omega d\mathbf{r} \left\{ (\nabla \mathbf{l})^2 + \frac{1}{\Delta_1^2} l_z^2 + F(l^2) \right\}. \tag{7}$$

(at finite temperatures, it is more expedient to speak of the thermodynamic potential.

Here $A > 0$ is the nonuniform exchange constant, $F(l^2)$ the function determined by the exchange interaction and describing the change in the AFM energy upon a change in the length of the vector $\mathbf{l}$, and Δ_1 the characteristic scale of length associated with anisotropy energy; the value of $\Delta_l \gg a$ for weakly anisotropic magnets. The integration domain Ω is the xy plane with a cut emerging from the dislocation center. The boundary conditions at the upper and lower banks of the cut can be written in the form $\mathbf{l}_{(+)} = -\mathbf{l}_{(-)}$.

For the quantity $\mathbf{l}$, we introduce the parametrization

$$\mathbf{l} = l\mathbf{e}_z \cos \theta + l \sin \theta (\mathbf{e}_x \cos \varphi + \mathbf{e}_y \sin \varphi).$$

The distribution of $\mathbf{l}$ can be obtained from the Euler–Lagrange equations for energy functional. Variation leads to the following system of equations:

$$\nabla^2 l - l \left((\nabla \theta)^2 + (\nabla \varphi)^2 \sin^2 \theta + \frac{1}{\Delta_1^2} \cos^2 \theta \right) - l \frac{dF}{dl^2} = 0,$$

$$\nabla(l^2 \nabla \theta) - l^2 \sin \theta \cos \theta \left((\nabla \varphi)^2 - \frac{1}{\Delta_1^2} \right) = 0,$$

$$\nabla(l^2 \sin^2 \theta \nabla \varphi) = 0.$$

Let us go over to polar coordinates (r, χ). The substitution $l = l(r)$, $\theta = \pi/2$, $\varphi = \nu\chi + \varphi_0$, where φ_0 is an arbitrary number, transforms the last two equations into identities. This is in accord with the results of analysis based on the discrete model, according to which all the spins in the disclination lie in plane, i.e., $\theta = \pi/2$. Considering that $\varphi_0 = 0$ at the cut, we arrive at the condition $\varphi = \chi/2$ obtained above for a region far away from the disclination center. The boundary condition at the cut $(\mathbf{l}_{(+)} = -\mathbf{l}_{(-)})$ defines ν as half-integral. The equation for l assumes the form

$$\frac{d^2 l}{dr^2} + \frac{1}{r} \frac{dl}{dr} - l \frac{\nu^2}{r^2} - l \frac{dF}{dl^2} = 0. \tag{8}$$

For definiteness, we assume the form of the function $F(l^2)$ following from the Landau expansion:

$$F(l^2) = \frac{1}{2\Delta_0^2} (l^2 - \tau)^2,$$

where $\tau = (T_N - T)/T_N$, and Δ_0 is of the order of the lattice constant a. In this case, we can introduce the new unknown
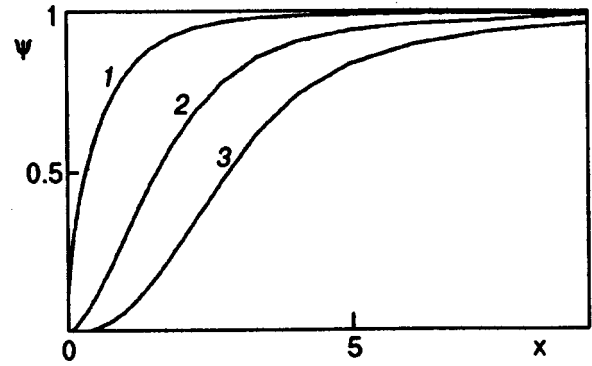

FIG. 3. Dependence $\psi(x)$, $x = r/\Delta(T)$ for various values of the topological parameter ν. Numbers 1, 2, 3 on the curves correspond to $\nu = 1/2, 3/2, 5/2$, respectively.

function $\psi(x) = l\tau^{-1/2}$ depending on the variable $x = r/\Delta(T)$, $\Delta(T) = \Delta_0 \tau^{-1/2}$, and write the universal dimensionless equation for $\psi(x)$:

$$\frac{d^2\psi}{dx^2} + \frac{1}{x} \frac{d\psi}{dx} - \psi \frac{\nu^2}{x^2} + \psi - \psi^3 = 0. \tag{9}$$

We choose the boundary conditions from the requirement of the absence of singularity at the center of disclination and equilibrium at infinity, $\psi(0) = 0$ and $\psi(\infty) = 1$. This equation differs from the static version of the Gross–Pitaevskii equation for a vortex in liquid helium[13] only in that the coefficient of the term $1/x^2$ is half-integral. Consequently, the asymptotic behavior of $l(r)$ can be described as $l \to (r/r_0)^\nu$, $r_0 = x_* \tau^{-1/2} \Delta_0$ for $r \to 0$ and $l \to 1 - \nu^2 \Delta_0^2 / 2\tau r^2$ for $r \to \infty$. The parameter x_* can be determined numerically (see below). The value of l differs from unity only in the region $r \lesssim r_0 \sim \tau^{-1/2} \Delta_0$, which can be identified with the disclination core.

Using the asymptotic behavior for $r \to \infty$, we can prove that the energy of disclination contains the logarithmic dependence on the size R of the system, which is typical of inhomogeneities of the type of vortices:

$$E = \tau A \frac{\nu^2}{4} \ln \left(D \frac{\sqrt{\tau} R}{\Delta_0} \right), \tag{10}$$

where R is the radius of the AFM sample (which is regarded as cylindrical) and D the numerical constant which can be determined after the solution of the differential equation (9). The solution of this equation with the boundary conditions $l(0) = 0$, $l(\infty) = 1$ can be constructed numerically by the target method (see Ref. 3 for details), and its form is presented in Fig. 3. In order to simplify calculations of energy, it is convenient to use the identity $2E\Delta_0^2 = \tau \int r dr (1 - l^4)$, which can be obtained by multiplying Eq. (9) by dl/dr and integrating with respect to r from 0 to ∞.

We obtained the following values for the constant x_* for $\nu = 1/2$, $3/2$, and $5/2$: 1.272, 2.140, and 2.964. For these values of the topological parameter, the constants D are equal to 5.50, 0.82, and 0.44, respectively. The anomalously large value of D for $\nu = 1/2$ can be explained by the fact that, in contrast to disclinations with $\nu = 3/2$ and $5/2$ or a magnetic vortex in which $l \to r/r_0$ for $r \to 0$, the value of dl/dr di-

verges for $r \to 0$. It should be noted that, since the values of D for $\nu = 1/2$ and $3/2$ differ significantly, the disclination with $\nu = 3/2$ can become more advantageous than that with $\nu = 1/2$ for a certain value of $R \approx \tau^{-1/2} \Delta_0$. However, for macroscopic AFM samples, this can take place only in the immediate vicinity of the Néel point, and we will henceforth consider only the case with $\nu = 1/2$.

4. ON THE POSSIBILITY OF PHENOMENOLOGICAL DESCRIPTION OF DISCLINATIONS AT LOW TEMPERATURES

Thus, the disclination energy exhibits a logarithmic dependence on the sample size both in the discrete and in the continual models, and the formula $\varphi = \chi/2$ of the continual theory is also valid in the discrete theory. Let us consider the possibility of constructing a version of the continual theory which could describe the properties of disclinations at low temperatures at least semiquantitatively.

Away from the disclination core, the gradient of l is small, $\Delta_0 (dl/dr) \sim (\Delta_0/r)^3$, and the continual model can be used for $\Delta_0 \lesssim a$ as well. Near the disclination core, the situation is obviously worse, but a comparison of the results of analysis for an out-of-plane magnetic vortex in the discrete and continual models revealed[8] that the data obtained by using these two approaches are in good agreement even for $\Delta_0 \sim a$. Consequently, the condition of smallness for the gradient of vector $\mathbf{l}$ is probably not very critical.

Another problem is associated with the fact that the required continual model must predict the contraction of the length of vector $\mathbf{l}$ to zero at the center of the disclination. Usually, the low-temperature phenomenology of AFM is constructed by introducing two sublattices with the spins $\mathbf{S}^{(1)}$ and $\mathbf{S}^{(2)}$ as well as normalized vectors of magnetization $\mathbf{m} = (\mathbf{S}^{(1)} + \mathbf{S}^{(2)})/2S$ and the antiferromagnetism vectors $\mathbf{l} = (\mathbf{S}^{(1)} - \mathbf{S}^{(2)})/2S$ which are connected through the conditions $\mathbf{l}^2 + \mathbf{m}^2 = 1$, $\mathbf{m} \cdot \mathbf{l} = 0$ by virtue of the relations $|\mathbf{S}^{(1)}| = |\mathbf{S}^{(2)}| = S$.[2,3] For an AFM with a square lattice, sublattices are chosen in such a way that they are transformed into each other through elementary translation along the x or y axes by vectors $a\mathbf{e}_x$ or $a\mathbf{e}_y$. In the case of a noncollinear orientation of spins, the value of $|\mathbf{l}|$ calculated in this way is smaller than unity. It can easily be seen, however, that for the spin configuration constructed above, which describes a disclination, the value of $|\mathbf{l}|$ at not very large distances from the center of the disclination depends on the choice of this translation vector. In this case, the coordinate dependence of $|\mathbf{l}|$ is anisotropic, and the quantity $1 - |\mathbf{l}|$ vanishes along a certain direction in the lattice. Moreover, these directions are different in the case when such alternative definitions are used.

The emergence of anisotropy with the second-order axis in the distribution of $\mathbf{l}$ is not surprising. For such a definition of the vector $\mathbf{l}$, the symmetry of a magnetic unit cell in the form of a rectangle with sides a and $2a$ is lower than symmetry of a crystallochemical unit cell. Generally, this does not create any problem since disclinations can be described in terms of anisotropic solutions of the corresponding equations for the vector $\mathbf{l}$ for such a definition of $\mathbf{l}$. Simultaneous rotation of the magnetic unit cell and the function $l(\mathbf{r})$ through 90° restores the initial symmetry of the solution. For

our purposes, however, it is more convenient to introduce a model in which the disclination would be described by symmetric solutions of the type $l = l(r)$, $\theta = \pi/2$, $\varphi = \chi/2$ considered in the previous section.

Let us consider various methods of determining the antiferromagnetism vector $\mathbf{l}$. According to the approach developed by Andreev and Marchenko,[14] this vector is equal to the dipole moment of the microscopic spin density, calculated for a magnetic unit cell.[1] We choose this cell in the form of a square with side $\sqrt{2}a$ and with its center at the point $\mathbf{i}$ corresponding to the first site of magnetic sublattice atom site (the division of a crystal with a dislocation into sublattices was discussed at the beginning of the previous section). We define the antiferromagnetism vector $\mathbf{l_i}$ by the formula

$$\mathbf{l_i} = \frac{1}{2S} \left(\mathbf{S}^{(\mathbf{i})} - \frac{1}{4} \sum_{\mathbf{a}} \mathbf{S}^{(\mathbf{i}+\mathbf{a})} \right), \tag{11}$$

where the summation is carried out over the four vectors of elementary translations: $\pm a\mathbf{e}_x$ and $\pm a\mathbf{e}_y$. The equilibrium value of $|\mathbf{l}|$ is equal to unity. It can be stated that this definition follows from a certain averaging over the magnetic cell orientations, which was written above anisotropically, as well as from averaging over the direction of spins in the given sublattice.

Since the transformation properties of the antiferromagnetism vector $\mathbf{l}$ with such a definition coincide with the standard properties, the phenomenological energy of an AFM written in the form of a functional of the vector $\mathbf{l}$ must also be defined by formula (7) with different numerical values of parameters.[2] Accordingly, the general structure of the solution and the form of Eq. (8) for the functions $l(r)$ remain unchanged. Since we are interested only in a semiquantitative description of the solution, we can use for the function $F(l^2)$ the Landau expansion by putting $\tau = 1$ in it. In this case, the function $l(r)$ can be described by the solution of the universal equation (9) constructed above, i.e., $l(r = \psi(r/\Delta_0)$, and the energy of the disclination with $\nu = 1/2$ is defined as

$$E = (\pi A/4) \ln(5.5R/\Delta_0). \tag{12}$$

This expression contains the parameters A and Δ_0. The quantity A can be defined by using the microscopic expressions (1) and (11), but it is easier to make use of the coincidence of logarithmic asymptotic forms of energy in different approaches. Comparing (6) and (12), we find that $A = JS^2$. As regards the parameter Δ_0, its value can be determined most consistently by comparing the function $l(r)$ in the continual theory with the value of l at discrete points obtained in the lattice model. We shall use the asymptotic form of the continual solution for large values of r, according to which $1 - l = \Delta_0^2/8r^2$. Calculating the same quantity by formula (11) by using the asymptotic form $\varphi = \chi/2$, we can easily obtain $l(r) \approx 1 - a^2/32r^2$. Comparing these expressions, we find that $\Delta_0 = a/2$.

This relation does not ensure the smallness of gradients near the core, but it can be obtained only from the asymptotic properties of distributions. It does not depend on many details of the continual or discrete model, for example, on the atomic structure of the dislocation core or the form of

640   Low Temp. Phys. **23** (8), August 1997

Ivanov *et al.*   640

the function $F(l^2)$. Indeed, away from the core, when $l \simeq 1$, the asymptotic form contains only $d^2F(l^2)/d(l^2)^2$ for $l=1$, and the asymptotic form can be obtained by replacing Δ_0^2 by $1/[d^2F(l^2)/d(l^2)^2]$ for any form of the function $F(l^2)$. Consequently, taking such a substitution into account, we can assume that this formula is valid for all continual and discrete models.

The correctness of the complete phenomenological analysis of a disclination, including the description of the core region, can be verified by comparing the expressions for energy, which, unlike asymptotic formulas, strongly depend on the details of the atomic structure of the core. It was noted above that $E = (\pi A/4)\ln(CR/a)$ in the discrete model, and the values of C differ significantly for different discrete models: $C = 3.15$ and 11.75 in the cases with a pentagon and a triangle of atoms at the center, which are coupled through the exchange interaction.

In the case of the continual model, the expression for energy contains the parameter Δ_0. If we consider this quantity as a fitting parameter and compare this dependence with the expression for the disclination energy in the discrete model, we can also find the relation between the parameter Δ_0 and the lattice constant. Comparing the two expressions for energy, we find that $\Delta_0 = 0.47a$ for the model with a triangle of central atoms, which is in good agreement with the result $\Delta_0 = 0.5a$ obtained from an analysis of asymptotic forms. Thus, we obtained astonishingly good (taking into account the semiquantitative nature of the theory) agreement between the results of alternative approaches to an analysis of a disclination in an AFM (both its core and asymptotic forms) for two specific models, viz., the discrete model with the dislocation core structure presented in Fig. 1b and the continual model with the function $F(l^2)$ in the form of the Landau expansion.

This result can be regarded as accidental in a certain sense. For the model with a pentagon of central atoms, a comparison of the expressions for energy gives $\Delta_0 = 1.75a$, and the difference is significant. The origin of this different is quite clear: as a matter of fact, the coefficient C in the expression for energy is determined above all by the region of the disclination core. Obviously, these constants must be different for models with different arrangements of atoms. The difference is if only due to the fact that the atomic density in the dislocation core region differs from the equilibrium value. In all cases (e.g., in the description of atomic models with different values of exchange integrals in the dislocation core and away from it), it would be appropriate to generalize the continual model (6) by supplementing the expression for energy with a term of the form $l^2/U(r)$, where $U(r)$ is a certain function localized at a distance of the order of the dislocation core radius. By varying the intensity of this additional term, we can ''control'' the contribution of the core region to the disclination energy without changing the asymptotic behavior away from the core and construct a continual theory for any discrete model. Detailed discussion of such ''inhomogeneous'' models is beyond the scope of this paper. It is important for our analysis that we can indicate a lattice model of dislocation that is quite simple and physically reasonable, but nevertheless provides a description of the disclination on the basis of the solution of variational equations of the simple continual theory (6), which is in good agreement with the accurate discrete approach. Consequently, the proposed continual model based on the contraction of the length of the vector $\mathbf{l}$ (or its inhomogeneous generalizations) is in all probability quite adequate and can be used for solving other (more complex) problems in the theory of disclinations in AFM, e.g., an analysis of magnon modes localized at a disclination, and analysis of the contribution of disclinations to magnon damping, neutron scattering, or scattering of light.

*E-mail: vbaryakhtar@gluk.apc.org

[1)]This explains formally the ambiguity in the definition of $\mathbf{l}$. The dipole moment of a system of charges is determined uniquely and does not depend on the choice of the reference point only if the total charge of the system is zero. In our case, this corresponds to complete compensation of spins within a magnetic unit cell, and this condition is satisfied only approximately. On the other hand, the definition of $\mathbf{l}$ introduced by us is preferable since the total spin of a magnetic unit cell with a higher symmetry is smaller than for the standard magnetic unit cell.

[2)]It follows from the same considerations that the Lagrangian of this model of AFM can be written in terms of the antiferromagnetism vector $\mathbf{l}$ in the same way as in the two-sublattice model, and the dynamic term has the standard form $(A/c^2)(\partial\mathbf{l}/\partial t)^2$, where c is the phase velocity of magnons.

[1] H.-J. Mikeska and M. Steiner, Adv. Phys. **40**, 191 (1991).

[2] B. A. Ivanov and A. K. Kolezhuk, Fiz. Nizk. Temp. **21**, 355 (1995) [Low Temp. Phys. **21**, 275 (1995)].

[3] A. M. Kosevich, B. A. Ivanov, and A. S. Kovalev, *Nonlinear Magnetization Waves. Dynamic and Topological Solitons* [in Russian], Naukova Dumka, Kiev (1983).

[4] R. S. Gekht, Usp. Fiz. Nauk **59**, 261 (1989) [Sov. Phys. Uspekhi **32**, 871 (1989)].

[5] J. N. Reimers and A. J. Berlinsky, Phys. Rev. B **48**, 9539 (1993).

[6] I. E. Dzyaloshinskii, Pis'ma Zh. Éksp. Teor. Fiz. **25**, 110 (1977) [JETP Lett. **25**, 98 (1977)].

[7] A. S. Kovalev and A. M. Kosevich, Fiz. Nizk. Temp. **3**, 259 (1977) [Sov. J. Low Temp. Phys. **3**, 125 (1977)].

[8] B. A. Ivanov, A. K. Kolezhuk, and G. M. Wysin, Phys. Rev. Lett. **76**, 511 (1996).

[9] G. M. Wysin, Phys. Rev. B **49**, 8780 (1995).

[10] A. S. Kovalev, Fiz. Nizk. Temp. **20**, 1034 (1994) [Low Temp. Phys. **20**, 815 (1994)].

[11] A. M. Kosevich, *Dislocations in the Theory of Elasticity* [in Russian], Naukova Dumka, Kiev (1978).

[12] E. G. Galkina, B. A. Ivanov, and V. A. Stephanovich, JMMM **118**, 373 (1993).

[13] L. P. Pitaevskii, Zh. Éksp. Teor. Fiz. **40**, 646 (1961) [Sov. Phys. JETP **13**, 451 (1962)].

[14] A. F. Andreev and V. I. Marchenko, Usp. Fiz. Nauk **130**, 39 (1980) [Sov. Phys. Uspekhi **23**, 21 (1980)].

Translated by R. S. Wadhwa

LOW-DIMENSIONAL AND DISORDERED SYSTEMS

Dilatometric size effect in thin C_{60} films

A. T. Pugachev, N. P. Churakova, and N. I. Gorbenko

Kharkov State Polytechnical University, 310002 Kharkov, Ukraine

The change in the lattice parameter $\Delta a/a$ of monocrystalline C_{60} films of thickness less than 10 nm is determined by the transmission high-energy electron diffraction method. In the temperature range 90–260 K, the value of $\Delta a/a$ increases with decreasing film thickness. The results are used for calculating the coefficients α_f and α_s of linear thermal expansion of the films and of the surface atomic layer. The value of α_s along the (111) plane is equal to $(55 \pm 15) \times 10^{-6}$ K^{-1}. © *1997 American Institute of Physics.* [S1063-777X(97)01008-6]

The properties of nanosize objects (films and crystals) are determined by the properties of not only bulk, but also surface and subsurface layers.[1] An analysis of the properties of such objects is of independent interest and makes it possible in some cases to obtain useful information on the dynamics of the surface lattice. Various aspects of the structure and properties of fullerite were studied by many authors.[2] However, thermal expansion of films has not yet been studied. In this communication, we report on the results of electron-diffraction investigations of the thermal expansion of monocrystalline fullerite C_{60} films of thickness less than 10 nm. The experimental data on thermal expansion are used for determining the thermal expansion coefficient for the outer atomic layer of fullerite.

Fullerite films were obtained by evaporation of C_{60} single crystals with a purity not worse than 99.9% and condensation on the cleavage plane of NaCl at room temperature in a vacuum $\sim 10^{-3}$ Pa. For subsequent electron-optical investigations, the films were separated in water and fished out on nets. In view of the small film thickness, the films covered only a small fraction of cells of the net so that each segment could be regarded as a console, i.e., free.

Electron diffraction patterns were recorded (by transmission of electrons) in an accelerating potential of 40 keV for a current density lower than 10^{-5} A·cm^{-2}. Possible instrumental errors in the measurements of lattice spacing were taken into account by using a standard and by controlling the position of the sample under investigation relative to the photographic plate during the experiment.[3] The temperature was varied from room to nitrogen temperature. The attachment with the sample was surrounded by a screen cooled to the temperature of liquid nitrogen. The temperature of the attachment was measured by a copper-constantan thermocouple to within $\pm 3°$.

The thickness t of such thin monocrystalline films was preset by the mass of the evaporant and the geometry of the evaporation, and was then determined by the electron-diffraction method from the size of the reciprocal lattice site in the direction of the normal to the film[4]:

$$t = d(\Delta \varphi)^{-1}, \qquad (1)$$

where d is the lattice spacing and $\Delta \varphi$ the angle within which

the reflecting sphere still intersects the given point of the reciprocal lattice with the Miller indices hkl. The angle $\Delta \varphi$ was determined by tilting the film relative to the electron beam, and the angle within which a reflex with the chosen indices hkl is still observed on the electron diffraction pattern was measured by a tilt goniometer. The film thickness was determined from (220) reflexes with an error of 10%. We investigated two series of films of thickness 3.5 and 6 nm.

The thermal expansion coefficient α was determined from the results of measurements of the lattice period variation as a function of temperature:

$$\alpha = \Delta d/d(\Delta T)^{-1}, \qquad (2)$$

where $\Delta d/d$ is the relative change in the lattice spacing as a result of thermal expansion upon a change in temperature by ΔT. Since $\Delta d/d = -2\Delta r/2r$, the value of $\Delta d/d$ was measured from the change in the spacing $2r$ between diffraction reflexes on the electron diffraction pattern for (422) reflexes. The error $2\Delta r/2r$ of measurements on an optical microscope was 5×10^{-4}, which leads to the error $\pm 3 \times 10^{-6}$ K^{-1} in the measurements of α. It should be noted that the average value of α was determined for the temperature range indicated above. When the electron beam was incident along the normal to the film, the values of $\Delta d/d$, and hence of α, were determined in a direction parallel to the film surface.

According to the results of electron diffraction and electron microscopic investigations, C_{60} films were continuous, monocrystalline, and had an fcc lattice with a period close to that for a bulk sample. Electron diffraction patterns (Fig. 1) contained reflexes (220) and (422), indicating that the (111) plane of the C_{60} film was parallel to the (100) plane of NaCl. At the same time, reflexes with lattice spacings of 0.86 and 0.43 nm which were also observed can be identified as the reflexes associated with stacking faults of 1/3 (422) and 2/3 (422).[5] An analysis shows that in spite of considerable differences in the lattice periods $a = 0.564$ nm for NaCl and $a = 1.42$ nm for fullerite C_{60}, favorable orientational relations required for the monocrystalline growth of C_{60} films are created in the given film–substrate system. For example, the two periods of the C_{60} lattice correspond (to within 1%) to five periods of the NaCl lattice.
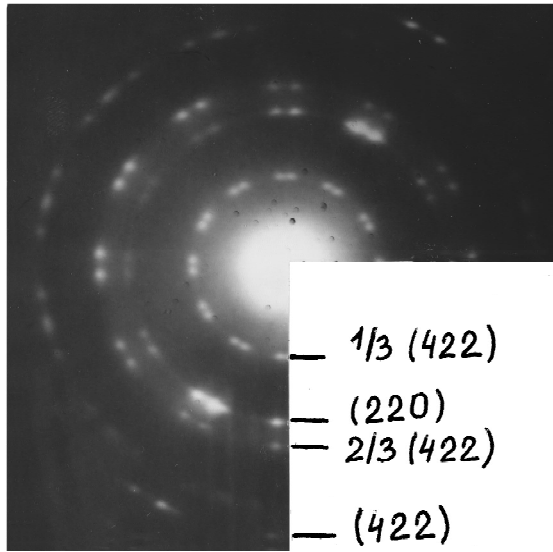
FIG. 1. Electron diffraction pattern for a fullerite C_{60} film of thickness 3.5 nm at $T = 270$ K. The scale of the electron diffraction pattern is $2L\lambda = 20.6$ nm·mm.

Table I gives the results of precision measurements of lattice spacing $\Delta d/d$ for C_{60} films in the temperature interval from T_1 to T_2. The value of $\Delta d/d$ increases upon a decrease in the film thickness. For example, the value of $\Delta d/d$ for a film of thickness 3.5 nm is 1.6 times the value of $\Delta d/d$ for bulk fullerite.

The measured dilatometric effect of lattice spacing in the temperature range under investigation is due to thermal expansion as well as the phase transition of fullerite from the fcc lattice to a simple cubic lattice at $T \approx 260$ K. According to the results of dilatometric and x-ray diffraction studies, for this phase transition the value of $\Delta d/d$ amounts to 3.4×10^{-3}.[6,7] This value was used for calculating the linear expansion coefficients α_f for the films, which are given in Table I. The temperature interval under investigation included the region 90–260 K of the ordered C_{60} phase. The obtained average values of the thermal expansion coefficient correspond to this phase.

The obtained data on the linear expansion coefficient for very thin films make it possible to estimate the thermal expansion coefficient α_s of the surface layer associated with the linear expansion coefficient α_v in the volume through the relation[8]

$$\alpha_s / \alpha_v = \overline{u_s^2} / \overline{u_v^2}, \tag{3}$$

TABLE I. Relative changes if the lattice spacing $\Delta d/d$ and average linear thermal expansion coefficient α_f of fullerite C_{60} films in the temperature range $T_1 - T_2$.

t, nm	$T_1 - T_2$, K	$\Delta d/d \cdot 10^3$	$\alpha_f \cdot 10^6$, K^{-1}
3.5	269–83	11.6	44
6	273–80	8.2	25
∞	273–80	6.8^7	19^7
∞	273–80	7.1^6	19.5^6

where $\overline{u_s^2}$ and $\overline{u_v^2}$ are the mean square displacements of atoms on the surface and in the volume, respectively. The values of $\overline{u_s^2}$ are higher than the values of $\overline{u_v^2}$ and tend exponentially to the volume value.[1] In this approximation, the linear expansion coefficient of the nth atomic layer can be written in the form

$$\alpha_n = \alpha_v + (\alpha_s - \alpha_v) e^{-n}. \tag{4}$$

The linear thermal expansion coefficient α_f of the film can be presented as a superposition of the linear thermal expansion coefficients α_n of individual atomic layers taking into account the relative film volume η occupied by them. In these calculations, we assumed that $\eta = (m-1)^{-1}$ (m is the number of atomic layers in the film thickness) and that the relative volume of the surface layer is equal to 0.5η. Thus, the thermal expansion coefficient of the film can be presented in the form of a linear combination of α_s and α_v:

$$\alpha_f = \alpha_1 \alpha_s + \alpha_2 \alpha_v. \tag{5}$$

Each value of the film thickness corresponds to its own coefficients a_1 and a_2. For example, a monocrystalline fullerite film of thickness 3.5 nm, which is oriented along the (111) plane, corresponds approximately to four lattice periods $d_{111} = 0.82$ nm, i.e., five atomic layers fit into the film thickness. In this case, $a_1 = 0.47$ and $a_2 = 0.53$. For a film of thickness 6 nm containing eight (111) layers, the values of a_1 and a_2 are equal to 0.30 and 0.70, respectively.

From the measured values of α_f and the value of α_v known from the literature,[6,7] expression (5) can be used for estimating the value of α_s: $\alpha_s = 40 \times 10^{-6}$ K^{-1} and 70×10^{-6} K^{-1} for films of thickness 6 and 3.5 nm, respectively.

Thus, the thermal expansion coefficient of the surface atomic layer (111) parallel to the surface $\alpha_{s\parallel} = (55 \pm 15) \times 10^{-6}$ K^{-1} in the temperature range under investigation. This value of $\alpha_{s\parallel}$ is apparently somewhat exaggerated since the contribution to the measured dilatometric effect comes not only from the parallel, but also from the perpendicular component of thermal expansion relative to the surface in view of natural roughness of the film.[9]

[1] A. Maradudin, *Theoretical and Experimental Aspects of Effects of Point Defects and Disorder on the Vibrations of Crystals*, New York (1966).
[2] V. M. Loktev, Fiz. Nizk. Temp. **18**, 217 (1992) [Sov. J. Low Temp. Phys. **18**, 149 (1992)].
[3] A. T. Pugachev and N. P. Churakova, Izv. RAN, Ser. Fiz. **57**, 126 (1993).
[4] P. Hirsch, A. Howie *et al.*, *Electron Microscopy of Thin Crystals*, London (1965).
[5] W. B. Zhao, X.-D. Zhang, K. J. Luo *et al.*, Thin Solid Films **232**, 149 (1993).
[6] F. Gugenberger, R. Heid, C. Meingast *et al.*, Phys. Rev. Lett. **69**, 3774 (1992).
[7] L. S. Fomenko, V. D. Natsik, S. V. Lubenets *et al.*, Fiz. Nizk. Temp. **21**, 465 (1995) [Low Temp. Phys. **21**, 364 (1995)].
[8] V. E. Kenner and R. E. Allen, Phys. Lett. **39A**, 245 (1972).
[9] I. A. Gospodarev, E. S. Syrkin, and S. B. Feodos'ev, Poverkhnost' No. 2, 23 (1996).

Translated by R. S. Wadhwa

Peculiarities of nonlinear electrical conductivity of two-dimensional ballistic contacts

M. V. Moskalets

Prospect Il'icha, 93ᵃ, Flat 48, 310020 Kharkov, Ukraine

Peculiarities of the conductivity of two-dimensional ballistic contacts that are sensitive to the nature of the confining potential as well as the existence of electrostatic potential inside the microconstriction are considered. It is shown that the position, amplitude, and shape of the peculiarities carry direct information about the position of quantization levels, the magnitude of potential inside the microconstriction, and the probability of passage of an electron through the contact. © *1997 American Institute of Physics.* [S1063-777X(97)01108-0]

1. INTRODUCTION

Conducting structures of small size[1] are unique objects for studying the wave properties of charge carriers in solids. A quantum point contact in the form of a narrow constriction (whose size d is comparable with the electron wavelength λ_F) connecting two macroscopic regions is an object of this type. Quantization of the transverse motion of electrons in the region of microconstriction changes the electron spectrum. Each transverse quantization level $\varepsilon_n = (\pi n \hbar / d)^2 / (2m)$ $(n = 1, 2, \ldots)$ has a one-dimensional subband $\varepsilon_n(p_x) = p_x^2 / (2m) + \varepsilon_n$ (the x-axis is directed along the contact axis) with conductivity $G_0 = 2e^2 / h$ corresponding to it. The quantization of the conductance of two-dimensional ballistic contacts discovered in Refs. 2 and 3 is a direct experimental evidence for the existence of quasi-one-dimensional conducting subbands in a ballistic microconstriction.

It was revealed as a result of theoretical analysis[4–12] that conductance quantization takes place for contacts with a sharp geometry, as well as contacts with a smooth shape (adiabatic contacts). According to Landauer's multichannel formula,[13] the conductivity of a contact can be defined as $G = N G_0$ (N is the number of conducting subbands). A one-dimensional subband n is conducting if the condition $\varepsilon_n < \varepsilon_F$ is satisfied (ε_F is the Fermi energy of electrons at the banks of the structure). A variation of the gate voltage V_g changes the contact diameter, leading to a variation of the position of the quantization levels. Consequently, the number of conducting subbands varies, and this is reflected in the form of steps of equal height on the dependence $G(V_g)$.

A variation of the voltage V applied to the contact can also change the number of conducting subbands.[14] Depending on the type of conductivity, the subbands are divided into three classes: conducting subbands, for which the relation $\varepsilon_n < \varepsilon_F - |eV|/2$ is satisfied, nonconducting subbands, for which the relation $\varepsilon_n > \varepsilon_F + |eV|/2$ is satisfied, and subbands which conduct only in one direction: $\varepsilon_F - |eV|/2 < \varepsilon_n < \varepsilon_F + |eV|/2$.[15] The change in the nature of conductivity in a subband is manifested in the form of spikes (peaks) on the dependence $d^2 I / dV^2(V)$ arranged at $(eV)_n = 2|\varepsilon_n - \varepsilon_F|$.[16] These peculiarities were observed experimentally in Refs. 15, 17 and 18.

The position of the levels ε_n is determined by the contact size and nature of the potential barrier confining the transverse motion of electrons in the contact. Normally, the ''hard wall'' model is used, in which the electron wave function vanishes at the contact boundary $y = y(x)$, and the spectrum of the transverse motion is the spectrum of a particle in a potential well (with vertical walls). However, experimental results indicate[18] that the ''soft wall'' model is preferable for $n \simeq 1$.[19] This model employs the parabolic potential $U(x, y) = U_0(x) + \omega^2 y^2 / 2$ which confines the transverse motion of electrons with the harmonic oscillator spectrum. However, further investigations are needed to determine finally the nature of potential barrier in a microconstriction.

In the present work, it is shown that the peculiarities of the potential forming a microconstriction can be determined from an analysis of nonlinear singularities of conductivity of two-dimensional ballistic contacts, associated with a change in the number of subbands or a change in the contact diameter or voltage. The present communication consists of the following parts. In Sec. 2, we analyze the dependence $dI/dV_g(V_g)$. It will be shown in Sec. 3 that the dependence $\partial I / \partial T(V)$ has peaks whose position corresponds to the distance between the transverse quantization levels ε_n and the Fermi level ε_F. In Sec 4, we shall show that an electrostatic potential relative to the contact edges exists in a microconstriction, and analyze its effect on nonlinear singularities of the contact conductivity.

2. NONLINEAR CONDUCTIVITY OF A TWO-DIMENSIONAL BALLISTIC CONTACT

We shall start from the expression for current passing through a ballistic adiabatic contact with a voltage V applied across its banks[1] in nonlinear response regime ($eV \ll \varepsilon_F$):

$$I = \frac{2e}{h} \sum_n \int d\varepsilon \, T_n(\varepsilon) \left\{ f_0\left(\varepsilon - \varepsilon_F - \frac{eV}{2} \right) - f_0\left(\varepsilon - \varepsilon_F + \frac{eV}{2} \right) \right\}. \tag{1}$$

Here, $T_n(\varepsilon)$ is the probability of passage of an electron with energy ε through the contact in channel n, and $f_0(\varepsilon) = (\exp(\varepsilon/T) + 1)^{-1}$ is the Fermi function.

It was mentioned in the Introduction that the existence of quasi-one-dimensional conducting subbands leads to a strong

nonlinearity of the current–voltage characteristics (IVC) of a quantum ballistic contact. An increase in the voltage may bring the bottom of one of the subbands ε_n in the band of current states $\pm eV/2$ near the Fermi level ε_F, which results in a sharp variation of the contact conductivity and is manifested in the form of a spike (peak) on the dependence of the second derivative of current d^2I/dV^2 with respect to voltage V.

On the other hand, a change in the contact diameter d for a fixed voltage, accomplished by a variation of the gate voltage V_g, also leads to a change in the number of conducting subbands and hence to the emergence of conductance jumps on the $G(V_g)$ dependence (for $V\to 0$),[2,3] as well as current jumps on the $I(V_g)$ dependence (for $V\neq 0$).[14] Thus, the dependence of the first derivative of current dI/dV_g with respect to the gate voltage on V_g for $V=$ const (just like the dependence of the second derivative of current d^2I/dV^2 with respect to voltage V for $V_g=$ const) contains peaks corresponding to a change in the number of conducting subbands.

Let us evaluate the derivative dI/dV_g by taking into account the fact that the only quantity depending on V_g in formula (1) is T_n, which is a function of ε_n:

$$\frac{dI}{dV_g} = \sum_n \left(\frac{dI}{dV_g}\right)_n,$$

$$\left(\frac{dI}{dV_g}\right)_n = \frac{2e}{h}\int d\varepsilon\,\frac{dT_n}{d\varepsilon}\left(-\frac{d\varepsilon_n}{dV_g}\right)\left\{f_0\left(\varepsilon-\varepsilon_F-\frac{eV}{2}\right)\right.$$
$$\left.-f_0\left(\varepsilon-\varepsilon_F+\frac{eV}{2}\right)\right\}. \tag{2}$$

A peculiar feature of the quantity $T_n(\varepsilon)$ is that it varies from zero (for $\varepsilon<\varepsilon_n$) to unity (for $\varepsilon>\varepsilon_n$) in a narrow energy interval $\Delta\varepsilon\simeq\Delta_n$ in the vicinity of ε_n. Hence we can single out two limiting cases

(1) $4T\ll\Delta_n$ (T is the temperature at the contact banks). In this case, we can put $f_0(\varepsilon)=\theta(-\varepsilon)$:

$$\left(\frac{dI}{dV_g}\right)_n = \frac{2e}{h}\left(-\frac{d\varepsilon_n}{dV_g}\right)\left\{T_n\left(\varepsilon_F+\frac{eV}{2}\right)-T_n\left(\varepsilon_F-\frac{eV}{2}\right)\right\}, \tag{3a}$$

or, for $V\ll\Delta_n$

$$\left(\frac{dI}{dV_g}\right)_n = \frac{2e^2}{h}\,V\left(-\frac{d\varepsilon_n}{dV_g}\right)\frac{dT_n}{d\varepsilon}. \tag{3b}$$

(2) $4T\gg\Delta_n$. In this case, we can put $T_n(\varepsilon)=\theta(\varepsilon-\varepsilon_n)$:

$$\left(\frac{dI}{dV_g}\right)_n = \begin{cases} \dfrac{2e}{h}\left(-\dfrac{d\varepsilon_n}{dV_g}\right)\Omega(\varepsilon_n-\varepsilon_F+eV/2), & V\gg T,\\[2ex] \dfrac{e^2}{2h}\dfrac{V}{T}\left(-\dfrac{d\varepsilon_n}{dV_g}\right)\cosh^{-2}\!\left(\dfrac{\varepsilon_n-\varepsilon_F}{T}\right), & V\ll T. \end{cases} \tag{4}$$

Here, $\Omega(x)=[1+\exp(-x/T)+\exp((x-V)/T)]^{-1}$. Let us also consider the expression for the peak amplitude [for $\varepsilon_n(V_g)=\varepsilon_F$] for an arbitrary relation between V and T:

$$\left(\frac{dI}{dV_g}\right)_{\varepsilon_n=\varepsilon_F} = \frac{2e}{h}\left(-\frac{d\varepsilon_n}{dV_g}\right)A_n(V,T),$$

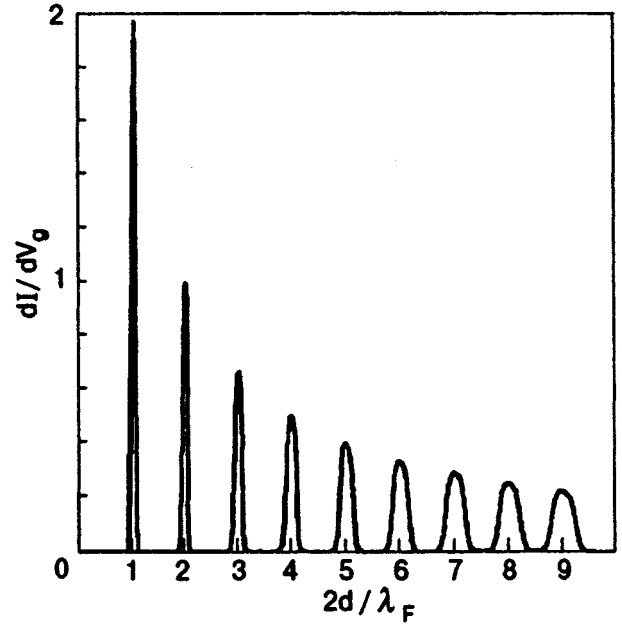

FIG. 1. Dependence of dI/dV_g on contact diameter for $T=0.01\varepsilon_F$ and $V=0.1\varepsilon_F$.

$$A_n(V,T)=\tanh\left(\frac{V}{4T}\right). \tag{5}$$

Let us analyze the above expressions. The dependence $dI/dV_g(V_g)$ consists of a sequence of peaks arranged at $\varepsilon_n(V_g)=\varepsilon_F$ and corresponding to the ''passage'' of the quantization level n through the current interval $\pm eV/2$ in the vicinity of the Fermi level ε_F: $\varepsilon_F-eV/2<\varepsilon_n(V_g)<\varepsilon_F+eV/2$. The amplitudes of the peaks are defined by the quantities $d\varepsilon_n/dV_g$ and $A_n(V_g,V,T)$. For $4T\gg\Delta_n$, the dependences $A_n(V_g)$ are identical for all n. Hence, the ratio of the peak amplitudes in this case is determined exclusively by the quantity $d\varepsilon_n/dV_g$. In the following, we shall consider two traditionally used models of the potential corresponding to the motion of electrons in the contact region, viz., the ''hard wall'' and the ''soft wall'' models.[19]

In the ''hard wall'' model, the contact boundary is assumed to be impermeable to electrons with any energy. The quantization levels $\varepsilon_n=(\pi n\hbar/d)^2/(2m)$ depends on the contact diameter d which is assumed to be proportional to the gate voltage V_g. In this model, the variable V_g can be replaced by the variable d (it is more convenient to use the dimensionless quantity $\xi=2d/\lambda_F$). Computing $d\varepsilon_n/d\xi=-2\varepsilon_n/\xi$, we can easily show that the ratio of peak amplitudes in the ''hard wall'' model (for $4T\gg\Delta_n$) is defined as (Fig. 1)

$$\left(\frac{dI}{dV_g}\right)_1 : \left(\frac{dI}{dV_g}\right)_2 : \left(\frac{dI}{dV_g}\right)_3 :\dots = \frac{1}{1}:\frac{1}{2}:\frac{1}{3}:\dots. \tag{6}$$

In the ''soft wall'' model, the transverse motion of electrons is confined by a parabolic potential. The quantization levels are equidistant: $\varepsilon_n=U_0(V_g)+\hbar\omega(n+1/2)$. It is assumed that the gate voltage does not change the relative separation between levels, i.e., the frequency ω, but varies only the potential U_0 inside the contact. The dependence

$U_0(V_g)$ is assumed to be linear. In this case, the quantity $d\varepsilon_n/dV_g = $ const and does not depend on n. Hence all peaks in the ''soft wall'' model (for $4T \gg \Delta_n$) have the same height:

$$\left(\frac{dI}{dV_g}\right)_1 : \left(\frac{dI}{dV_g}\right)_2 : \left(\frac{dI}{dV_g}\right)_3 : \ldots = 1:1:1:\ldots . \qquad (7)$$

A comparison of formulas (6) and (7) leads to the conclusion that an analysis of the relative amplitudes of the dependence $dI/dV_g(V_g)$ makes it possible to choose between various models of the potential confining the transverse motion of electrons in the constriction region.

As the temperature decreases ($4T \ll \Delta_n$), formulas (6) and (7) remain valid for $V \gg \Delta_n$ [see formula (3a)]. However, an additional factor $dT_n/d\varepsilon \simeq 1/\Delta_n$ appears for $V \ll \Delta_n$ (see formula (3b)). In the ''soft wall'' model,[19] $\Delta_n \approx $ const, and formula (7) remains valid. In the ''hard wall'' model, $\Delta_n \simeq 1/n$ (see, for example, Refs. 4 and 6) and amplitudes of all peaks become equal. It should be mentioned, however, that Zagoskin and Kulik[11] obtained $\Delta_n = $ const for a contact with special geometry in the ''hard wall'' model. Hence formula (6) remains valid in this model for the entire range of variation of temperature T and bias voltage V.

An analysis of the dependence of the width $(\Delta V_g)_n$ of peaks on their number n also makes it possible to choose between models of confining potential in the contact:

$$(\Delta V_g)_n \simeq \begin{cases} n \cdot \max(T,V,\Delta_n) & \text{in the hard wall model,} \\ \max(T,V,\Delta_n) & \text{in the soft wall model.} \end{cases} \qquad (8)$$

Moreover, an analysis of the dependence of the peak width on temperature T and bias voltage V allows us to determine experimentally the quantity Δ_n.

An increase in the bias voltage V or temperature T increases the width of peaks and the peaks merge. In this case, the dependence $dI/dV_g(V_g)$ becomes smooth and attains a classical asymptotic form. In the classical (not quantum) limit ($d \gg \lambda_F$), the current I passing through a ballistic contact is equal to $4e^2 dV/(h\lambda_F)$, and hence $dI/d\xi = G_0 V$ ($G_0 = 2e^2/h$ is the conductance quantum). The current attains the classical value when the bias voltage V or the width of temperature blurring of Fermi steps becomes equal to the separation between quantization levels (see Fig. 2):

$$\Delta \varepsilon_n \simeq \max(V, 4T). \qquad (9)$$

3. TEMPERATURE AND FIELD SPECTROSCOPY OF TRANSVERSE QUANTIZATION LEVELS IN A CONTACT

In the preceding section, we considered the peculiarities of the $I-V_g$ characteristics of a contact associated with the ''passage'' of the quantization level ε_n through the current interval $\pm eV/2$ in the vicinity of the Fermi level. In this section, we shall consider the IVC nonlinearity associated with the ''passage'' of the quantization levels through the region of temperature blurring of the edge of the Fermi step. This nonlinearity is manifested on the dependence of $\partial I/\partial T$ on the bias voltage V. Differentiating formula (1) with respect to temperature, we obtain
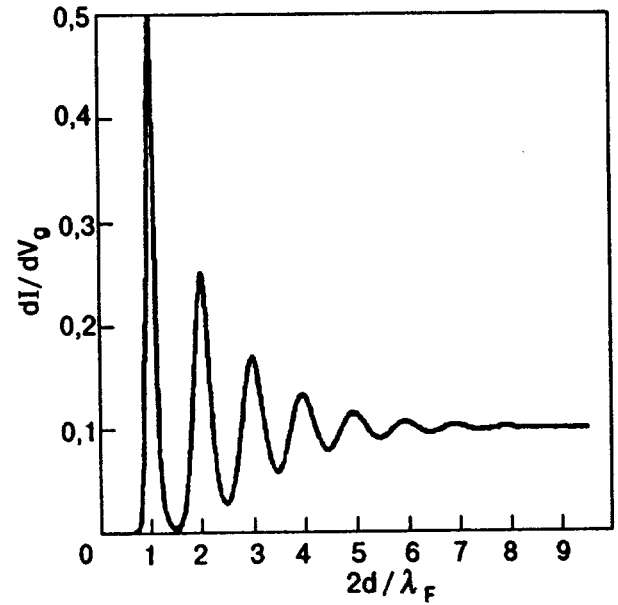

FIG. 2. Dependence of dI/dV_g on contact diameter for $T,V > \Delta_n$. The values of parameters are $T = 0.1\varepsilon_F$ and $V = 0.1\varepsilon_F$.

$$\frac{\partial I}{\partial T} = \frac{2e}{h} \sum_n \int d\varepsilon \, \frac{dT_n}{d\varepsilon} \left\{ \Psi\left(\frac{\varepsilon - \varepsilon_F - eV/2}{T}\right) \right.$$
$$\left. - \Psi\left(\frac{\varepsilon - \varepsilon_F + eV/2}{T}\right) \right\}. \qquad (10)$$

Here, $\Psi(x) = \ln[1+\exp(x)] - x[1+\exp(-x)]^{-1}$. Formula (10) is simplified in two limiting cases:

(a) for $4T \gg \Delta_n$

$$\frac{\partial I}{\partial T} = \frac{2e}{h} \sum_n \left\{ \Psi\left(\frac{\varepsilon_n - \varepsilon_F - eV/2}{T}\right) \right.$$
$$\left. - \Psi\left(\frac{\varepsilon_n - \varepsilon_F + eV/2}{T}\right) \right\}; \qquad (11)$$

(b) for $4T \ll \Delta_n$

$$\frac{\partial I}{\partial T} = 6.6 T \frac{e}{h} \sum_n \left\{ \frac{dT_n}{d\varepsilon}(\varepsilon_F + eV/2) - \frac{dT_n}{d\varepsilon}(\varepsilon_F \right.$$
$$\left. - eV/2) \right\}. \qquad (12)$$

Thus, the dependence $\partial I/\partial T(V)$ consists of a set of positive and negative peaks arranged at $(eV)_n = 2|\varepsilon_n - \varepsilon_F|$ (see Fig. 3, curve 1). In the case (a) corresponding to the situation when the region of temperature blurring of the Fermi step exceeds Δ_n, the shape of the peak does not depend on n and is determined by the function $\Psi(x)$. Note that the amplitude of the peak in this case does not depend on its number and temperature: $(\partial I/\partial T)_{\varepsilon_n=\varepsilon_F} = (2e/h)\ln 2$, while the peak width is proportional to temperature. As the temperature decreases ($4T \ll \Delta_n$), the shape of the peak is determined by the energy derivative of the transmission coefficient $dT_n/d\varepsilon(\varepsilon)$. In this case, the width of the peak is independent of temperature (and is equal to Δ_n) and the amplitude is proportional to the ratio T/Δ_n. The effect vanishes at $T = 0$.
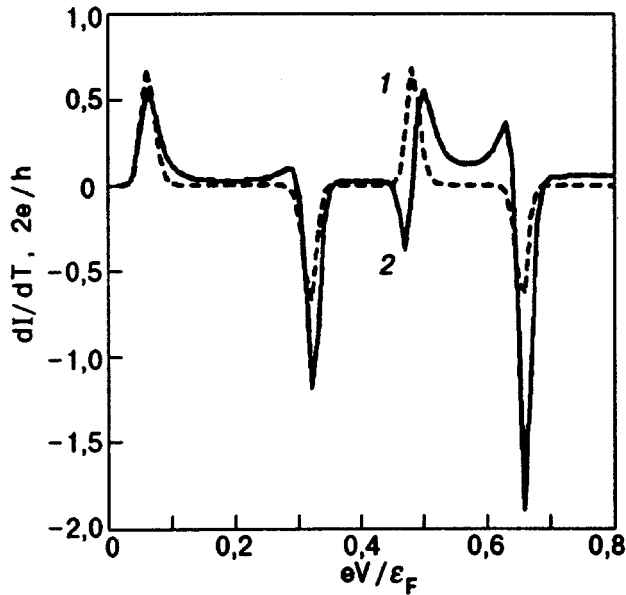
FIG. 3. Dependence of $\partial I/\partial T$ on voltage V. Curve 1 is obtained without consideration of the potential at the center of microconstriction. Curve 2 takes the potential Φ into account. The values of parameters are $T = 0.002\varepsilon_F$ and $d = 5.25\lambda_F$.

FIG. 4. Dependence of potential Φ on the microconstriction diameter.

Thus, an analysis of the dependence $\partial I/\partial T(V)$ makes it possible to determine the position of quantization levels $(eV)_n = 2|\varepsilon_n - \varepsilon_F|$ in the contact (for a fixed contact diameter d). Moreover, the temperature dependence of the peak width leads to the value of Δ_n. Note that the position of quantization levels can also be determined from the position of the peaks on the dependence $d^2I/dV^2(V)$,[16] although only broad singularities are observed instead of peaks in actual experiments.[18]

4. EFFECT OF QUANTUM ELECTROSTATIC POTENTIAL ON THE CONDUCTIVITY OF A BALLISTIC CONTACT

We shall show that one-dimensionalization of electron spectrum in the region of microconstriction leads to the existence of a potential difference in thermodynamic equilibrium between the constriction and contact banks (quantum electrostatic potential).[20] We shall study the effect of this potential difference on nonlinear singularities of the conductivity of the contact considered in the previous section.

For the sake of simplicity, we shall consider a ballistic contact in the form of a channel of width d and length $L > d$. The potential difference between the contact and the banks is denoted by $\Phi(d)$. In this case, the electron number density $n(d)$ in the contact can be written in the form

$$n(d) = \frac{2}{hd} \sum_n \int dp_x f_0[\varepsilon_n + e\Phi(d) + p_x^2/(2m) - \varepsilon_F].$$
(13)

Here, ε_F is the chemical potential of electrons at the banks (the potential of the banks is assumed to be zero). The potential $\Phi(d)$ is determined from the self-consistency condition which, in the limit of strong screening
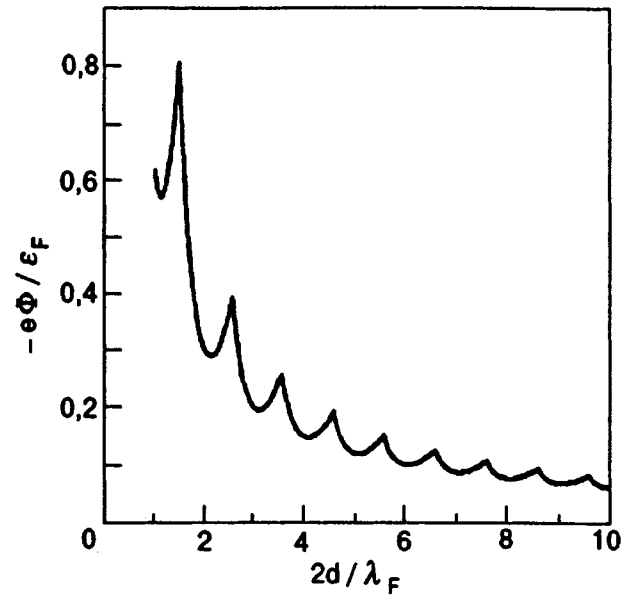
$$L, d \gg r_s$$
(14)

(r_s is the screening radius) is reduced to the condition of electrical neutrality. Assuming that the background of positive charge is the same at the banks and in the channel, we obtain from the electroneutrality condition

$$n(d) = n_0,$$
(15)

where $n_0 = 2\pi/\lambda_F^2$ is the electron density at the banks. Thus, formulas (13) and (15) lead to the self-consistency condition which determines the quantity $\Phi(d)$:

$$\frac{\lambda_F^2}{\pi hd} \sum_n \int dp_x f_0(\varepsilon_n + e\Phi(d) + p_x^2/(2m) - \varepsilon_F) = 1.$$
(16)

In the ''hard wall'' model at zero temperature ($T = 0$), this relation gives

$$\frac{4}{\pi\xi} \sum_n (1 + \varphi(d) - n^2/\xi^2)^{1/2} \theta(1 + \varphi(d) - n^2/\xi^2) = 1.$$
(17)

Here, $\varphi(d) = -e\Phi(d)/\varepsilon_F$. The dependence $\varphi(d)$ is plotted in Fig. 4. The peaks on this dependence correspond to the ''inclusion'' of the next conductivity channel, which occurs when the following condition is satisfied:

$$\varepsilon_n + e\Phi(d) = \varepsilon_F.$$
(18)

The corresponding channel width d_n is given by

$$d_n = \frac{\lambda_F}{2} \frac{n}{(1 + \varphi_n)^{1/2}},$$
(19)

The potential in the channel is defined as

$$\varphi_n = \frac{\pi}{4} n \left(\sum_{k=1}^{n-1} \left(1 - \frac{k^2}{n^2} \right)^{1/2} \right)^{-1} - 1.$$
(20)

It can easily be shown that, if we take into account the quantum electrostatic potential (QEP) $\Phi(d)$, the "inclusion" of a conducting subband with number n occurs for $\xi_n \simeq n - 0.5 (n \gg 1)$.

Upon a decrease in the contact diameter $(d \simeq \lambda_F)$, the screening radius $(r_s \simeq \lambda_F)$ becomes comparable with d, and the strong screening approximation becomes invalid. In this case, a charge layer formed near the channel edges hampers an increase in the potential inside the channel upon a decrease in its diameter. Hence the variation of the potential Φ will no longer compensate the increase in the energy $\varepsilon_1 \simeq 1/d^2$ and the channel will become nonconducting. Note that the channel would have remained conducting in the strong screening limit even for $d \to 0$.

In the current state, the potential Φ also depends on the voltage applied to the contact. In this case, the self-consistency condition assumes the form

$$\frac{\lambda_F^2}{\pi h d} \sum_n \int dp_x \theta(p_x) \{ f_0[\varepsilon_n + e\Phi(d,V,T) + p_x^2/(2m)$$
$$- \varepsilon_F - eV/2] + f_0[\varepsilon_n + e\Phi(d,V,T) + p_x^2/(2m) - \varepsilon_F$$
$$+ eV/2] \} = 1. \tag{21}$$

Formulas (16) and (21) are also applicable for a contact of arbitrary shape. The quantity d stands for the contact size at the narrowest position. Moreover, the change in the contact diameter over a distance $\sim \lambda_F$ must be small: $d(\ln d)/dx \ll \lambda_F^{-1}$. Note that the expressions presented above were obtained under the assumption $T_n = \theta(\varepsilon - \varepsilon_n)$, which is valid at least for $4T \gg \Delta_n$.

Let us now study how the existence of a potential $\Phi(d,V,T)$ changes the results obtained in previous sections. Note that the results obtained in this section are applicable for a broad contact $(d > \lambda_F)$ for which the "hard wall" model of confining potential is more suitable.

The existence of the potential Φ can be taken into account easily by replacing ε_n with $\varepsilon_n + e\Phi$. As a result, the expression for dI/dV_g assumes the form

$$\frac{dI}{dV_g} = \frac{2e}{h} \sum_n \int d\varepsilon \frac{dT_n}{d\varepsilon} \left(-\frac{d\varepsilon_n}{dV_g} - e\frac{d\Phi}{dV_g} \right) \left\{ f_0 \left(\varepsilon - \varepsilon_F \right.\right.$$
$$\left.\left. -\frac{eV}{2} \right) - f_0 \left(\varepsilon - \varepsilon_F + \frac{eV}{2} \right) \right\}. \tag{22}$$

It can easily be shown that the peak amplitude for $4T \gg \Delta_n$ is proportional to the quantity

$$\left(\frac{dI}{dV_g} \right)_n \simeq \frac{(1 + \varphi_n)^{3/2}}{n}, \tag{23}$$

where φ_n is defined by formula (20) for $T = 0$ and $V = 0$. If T and V are not equal to zero, we must solve Eq. (21) numerically to obtain the quantity φ_n. It follows from formula (23) that, if we take QEP into consideration, the ratios of peak amplitudes on the dependence $dI/dV_g(V_g)$ no longer satisfy the simple relation (6), which can be used for experimentally determining the potential inside the microconstriction.

The expression for $\partial I/\partial T$ also changes and assumes the following form for $4T \gg \Delta_n$:

$$\frac{\partial I}{\partial T} = \frac{2e}{h} \sum_n \left\{ \Psi\left(\frac{\varepsilon_n + e\Phi - \varepsilon_F - eV/2}{T} \right) \right.$$
$$- \Psi\left(\frac{\varepsilon_n + e\Phi - \varepsilon_F + eV/2}{T} \right) - e\frac{\partial \Phi}{\partial T} \left[f_0 \left(\varepsilon_n + e\Phi \right.\right.$$
$$\left.\left.\left. - \varepsilon_F - \frac{eV}{2} \right) - f_0 \left(\varepsilon_n + e\Phi - \varepsilon_F + \frac{eV}{2} \right) \right] \right\}. \tag{24}$$

It follows from the above expression that the presence of QEP leads to the asymmetry of positive and negative peak amplitudes in the dependence $\partial I/\partial T(V)$ (see Fig. 3, curve 2).

5. CONCLUSION

In this work, we have shown that the investigation of nonlinear singularities of two-dimensional ballistic contacts makes it possible to obtain direct information about the nature of electrostatic potential forming the microconstriction. For example, the measurement of relative amplitude of peaks on the dependence $dI/dV_g(V_g)$ determines whether the confining potential is impenetrable for electrons or the transverse electron movement occurs in the parabolic ("soft wall") potential.

It is also shown that the presence of electrostatic potential in the microconstriction region is a characteristic feature of quantum ballistic contacts. This potential emerges due to a difference in the nature (dimensions) of the electron spectrum in the region of microconstriction and at the contact edges. It should be observed that in the "soft wall" model[19] which is applicable for $d \simeq \lambda_F$, the electrostatic potential in the microconstriction region is induced by the gate voltage V_g. According to our investigations, the electrostatic potential in the contact does not vanish upon an increase in the contact diameter $(d > \lambda_F)$, although its physical nature changes. In this case, the potential in the microconstriction is not connected with the gate voltage V_g determining the shape of the contact, but is due entirely to the manifestation of the quantum nature of electron motion in the contact.

[1] Y. Imry, in *Directions in Condensed Matter Physics* [ed. by G. Grinstein and G. Mazenco], World Scientific, Singapore (1986).
[2] B. J. van Wees, H. van Houten, C. W. J. Beenakker *et al.*, Phys. Rev. Lett. **60**, 848 (1988).
[3] D. A. Wharam, T. J. Thornton, R. Newbury *et al.*, J. Phys. C **21**, L209 (1988).
[4] L. I. Glazman, G. B. Lesovik, D. E. Khmel'nitskii, and R. I. Shekhter, Pis'ma Zh. Éksp. Teor. Fiz. **48**, 218 (1988) [JETP Lett. **48**, 238 (1988)].
[5] I. B. Levinson, Pis'ma Zh. Éksp. Teor. Fiz. **48**, 273 (1988) [JETP Lett. **48**, 301 (1988)].
[6] A. Szafer and A. D. Stone, Phys. Rev. Lett. **62**, 300 (1989).
[7] G. Kirczenow, Phys. Rev. **B39**, 10452 (1989).
[8] L. Escapa and N. Garsia, J. Phys. Cond. Mat. **1**, 2125 (1989).
[9] D. van der Marel and E. G. Haanappel, Phys. Rev. **B39**, 7811 (1989).
[10] A. Kawabata, J. Phys. Soc. Jpn. **58**, 372 (1989).
[11] A. M. Zagoskin and I. O. Kulik, Fiz. Nizk. Temp. **16**, 911 (1990) [Sov. J. Low Temp. Phys. **16**, 533 (1990)].
[12] E. Castano and G. Kirczenow, Phys. Rev. **B45**, 1514 (1992).
[13] M. Büttiker, Y. Imry, R. Landauer, and S. Pinhas, Phys. Rev. **B31**, 6207 (1985).

[14] L. I. Glazman and A. V. Khaetskii, Pis'ma Zh. Éksp. Teor. Fiz. **48**, 546 (1988) [JETP Lett. **48**, 591 (1988)].

[15] L. P. Kouwenhoven, B. J. van Wees, C. J. P. M. Harmans *et al.*, Phys. Rev. **B39**, 8040 (1989).

[16] A. M. Zagoskin, Pis'ma Zh. Éksp. Teor. Fiz. **52**, 1043 (1990) [JETP Lett. **52**, 435 (1990)].

[17] N. K. Patel, L. Martin-Moreno, M. Pepper *et al.*, J. Phys. Cond. Mat. **2**, 7247 (1990).

[18] N. K. Patel, J. T. Nichols, L. Martin-Moreno *et al.*, Phys. Rev. **B44**, 13549 (1991).

[19] M. Büttiker, Phys. Rev. **B41**, 7906 (1995).

[20] M. V. Moskalets, Pis'ma Zh. Éksp. Teor. Fiz. **62**, 702 (1995) [JETP Lett. **62**, 719 (1995)].

Translated by R. S. Wadhwa

Thomas–Fermi screening of a moving surface charge

I. O. Kulik

Department of Physics, Bilkent University, Bilkent 06533, Ankara, Turkey and B. Verkin Institute for Low Temperature Physics and Engineering, National Academy of Sciences of Ukraine, 47 Lenin ave., Kharkov 310164, Ukraine[*]

The dynamical screening effects in the skin layer of a metal are investigated. The electric charge density near the metal surface induced by a moving charged body outside the metal is screened at the Thomas–Fermi length if the velocity parallel to the surface is smaller than the Fermi velocity. Crisis of screening is found at the velocity approaching the Fermi velocity, which results in the electric field penetration inside the metal at large distances, and in the distortion of the electric field distribution outside the metal. The energy dissipation from a moving charged body as a function of the velocity has a pronounced singularity near the Fermi velocity. © *1997 American Institute of Physics.* [S1063-777X(97)01208-5]

1. INTRODUCTION

Macroscopic charge cannot exist inside a metal. Upon introduction into a metallic sample, any external charge concentrates near its surface in a thin layer, whose characteristic thickness is[1,2]

$$\lambda_{TF} = [4\pi e^2 N(\varepsilon_F)]^{-1/2}, \qquad (1)$$

the so-called Thomas–Fermi screening length, which is typically of the order of a few angstroms. [$N(\varepsilon_F)$ is the density of electronic states at the Fermi energy, ε_F.]

If the external charge is fixed in space, the emerging Coulomb potential will be screened inside the metal at the same distance. Along the surface, charge density can be localized within some area, and can be translated parallel to the surface without changing its shape. It is tempting to consider the surface charge, which is generated due to the motion of a charged body in vacuum near the metal surface, as a separate entity, and to investigate the effects related to its dynamical behavior. At the velocity smaller than the Fermi velocity, the nonlinearity in the response to an external perturbation may occur if the former approaches the phonon propagation velocity, which results in phonon emission followed by extra energy release from the surface sheet. In the case of fast motion with a velocity greater than the Fermi velocity, the oscillatory potential emerges in the wake behind the charged body (e.g., an ion moving in a metal), which can trap conduction electrons in the wake-bound state.[3,4] At a velocity approaching the Fermi velocity, the charged body wake is at ''resonance'' with the conduction electrons, which accounts for the singularity of the dissipation in the surface sheet and for the stopping power of body motion. In the case of motion of a charged body outside the metal, this results in the nonlinear interaction between the external moving charge and the induced charge near the surface. The dependence of drag force and power dissipation on the velocity is nonlinear and possibly nonmonotonic.

The information concerning the electron states in metal, which can be obtained in the corresponding experiments, is similar to that found from the conventional conductivity measurements except that (1) it is directly related to the relaxation processes and mechanisms very near the metal surface; (2) the nonlinear output is expected in the linear amplitude regime (small charges and fields) since the nonlinearity may be concerned with the large velocity of collective motion rather than with the drift velocity of electrons.

In the present paper we investigate the dependence of the charge distribution inside the metal and the electrostatic potential outside the metal, on the velocity of the surface sheet motion produced by a charged body (known as the ''tip'') outside the metal moving parallel to the metal surface. It is shown that the surface charge follows the tip motion adiabatically only if the velocity of motion is much smaller than the Fermi velocity V_F. A velocity greater than V_F causes a crisis of the Thomas–Fermi screening, which results in the nonlinear charge penetration deep into the metal and in the distortion of the screening electric field inside and outside the metal.

The questions considered can have relevance to scanning tunneling microscopy,[5] to the effects of charge quantization in small metallic electrodes,[6] to ballistic electron transport in narrow metallic constrictions and point contacts,[7,8] and to general aspects of ''fermiology,'' i.e., Fermi surface reconstruction in metals, since the dynamical screening effects in the surface sheet depend essentially on the topology and shape of the Fermi surface. The interaction of a moving surface charge with phonons can be viewed as a kind of ''surface spectroscopy'' of conduction electrons in metals.[9]

Another type of experiment involves charged ion motion inside a metal[3] or a traversal of the interface between metal and vacuum.[4] If the velocity of ion motion approaches V_F from above, the wake-bound state of an electron and stopping power for ion motion reveal a singularity in the limit $V \to V_F$. In the case of small velocity, the surface charge follows the external perturbation adiabatically, allowing for a semiclassical description of the interaction of external electric field and the induced charge. Important difference between the case $V \gg V_F$ and $V \lesssim V_F$ is that semiclassical approximation may present a reasonable approximation of the problem.

After the discussion of the validity of different approxi-

mations (semiclassical or random-phase), which are applicable to the problem of dynamical screening in Sec. 2, we investigate in Sec. 3 the dynamical screening in a two-dimensional metal with a cylindrical Fermi surface since it most clearly illustrates the theoretical method adopted by us and the origin of the velocity-dependent anomaly predicted. In Sec. 4, similar effects are considered for a three-dimensional metal with a spherical Fermi surface. Energy dissipation and drag force induced in a moving body are calculated in Sec. 5, followed in Sec. 6 by the discussion of the physical aspects of the surface charge dynamics and possible realization of its fast motion in metals.

2. SEMICLASSICAL APPROXIMATION FOR A DYNAMICAL SCREENING

Linear response of a degenerate electron gas to a time- and space-dependent electric potential

$$\phi(\mathbf{r},t)=\int \frac{d\mathbf{k}}{(2\pi)^3}\int_{-\infty}^{\infty}\frac{d\omega}{2\pi}\,\phi_{\mathbf{k}\omega}\exp(i\mathbf{k}\mathbf{r}-i\omega t)$$

is described by the quantum kinetic equation[10] (assuming $\hbar = 1$)

$$(\omega-\varepsilon_{\mathbf{p}+\mathbf{k}/2}+\varepsilon_{\mathbf{p}-\mathbf{k}/2})f^1_{\mathbf{k}\omega}+e\,\phi_{\mathbf{k}\omega}(f^0_{\mathbf{p}-\mathbf{k}/2}-f^0_{\mathbf{p}+\mathbf{k}/2})=0, \tag{2}$$

where $f^0_{\mathbf{p}}$ is the unperturbed electron distribution function $(\exp[(\varepsilon_{\mathbf{p}}-\mu)/T]+1)^{-1}$, and $f^1_{\mathbf{k}\omega}$ is the first order correction to $f_{\mathbf{k}\omega}(\mathbf{p})$. (Assuming that the velocity of motion is much less than the light velocity c, we can ignore the magnetic field effects and eliminate the vector potential A, leaving only a scalar potential ϕ.)

Equation (2) results in the Lindhard formula (e.g., see Ref. 1) for the relation between the electric displacement and the electric field

$$\mathbf{D}_{\mathbf{k}\omega}=\mathbf{E}_{\mathbf{k}\omega}+4\pi\mathbf{P}_{\mathbf{k}\omega}=\epsilon(\mathbf{k},\omega)\mathbf{E}_{\mathbf{k}\omega},$$

where $\rho_{\mathbf{k}\omega}=-(4\pi)^{-1}i\mathbf{k}\mathbf{P}_{\mathbf{k}\omega}$ is the external charge density, and

$$\varepsilon(\mathbf{k},\omega)=1+\frac{4\pi e^2}{\mathbf{k}^2}\int\frac{2d\mathbf{p}}{(2\pi)^3}\frac{f^0_{\mathbf{p}+\mathbf{k}/2}-f^0_{\mathbf{p}-\mathbf{k}/2}}{\omega-\varepsilon_{\mathbf{p}+\mathbf{k}/2}+\varepsilon_{\mathbf{p}-\mathbf{k}/2}-i\delta}. \tag{3}$$

At $\omega = 0$, the dielectric function within the random-phase approximation (RPA) [Eq. (2)] is

$$\epsilon(\mathbf{k})=1+\frac{\kappa^2_{TF}}{k^2}L(x), \quad L(x)=\frac{1}{2}+\frac{1-x^2}{4x}\ln\left|\frac{1+x}{1-x}\right|, \tag{4}$$

where $x = 2k/k_F$. At small $\mathbf{k}$, the kinetic equation (2) reduces to a semiclassical (SA) Boltzmann kinetic equation for the distribution function $f(\mathbf{p},\mathbf{r},t)$, and Eq. (3) reduces to an expression for the dielectric function

$$\epsilon(\mathbf{k})=1+\kappa^2_{TF}/k^2, \tag{5}$$

which is equivalent to (1) with $\kappa_{TF} = 1/\lambda_{TF}$.

To clarify the difference between various approximations, let us consider the screening of the electrostatic potential produced by a charged plane immersed inside the metal.

The scalar potential in a metal emerging from an external electric charge uniformly distributed with the density σ in a plane $z = 0$ is

$$\phi(z)=2\sigma\int_{-\infty}^{\infty}\frac{\exp(ikz)}{k^2\epsilon(\mathbf{k})}\,dk. \tag{6}$$

It reduces to an exponential dependence $\phi(z) = \phi(0)\exp(-\kappa_{TF}|z|)$ within the SA. Within the RPA, by introducing a parameter

$$\alpha=\left(\frac{\kappa_{TF}}{2k_F}\right)^2 \tag{7}$$

we obtain

$$\phi(z)=\int_0^{\infty}\frac{\cos(2k_Fzx)}{x^2+\alpha f(x)}\,dx. \tag{8}$$

For typical metals, α falls within the interval

$$0.3<\alpha<1 \tag{9}$$

[α is related to the most commonly used quantity[2] $r_s = r_0/a_0$, where a_0 is the Bohr radius, and r_0 is the average distance between electrons, since $\alpha = \pi^{-1}(4/9\pi)^{1/3}\,r_s = 0.1659r_s$.]

The normalized potential distribution $\phi(z)/\phi(0)$ as a function of $2k_Fz$ is shown in Fig. 1a for various α. However, since it is nonexponential (power-like and oscillating with a period π/k_F^1 at large z), $\phi(z)$ is very small in the region in which, within the SA, it decays exponentially. If replotted as a function of $\kappa_{TF}z = z/\lambda_{TF}$, all the dependences $\phi(z)/\phi(0)$ at different α fall nearly into a single line (Fig. 1b). The screening radius,

$$\bar{r}=\int_0^{\infty}\phi(z)dz/\phi(0), \tag{10}$$

within 10% accuracy equals the Thomas–Fermi screening length in the interval of α from 0 to 1. This has an implication that the semiclassical approximation, which is not exact, nevertheless gives a reasonable estimate of screening. We will use the approximation which can be used to trace the dynamical screening effects in metals. The solution proves to be quite complex even within the SA, and it would become intractable in the RPA scheme[11] since k in Eq. (2) must be considered as an operator id/dz. In any case, the validity of SA is indeed guaranteed as long as α is small (9).

3. THOMAS–FERMI SCREENING IN A TWO-DIMENSIONAL METAL

Consider the metallic semispace in the vicinity of a charged tip T moving parallel to the metal surface with a velocity V (Fig. 2). We shall investigate the steady-state distribution of electrons in a momentum space $f(\mathbf{r},\mathbf{p},t)$ and the electrostatic potential distribution $\phi(\mathbf{r},t)$ inside and outside the metal with the assumption that they make a self-similar configuration which depends on the relative coordinate $x - Vt$.

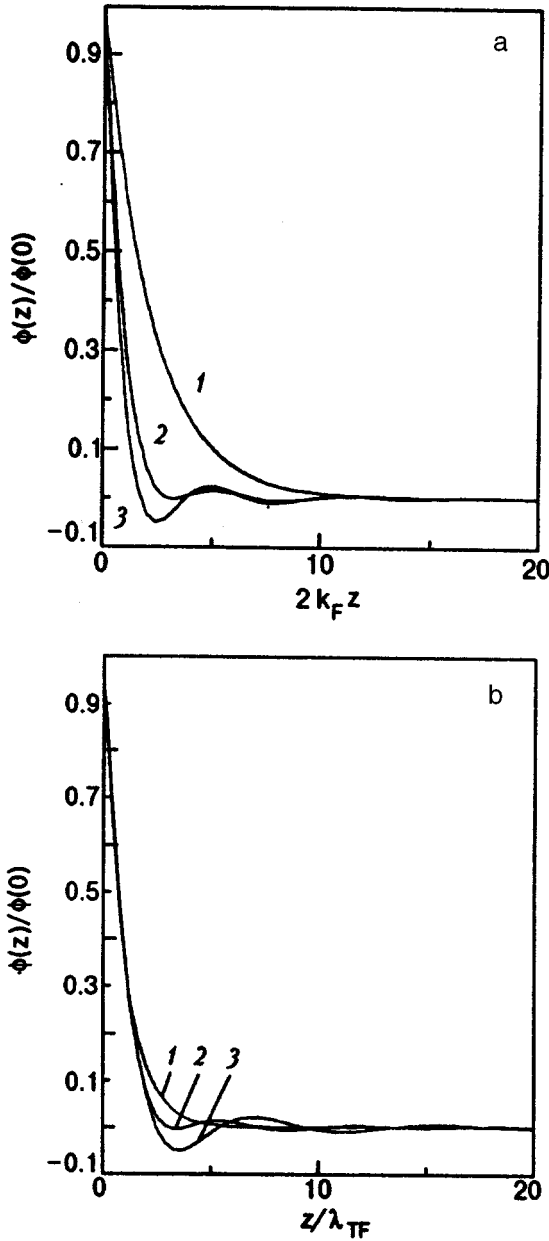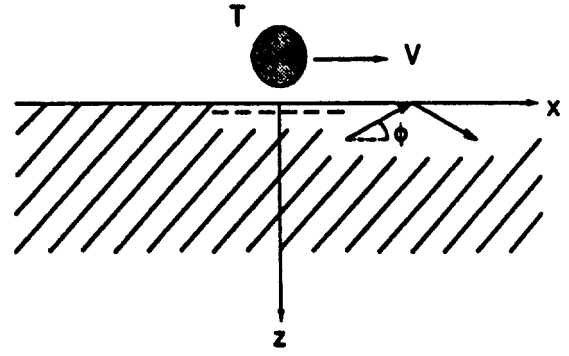In a semiclassical approximation, charge density ρ is expressed in terms of f as

FIG. 2. Schematic diagram of a charged tip (T) moving parallel to the metal surface with a velocity V. Surface charge (a dashed line) accumulates near the metal surface and moves with the same velocity. φ is the angle of incidence of the electron.

The charge density in a metal at $T = 0$ is

$$\rho = -eN(\varepsilon_F)\langle\chi_\varphi\rangle, \qquad (15)$$

where $\langle...\rangle$ denotes averaging over the Fermi surface.

We ignore scattering of electrons inside a metal, which is expected to be a good approximation if the electron mean free path is much larger than the Thomas–Fermi screening length, but include the scattering of electrons at the surface with the help of the diffuse boundary condition that introduces a diffusivity coefficient $q(0 < q < 1)$. Requiring that the electron current be zero at the metal surface,[12] we can write the boundary condition in case of a cylindrical Fermi surface directed along the y axis in the form

$$\chi_{-\varphi} = (1-q)\chi_\varphi + \frac{q}{2}\int_0^\pi \chi_\varphi \sin \varphi d\varphi, \qquad (16)$$

where q is the diffusivity coefficient of the metal surface, and φ is the angle between the direction of electron momentum and surface.

In the Fourier representation with respect to the surface coordinates x, y, the equations for ϕ_k and $\chi_{\varphi k}$ are (below we drop for clarity the index $\mathbf{k}$)

$$k^2\phi - d^2\phi/dz^2 = -4\pi eN(\varepsilon_F)\langle\chi_\varphi\rangle \qquad (17)$$

and

$$[\nu + ik_x(V_F \cos \varphi - V)]\chi_\varphi + V_F \sin \varphi \frac{d\chi_\varphi}{dz}$$
$$= eV_F\left(ik_x \cos \varphi + \sin \varphi \frac{d}{dz}\right)\phi. \qquad (18)$$

Although we are considering a clean metal (collision frequency v→0), a "trace" of the electron scattering (v=+0) should remain in order to ensure a proper analytical behavior of the electron distribution inside a metal as $z\to\infty$.

In the case of zero velocity, $V = 0$, Eq. (18) gives $\chi_\varphi = e\phi$, thus resulting in an exponential distribution of ϕ inside the metal

$$\phi = \phi(0)\exp(-\kappa_{TF}z) \quad \text{with} \quad \kappa_{TF} = \sqrt{\lambda_{TF}^{-2} + k_x^2}. \qquad (19)$$

FIG. 1. Normalized potential distribution inside a metal at various values of α as a function of $2k_F z$ (a) and $\kappa_{TF}z$ (b). 1—$\alpha = 0.2$; 2—$\alpha = 1.1$; 3—$\alpha = 2.0$.

$$\rho = 2e\int \frac{d\mathbf{p}}{(2\pi\hbar)^3}(f - f_0), \qquad (11)$$

where f_0 is the equilibrium Fermi distribution. The scalar potential can be found from the Poisson equation

$$\nabla^2\phi + 4\pi\rho = 0, \qquad (12)$$

and f satisfies the Boltzmann equation

$$\frac{\partial f}{\partial t} + \mathbf{v}\frac{\partial f}{\partial \mathbf{r}} - e\nabla\phi\frac{\partial f}{\partial \mathbf{p}} = -\hat{v}(f - f_0), \qquad (13)$$

in which $\hat{v}$ is an electron collision operator. The self-similar distributions of f and ϕ are

$$f = f_0 + \chi_\varphi(x - Vt, y, \mathbf{p})\partial f_0/\partial\varepsilon_\mathbf{p}, \quad \phi = \phi(x - Vt). \quad (14)$$

We shall use below the dimensionless units such that $\hbar = 1$, $e = 1$ and $N(\varepsilon_F) = 1$, $V_F = 1$, where V_F is the Fermi velocity. Thus, representing χ_φ in the form $\chi_\varphi = \phi + u_\varphi$, we obtain

$$\left(-k_x^2 + \frac{d^2}{dz^2}\right)\phi = \phi + \langle u_\varphi \rangle \tag{20}$$

and

$$\left(i\gamma_\varphi + \frac{d}{dz}\right)u_\varphi = \frac{ik_x V}{\sin \varphi}\,\phi, \tag{21}$$

where

$$\gamma_\varphi = \frac{k(\cos \varphi - V) - i\mathrm{v}}{\sin \varphi}, \quad \mathrm{v} = +0. \tag{22}$$

The solution of Eq. (21) is

$$u_\varphi = A_\varphi \exp(-i\gamma_\varphi) + \frac{ik_x V}{\sin \varphi}\int_0^z \phi(z')\exp[-i\gamma_\varphi(z - z')]dz', \tag{23}$$

from which it follows that $\phi(z)$ can be obtained with the Laplace transform

$$\phi_p = p\int_0^\infty \phi(z)\exp(-pz)dz,$$

giving for the space dependence of ϕ at $z > 0$

$$\phi(z) = \frac{1}{2\pi i}\int_{a-i\infty}^{a+i\infty} dp\, e^{pz}$$
$$\times \frac{p\phi(0) + \phi'(0) + \int_{-\pi}^{\pi}(d\varphi/2\pi)A_\varphi/(p+i\gamma_\varphi)}{p^2 - k_x^2 - S(p)}, \tag{24}$$

where $S(p)$ is a function

$$S(p) = 1 + k_x V\int_{-\pi}^{\pi}\frac{d\varphi}{2\pi}\frac{1}{k_x(\cos \varphi - V - i0) - ip \sin \varphi}. \tag{25}$$

Integral (24) is taken in a complex plane p along a vertical line which is situated to the right of all singularities (poles and branching lines) of the integrand (Fig. 3). The solution depends upon the analytical properties of $S(p)$ which will be discussed below, and is different at $V < 1$ (velocity smaller than the Fermi velocity) and at $V > 1$.

The requirement that $\phi(z)$ derived from (24) behaves regularly at $z \to \infty$ establishes the relation between $\phi(0)$ and $\phi'(0)$ (prime denotes derivative with respect to z) and thus allows the solution of the Poisson equation outside the metal, which for clarity we also represent in the form of a Poisson integral:

$$\phi = \frac{1}{2\pi i}\int_{a-i\infty}^{a+i\infty} dp\, e^{-pz}\frac{p\phi(0) - \phi'(0) - 4\pi Q e^{-ph}}{p^2 - k_x^2},$$
$$z < 0, \tag{26}$$

where for simplicity it is assumed that the tip is a point charge Q located at a height h above the metal surface. Re-
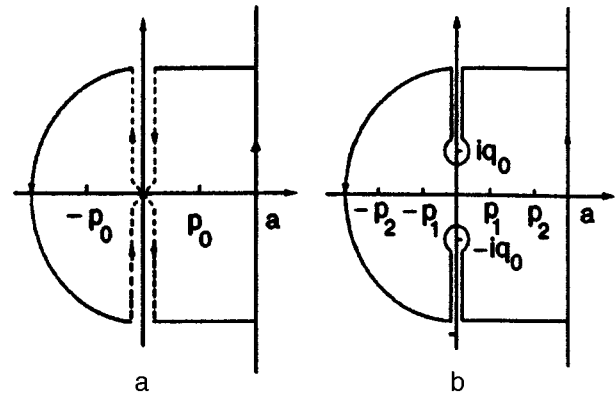

FIG. 3. Path of integration in Eq. (24) for $V < 1$ (a) and $V > 1$ (b). Integrals along broken lines cancel each other because $S(p)$ at $V < 1$ has the same value on both sides to the left and to the right of the imaginary axis.

quirement that $\phi(z)$ in (24) should properly behave at $z \to -\infty$ allows us to find the potential provided that the value of the ratio $\phi'(0)/\phi(0)$ is specified by the solution of the Poisson equation inside the metal.[13]

Evaluation of the integral (24) at $V < 1$ gives

$$\phi(z) = \phi(0)e^{-p_0 z} + \int_{-\pi}^{\pi}\frac{e^{-p_0 z} - e^{-i\gamma_\phi z}}{p_0^2 + \gamma_\varphi^2}A_\varphi, \tag{27}$$

where $\phi'(0)$ is related to $\phi(0)$ according to

$$\phi' = -p_0\phi(0) - \int_{-\pi}^{\pi}\frac{d\varphi}{2\pi}\frac{A_\varphi}{p_0 + i\gamma_\varphi}. \tag{28}$$

This is a consequence of the vanishing $\exp(p_0 z)$ terms in $\phi(z)$, where p_0 is the pole of the denominator of the integrand of Eq. (24).

Substitution of Eq. (27) into (23) gives

$$u_\varphi = A_\varphi \exp(-i\gamma_\varphi) + \frac{k_x V}{\sin \varphi}\left[\frac{\phi_0}{\gamma_\varphi + ip_0}[\exp(-p_0 z) - \exp(-i\gamma_\varphi z)]\right.$$
$$\left. + \int_{-\pi}^{\pi}\frac{d\varphi}{2\pi}\frac{A_{\varphi'}}{p_0^2 + \gamma_{\varphi'}^2}\frac{\exp(-i\gamma_{\varphi'} z) - \exp(-i\gamma_{\varphi'} z)}{\gamma_\varphi - \gamma_{\varphi'}}\right], \tag{29}$$

where

$$\phi_0 = \phi(0) + \int_{-\pi}^{\pi}\frac{d\varphi}{2\pi}\frac{A_\varphi}{p_0^2 + \gamma_\varphi^2}. \tag{30}$$

The positive values of $\varphi(0 < \varphi < \pi)$ correspond to electrons reflected from the surface and the negative values of $\varphi(-\pi < \varphi < 0)$ correspond to electrons arriving from the bulk of the metal. The quantity A_φ in Eq. (29) satisfies at $\varphi < 0$ the same relation (16) as χ_φ does. For positive φ, the exponents $\exp(-i\gamma_\varphi)$ taken with the finite value of v increase exponentially inside the metal and therefore should cancel themselves out. This condition gives the relation, which is valid at $-\pi < \varphi < 0$:

$$A_\varphi = \frac{k_x V}{\sin \varphi} \left[\frac{\phi_0}{\gamma_\varphi + i p_0} \right.$$

$$\left. - \int_{-\pi}^{\pi} \frac{d\varphi'}{2\pi} \frac{A_{\varphi'}}{(p_0^2 + \gamma_{\varphi'}^2)(\gamma_\varphi - \gamma_{\varphi'})} \right]. \quad (31)$$

This relation closes the set of equations necessary for the determination of the field distribution inside the metal. Combination of Eq. (24) with the boundary condition for A_φ results in an integral equation for A_φ in the domain $0 < \varphi < \pi$

$$\hat{L} A_\varphi + \frac{k_x V}{\sin \varphi} \int_0^\pi \frac{d\varphi'}{2\pi} \frac{1}{p_0^2 + \gamma_{\varphi'}^2} \left(\frac{A_{\varphi'}}{\gamma_\varphi + \gamma_{\varphi'}} + \frac{\hat{L} A_{\varphi'}}{\gamma_\varphi - \gamma_{\varphi'}} \right)$$

$$= \frac{k_x V}{\sin \varphi} \frac{\phi_0}{\gamma_\varphi - i p_0}, \quad (32)$$

where ϕ_0 is taken from Eq. (30), and $\hat{L}$ is the operator of diffusive reflection

$$\hat{L} A_\varphi = (1 - q) A_\varphi + \frac{q}{2} \int_0^\pi A_\varphi \sin \varphi d\varphi. \quad (33)$$

Once solved, Eq. (32) can be used to find the ratio ϕ'/ϕ at the metal surface, which is our goal in solving self-consistently for the field distribution inside and outside the metal.

Let us evaluate p_0 and $S(p)$. Consider separately the cases $V < 1$ and $V > 1$.

Expression (25) can be reduced to an integral along the unit circle $z = \exp(i\varphi)$ in the complex plane z,

$$S(p) = 1 + \oint \frac{dz}{2\pi i} \frac{2k_x V}{(k_x - p)z^2 - 2(k_x V + i0)z + k_x + p}. \quad (34)$$

At $V < 1$, the poles of the denominator in the integrand,

$$z_{1,2} = (k_x V + i\text{v} \pm \sqrt{(k_x V + i\text{v})^2 + p^2 - k_x^2})/(k_x - p),$$

lie either inside or outside the unit circle and therefore the integral is equal to zero (except for Re $p = 0$). We therefore have

$$S(p) = 1 + \frac{i}{(1 - V^2)^{1/2}} \frac{\delta(p)}{\delta(0)}, \quad V < 1. \quad (35)$$

The poles of the denominator of the integrand in Eq. (24) are $\pm p_0$, where

$$p_0 = \sqrt{1 + \mathbf{k}^2}. \quad (36)$$

Typical values of $|\mathbf{k}|$ are of the order of the inverse distance from the tip to the metal surface, which is assumed to be much larger than the Thomas-Fermi screening length λ_{TF}, and therefore $|\mathbf{k}|$ is much smaller than the characteristic momentum κ_{TF} [$\kappa_{TF} = (4\pi)^{1/2}$ in dimensionless units].

In the case $V > 1$, the behavior of $S(p)$ is quite different. At the real axis $S(p)$ is

$$S(p) = 1 - \frac{|k_x| V}{[p^2 + k_x^2(V^2 - 1)]^{1/2}}, \quad V > 1. \quad (37)$$

This function has branching points at the imaginary axis $p = \pm i q_0$, where $q_0 = k_x(V^2 s - 1)^{1/2}$. At the real axis, the denominator of the integrand of Eq. (24) has two pairs of poles $\pm p_1$ and $\pm p_2$. For example, in the case $k_y = 0$ the equation for the poles

$$p^2 = k_x^2 + 1 - \frac{|k_x| V}{[p^2 + k_x^2(V^2 - 1)]^{1/2}} \quad (38)$$

gives two values for $p > 0$:

$$p = p_1 = k_x, \quad \text{and} \quad p = p_2 = 1 - \frac{1}{2} k_x V, |k_x| \ll 1. \quad (39)$$

The first pole signals that the electric field distribution breaks the Thomas–Fermi barrier and penetrates into a metal to distances $|k_x|^{-1}$ of the order of the tip-to-surface distance, which is much larger than λ_{TF}. This, however, is not an equilibrium charge distribution.

With the two poles $p_{1,2}$, the potential $\phi(z)$, which is derived from Eq. (24) by integration along the contour shown in Fig. 3b has two exponentially increasing terms $\exp(p_1 z)$ and $\exp(p_2 z)$, and also the nonsingular terms $\exp(-p_1 z)$, $\exp(-p_2 z)$, $\exp(\pm i q_0 z)$, and $\exp(-i\gamma_\varphi z)$, where $q_0 = k_x(V^2 - 1)^{1/2}$. Elimination of singular contributions results in the number of equations which is larger than the number of variables. This means that the only admissible solution in this case is a trivial one, $A_\varphi = 0$, $u_\varphi = 0$, $\phi_0 = 0$. We thus find that $\phi(0) = \phi'(0) = 0$, which is inconsistent with the equation for the potential value outside the metal [Eq. (26)]. In fact, if $\phi(0) = \phi'(0) = 0$ (note that these quantities are functions of $\mathbf{k}$) in some domain of $\mathbf{k}$, then in this same domain the potential will become infinite at large z. We conclude, therefore, that there is no regular solution for $\phi(z)$ if the velocity of the tip V is greater than the Fermi velocity.

This means that the solution $\phi(z)$ does not exist *in the linear approximation* in χ_φ, and higher-order terms in the electron distribution should be taken into account on the right side of the Poisson equation (17).

4. DYNAMICAL SCREENING IN A THREE-DIMENSIONAL METAL

It can be assumed that the instability of the steady-state motion of a surface sheet at high velocity found in the previous section is specific to the two-dimensional Fermi surface. We shall see, however, that similar property is also seen in a three-dimensional metal.

In a metal with a spherical Fermi surface, an equation for the angular-dependent part of the electron distribution analogous to (21) is

$$\left(i\gamma_\varphi + \frac{d}{dz} \right) u_\varphi = \frac{ik_x V}{\sin \theta \sin \varphi} \phi, \quad (40)$$

where θ is a polar angle of the electron momentum at the Fermi surface, and γ_φ is a quantity

$$\gamma_\varphi = \frac{k_x(\sin \theta \cos \varphi - V) + k_y \cos \theta - i\text{v}}{\sin \theta \sin \varphi}. \quad (41)$$

The boundary condition of diffuse scattering at $z = 0$ and $0 < \varphi < \pi$ is
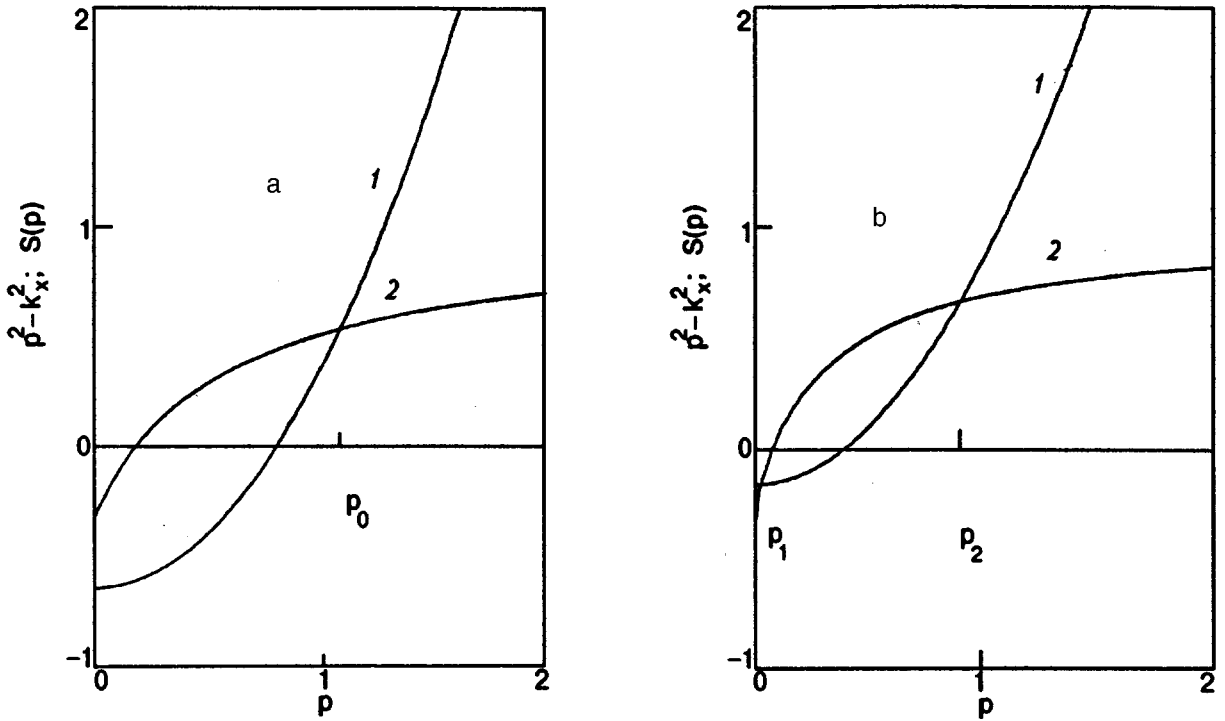
FIG. 4. Poles of the denominator in Eq. (44) at $k_y = 0$ and $V = 0.9$. (a) large value of k_x ($k_x = 0.8$) corresponding to one pole p_0; (b) small k_x ($k_x = 0.4$, two poles $-p_1, p_2$). Curve 1—the dependence $p^2 - k_x^2$, curve 2—the dependence $S(p)$.

$$u_{-\varphi} = (1-q)u_\varphi + \frac{q}{\pi} \int_0^\pi \sin\theta\, d\theta \int_0^\pi d\varphi\, u_\varphi \sin\theta \sin\varphi. \tag{42}$$

The dynamical screening is represented by a three-dimensional S-function analogous to (25)

$$S = 1 + \int \frac{d\Omega}{4\pi}$$

$$\times \frac{k_x V}{k_x(\sin\theta \cos\varphi - V) + k_y \cos\theta - ip \sin\theta \sin\varphi - iv}, \tag{43}$$

where $d\Omega = \sin\theta\, d\theta\, d\varphi$, which gives the potential distribution

$$\phi(z) = \frac{1}{2\pi i} \int_{a-i\infty}^{a+i\infty} dp\, e^{pz}$$

$$\times \frac{\phi(0) + p\phi'(0) + \int (d\Omega/4\pi)[A_\varphi/(p+i\gamma_\varphi)]}{p^2 - \mathbf{k}^2 - S(p)}. \tag{44}$$

Evaluation of an integral (43) at $k_y = 0$ and $V < 1$ gives

$$S =$$

$$\begin{cases} 1 - \dfrac{V}{(1-p^2/k_x^2)^{1/2}} \ln \dfrac{V + (1-p^2/k_x^2)^{1/2}}{V_p/k_x + (1-V^2)^{1/2}(1-p^2/k_x^2)^{1/2}}, \\ \qquad p < |k_x|, \\ 1 - \dfrac{V}{(p^2/k_x^2 - 1)^{1/2}}\left[\arcsin \dfrac{(p^2/k_x^2 - 1)^{1/2}}{(p^2/k_x^2 - 1 + V^2)^{1/2}} \right. \\ \qquad \left. - \arcsin \dfrac{(1-V^2)^{1/2}(p^2/k_x - 1)^{1/2}}{(p^2/k_x^2 - 1 + V^2)^{1/2}}, \quad p > |k_x|. \right. \end{cases} \tag{45}$$

At $p = +0$, the function (43) is

$$S(p,V,\eta) = 1 - \frac{V}{2} \int_{-1}^1 dx\, \frac{\operatorname{sgn}(V - \eta x)}{((V-\eta x)^2 - 1 + x^2)^{1/2}}\, \theta((V - \eta x)^2 - 1 + x^2), \tag{46}$$

where $\eta = k_y/k_x$. Recall that at $p \to \infty\, S$ equals 1, whereas at $p = 0$ it is smaller than unity and becomes negative at large V.

Looking for the poles of an integrand of Eq. (44) with real axis,

$$p^2 = k_x^2 + k_y^2 + S(p,V,\eta), \tag{47}$$

we note that when $S_0 = S(p \to +0)$ is negative, there always will be two roots $p_1 > 0$ and $p_2 > 0$ of (47) in the certain domain of $\mathbf{k}$. This is seen from the graphical solution of Eq. (47), as shown in Fig. 4. Therefore, in this domain of

wave vectors there will not exist any regular solution for the electric field, and therefore there is a crisis of the Thomas-Fermi screening. Let us specify the domain of the latter.

Evaluation of $S_0(V,\eta)$ gives

S_0

$$
= \begin{cases}
1 - \dfrac{V}{2(1+\eta^2)^{1/2}} \ln\left|\dfrac{1-\alpha+((1-\alpha)^2-\beta^2)^{1/2}}{1+\alpha-((1+\alpha)^2-\beta^2)^{1/2}}\right|, \\
\quad V > \eta \\[2mm]
1 - \dfrac{V}{2(1+\eta^2)^{1/2}} \ln \\[2mm]
\quad \times \dfrac{\beta^2}{[1+\alpha-((1+\alpha)^2-\beta^2)^{1/2}][1-\alpha+((1-\alpha)^2-\beta^2)^{1/2}]}, \\
\quad V < \eta,
\end{cases}
$$
(48)

where

$$
\alpha = V\frac{\eta}{1+\eta^2}, \quad \beta^2 = \frac{1+\eta^2-V^2}{(1+\eta^2)^2}, \quad \eta = \frac{k_y}{k_x}.
$$
(49)

The function $S_0(V,\eta)$ for different η is shown in Fig. 5. The smallest value of V at which S_0 is negative is achieved at $\eta = 0$, where

$$
S_0(V,0) = 1 - \frac{V}{2}\ln\left|\frac{1+V}{1-V}\right|.
$$
(50)

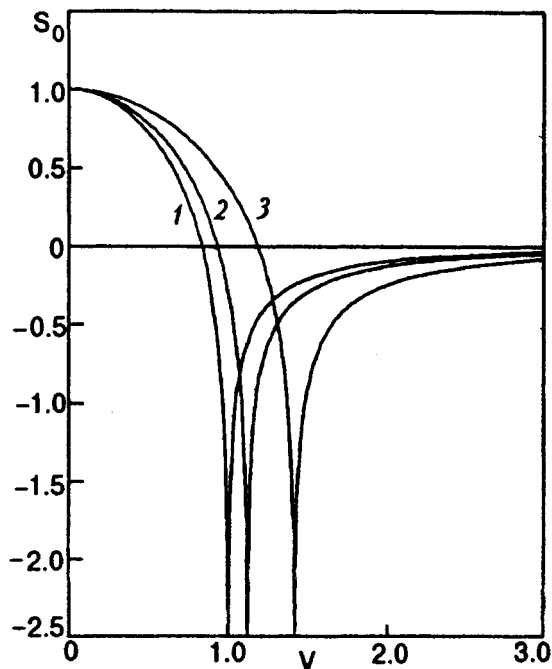This expression is negative at $V > V_c$ where $V_c = 0.8335$ is the solution of an equation

FIG. 5. Dependence of S_0 on V. Curves *1*, *2*, and *3* correspond to $\eta = 0$, 0.5, and 1.0, respectively.

$$
V_c = \tanh\frac{1}{V_c}.
$$
(51)

Therefore, the instability of laminar flow occurs in a three-dimensional metal at a velocity slightly smaller than the Fermi velocity. Near the critical value of V, the instability takes place at a small k_y-to-k_x ratio. The smaller is $|k_y|$, the stronger is the distortion from the unperturbed $\phi(z)$ distribution. In effect, the large-k_y Fourier components of the potential are virtually unaffected, whereas small the components are depressed. This implies a change of the potential and of the charge distribution inside a metal, which is shown schematically in Fig. 6. The shape of the image of (symmetrical) external charge in the surface sheet is compressed in the direction perpendicular to the direction of motion and is elongated in the opposite direction. At the same time, the penetration depth of electric field inside the metal increases. Near the critical velocity, the characteristic compression is

$$
\Delta z - \frac{\lambda_{TF}}{(V_c - V)^{1/2}}.
$$
(52)

The effect of potential redistribution strongly manifests itself if the distance between the tip and the metal is of the order of a few unperturbed Thomas–Fermi screening lengths.

Let us analyze the analytical properties of S in the complex plane p. $S(p)$ has a singularity along the imaginary axis $p = iq$, which is in effect a manifestation of the existence of the branching points of two-dimensional S [Eq. (37)]. In a three-dimensional metal, maximal velocity of electron motion parallel to the metal surface $V_\| = \sin\theta$ may be smaller than 1 at $V < 1$ in some range of θ. The function $S(iq)$ attains different values when the imaginary axis is approached from the left and from the right, and remains analytical in the subspaces Re $p < 0$ and Re $p > 0$. The values of $S(p)$ to the left and to the right of the imaginary axis are

$$
S_\pm(iq) = 1 + \frac{V}{2}\int_0^\pi d\theta R_\pm(v, q/k_x),
$$
(53)

$$
v = \frac{V - \eta\cos\theta}{\sin\theta},
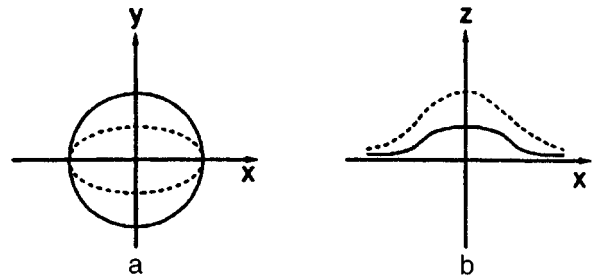$$

where $\eta = k_y/k_x$, and

FIG. 6. Schematic diagram of the charge penetration inside a metal along the metal surface (a) and along the cross-sectional plane (b). Solid lines correspond to $V < V_c$, and dotted lines correspond to $V > V_c$.
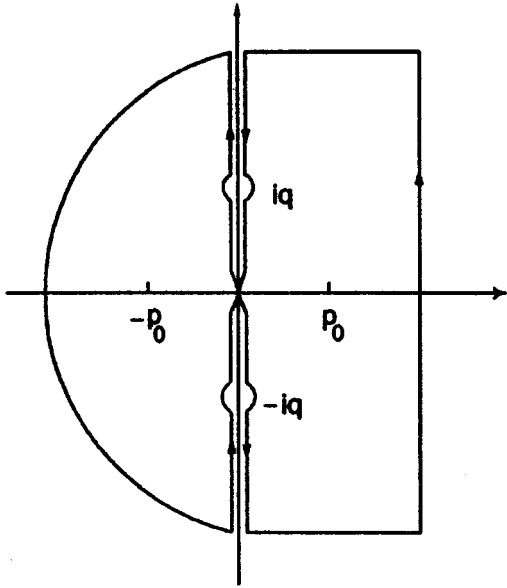
FIG. 7. Contour of integration for the calculation of the potential $\phi(z)$ [Eq. (24)] in a three-dimensional metal.

$$R_{\pm}(v) = \begin{cases} 0, & |v| < 1 \\ -\dfrac{\mathrm{sgn}(v)}{(v^2 - 1 - x^2)^{1/2}}, & |v| > 1, |x| < \sqrt{v^2 - 1} \\ \pm\dfrac{i\,\mathrm{sgn}(vx)}{(x^2 - v^2 + 1)^{1/2}}, & |v| > 1, |x| > \sqrt{v^2 - 1} \end{cases} \tag{54}$$

where $x = q/k_x$.

We can now calculate from (24) the potential $\phi(z)$. Integrating along the path shown in Fig. 7, we obtain

$$\phi(z) = \phi_0 \exp(-p_0 z) + \int \frac{d\Omega}{4\pi} Z_\varphi \exp(-i\gamma_\varphi z)$$

$$+ \int_{-\infty}^{\infty} \frac{dq}{2\pi} X_q \exp(iqz), \tag{55}$$

where, as follows from the requirement that $\phi(z)$ vanish at $z \to \infty$, a relation between $\phi(0)$ and $\phi'(0)$ is

$$\phi'(0) = -p_0 \phi(0) - \int \frac{d\Omega}{4\pi} \frac{A_\varphi}{p_0 + i\gamma_\varphi}. \tag{56}$$

The coefficients ϕ_0, Z_φ, and X_q in the expression (55) are

$$\phi_0 = \frac{2p_0}{D'(p_0)} \left[\phi(0) + \int \frac{d\Omega}{4\pi} \frac{A_\varphi}{p_0^2 + \gamma_\varphi^2} \right], \tag{57}$$

$$Z_\varphi = \frac{1}{2} \left[\frac{1}{D_+(i\gamma_\varphi)} + \frac{1}{D_-(i\gamma_\varphi)} \right] A_\varphi, \tag{58}$$

$$X_q = \left(\frac{1}{D_+(i\gamma_\varphi)} - \frac{1}{D_-(i\gamma_\varphi)} \right) \left[(iq - p_0)\phi(0) \right.$$

$$\left. - \int \frac{d\Omega}{4\pi} \frac{q + ip_0}{(p_0 + i\gamma_\varphi)(q + \gamma_\varphi)} \right] A_\varphi, \tag{59}$$

where $D(p) = p^2 - \mathbf{k}^2 - S(p)$ is the denominator of an integrand of Eq. (24), which is appropriate for the $3d$ case.

Proceeding further in the same manner as in Sec. 2, we calculate with the help of Eq. (55) the function u_φ

$$u_\varphi = A_\varphi \exp(-i\gamma_\varphi z) + \frac{k_x V}{\sin\theta \sin\varphi} \left[\frac{\phi_0}{\gamma_\varphi + ip_0} \right.$$

$$\times (\exp(-p_0 z) - \exp(-i\gamma_\varphi z))$$

$$+ \int \frac{d\Omega'}{4\pi} Z_{\varphi'} \frac{\exp(-i\gamma_{\varphi'} z) - \exp(-i\gamma_\varphi z)}{\gamma_{\varphi'} - \gamma_{\varphi'}}$$

$$\left. + \int_{-\infty}^{\infty} \frac{dq}{2\pi} X_q \frac{\exp(iqz) - \exp(-i\gamma_\varphi z)}{q + \gamma_\varphi} \right],$$

where A_φ is an arbitrary constant. Requiring that the terms proportional to $\exp(-i\gamma_\varphi z)$ cancel each other out at $\varphi > 0$, and using, at $\varphi < 0$, the boundary condition (42), we obtain

$$A_\varphi = \frac{k_x V}{\sin\theta \sin\varphi} \left[\frac{\phi_0}{\gamma_\varphi + ip_0} + \int \frac{d\Omega'}{4\pi} \frac{Z_{\varphi'}}{\gamma_\varphi - \gamma_{\varphi'}} \right.$$

$$\left. + \int_{-\infty}^{\infty} \frac{X_q}{q + \gamma_\varphi} \right] \tag{60}$$

at $-\pi < \varphi < 0$, and

$$A_{-\varphi} = (1 - q)A_\varphi + \frac{q}{\pi} \int_0^{\pi} \sin\theta\, d\theta \int_0^{\pi} d\varphi A_\varphi \sin\theta \sin\varphi$$

$$= \hat{L}A_\varphi \tag{61}$$

at $0 < \varphi < \pi$, where $\hat{L}$ is a three-dimensional operator of a diffuse reflection, which can be written in the form

$$\hat{L} = 1 - q + \hat{q}, \tag{62}$$

where $\hat{q}$ is an operator

$$\hat{q}A_\varphi = \frac{q}{\pi} \int d\Omega_+ A_\varphi \sin\theta \sin\varphi \tag{63}$$

($d\Omega_+$ means a solid-angle integration with a positive φ). It follows also that the inverse operator is

$$\hat{L}^{-1} = \frac{1 - \hat{q}}{1 - q}. \tag{64}$$

Combining Eqs. (57) and (60), we obtain an integral equation for A_φ in the domain $0 < \varphi < \pi$

$$\hat{L}A_\varphi - \frac{k_x V}{\sin\theta \sin\varphi} \left\{ \int \frac{d\Omega'_+}{8\pi} \left(\frac{A_{\varphi'}}{\gamma_\varphi + \gamma_{\varphi'}} + \frac{\hat{L}A_{\varphi'}}{\gamma_\varphi - \gamma_{\varphi'}} \right) \right.$$

$$\times \left(\frac{1}{D_+(i\gamma_\varphi)} + \frac{1}{D_-(i\gamma_\varphi)} \right)$$

$$- \int_{-\infty}^{\infty} \frac{dq}{2\pi} \frac{q + ip_0}{q - \gamma_\varphi} \int \frac{d\Omega'_+}{4\pi} \left[\frac{A_{\varphi'}}{(p_0 + i\gamma_{\varphi'})(q + \gamma_{\varphi'})} \right.$$

$$\left. + \hat{L} \frac{A_{\varphi'}}{(p_0 - i\gamma_{\varphi'})(q - \gamma_{\varphi'})} \right] \right\} = \frac{k_x V}{\sin\theta \sin\varphi} \left[\frac{\phi_0}{\gamma_\varphi - ip_0} \right.$$

$$\left. + \phi(0) \int_{-\infty}^{\infty} \frac{dq}{2\pi} \frac{iq - p_0}{\gamma_\varphi - iq} \left(\frac{1}{D_+(iq)} - \frac{1}{D_-(iq)} \right) \right], \tag{65}$$

where $D_\pm(iq)$ is a value of $D(p)$ to the left/right of an imaginary axis $p = iq \pm 0$.

Equation (66) is valid at $V < V_c$ when the linear regime of the surface sheet motion is realized. In this case the solution for A_φ, together with Eq. (56), permits determination of the effective boundary condition, i.e., the value of the ratio ϕ'/ϕ at $z = 0$.

5. ENERGY DISSIPATION IN A MOVING SURFACE SHEET

In this section we will consider the energy losses in a surface sheet as a result of its interaction with the external charge that pulls the sheet. The force acting on the sheet is

$$\mathbf{F} = \mathbf{E}\rho, \tag{66}$$

where the surface charge density ρ is determined as $(1/4\pi) \times (\partial\phi/\partial z)_{z=0}$, and $E_x = -(\partial\phi/\partial z)_{z=0}$. The product $F_x V = W$ gives the power dissipated in a metal. Integrating with respect to space coordinates x, y and performing the Fourier transformation, we obtain

$$W = \frac{V}{4\pi} \int \frac{d^2 k}{(2\pi)^2} k_x p_0(\mathbf{k}) |\phi_\mathbf{k}(0)|^2 \, \mathrm{Im}\, \zeta(\mathbf{k}), \tag{67}$$

where $\mathbf{k} = (k_x, k_y)$. The quantity $\zeta(\mathbf{k})$ is the coefficient in the boundary condition at the metal surface

$$\phi'(0) = -p_0(1 + \zeta(\mathbf{k}))\phi(0) \tag{68}$$

[we dropped the index $\mathbf{k}$ in $\phi_\mathbf{k}(0)$ and $\phi'_\mathbf{k}(0)$]. Using Eq. (56), we obtain

$$\zeta(\mathbf{k}) = \frac{1}{p_0} \int \frac{d\Omega_+}{4\pi} \left(\frac{A_\varphi}{p_0 + i\gamma_\varphi} + \frac{\hat{L}A_\varphi}{p_0 - i\gamma_\varphi} \right) / \phi(0), \tag{69}$$

where A_φ is found from the integral equation (66).

In the case of absence of a y-dependence of the potential (for example, for an infinite rod moving parallel to the surface), an expression for the rate of the energy dissipation per unit length is

$$W = \frac{V}{4\pi} \int \frac{dk_x}{2\pi} k_x p_0(k_x) |\phi_{k_x}(0)|^2 \, \mathrm{Im}\, \zeta(k_x), \tag{70}$$

where $\zeta(k_x)$ is found by setting $k_y = 0$ in (70). In the case of small $|\mathbf{k}|$, Eq. (66) can be solved iteratively in k_x:

$$A_\varphi = A_\varphi^0 + k_x A_\varphi^1 + \dots \, . \tag{71}$$

In the lowest approximation we obtain

$$\hat{L}A_\varphi = \frac{k_x V}{\sin\theta \sin\varphi} \left[\frac{1}{\gamma_\varphi - ip_0} \right.$$

$$\left. + \int_{-\infty}^{\infty} \frac{dq}{2\pi} \frac{p_0 - iq}{q - \gamma_\varphi} \left(\frac{1}{D_+(iq)} - \frac{1}{D_-(iq)} \right) \right] \phi(0), \tag{72}$$

where γ_φ is determined in (41) with $v = +0$. Typical values of q are on the order of k_x, i.e., much smaller than the inverse Thomas–Fermi screening length κ_{TF} (in the dimensionless units we have $|k_x| \ll 1$). We introduce the function

$$R(q) = \frac{1}{2i} \left(\frac{1}{D_+(iq)} - \frac{1}{D_-(iq)} \right), \tag{73}$$

where

$$D_\pm(iq) = -\mathbf{k}^2 - q^2 - S_\pm(iq); \quad S_\pm(iq) = S(iq \pm 0). \tag{74}$$

Setting $S_\pm(iq) = S_1(q) \pm iS_2(q)$, we obtain from (53)

$$S_1(q) = 1 - \frac{V}{2} \int_{-1}^{1} dx \, \frac{\mathrm{sgn}(V - \eta x)}{(\Lambda(x) - q^2/k_x^2)^{1/2}} \, \theta(\Lambda(x)$$

$$- q^2/k_x^2), \tag{75}$$

$$S_2(q) = \frac{V}{2} \int_{-1}^{1} dx \, \frac{\theta(\Lambda(x))\mathrm{sgn}(V - \eta x)}{(q^2/k_x^2 - \Lambda(x))^{1/2}} \, \theta\left(\frac{q^2}{k_x^2} \right.$$

$$\left. - \Lambda(x) \right) \mathrm{sgn}\left(\frac{q}{k_x} \right), \tag{76}$$

where $x = \cos\theta$, and $\Lambda(x) = (V - \eta x)^2 + x^2 - 1$. At $\eta = 0$, a direct integration gives the following expression for the positive values of q and k_x:

$$S_1(q) = \begin{cases} 1 - V \ln \dfrac{1 + (V^2 - q^2/k_x^2)^{1/2}}{(1 - V^2 + q^2/k_x^2)^{1/2}}, & q/k_x < V, \\[3mm] 1, & q/k_x > V \end{cases} \tag{77}$$

and

$$S_2(q) = \begin{cases} V\left(\dfrac{\pi}{2} - \arcsin \dfrac{(1 - V^2)^{1/2}}{(1 - V^2 + q^2/k_x^2)^{1/2}} \right), & q/k_x < V \\[3mm] V\left(\arcsin \dfrac{1}{(1 - V^2 + q^2/k_x^2)^{1/2}} \right. \\[3mm] \left. - \arcsin \dfrac{(1 - V^2)^{1/2}}{(1 - V^2 + q^2/k_x^2)^{1/2}}, \right. & q/k_x > V. \end{cases} \tag{78}$$

The dependences $S_{1,2}(q)$ at various V and η are shown in Fig. 8. An approximate value of $R(q)$ at $|k_{x,y}| \ll 1$ is

$$R(q) \approx \frac{S_2(q)}{S_1^2(q) + S_2^2(q)}. \tag{79}$$

$R(q)$ is an odd function of q, which vanishes linearly at small $|q/k_x|$ and which behaves at $1/q$ at $|q| \gg |k_x|$.

The two terms on the right side of Eq. (73) represent the contributions to the dissipation emerging from the main pole $p = p_0$ in the complex plane p, and from the branching point along the imaginary axis. The contributions to $\zeta(\mathbf{k})$, $\zeta_1(\mathbf{k})$, and $\zeta_2(\mathbf{k})$ prove to be of the same order of magnitude. Substitution of Eq. (73) into Eq. (70) at $p_0 \approx 1$ and small k_x [see Eq. (36)] gives

$$\mathrm{Im}\, \zeta_1(\mathbf{k}) = \frac{k_x V}{1 - q} \int \frac{d\Omega_+}{4\pi} \frac{2 - q - q\gamma_\varphi^2}{(1 + \gamma_\varphi^2)^2 \sin\theta \sin\varphi}$$

$$- \frac{k_x V}{1 - q} \int \frac{d\Omega_+}{4\pi} \frac{1}{1 + \gamma_\varphi^2} \int \frac{d\Omega_+}{\pi} \frac{q}{1 + \gamma_\varphi^2}$$

$$+ \frac{k_x V}{1 - q} \int \frac{d\Omega_+}{4\pi} \frac{\gamma_\varphi}{1 + \gamma_\varphi^2} \int \frac{d\Omega_+}{\pi} \frac{q\gamma_\varphi}{1 + \gamma_\varphi^2}, \tag{80}$$

FIG. 9. Dependence of μ on V. Curves *1*, *2*, *3*, and *4* correspond to $\eta = 0$, 0.2, 0.4 and 0.6.
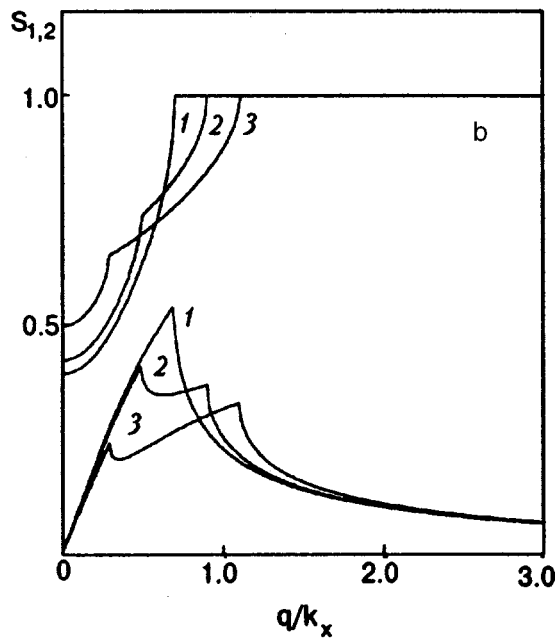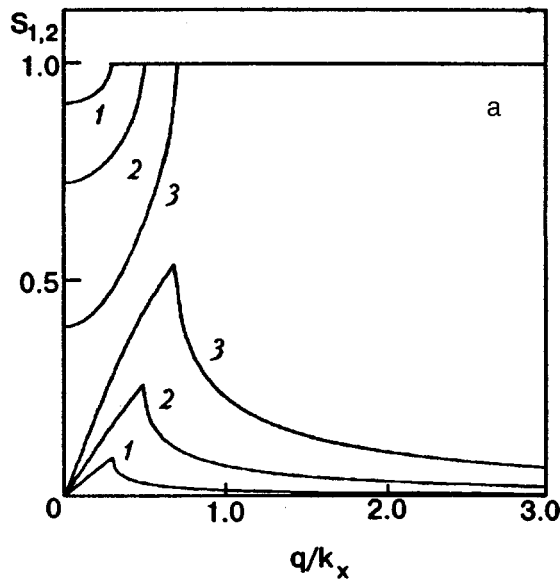
FIG. 8. Dependences of S_1 (upper curves) and S_2 (lower curves) on q. (a) $\eta = 0$. Curves *1*, *2*, and *3* correspond to $V = 0.3$, 0.5, and 0.7; (b) $V = 0.7$. Curves *1*, *2*, and *3* correspond to $\eta = 0$, 0.2, and 0.4.

$$\mathrm{Im}\, \zeta_2(\mathbf{k}) = \frac{k_x V}{1-q} \int \frac{d\Omega_+}{4\pi}$$

$$\times \frac{(2-q)R_0(q) - q\gamma_\varphi R_1(\gamma_\varphi) - \gamma_\varphi R(\gamma_\varphi)}{(1+\gamma_\varphi^2)\sin\theta \sin\varphi}$$

$$+ \frac{k_x V}{1-q} \int \frac{d\Omega_+}{4\pi} \frac{1}{1+\gamma_\varphi^2} \int \frac{d\Omega_+}{\pi}$$

$$\times \left[-qR_0(\gamma_\varphi) + \frac{q}{2}\gamma_\varphi R(\gamma_\varphi) \right]$$

$$+ \frac{k_x V}{1-q} \int \frac{d\Omega_+}{4\pi} \frac{\gamma_\varphi}{1+\gamma_\varphi^2} \int \frac{d\Omega_+}{\pi}$$

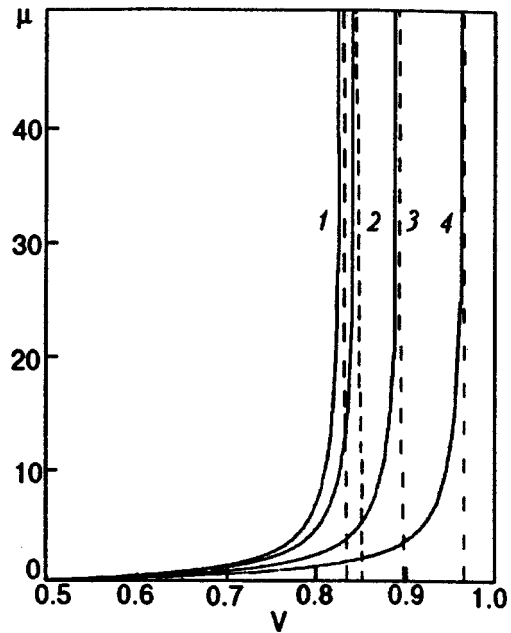$$\times \left[qR_1(\gamma_\varphi) + \frac{q}{2} R(\gamma_\varphi) \right], \tag{81}$$

where

$$R_n(x) = \frac{1}{\pi}\,\mathrm{V.p.}\!\int_{-\infty}^{\infty} \frac{R(q)q^n}{q-x}\, dq. \tag{82}$$

Inspection of integrals in Eqs. (81) and (82) shows that at $k_x \to 0 \int d\Omega_+ /(1+\gamma_\varphi^2)$ takes a constant value, whereas $\int d\Omega_+ \gamma_\varphi/(1+\gamma_\varphi^2)$ behaves as $k_x \ln(1/k_x)$. This means that the last term in Eq. (82) can be ignored at small value of $\mathbf{k}$. The second term is of the order of k_x, whereas the first term behaves as $k_x \ln(1/k_x)$.

For orientation, we assume that $R(q)$ is $Cq/(q^2 + a^2)$, which gives from Eq. (81) $R_0(q) = Ca/(q^2 + a^2)$ and $R_1(q) = -Caq/(q^2 + a^2)$. One can then evaluate integrals in (82). It appears that the last term in this expression is of the same order of magnitude as the corresponding term in Eq. (81); therefore, it can be ignored. The second term in Eq. (82) is proportional to $k_x \ln(1/k_x)$. Evaluation of the leading (logarithmic) term in ζ_2 requires the knowledge of the functions $R_{0,1}$ at $q = 0$. After some algebra, we obtain

$$\mathrm{Im}\,\zeta(\mathbf{k}) = k_x V\, \frac{1-q/2}{1-q}\left[\ln \frac{C_1}{k_x} + \mu \ln \frac{C_2}{k_x} \right], \tag{83}$$

where $C_{1,2} \sim 1$ are complex functions of V, η, and q and μ is a quantity

$$\mu = \frac{2}{\pi} \int_0^{\infty} \frac{R(x)}{x}\, dx, \tag{84}$$

which is shown for different values V and η in Fig. 9.

Since ζ is a small quantity ($|\zeta| \ll 1$), the field outside the metal is almost equal to its value calculated for an ideally
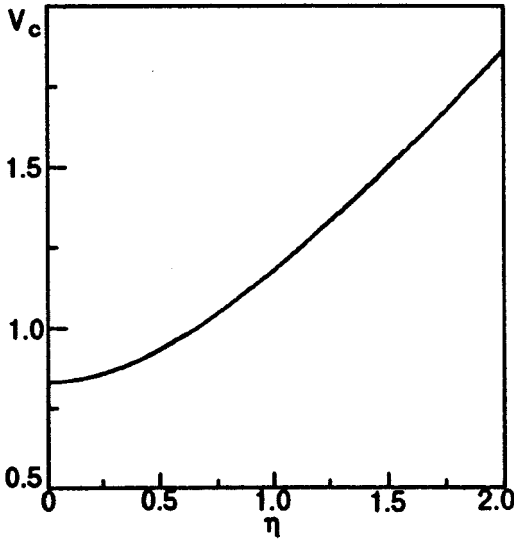
FIG. 10. Dependence of V_c on η.

reflecting metallic surface ($\lambda_{TF} = 0$). The power dissipated due to the tip motion becomes (in the dimensionless units)

$$W \simeq \frac{V}{4\pi} \int \frac{d^2k}{(2\pi)^2} k_x \frac{|\phi'_{\mathbf{k}}(0)|^2}{p_0(\mathbf{k})} \operatorname{Im} \zeta(\mathbf{k}). \qquad (85)$$

In the dimensional units, the dissipated power is

$$W = \frac{V^2}{4\pi e^2 N(\varepsilon_F) V_F} \frac{1 - q/2}{1 - q}$$

$$\times \int \frac{d^2k}{(2\pi)^2} k_x^2 |\phi'_{\mathbf{k}}(0)|^2$$

$$\times \left[\ln \frac{\widetilde{C}_1}{|k_x|\lambda_{TF}} + \mu \ln \frac{\widetilde{C}_2}{|k_x|\lambda_{TF}} \right]. \qquad (86)$$

Assuming that the tip is a point charge Q, we obtain an estimate of W valid at $V \ll V_c$

$$W_1 \simeq \frac{V^2 Q^2 \lambda_{TF}^2}{V_F d^4} \frac{1 - q/2}{1 - q}, \qquad (87)$$

where d is a distance between the tip and the metal surface. At small $d \simeq \lambda_{TF}$, this expression matches in order of magnitude the loss of a charged particle that moves inside a metal.

For a charged rod with a charge Q per unit length, an estimate of the loss per unit length is

$$W_2 \sim \frac{V^2 Q^2 \lambda_{TF}^2}{V_F d^3} \frac{1 - q/2}{1 - q}. \qquad (88)$$

The quantity μ in (84) increases dramatically at V near the critical velocity V_c. At a value of V larger than V_c, the linear regime of the surface screening breaks down. An asymptotic behavior of μ near V_c

$$\mu \simeq \frac{1}{|\mathbf{k}|^2 + S_0(V,\eta)}, \qquad |\mathbf{k}| \ll 1, \qquad (89)$$

where $S_0 \to 0$ in the limit $V \to V_c(\eta)$. The function $V_c(\eta)$ is shown in Fig. 10.

Sharp resonances of μ versus V occur at a fixed values of the momenta k_x and k_y. Dissipated power W can be determined by integration of μ in Eq. (85) with respect to $\mathbf{k}$. Whether the dissipated power W vs V will have similar sharp resonances depends on the actual potential distribution at the metal surface.

Let us consider as an example a point charge Q at a height h above the metal surface giving at $\lambda \to 0$

$$\phi(\mathbf{r}) = Q \left(\frac{1}{(x^2 + y^2 + (z - h)^2)^{1/2}} \right.$$

$$\left. - \frac{1}{(x^2 + y^2 + (z + h)^2)^{1/2}} \right), \qquad (90)$$

from which we have

$$\phi'_{\mathbf{k}}(0) = 4\pi Q \exp(-2|\mathbf{k}|h) \qquad (91)$$

and an infinite thin rod with the linear charge density Q, for which

$$\phi(\mathbf{r}) = \frac{Q}{2} \ln \frac{x^2 + (z - h)^2}{x^2 + (z + h)^2} \qquad (92)$$

and, correspondingly

$$\phi'_{\mathbf{k}_x}(0) = 2\pi Q \exp(-2|k_x|h). \qquad (93)$$

In the second case we then obtain

$$W \sim \frac{W_2(V)}{S_0(V,0) + 1/4h^2}, \qquad h \gg 1, \qquad (94)$$

and in the first case

$$W \sim W_1(V) \int_0^\infty \frac{d\eta}{(1 + \eta^2)^2} \frac{1}{S_0(V,\eta) + (1 + \eta^2)/4h^2}. \qquad (95)$$

The dependences (95) and (96) are shown in Fig. 11.

6. DISCUSSION

Dynamical interaction of a moving charge with a metal surface reveals singularities in the dissipated power as a function of the velocity of motion V. Depending on the topology of the Fermi surface, the maximum of power dissipation in the surface sheet occurs either at the Fermi velocity or slightly below it. At the same value of V, the electric field begins penetrating the metal to a depth much greater than the Thomas–Fermi length, thus breaking the Thomas–Fermi screening barrier.

Crucial for the observation of such effects is the possibility of realization of fast motion of a surface charge. This can be achieved by propagating charged particles or small charged bodies above and near the metal surface. The other possibility may be in creating an electronically driven motion of a surface charge parallel to the metal surface. Concerning the latter, we envisage a setup with an array of equally spaced metallic electrodes near the bulk metal (Fig. 12a) biased periodically in time with the short electric pulses of fixed polarity. This will create maxima in the surface charge distribution in a metal moving between subsequent locations in the metal surface with an average velocity $\overline{V} = \Delta x / \Delta t$ (Δx is the distance between electrodes, and Δt is
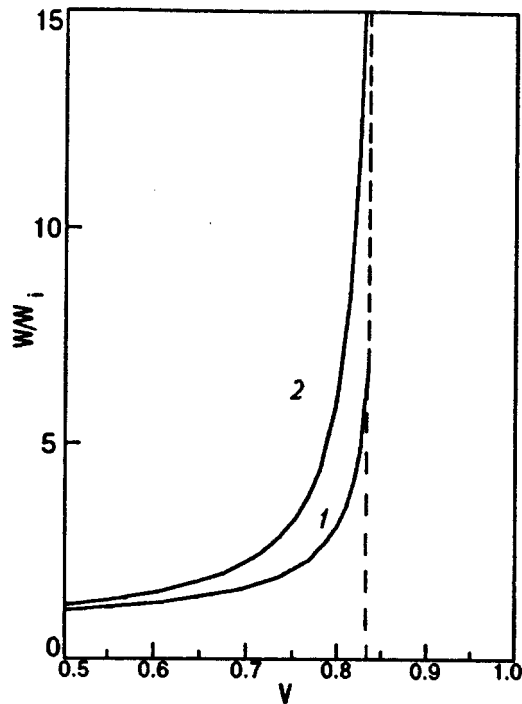
FIG. 11. Normalized dissipation W/W_1 (curve *1*) and W/W_2 (curve *2*) as a function of the velocity V at $h = 2.5$.

the interval between pulses). The velocity of the order of the Fermi velocity $V_F \sim 10^8 - 10^6$ cm/s can be easily obtained with the corresponding choice of Δx and Δt.

The other possibility is a motion of a charged soliton of some kind in a semiconducting or a superconducting film overlaying the metal (Fig. 12b). For instance, in the case of the Gunn effect in semiconductors, a moving charged soliton is formed due to an N-shaped current-voltage characteristic of the semiconductor.[14] The size of the soliton in GaAs is of
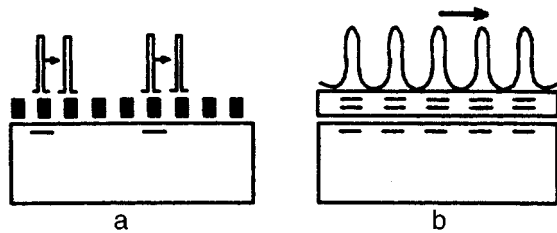

FIG. 12. Schematic diagram of the electronically driven motion of a surface charge. (a) Electric pulses switched periodically between metallic electrodes near the metal surface; (b) Propagating solitons in the semiconductor layer overlaying the bulk metal.

the order of 10 μm. The velocity of soliton motion can be made quite large, $V \sim 10^7$ cm/s. As a result of the interaction of solitons with the induced surface charges in a metal, the current-voltage characteristic of a semiconductor film overlaying the metal attains a singularity at V near the Fermi velocity of the metal.

Another possibility is propagating low-frequency charged plasmons[15–17] in a thin superconducting film in the vicinity of a bulk metallic electrode.

It should be noted that the effect considered in this paper, an additional dissipation related to the surface charge, may have relevance to an evaluation of the quality factor Q_f of an rf cavity, in particular, a superconducting cavity. At the lowest temperature at which the power absorption due to the electronic excitations in a superconductor is quite small (and, therefore, Q_f large), a dissipation related to the surface charge may contribute to the residual value of Q_f attained at the lowest temperature in a very high-quality cavities ($Q_f \sim 10^{10}$).[18]

*E-mail:kulik@fen.bilkent.edu.tr

[1] J. M. Ziman, *Principles in the Theory of Solids*, Cambridge University Press, Cambridge (1972).
[2] D. Pines, *Elementary Excitations in Solids*, Benjamin, New York (1964).
[3] M. H. Day, Phys. Rev. **B12**, 514 (1975).
[4] M. Day and M. Ebel, Phys. Rev. **B19**, 3434 (1979).
[5] *Scanning Tunneling Microscopy and Related Methods*, R. J. Behm, N. Garcia, and H. Rohrer (Eds.), Kluwer, Deventer (1990).
[6] D. V. Averin and K. K. Likharev, in *Mesoscopic Phenomena in Solids*, p. 173, B. L. Altshuler, P. A. Lee, and R. A. Webb (Eds.), North-Holland, Amsterdam (1991).
[7] I. K. Yanson, Fiz. Nizk. Temp. **9**, 676 (1983) [Sov. J. Low Temp. Phys. 9, 343 (1983)].
[8] I. O. Kulik, Fiz. Nizk. Temp. **18**, 450 (1992) [Sov. J. Low Temp. Phys. 18, 302 (1992)].
[9] I. O. Kulik, Physica B, Cond. Matter (Amsterdam) **218**, 252 (1996).
[10] E. M. Lifshitz and L. P. Pitaevskil, Theoretical Physics, Vol. X. [Fizicheskaya Kinetika (Physical Kinetics), Nauka Publ., Moscow (1979)].
[11] P. M. Echenique, F. Flores, and R. H. Ritchie, in *Solid State Physics: Advances in Research and Applications* 43, p. 229, H. Ehrenreich and D. Turnbull (Eds.), Academic Press, New York (1990).
[12] A. A. Abrikosov, *Fundamentals of the Theory of Metals*, North-Holland, Amsterdam (1988).
[13] L. D. Landau and E. M. Lifshitz, *Electrodynamics of Continuous Media*, Pergamon, Press, Oxford (1984).
[14] B. K. Ridley, in *Negative Differential Resistance and Instabilities in* 2*D Semiconductors*, N. Balkan, B. K. Ridley, and A. J. Vickers (Eds.), Plenum Press, New York (1993).
[15] I. O. Kulik, Zh. Éksp. Teor. Fiz. **65**, 2016 (1073) [Sov. Phys. JETP **38**, 1008 (1974)].
[16] J. E. Mooij and G. Schon, Phys. Rev. Lett. **55**, 114 (1985).
[17] O. Bulsson, P. Xavier, and J. Richard, Phys. Rev. Lett. **73**, 3153 (1994).
[18] D. M. Ginsberg and L. C. Hebel, In Superconductivity, Vol. 1, p. 193, R. D. Parks (Ed.), Marcel Dekker, New York (1969).

Study of surface phenomena in the ferroelastic phase transition in a semi-infinite crystal

N. M. Lavrinenko

A. Galkin Physicotechnical Institute, 340114 Donetsk, Ukraine[*]

Surface phenomena are studied during ferroelastic phase transition in a semi-infinite crystal with tetragonal symmetry. It is shown that the strictional bond between the order parameter and lattice deformation leads to the emergence of a spatially modulated structure with a finite value of the wave vector at the surface phase transition point. The surface phase transition always precedes the ferroelastic phase transition in the bulk. © *1997 American Institute of Physics.* [S1063-777X(97)01308-X]

The role of surface in phase transitions in magnetic materials has recently attracted ever-increasing attention of researchers. The possibility for the existence of surface magnetic anisotropy was first indicated by Néel.[1] It was predicted theoretically in 1970 that under certain conditions the surface of magnetic crystals may possess magnetization at temperatures higher than the Curie point (see Ref. 2). If an orientational phase transition occurs in the bulk of the crystal, it is accompanied by a reversal of orientation of the magnetic moments at the surface. The difference between surface forces and bulk forces results in a nonuniformity of the order parameter and affects the phase transition temperature. The existence of a ''transition'' surface layer with properties differing from those in the bulk was first confirmed experimentally by Krinchak and Zubov.[3] Such a relatively simple pattern of phase transition is justified only in the case where the magnetization at the surface and in the bulk of the sample is parallel to the surface, thus excluding the influence of long-range dipole–dipole forces, i.e., demagnetizing fields. In the opposite case, the surface effects lead to the emergence of a strip domain structure.[4,5] A similar picture is also observed when long-range elastic forces are taken into consideration.[6,7] In other words, the strictional bond between the order parameter and lattice deformation leads to the emergence of a spatially modulated structure in the plane at the ferroelastic phase transition point. Earlier, we considered[7] a plane–parallel plate in which a ferroelastic phase transition takes place, and the surface is taken into account through boundary conditions, viz., free elastic boundary conditions and an uncoupled order parameter. Under certain conditions, the strictional coupling of the order parameter with lattice deformation leads to the emergence of a spatially modulated structure instead of a homogeneous phase at the transition point. The wave vector of the emerging structure depends on the plate thickness and on the constant of interaction between the order parameter and elastic deformation. We did not consider in Ref. 7 the possibility of a surface phase transition. From the physical point of view, an interesting situation arises when the ferroelastic phase transition can occur in the bulk of the crystal as well as at the surface. In the present paper we consider the possibility of a competition between the bulk and surface phenomenological

(interaction) constants, measure the surface phase transition temperature, and determine whether the system splits into domains.

An intrinsic ferroelastic phase transition is one whose order parameter is coupled linearly with nonisomorphic striction, i.e., with macroscopic deformations of the crystal lattice. To a considerable extent, this coupling determines the peculiarities of the critical behavior of the system in the broadest possible sense[8–11] and is independent of the microscopic realization of the order parameter. Since only long-wave fluctuations of the characteristic parameter increase at the phase transition point, the free energy can be written in the continuous medium approximation. For definiteness, we shall consider a semi-infinite crystal of tetragonal symmetry which occupies the region $z \leq 0$ and whose order parameter η is linearly connected with the elastic strain $(u_{xx} - u_{yy})$.

In the absence of external fields, the expansion of free energy in powers of the order parameter η and the strain tensor $u_{ik} = (u_{i,k} + u_{k,i})/2$ during the ferroelastic phase transition has the structure

$$F_v = \int d^3x [A\,\eta^2 + B\,\eta^4 + \alpha(\nabla\eta)^2 + \lambda_v\,\eta(u_{xx} - u_{yy}) + f_y], \tag{1}$$

where the elastic energy density f_y has the form

$$f_y = \frac{1}{2}\,C_{11}(u_{xx}^2 + u_{yy}^2) + \frac{1}{2}\,C_{33}u_{zz}^2 + C_{13}u_{zz}(u_{xx} + u_{yy})$$
$$+ C_{12}u_{xx}u_{yy} + 2C_{66}u_{xy}^2 + 2C_{44}(u_{xz}^2 + u_{yz}^2). \tag{2}$$

Apart from the volume component F_v, the total free energy of the system also contains the free surface energy: $F = F_v + F_s$, where

$$F_s = \sum_{z \in s} [a\,\eta^2 + g(\nabla\eta)^2 + \lambda_s\,\eta(u_{xx} - u_{yy})]. \tag{3}$$

The role of the gradient in the bulk of the crystal $(z \to -\infty)$ is insignificant, and the solution of the equilibrium equations for the order parameter and elastic deformations is the same as that in an infinite medium:

$$u_{xx}^0 - u_{yy}^0 = -\lambda_v \eta^0/C, \quad \eta^{0\,2} = -A*/2B,$$

$$C = (C_{11} - C_{22})/2, \quad A^* = A - \lambda_v^2/2C < 0. \tag{4}$$

The bulk ferroelastic phase transition point is defined by the relation

$$A_c = A' \tau_c = \lambda_v^2/2C, \quad \tau = (T - T_{c0})/T_{c0} \tag{5}$$

(T_{c0} is the temperature of transition in the system that does not interact with the lattice deformations, $u_{xx} - u_{yy} = 0$).

Let us compute the mean-square fluctuation of the order parameter at the crystal surface, which makes it possible to determine the singularities of the surface phase transition and its temperature. In order to determine the fluctuation probability, we must consider the highest possible equilibrium, i.e., the lowest value of the thermodynamic potential. Obviously, this condition is satisfied if fluctuations of the order parameter and displacement vector are at equilibrium in the bulk. Using the equilibrium conditions in the bulk

$$2A\eta + 4B\eta^3 + \lambda_v(u_{xx} - u_{yy}) - 2\alpha\Delta\eta = 0,$$

$$\frac{\partial\sigma_{ik}}{\partial x_k} = 0 \quad (i,k = x,y,z) \tag{6}$$

($\sigma_{ik} = \partial F_v/\partial u_{ik}$ is the bulk tensor of stresses), we transform Eqs. (1)–(3) to the form

$$F_s = \sum_{z \in s} \left[a\eta^2 + g(\nabla\eta)^2 + \lambda_s\eta(u_{xx} - u_{yy}) + \frac{1}{2}\sigma_{iz}u_i \right.$$

$$\left. + 2\eta\eta'\alpha \right]. \tag{7}$$

Here and below, the prime indicates differentiation with respect to the coordinate normal to the surface. It should be emphasized that bulk equilibrium equations (6) must be valid everywhere in the bulk right up to the surface. Otherwise, the physical quantities will not have static fluctuations.

If the fluctuating quantities correspond to plane sinusoidal waves in the XY plane

$$u_i(x,y,z) = \exp(i(k_1 x + k_2 y))u_i(k_1,k_2,z),$$

$$\eta(x,y,z) = \exp(i(k_1 x + k_2 y))\eta(k_1,k_2,z),$$

$$k_1^2 + k_2^2 = k^2, \quad i = x,y,z,$$

Eqs. (6) will assume the form

$$C_{44}u_x'' + ik_1 C_{44}^* u_z' = -ik_1\lambda_v\eta + (C_{11}k_1^2 + C_{66}k_2^2)u_x$$
$$+ k_1 k_2(C_{66} + C_{12})u_y;$$

$$C_{44}u_y'' + ik_2 C_{44}^* u_z' = ik_2\lambda_v\eta + k_1 k_2(C_{66} + C_{12})u_x$$
$$+ (C_{11}k_2^2 + C_{66}k_1^2)u_y;$$

$$C_{33}u_z'' + C_{44}^*(ik_1 u_x' + ik_2 u_y') = C_{44}k^2 u_z;$$

$$\eta'' = \frac{A_k}{\alpha}\eta + \frac{\lambda_v}{2\alpha}(ik_1 u_x - ik_2 u_y), \tag{8}$$

where $C_{44}^* = C_{44} + C_{13}$, and $A_k = A + 6B_\eta^{02} + \alpha k^2$. Solving the bulk equilibrium equations (8), we can determine the unknown derivatives η', u_i' ($i = x,y,z$) for $z = 0$ appearing in (7) in terms of the order parameter η and displacements u_i ($i = x,y,z$) for $z = 0$:

$$u_x' = a_{11}u_x + a_{12}u_y + ik_1 Du_z - ik_1 E\eta;$$

$$u_y' = a_{12}u_x + a_{22}u_y + ik_2 Du_z + ik_2 E\eta;$$

$$u_z' = \left(\frac{C_{11}}{C_{33}}\right)^{1/2} D(ik_1 u_x + ik_2 u_y) + a_{33}u_z + a_{34}\eta;$$

$$\eta' = E\frac{C_{44}}{2\alpha}(ik_1 u_x - ik_2 u_y) + a_{34}\frac{C_{33}}{2\alpha}u_z + a_{44}\eta, \tag{9}$$

where

$$a_{11} = \frac{b_1 k_2^2}{k^2} + \frac{b_2 k_1^2}{k^2}; \quad a_{22} = \frac{b_1 k_1^2}{k^2} + \frac{b_2 k_2^2}{k^2};$$

$$a_{12} = \frac{k_1 k_2(b_2 - b_1)}{k^2}; \quad b_2 = k\left(\frac{C_{11}}{C_{44}}(1 - D^2)\right)^{1/2};$$

$$b_1 = k\left(\frac{C_{66}}{C_{44}}\right)^{1/2}; \quad a_{33} = k\left(\frac{C_{44}}{C_{33}}(1 - D^2)\right)^{1/2};$$

$$a_{34} = \frac{k_2^2 - k_1^2}{k^2}\frac{C_{44}E}{D(C_{11}C_{33})^{1/2}}(b_2 - b_1);$$

$$a_{44} = (A_k/\alpha)^{1/2}; \quad D = -\frac{C_{44}^*}{C_{44} + (C_{11}C_{33})^{1/2}};$$

$$E = \frac{\lambda_v}{C_{44}}[(A_k/\alpha)^{1/2} + k(C_{66}/C_{44})^{1/2}]^{-1}. \tag{10}$$

It is important to note that the surface energy is a function of only η, u_i ($i = x,y,z$) if the bulk equilibrium equations (8) are satisfied. Otherwise, the volume of the crystal adjoining the surface, and hence the surface itself, will not be at equilibrium.

Minimizing the surface energy (7) with respect to displacement vectors $u_i(k)$ for given values of $\eta(k)$, we obtain

$$F_s = \int d^2 k(a + gk^2 + 2\alpha a_{44} + \nabla f/2)|\eta(k)|^2, \tag{11}$$

where the increment ∇f in (11), which is negative and linear in the wave vector, has the form

$$\nabla f = -C_{33}a_{33}\left(\frac{3a_{34}}{2a_{33}}\right)^2$$

$$- \frac{k_1^2\lambda_+^2 A_{22} + k_2^2\lambda_-^2 A_{11} + 2k_1 k_2\lambda_+\lambda_- A_{12}}{A_{11}A_{22} - A_{12}^2}. \tag{12}$$

The quantities $A_{\alpha\beta}$ ($\alpha,\beta = 1,2$) are defined by the relation

$$A_{\alpha\beta} = C_{44}a_{\alpha\beta} - \frac{k_\alpha k_\beta C_{44}^2(1 + D)^2}{C_{33}a_{33}}, \tag{13}$$

and $\lambda_\pm$ are linear combinations of surface and volume "magnetostriction" coefficients

$$\lambda_\pm = \lambda_s + \frac{3C_{44}E}{2} \pm \frac{C_{44}(1 + D)3a_{34}}{2a_{33}}, \tag{14}$$

which depend on the direction of the wave vector (through a_{34}) and on the temperature (through E). The correction ∇f in (11) is determined entirely by the long-range elastic forces. This quantity is also nonzero in two limiting cases:

(1) a ferroelastic phase transition ($\lambda_v \neq 0$) occurs in the bulk of the crystal and an order–disorder phase transition ($\lambda_s = 0$) occurs at the surface of the crystal;

(2) a conventional order–disorder phase transition occurs in the bulk of the crystal ($\lambda_v = 0$), and a ferroelastic phase transition ($\lambda_s \neq 0$) occurs at the surface of the crystal.

Consequently, as a result of taking strictional effects into account, a phase with spatially modulated order parameter, which is characterized by a finite value of the wave vector, always emerges at the surface phase transition point.

It is easy to see that ∇f is nonzero for all directions of the wave vector, and that it assumes the minimum value for $k_1^2 = k_2^2$:

$$\nabla f = -k\left(\lambda_s + \frac{3}{2}\lambda_v(\alpha/A)^{1/2}\right)^2/(C_{66}C_{44})^{1/2}.$$

Thus, in contrast to an infinite crystal, the system under consideration does not possess any directions of wave vectors with anomalous fluctuations of the order parameter or the softening modes corresponding to them.[12] The Landau theory describes such a phase transition quite accurately.

The surface phase transition temperature is determined from the condition

$$a + 2\alpha a_{44} = 0. \tag{15}$$

This relation is satisfied only when the coefficient a in the surface energy is negative, i.e., when the surface facilitates the formation of an ordered phase. The surface phase transition temperature can be determined from the formula $a^2 = 4\alpha A_s = 4\alpha A' \tau_s$. Using Eqs. (4) and (10), we obtain the following expression from Eq. (15) for $A^* > 0$:

$$\frac{a^2}{4\alpha} - \frac{\lambda_v^2}{2C} = A_s^* = A'\frac{T_s - T_c}{T_{c0}} > 0. \tag{16}$$

In other words, the surface phase transition always occurs earlier than the phase transition in the bulk. For $a^2/4\alpha = \lambda_v^2/2C$ the surface and bulk phase transition temperatures coincide, and a "special" phase transition takes place (see Refs. 2 and 13). In contrast with the order–disorder phase transition in which the "special" phase transition is characterized by the relation $a = 0$,[2] the point at which the "special" phase transition takes place is displaced in the case of a ferroelastic phase transition. It is interesting to note that this displacement $\lambda_v^2/2C$ is determined entirely by the bulk constants and coincides with the gap in the vibrational spectrum of the order parameter of an infinite sample.

Thus, in a semi-infinite crystal in which a ferroelastic phase transition is possible in the bulk of the crystal as well as at the surface, strictional coupling of the order parameter and lattice deformation always leads initially to a surface phase transition occurring at a temperature higher than the temperature of phase transition in the bulk. This surface transition leads to the emergence of a spatially modulated structure which is characterized by a finite value of the wave vector k_0. This quantity is defined by a linear combination of constants of interaction of order parameter with lattice deformations at the surface and in the bulk of the crystal. In this case, the phenomenological approach to the problem of phase transition is justified at all temperatures since there are no wave vector directions in the system corresponding to anomalous (critical) fluctuations of the order parameter.

*E-mail: lavr@host.dipt.donetsk.ua

[1] L. J. Neel, Phys. Radium **15**, 225 (1954).

[2] M. I. Kaganov and A. B. Chubukov, in *Magnetic Properties of Crystalline and Amorphous Media* [in Russian], Nauka, Novosibirsk (1989).

[3] G. S. Krinchak and V. E. Zubov, Zh. Éksp. Teor. Fiz. **69**, 707 (1975) [Sov. Phys. JETP **42**, 359 (1975)].

[4] Yu. I. Bespyatnykh, I. E. Dikshtein, and V. V. Tarasenko, Fiz. Tverd. Tela (Leningrad) **22**, 3335 (1980) [Sov. Phys. Solid State **22**, 1953 (1980)].

[5] A. V. Chubukov, Fiz. Tverd. Tela (Leningrad) **24**, 2465 (1982) [Sov. Phys. Solid State **24**, 1399 (1982)].

[6] A. F. Andreev, Pis'ma Zh. Éksp. Teor. Fiz. **32**, 654 (1980) [JETP Lett. **32**, 640 (1980)].

[7] N. M. Lavrinenko, Fiz. Nizk. Temp. **22**, 1132 (1996) [Low Temp. Phys. **22**, 865 (1996)].

[8] R. Folk, H. Iro, and F. Shwable, Phys. Lett. **A57**, 112 (1976).

[9] F. Shwable, J. Stat. Phys. **39**, 719 (1985).

[10] A. P. Levanyuk and A. A. Sobyanin, Pis'ma Zh. Éksp. Teor. Fiz. **11**, 540 (1970) [JETP Lett. **11**, 371 (1970)].

[11] I. M. Vitebskii, A. S. Zel'tser, and N. M. Lavrinenko, Ukr. Fiz. Zh. **33**, 892 (1988).

[12] V. G. Bar'yakhtar, I. M. Vitebskii, N. M. Lavrinenko, and V. L. Sobolev, J. Phys.: Cond. Matter **2**, 2579 (1990).

[13] A. J. Bray and M. A. Moore, J. Phys. **A10**, 1927 (1977).

Translated by R. S. Wadhwa

664   Low Temp. Phys. **23** (8), August 1997

N. M. Lavrinenko   664

DYNAMICS OF THE CRYSTAL LATTICE

Neutron scattering and diffusive x-ray diffraction in acoustic modes in Nd$_2$CuO$_4$

D. V. Fil and A. L. Zazunov

Institute of Single Crystals, Ukrainian National Academy of Sciences, 310001 Kharkov, Ukraine

The differential cross section of thermal neutron scattering and x-ray scattering by acoustic excitations are calculated in the framework of an anisotropic elastic medium model with an additional two-dimensional acoustic-type mode which interacts with elastic deformation. This model was proposed earlier for describing the anomalous behavior of sound velocities in Nd$_2$CuO$_4$. The influence of plane mode on the angular dependence of neutron scattering and on the shape of diffusive spot in x-ray diffraction pattern is studied. © *1997 American Institute of Physics.* [S1063-777X(97)01408-4]

A peculiar behavior of sound velocities in single crystals of Nd$_2$CuO$_4$ and Pr$_2$CuO$_4$ has been described in Refs. 1 and 2. This peculiarity consists in the anomalous dependence of quasitransverse mode velocities on the direction of a rotating wave vector in the symmetry planes parallel to the c_4 axis. A phenomenological model based on the assumption about the existence of a collective mode which has an acoustic energy-momentum relation and which propagates along the CuO$_2$ planes in the single crystals under consideration was proposed. In this model, interaction of the lattice with additional degrees of freedom corresponding to the plane mode may lead to a dependence of acoustic vibration velocities on the direction of wave vector **q** similar to those observed in experiments.[1,2] For a definite choice of parameters of the model, hybridization of a quasitransverse elastic vibration with a plane mode leads to the emergence of two intrinsic vibrations (fast and slow) which are mainly responsible for transfer of the transverse elastic signal with **q** directed at an angle $\theta \neq 0$, $\pi/2$ to the axis c_4 and polarization lying in the plane defined by the direction of **q** and c_4 axis. For θ close to 0, the fast mode gives the main contribution; for θ close to $\pi/2$ the main contribution comes from the slow mode, and both modes give similar contributions in a small region of θ in the interval ($0 < \theta < \pi/2$). This explains the experimentally observed abrupt changes in the transverse signal velocity as a function of θ and the detection of two transverse signals with identical polarization and radically different velocities in the region of the jump.

We believe that the hypothesis about the existence of a plane mode calls for an independent experimental confirmation. Earlier, we considered[3] the theory of Brillouin scattering of light for a lattice with an additional plane mode. In the present work we aim at an analysis of the effects associated with the existence of a plane mode which may be manifested in experiments on neutron scattering and diffusive diffraction of x-rays by acoustic phonons.

The analysis carried out in the present work is based on the phenomenological approach for describing the additional mode. The important circumstance for the problem under consideration as regards the microscopic nature of the addi-

tional mode is that, firstly, the additional oscillation is not connected with longwave fluctuations of the electron density since the existence of Coulomb interaction would determine the gap nature of the spectrum of such oscillations. Secondly, since the application of a strong constant magnetic field does not change the nature of the angular dependences of the acoustic signal velocities,[1,2] it can also be stated that the additional mode is not connected with spin oscillations. Hence the degrees of freedom corresponding to this mode do not interact directly with neutrons or the electromagnetic field, i.e., the scattering mechanism of the latter is determined by the nuclear and electromagnetic potentials of lattice atoms, and the effect of the plane mode is manifested through its interaction with longwave elastic vibrations. The subsequent analysis is based on this assumption.

1. SCATTERING OF NEUTRONS BY ACOUSTIC MODES

Following the approach described in Ref. 3, we write the Hamiltonian of the model in the form

$$H = H_u + H_a + H_{\text{int}}. \tag{1}$$

The elastic part of this equation has the standard form

$$H_u = \frac{1}{2} \int d^3r (\rho \dot{u}_i^2 + \lambda_{iklm} u_{ik} u_{lm}), \tag{2}$$

where u_i are the components of elastic displacement vector, u_{ik} is the strain tensor components, ρ is the density of the elastic medium, and λ_{iklm} is the elastic moduli tensor. Since we are interested in the spectroscopy of the acoustic modes of the system, we shall not consider optical vibrations in the present approach. In order to simulate an acoustic plane mode, we introduce an additional degree of freedom like a $(2+1)$-dimensional gage field $(\mathbf{a}_n, a_{n0})$ in the nth layer (the layers are perpendicular to the c_4 axis). Such a field is characterized by a single independent component, which corresponds to the assumption concerning the existence of an additional mode in the system. The Hamiltonian H_a assumes the form

$$H_a = \frac{1}{8\pi} \sum_n \int d^2r (e_n^2 + v_a^2 b_n^2), \tag{3}$$

where $e_i = -\partial_i a_0 - \partial_t a_i$; $b = e_{ik}\partial_i a_k$, and v_a is the velocity of the plane wave along the layers. Taking into account the tetragonal symmetry of the system, we can present the interaction Hamiltonian in the form

$$H_{int} = \sum_n \int d^2r b_n (g_z u_{zz} + g_x(u_{xx} + u_{yy})), \tag{4}$$

where g_z and g_x are interaction constants. The choice of H_a and H_{int} in the form (3) or (4), respectively, may be justified, for example, in the model of an elastic medium containing two-dimensional layers of superfluid anyons in which anyon density fluctuations interact with the elastic strain tensor components.[3–5] Since we do not aim at a microscopic description of the effect in this work, we consider Hamiltonian (1) only as a convenient phenomenological model. Since the Hamiltonian (4) is invariant to the replacement of right-hand coordinate system by a left-hand one, we assume implicitly that the existence of an additional degree of freedom is associated with the emergence of the corresponding order parameter in the system that violates the symmetry for the given layer.

The differential cross section of inelastic neutron scattering calculated in the Born approximation per unit energy of the scattered neutron and per unit solid angle has the form[6,7]

$$\frac{d^2\sigma}{dEdo} = \frac{1}{2\pi} \frac{k'}{k} a_u^2 \sum_{lm} \exp(-i\mathbf{q}(\mathbf{R}_l - \mathbf{R}_m))$$

$$\int_{-\infty}^{\infty} dt e^{i\omega t} \langle e^{-i\mathbf{q}\mathbf{u}(l,t)} e^{i\mathbf{q}\mathbf{u}(m,0)} \rangle. \tag{5}$$

In this equation, a_u is the length of neutron scattering by a lattice atom (for simplicity, we assume that this quantity is the same for all atoms), $\mathbf{k}$ and $\mathbf{k}'$ are wave vectors of an incident and a scattered neutron, $\mathbf{q} = \mathbf{k}' - \mathbf{k}$, and $\omega = (2m_n)^{-1}(k^2 - k'^2)$ (m_n is the neutron mass).

In order to compute the mean in Eq. (5), we go over to the secondary quantization representation in the Hamiltonian (1). Choosing the calibration $a_0 = 0$, $\nabla_2 \mathbf{a} = 0 (\nabla_2 = i_x\partial_x + i_y\partial_y)$ and using the Fourier components of the fields $\mathbf{u}(\mathbf{r})$ and $\mathbf{a}_n(\mathbf{r})$, we can present the Hamiltonian (1) in the form

$$H = \frac{1}{2} \sum_{\mathbf{q}} \left[\rho\dot{u}_i^+(\mathbf{q})\dot{u}_i(\mathbf{q}) + \lambda_{ilkm}q_iq_lu_k^+(\mathbf{q})u_m(\mathbf{q}) \right.$$

$$+ \frac{1}{4\pi d}[\dot{Q}^+(\mathbf{q})\dot{Q}(\mathbf{q}) + v_a^2 q_{pl}^2 Q^+(\mathbf{q})Q(\mathbf{q})]$$

$$+ \frac{1}{d}(iq_{pl}Q^+(\mathbf{q})\{g_z q_z u_z(\mathbf{q}) + g_x(q_x u_x(\mathbf{q})$$

$$\left. + q_y u_y(\mathbf{q}))\} + \text{H.c.}) \right], \tag{6}$$

(here d is the separation between layers, and $q_{pl} = (q_x^2 + q_y^2)^{1/2}$. Going over to normal coordinates in the above equation, we obtain

$$H = \frac{1}{2} \sum_{\mathbf{q}\chi} (\dot{\alpha}_\chi^+(\mathbf{q})\dot{\alpha}_\chi(\mathbf{q}) + \omega_\chi^2(\mathbf{q})\alpha_\chi^+(\mathbf{q})\alpha_\chi(\mathbf{q})), \tag{7}$$

where $\omega_\chi^2(\mathbf{q})$ are the eigenvalues of the matrix

$$\begin{pmatrix} \tilde{c}_{11}q_x^2 + \tilde{c}_{66}q_y^2 + \tilde{c}_{44}q_z^2 & (\tilde{c}_{12} + \tilde{c}_{66})q_xq_y & (\tilde{c}_{13} + \tilde{c}_{44})q_xq_z & i\tilde{g}_xq_xq_{pl} \\ (\tilde{c}_{12} + \tilde{c}_{66})q_xq_y & \tilde{c}_{11}q_y^2 + \tilde{c}_{66}q_x^2 + \tilde{c}_{44}q_z^2 & (\tilde{c}_{13} + \tilde{c}_{44})q_yq_z & i\tilde{g}_xq_yq_{pl} \\ (\tilde{c}_{13} + \tilde{c}_{44})q_xq_z & (\tilde{c}_{13} + \tilde{c}_{44})q_yq_z & \tilde{c}_{44}q_{pl}^2 + \tilde{c}_{33}q_z^2 & i\tilde{g}_zq_zq_{pl} \\ -i\tilde{g}_xq_xq_{pl} & -i\tilde{g}_xq_yq_{pl} & -i\tilde{g}_zq_zq_{pl} & v_a^2q_{pl}^2 \end{pmatrix} \tag{8}$$

with $\tilde{c}_{ik} = c_{ik}/\rho$, and $\tilde{g}_{x(x)} = g_{z(x)}\sqrt{4\pi/d\rho}$. The above equation takes into account the symmetry of elastic tensor components for the Nd_2CuO_4 lattice. The direction of x and y axes is chosen along the Cu–O bonds in CuO_2 planes. In terms of the secondary quantization operators, the Hamiltonian (7) can be presented in the form

$$H = \sum_{\mathbf{q},\chi} \omega_\chi(\mathbf{q})\left(\beta_\chi^+(\mathbf{q})\beta_\chi(\mathbf{q}) + \frac{1}{2}\right), \tag{9}$$

where β^+ and β are the boson creation and annihilation operators. The quantities $\mathbf{u}(l,t)$ are presented in terms of the operators β as follows:

$$u_i(l,t) = \frac{1}{(2\rho V)^{1/2}} \sum_{\chi\mathbf{q}} \frac{\xi_{\chi i}(\mathbf{q})}{(\omega_\chi(\mathbf{q}))^{1/2}} (\beta_\chi(\mathbf{q}) + \beta_\chi^+(-\mathbf{q}))$$

$$\times \exp(i\mathbf{q}\mathbf{R}_l - i\omega_\chi(\mathbf{q})t), \tag{10}$$

where $\xi_{\chi i}$ are components of the eigenvectors of the operator defined by the matrix (8).

Calculating the mean in (5), integrating with respect to t and summing over the lattice sites, we obtain

$$\frac{d^2\sigma}{dEdo} = \frac{1}{2} \frac{k'}{k} \frac{a_u^2 N}{M} \sum_\chi \frac{1}{\omega_\chi(\mathbf{q})} |\mathbf{q}\xi_\chi(\mathbf{q})|^2 e^{-2W(\mathbf{q})}$$

$$\times \{(N(\omega_\chi(\mathbf{q})) + 1)\delta(\omega - \omega_\chi(\mathbf{q}))$$

$$+ N(\omega_\chi(\mathbf{q}))\delta(\omega + \omega_\chi(\mathbf{q}))\}, \tag{11}$$

where

$$W(\mathbf{q}) = \frac{1}{2\rho V} \sum_{\chi\mathbf{q}'} \frac{1}{\omega_\chi(\mathbf{q}')} |\mathbf{q}\xi_\chi(\mathbf{q}')|^2 \left(N(\omega_\chi(\mathbf{q}')) + \frac{1}{2}\right) \tag{12}$$

is the exponent in the Debye–Waller factor, $N(\omega)$ is the

Bose distribution function, M is the mass of a unit cell, N is the number of cells, and $\xi_\chi = \xi_{\chi 1}, \xi_{\chi 2}, \xi_{\chi 3}$. In the limit $T \gg \omega_\chi(\mathbf{q})$, Eq. (11) reduces to

$$\frac{d^2\sigma}{dE\,do} = \frac{1}{2}\frac{k'}{k}\frac{Ta_u^2 N}{M} \sum_\chi I_\chi(\mathbf{q})\{\delta(\omega - \omega_\chi(\mathbf{q})) + \delta(\omega + \omega_\chi(\mathbf{q}))\},$$ (13)

where

$$I_\chi(\mathbf{q}) = \frac{1}{\omega_\chi^2(\mathbf{q})}|\mathbf{q}\xi_\chi(\mathbf{q})|^2 e^{-2W(\mathbf{q})}.$$ (14)

It follows from Eq. (13) that the existence of a plane mode leads to the emergence of an additional peak in the differential scattering cross section. Using the expression (14), we analyze the intensity of peaks as a function of the experimental geometry. Let us first consider the case $\mathbf{q} = \boldsymbol{\kappa} + \mathbf{q}'$ with $\boldsymbol{\kappa} \neq 0$ ($\boldsymbol{\kappa}$ is the reciprocal lattice vector) and $|\mathbf{q}'|/|\boldsymbol{\kappa}| \ll 1$, keeping in mind that we are interested in the spectroscopy of the longwave part of the spectrum. In this case, $W(\mathbf{q}) \approx W(\boldsymbol{\kappa})$, i.e., the Debye–Waller factor defines the anisotropy of intensities as a function of the direction $\boldsymbol{\kappa}$ (the magnitude of the anisotropy will be discussed below), and is constant for a fixed value of $\boldsymbol{\kappa}$. We assume the model parameters in accordance with the analysis of the experimental velocities of sound in Nd_2CuO_4 observed in Ref. 2: $(\tilde{c}_{11})^{1/2} = 6.05$; $(\tilde{c}_{33})^{1/2} = 5.85$; $(\tilde{c}_{12})^{1/2} = 4.59$; $(\tilde{c}_{13})^{1/2} = 4.19$; $(\tilde{c}_{44})^{1/2} = 2.46$; $(\tilde{c}_{66})^{1/2} = 4.22$; $v_a = 3.83$; $(\tilde{g}_z)^{1/2} = 3.95$ (in units of 10^5 cm/s), $g_z = 0$. The angular dependences $I_\chi(\theta)$ for $\boldsymbol{\kappa} = (0,0,2\pi/c)$ and $(2\pi/a, 2\pi/a, 2\pi/c)$ (where a and c are lattice parameters) and $\mathbf{q}'$ lying in (010) and ($1\bar{1}0$) planes, respectively, are shown in Figs. 1a and 1b (θ is the angle between $\mathbf{q}'$ and the z axis). The corresponding angular dependences of the energy shift for a scattered neutron are shown in Fig. 1c. For the geometry chosen by us, the intensity corresponding to a purely transverse elastic mode with polarization in the (001) plane is identically equal to zero. For comparison, Fig. 1 also shows the intensity corresponding to quasitransverse vibration for a system without a plane mode (with the same values of the elastic tensor components). For a quasilongitudinal mode, the corresponding dependence practically coincides with curve 1 in Figs. 1a and b. It follows from the dependences presented here that the existence of an additional mode does not affect the scattering spectrum for $\mathbf{q}'$ lying in the (x,y) plane. For the remaining $\mathbf{q}'$, the interaction with a plane mode leads to the splitting of the peak corresponding to a quasitransverse acoustic phonon. For $\theta \to 0$, the contribution from the additional mode determines the nonzero intensity of nearly elastic scattering with $\mathbf{q} \neq \boldsymbol{\kappa}$. The case $\theta = 0$ must be considered separately. For such a direction of the wave vector, the plane mode component vanishes, and the dependence $I_3(\theta)$ changes abruptly. Note that the departure of the plane mode spectrum from the purely two-dimensional case would cause a jump of finite width.

The angular dependences $I_\chi(\theta)$ for $\boldsymbol{\kappa} = 0$ and $\mathbf{q}$, which lies in the (x,z) plane, are shown in Fig. 2. For a system without the plane mode, the scattering intensity correspond-
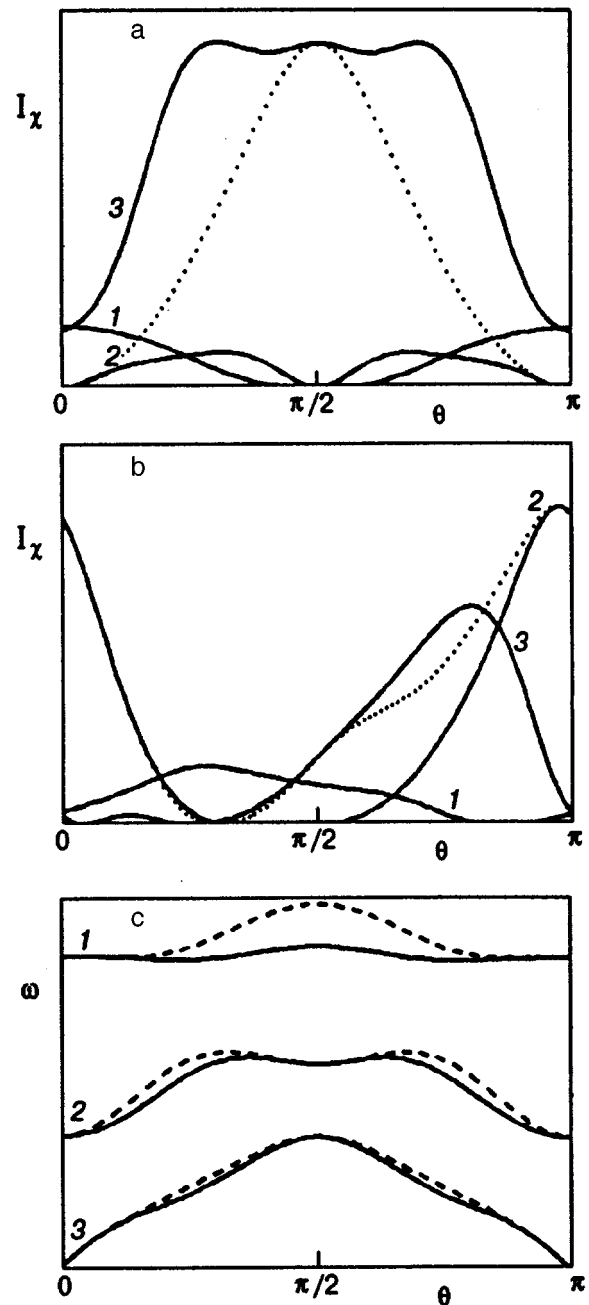

FIG. 1. Dependence of the neutron scattering intensities I_χ on θ for $\boldsymbol{\kappa} = (0,0, 2\pi/c)$, $\mathbf{q}' \perp [010]$ (a), $\boldsymbol{\kappa} = (2\pi/a, 2\pi/a, 2\pi/c)$, $\mathbf{q}' \perp [1\bar{1}0]$ (b), the scattered neutron energies corresponding to them (solid curves correspond to $\mathbf{q}' \perp [010]$, and the dashed curves correspond to $\mathbf{q}' \perp [1\bar{1}0]$) (c). The dashed curves in Figs. (a) and (b) show the intensity of scattering by the quasitransverse sound in a system without a plane mode. The numbers on the curves are the intrinsic mode numbers.

ing to the quasilongitudinal mode practically coincides with curve 1 in Fig. 2, and the contribution from the quasitransverse mode is too small to be shown on the given scale. It can be seen from Fig. 2 that together with the quasilongitudinal mode of two other intrinsic oscillations of the system, the presence of a plane mode is responsible for a significant contribution to the total scattering intensity.
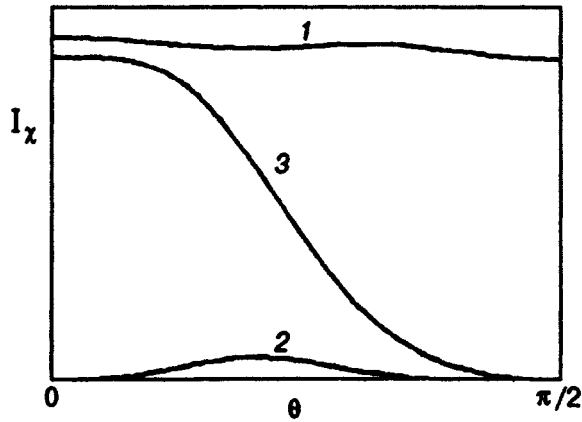
FIG. 2. Dependence of I_χ on θ for $\boldsymbol{\kappa}=0$, $\mathbf{q}'\perp[010]$.
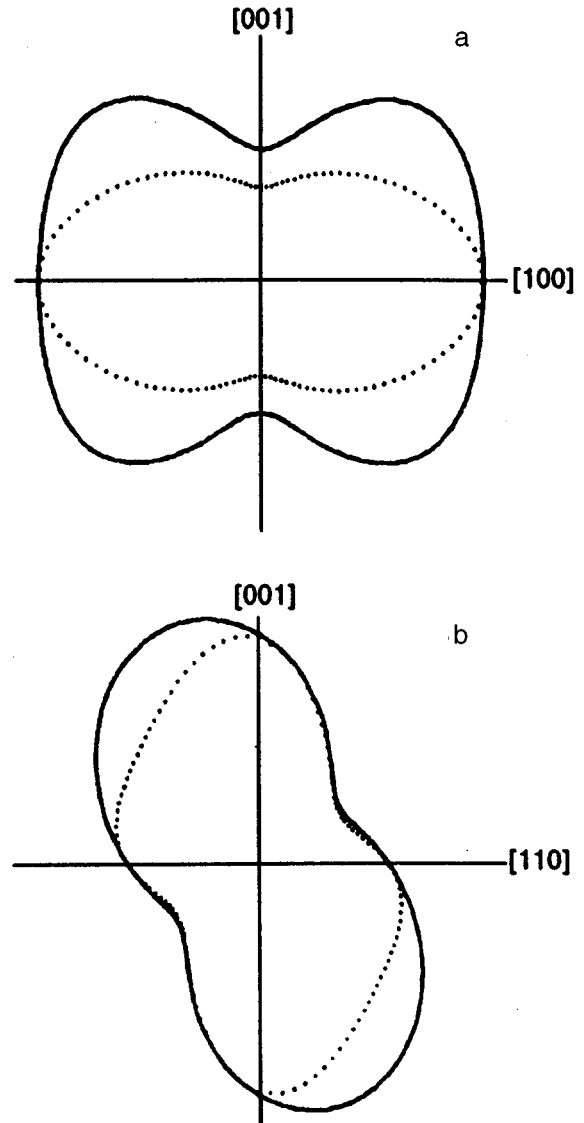

FIG. 3. Shape of the diffusive spot for x-ray scattering (the solid and dashed curves show the results for a system with and without an additional mode, respectively), $\boldsymbol{\kappa}=(0,0,\,2\pi/c)$, projection onto the (010) plane (a); $\boldsymbol{\kappa}=(2\pi/a,2\pi/a,2\pi/c)$, projection onto the ($1\bar{1}0$) plane (b).

2. DIFFUSIVE SCATTERING OF X-RAYS BY ACOUSTIC MODES

Let us now consider the diffusive scattering of x-rays by acoustic modes. Taking into account the displacements of lattice atoms, we can present the differential scattering cross section in the form[7,8]

$$\frac{d\sigma}{d\text{o}'} = \frac{1}{2}\left(\frac{e^2}{mc^2}\right)^2 (1+\cos^2\,\alpha)|f_\mathbf{q}|^2 \sum_{lm}\ \exp(-i\mathbf{q}(\mathbf{R}_l$$

$$-\,\mathbf{R}_m))\int_{-\infty}^{\infty}dt\int_{-\infty}^{\infty}\frac{d\omega}{2\pi}\,e^{i\omega t}\langle e^{-i\mathbf{q}\mathbf{u}(l,t)}e^{i\mathbf{q}\mathbf{u}(m,0)}\rangle,$$

(15)

where $f_\mathbf{q}$ is the Fourier component of the atomic scattering form factor (for simplicity, we assume the form factor to be the same for all atoms), and α is the angle between $\mathbf{k}$ and $\mathbf{k}'$ (the wave vectors of the incident and scattered electromagnetic waves). Substituting the expansion (10) into Eq. (15), we obtain in the limit $T\gg\omega_\chi(\mathbf{q})$ the following expression for the diffusive scattering cross-section of x-rays:

$$\frac{d\sigma}{d\text{o}'} = \frac{1}{2}\left(\frac{e^2}{mc^2}\right)^2 (1+\cos^2\,\alpha)\,\frac{|f_\mathbf{q}|^2 TN}{M}$$

$$\times\sum_\chi\ \frac{|\mathbf{q}\xi_\chi(\mathbf{q})|^2}{\omega_\chi^2(\mathbf{q})}\,e^{-2W(\mathbf{q})}.$$

(16)

Here $\mathbf{q}=\mathbf{k}-\mathbf{k}'=\boldsymbol{\kappa}+\mathbf{q}'$. Proceeding from this equation, we consider the effect of a plane mode on the form of the diffusive spot in the vicinity of the structural peaks. The curves corresponding to equal intensity of diffusive scattering, obtained from the condition

$$\sum_\chi\frac{|\mathbf{q}\xi_\chi(\mathbf{q})|^2}{\omega_\chi^2(\mathbf{q})}=\text{const},$$

are presented in Fig. 3a [$\boldsymbol{\kappa}=(0,0,\,2\pi/c)$, projection onto the (010) plane] and in Fig. 3b [$\boldsymbol{\kappa}=(2\pi/a,2\pi/a,2\pi/c)$, projection onto the ($1\bar{1}0$) plane]. The corresponding curves for a system without the additional mode are also shown in the figure. It can be seen from Fig. 3 that the existence of a plane mode causes a significant variation of the diffusive spot for the scattering geometry considered by us.

3. ANISOTROPY OF THE DEBYE–WALLER FACTOR

Finally, let us consider the effect of the additional mode on the dependence of the Debye–Waller factor on the direction of the scattering wave vector and temperature. We restrict the analysis to the Debye model. In this model, we shall carry out summation with respect to $\mathbf{q}'$ in (12) inside a sphere of radius q_D and assume that the linear dependence of vibration frequencies on the wave vector is valid in the summation region. In this case, we obtain for the quantity $W(\boldsymbol{\kappa})$

$$W(\boldsymbol{\kappa})=W_0(\boldsymbol{\kappa})+T^2 W_1(\boldsymbol{\kappa}),$$

(17)

where

$$W_0(\boldsymbol{\kappa})=\frac{q_D^2}{8(2\pi)^3\rho}\sum_\chi\int_0^{2\pi}d\varphi\int_{-1}^1 d\cos\,\theta\,\frac{|\boldsymbol{\kappa}\xi_\chi(\theta,\varphi)|^2}{s_\chi(\theta,\varphi)},$$

(18)

668   Low Temp. Phys. **23** (8), August 1997

D. V. Fil and A. L. Zazunov   668

FIG. 4. Dependence of W_0(a) and W_1(b) on θ_κ for $\kappa\perp[010]$ (solid and dashed curves show the results for a system with and without an additional mode, respectively).

$$W_1(\kappa) = \frac{1}{2(2\pi)^3\rho} \sum_\chi \int_0^{2\pi} d\varphi \int_{-1}^1 d\cos\theta \frac{|\kappa\xi_\chi(\theta,\varphi)|^2}{s_\chi^3(\theta,\varphi)}$$

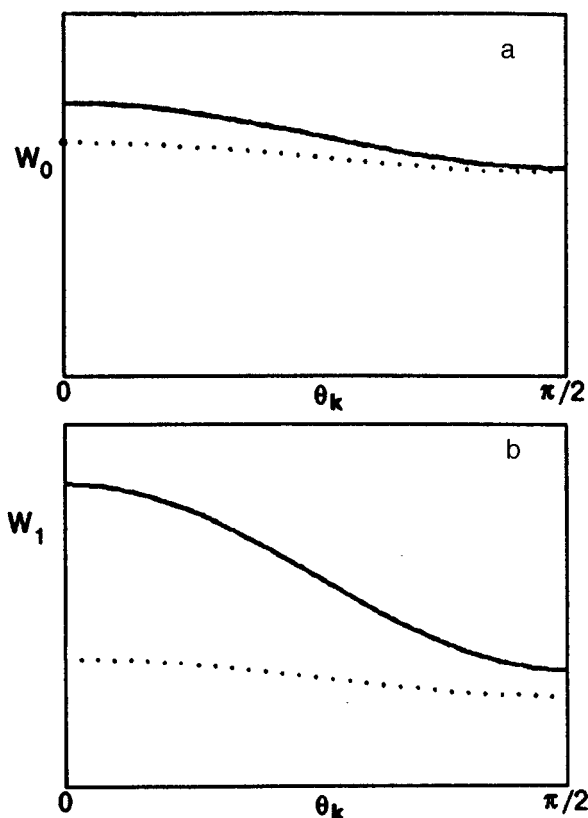$$\times \int_0^{s_\chi q_D/T} dx \frac{x}{e^x-1} \tag{19}$$

(s_χ are acoustic mode velocities). It can be shown that $W_1(\kappa)$ is independent of T in the low-temperature limit. The upper limit in the integral with respect to x in (19), in fact, can be made to tend to infinity for all χ, θ, and φ, except for a small region in the vicinity of $\theta=0$ for one of the modes. In this region, the integral with respect to x in (19) is $\sim T^{-1}$,

and the phase volume of this region is $\sim T$. The contribution from this region is also independent of temperature. Hence the qualitative behavior of the temperature dependence of the Debye–Waller factor is preserved. Nevertheless, the effect of lattice interaction with the plane mode is manifested in the variation of the nature of the dependence $W_0(\kappa)$ and $W_1(\kappa)$ on the direction κ. The dependences $W_0(\kappa)$ and $W_1(\kappa)$ on the angle θ_κ between κ and the c_4 axis for $\kappa\perp[010]$ are shown in Fig. 4. For comparison, the figure also shows analogous dependences for a system without the additional mode. The numerical values of W_0 and W_1 are estimated for $\kappa\|z$ and $\kappa\sim10^7$ cm^{-1} as $W_0\sim10^{-1}$ and $W_1\sim10^{-5}$ K^{-2}.

It can be seen from Fig. 4 that the interaction of the lattice with the plane mode is manifested in an additional anisotropy of the Debye–Waller factor and in its temperature dependence. As regards W_0, it should be noted that in spite of the validity of the qualitative conclusion about the plane mode determining the additional anisotropy W_0, its numerical value is sensitive to the choice of the approximation and may turn out to be quite different if the contribution of optical phonons is taken into account and upon integration over the entire Brillouin zone. The effect associated with the plane mode may be less significant than that expected from the model considered here. On the other hand, the model provides a quantitative description of the anisotropy of the temperature dependence of the Debye–Waller factor at low temperatures.

*E-mail: fil@isc.kharkov.ua

[1] I. G. Kolobov, V. D. Fil, D. V. Fil et al., Phys. Rev. **B49**, 744 (1994).
[2] D. V. Fil, I. G. Kolobov, V. D. Fil et al., Fiz. Nizk. Temp. **21**, 1225 (1995) [Low Temp. Phys. **21**, 937 (1995)]; D. V. Fil, I. G. Kolobov, V. D. Fil et al., Czech. J. Phys. **46** 2155 (1996).
[3] D. V. Fil and A. L. Zazunov, Preprint Int. Center Theor. Phys. IC/85/96 Trieste (1996); D. V. Fil and A. L. Zazunov, Fiz. Nizk. Temp. **22**, 1442 (1996) [Low Temp. Phys. **22**, 1095 (1996).
[4] O. I. Tokar and D. V. Fil, Fiz. Nizk. Temp. **19**, 928 (1993) [Low Temp. Phys. **19**, 660 (1993)].
[5] D. V. Fil and O. I. Tokar, Physica **C230**, 207 (1994).
[6] L. Van Hove, Phys. Rev. **89**, 1189 (1954).
[7] A. Maradudin, E. Montroll, and J. Weiss, Theory of Lattice Dynamics in the Harmonic Approximation, New York (1964).
[8] L. D. Landau and E. M. Lifshitz, Electrodynamics of Continuous Media [in Russian], Nauka, Moscow (1982).

Translated by R. S. Wadhwa

Effect of pressure on phase transitions in fluosilicate hexahydrates of bivalent metals

S. K. Asadov, È. A. Zavadskii, V. I. Kamenev, and B. M. Todris

A. Galkin Physicotechnical Institute, National Academy of Sciences of the Ukraine, 340114 Donetsk, Ukraine*

The results of experiments on hydrostatic pressure effect on the stability of crystalline phase states in fluosilicate hexahydrates of bivalent metals $MSiF_6 6(H_2O)$, where M = Mg, Mn, Fe, Co, Ni, and Zn, are considered in a wide temperature range. The results of measurements are presented on the P–T diagram of crystalline states. A generalized P–T diagram permitting the classification of the properties of individual compounds and identification of high-pressure phases is constructed. The obtained results are compared with theoretical models. © *1997 American Institute of Physics.* [S1063-777X(97)01508-9]

1. INTRODUCTION

Fluosilicate hexahydrates of bivalent metals (M–FSH) $MSiF_6 6(H_2O)$, where M = Mg, Mn, Fe, Co, Ni, and Zn, have similar crystal lattices which can be described as a trigonally distorted structure of the CsCl type, formed by octahedral ionic complexes $[SiF_6]^{2-}$ and $[M(H_2O)]^{2+}$. These M–FSH can be divided into three types according to the difference in the crystal lattice symmetry at room (T_r) and low temperatures. The first type includes Ni- and Zn-based FSH which can be described by the symmetry group $R\bar{3}$ in the entire temperature range.[1] Cobalt-based FSH belonging to the second type also possesses the $R\bar{3}$ symmetry at T_r,[1] but experiences a first-order phase transition (PT) upon cooling (at $T = 246$ K).[2,3] A comparison of the results obtained in Refs. 4 and 5 shows that the low-temperature modification of Co–FSH has the monoclinic symmetry $P2_1/c$. Fluosilicates of Mg, Fe, and Mn belonging to the third type are characterized by the presence of symmetry planes parallel to the trigonal axis of the crystal. It was shown initially by x-ray diffraction methods that Mg- and Fe–FSH belong to the space group $R\bar{3}m$,[6,7] while Mn–FSH belongs to the $P\bar{3}m1$ group.[4] Here we will use this symmetry identification for denoting phases, although the authors of subsequent publications[8,9] discovered reflexes on the x-ray diffraction patterns of Mg- and Fe–FSH , which are incompatible with the $R\bar{3}m$ group. In their opinion, the structure of the latter compounds can be interpreted as a pseudohexagonal structure based on periodically alternating elements of monoclinic lattice with the space group $P2_1/c$. All the M–FSH compounds of this type change their structure to $P2_1/c$ through a first-order PT upon cooling.[5] The transition temperature is 300 K for Mg–FSH and 230 and 225 K for Mn- and Fe–FSH respectively.

The results of analysis of the temperature dependence of the NMR line width for ^1H and ^{19}F nuclei indicate[10–12] that M–FSH display an intrinsic motion of octahedrons forming the crystal lattice in a certain temperature range. In the trigonal modification of the third-type M–FSH (M = Fe and Mn), the motion of ions $[SiF_6]^{2-}$ as well as $[M(H_2O)_6]^{2+}$ takes place. The temperature at which this intrinsic motion in these crystals ceases upon cooling coincides with the temperature

of PT to the monoclinic state. The high-temperature modification of M–FSH of this type has a trigonal dynamically disordered structure, while the low-temperature modification is a monoclinic $P2_1/c$ phase which is ordered not only as regards its diffraction properties, but also in view of the absence of intrinsic motion. The disorder existing in M–FSH of the first and second types at T_r can be regarded as partially dynamic since it involves the motion of $[SiF_6]^{2-}$ ions only. These ions rotate between two possible orientations appearing on x-ray diffraction patterns[1] in the surroundings of stationary $[M(H_2O)_6]^{2+}$ ions (if we neglect thermal vibrations). However, the termination of motion in Ni- and Zn–FSH upon cooling is not accompanied with a change of the diffraction pattern. In this case, a transition from the partially dynamic to a static disorder, i.e., to a state with a ''frozen'' disorder, probably occurs instead of the ordering of the crystalline structure. Cobalt fluosilicate belonging to the third-type M– FSH undergoes a transition to the $P2_1/c$ state upon cooling, but the temperature corresponding to termination of motion of $[SiF_6]^{2-}$ ions does not coincide with the temperature of PT to the monoclinic state. In all probability, such an peculiar behavior is associated with the bordering position of Co–FSH between M–FSH groups with different symmetries: $R\bar{3}m(P\bar{3}m1)$, and $R\bar{3}$.

In addition to structural PT considered above, some M–FSH display transitions associated with magnetic ordering. According to the results of measurements, Ni–FSH goes over to the ferromagnetic (FM) state at $T < 1$ K, while Mn- and Co–FSH experience a transition to the antiferromagnetic (AFM) state with weak ferromagnetism. It was shown in Refs. 13–15 that the AFM ordering in Co- and Mn–FSH is preserved up to pressures $P = 40$ and 80 MPa, respectively. Cooling at higher values of P leads to the FM ordering. Nickel-based FSH remains ferromagnetic in the entire range of pressures under investigation (up to 950 MPa and changes the magnetic anisotropy type from easy axis to easy plane only for $P = 130$ MPa. Two magnetization jumps observed in Fe–FSH are induced by magnetic fields $H_1 = 9.8$ MA/m and $H_2 = 34.38$ MA/m.[16] However, these jumps disappear for $P > 180$ MPa, and magnetization increases monotonically with the field.[17]

In this research, we carry out a detailed experimental

investigation of the effect of hydrostatic pressure on the stability of crystalline phase states, on the temperature of PT transitions between these states, and on the form of their realization. The solution of this problem enabled us to construct the $P-T$ phase diagrams, to discover triple points, new high-pressure phases, and wide regions of metastable states, to establish regularities in the behavior of various FSH under pressure, and to determine the relation between the variation of their crystalline structure, magnetic properties, and the type of ionic disorder in a PT.

2. EXPERIMENTAL TECHNIQUE

Experiments were made by two independent methods: difference–thermal analysis (DTA) and x-raying diffraction (XD). The samples were single crystals obtained from a supersaturated aqueous solution of salt according to the technique described in Ref. 18.

The DTA method was used for determining the PT temperature and for establishing the nature of thermal effects accompanying these transformations. The object under investigation of size $6\times6\times4$ mm, the standard crystal, and a differential thermocouple were placed in a high-pressure vessel which simultaneously served as a furnace in the DTA sense. The case made of beryllium bronze subjected to thermal treatment was connected with a gas membrane compressor through a steel capillary. The pressure was transmitted from the compressor to the vessel through gaseous helium. The choice of helium as the transmitting medium enabled us to make measurements under isothermal as well as isobaric conditions and to move along any trajectory on the $P-T$ plane up to $T\sim12$ K. The apparatus used made it possible to carry out experiments in the temperature range 12–350 K and in the pressure interval 0–200 MPa. The errors in measurements were ±0.5 K and 1.5 MPa, respectively.

The temperature and pressure dependences of the lattice spacing d_{440}, as well as the intensity and shape of the x-ray reflex (440) in the crystals under investigation (indices in hexagonal axes of a rhombohedral lattice) were determined as a result of XD measurements. Stability regions for crystalline phases on the $P-T$ plane, the presence and type of PT, as well as the values of T and P corresponding to them were determined from the presence of anomalies on these dependences and their forms. The choice of the reflex (440) for recording was primarily dictated by the convenience of experiments. The reflex was recorded from the natural face of the crystal. The high intensity of the reflex (which was 100 times the background intensity) enabled us to detect its variation to within $\pm$ 0.02°, which ensured the error of $\pm1.7\times10^{-2}\%$ in determining the relative change in the value of d_{440} in $CuK_{\alpha_1+\alpha_2}(2\theta_{440}\sim80°)$ radiation and complete standardization of conditions of x-ray diffraction. At the same time, the shape of the profile of this reflex is sensitive to loss of axial symmetry of the crystal.

Measurements were made in a high-pressure chamber made in the form of an attachment to the x-ray diffractometer DRON-3. The single crystal under investigation was placed in a thick-walled container made of beryllium and supported by a bandage manufactured from beryllium bronze subjected

to thermal treatment. As in the case of DTA measurements, the pressure was created by a gas membrane compressor. The construction of the chamber is described in greater detail in Ref. 19. The maximum pressure P which could be attained in the chamber was 140 MPa. The temperature was varied from 4.2 to 350 K.

3. DISCUSSION OF RESULTS

The results of experiments with M–FSH are presented in the sequence corresponding to the serial number N of arrangement of atoms (M) in the Periodic Table. The choice of such a sequence was dictated by the regularity which was indeed observed in the change in the behavior of these compounds under pressure and which is associated with an increase in the atomic number of the bivalent metal. This will be considered in greater detail below.

The results of measurements for each M–FSH are generalized in the form of corresponding $P-T$ phase diagrams. For convenience of comparison, the diagrams are plotted similarly. Dark figures denote points of thermal anomalies according to DTA data, while light figures correspond to anomalies on $d_{440}(T,P)$ according to the results of XD measurements. Arrows on the figures indicate the directions of variation of T or P at which these anomalies were detected, and the form of anomalies determine the type of phase transitions. For clarity, the regions of existence of different phases are hatched with different angles.

3.1. $P-T$ phase diagram of MgSiF$_6$6(H$_2$O)

In the case of Mg–FSH, a change in pressure up to 200 MPa does not lead to loss of stability in the high-temperature rhombohedral $R\bar{3}m$ or low-temperature monoclinic $P2_1/c$ phases. The temperature of the forward and backward first-order PT between these states (the temperature hysteresis width is 5 K) is virtually independent of pressure. The temperature stability boundaries of these phases on the $P-T$ phase diagram are straight lines parallel to the P-axis.

3.2. Stability of crystalline phases of Mn–FSH under pressure

The $P-T$ diagram for Mn–FSH is shown in Fig. 1. As in the case of Mg–FSH, the temperature of forward and backward PT between the high-temperature trigonal $P\bar{3}m1$ and low-temperature monoclinic $P2_1/c$ modifications is virtually independent of pressure, but the transitions are observed only up to $P\sim90$ MPa. The lines ab and $a'b'$ forward and backward phase transition $P\bar{3}m1\leftrightarrow P2_1/c$ converge at the triple point. The region on the $P-T$ diagram near the triple point is shown in Fig. 2 on magnified scale. Figure 3 presents in three-coordinate system (P,T,d_{440}) the data on the behavior of the quantity d_{440} upon a change in T and P in the vicinity of the triple point, which are required for identification of phases adjoining the triple point and establishing the nature of PT between these phases. The $fklmnopf$ curve in the (P,T) plane is the trajectory of variation of the independent thermodynamic coordinates T and P. The values of d_{440} assumed by this quantity upon a variation of P and T are
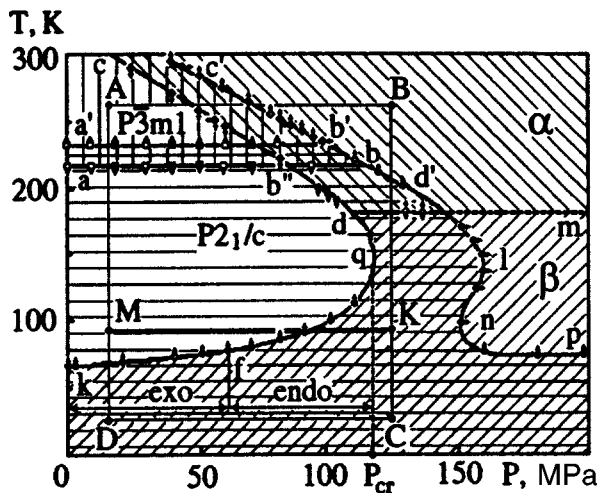
FIG. 1. $P-T$ phase diagram for MnSiF$_6$6(H$_2$O).

FIG. 3. Variation of the lattice separation d_{440} in MnSiF$_6$6(H$_2$O) near the triple point.

plotted along the vertical axis. Solid bold curves connecting these values describe the dependences $d_{440}(T)$ and $d_{440}(P)$ in various regions of the $P-T$ diagram. In order to illustrate the correspondence between anomalies manifested on the curves $d_{440}(T)$ and $d_{440}(P)$ and the lines on the $P-T$ diagram depicted in Fig. 2, the latter are presented by dashed curves in the horizontal plane (P,T) in Fig. 3.

A comparison of the results presented in Figs. 2 and 3 leads to the following conclusions.

(1) The pressure dependence of the temperature corresponding to the first-order PT $P\bar{3}m1 \rightarrow P2_1/c$ forms the curve ab on the $P-T$ diagram. The reverse transition occurs along the curve $a'b'$. The temperature hysteresis between these curves is ~ 11 K. The bifurcation of the d_{440} curve in the $P2_1/c$ phase is a consequence of bifurcation of the diffraction maximum (440), which is associated with the loss of the trigonal symmetry in the lattice and the division of the sample into crystal domains as a result of a transition to the $P2_1/c$ state.[9]

(2) Heating or compression of the sample which was initially in the $P\bar{3}m1$ state leads to an abrupt decrease in the value of d_{440} on the bc' curve by $\sim 1.6\%$. This characterizes the bc' curve as the first-order PT curve. The phase α formed as a result of this transition appar-
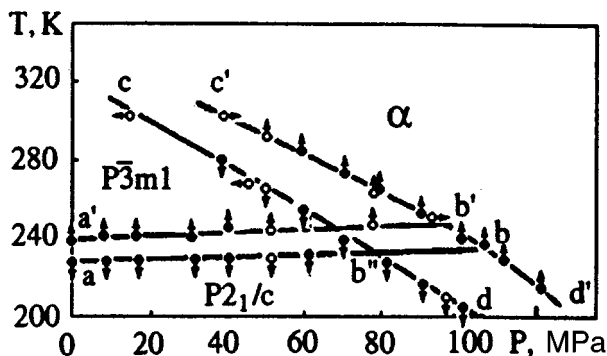

FIG. 2. Region of the $P-T$ phase diagram for MnSiF$_6$6(H$_2$O) near the triple point.

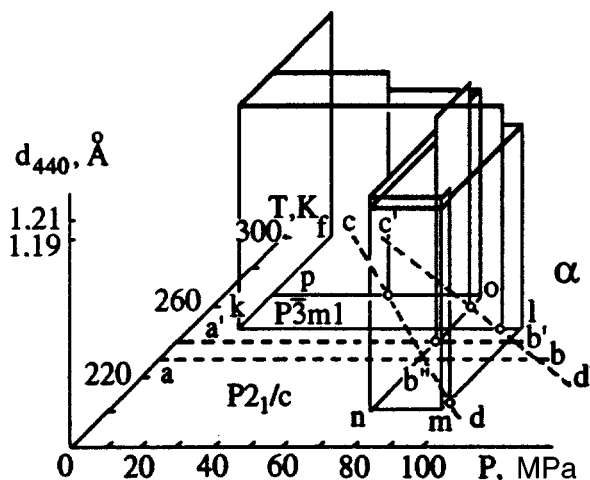ently preserves the trigonal symmetry since the phase transition $P\bar{3}m1 \rightarrow \alpha$ is not accompanied with a change in the shape of the peak at (440). The negative slope of the bc' curve indicates that the phase α is simultaneously a high-pressure phase (HPP) and a high-temperature phase relative to the $P\bar{3}m1$ state. For this reason, the samples go over upon heating from the $P\bar{3}m1$ state to the state α as in a HPP upon a decrease in specific volume, which is a rare effect in solid state physics.

(3) By an appropriate change in T and P, the sample can be returned from the state α to the $P\bar{3}m1$ phase on the $b''c$ curve or transformed to the $P2_1/c$ state on the $b''d$ through a first-order PT. The transition $P2_1/c \rightarrow \alpha$ occurs along the $b'd'$ curve.

Thus, the triple point on the $P-T$ diagram of MnSiF$_6$6(H$_2$O) is formed by three curves of first-order PT: $P\bar{3}m1 \leftrightarrow P2_1/c$, $P\bar{3}m1 \leftrightarrow \alpha$, and $\alpha \leftrightarrow P2_1/c$. As a result of hysteresis phenomena, the triple point appears on the $P-T$ diagram at point b for a transition from the $P\bar{3}m1$ state, at point b'' for a transition from the α state, and at point b' for a transition from the $P2_1/c$ state.

Let us return to the $P-T$ diagram depicted in Fig. 1. The $P2_1/c$ phase is formed upon cooling at the moment of intersection of the curve $ab''dq$ and is preserved down to helium temperatures. For $P > P_{cr}$, the $P2_1/c$ phase is not formed at all, and the sample exhibits anomaly in the temperature behavior on the dm curve. This anomaly is illustrated in Fig. 4 by the $d_{440}(T)$ curve typical of $P > P_{cr}$ and corresponds to its kink. The points at which the kink is observed form the dm curve. On the $P-T$ diagram, this curve separates two states α and β characterized by larger and smaller values of the thermal expansion coefficient of the crystal lattice along the [440] direction. Since the value of the coefficient changes abruptly upon the intersection of this curve, while the quantity d_{440} changes continuously, the dm curve can be classified according to formal features as a curve of the second-order PT $\alpha \leftrightarrow \beta$. A transition through the dm curve is not accompanied by a change in the shape of the
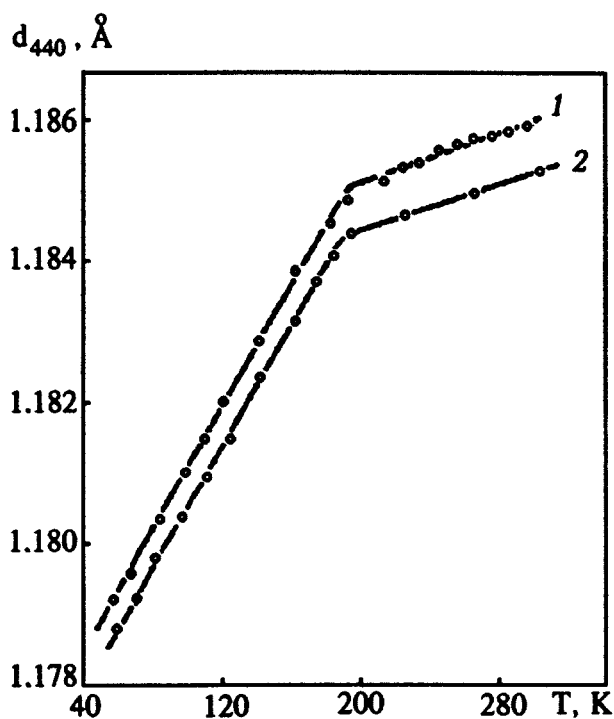
FIG. 4. Temperature dependence of the quantity d_{440} in $MnSiF_66(H_2O)$ for different values of pressure P, MPa: 130 (curve *1*) and 135 (curve *2*).

FIG. 5. Thermograms of heating of $MnSiF_66(H_2O)$ for different values of pressure P, MPa: 50 (a) and 110 (b). The initial state is β.

profile of the peak at (440). This means that the crystal lattice in the state β as well as in the state α has a trigonal symmetry axis. Since the XD experiments were confined to pressure $P = 140$ MPa, and the DTA method did not reveal this anomaly, the data on the transition temperature at higher pressures are not available. We can assume, however, that the dm curve will be continued for higher values of P. The first-order PT $\beta \rightarrow P2_1/c$ occurs along the $dqfk$ curve. It takes place if the sample is transformed from the phase β to the absolute stability region of the monoclinic state with the characteristic parabolic shape of the boundary ($ab''dqfk$ curve) by changing pressure P (e.g., along the trajectory KM) or by varying P and T (e.g., along the trajectory CDM). The transformation $\beta \rightarrow P2_1/c$ is irreversible in the parameter T since the qfk curve is not manifested upon subsequent cooling from the $P2_1/c$ phase, and the monoclinic state is preserved down to helium temperatures. In order to carry out the PT $\beta \rightarrow P2_1/c$ again, we must carry the sample through the curve $a'b'bd'lnp$ corresponding to the vanishing of the $P2_1/c$ state and return to the region of phase β on the P–T diagram. It should also be noted that the reverse transition $P2_1/c \rightarrow \beta$ takes place on the boundary $mlnp$ of a typically S-shaped curve.

The P–T diagram (Fig. 1) contain regions of metastable states shown by double hatching between the curves corresponding to the formation and disappearance of the corresponding phases. Depending on the previous history of the sample and the thermodynamic route of its transition to the relevant region in these states, any phase whose hatching covers the given region can be realized. For example, if we transfer the sample from the initial point A ($P\bar{3}m1$ phase) to the point D (the region of metastable states $P2_1/c$ and β),
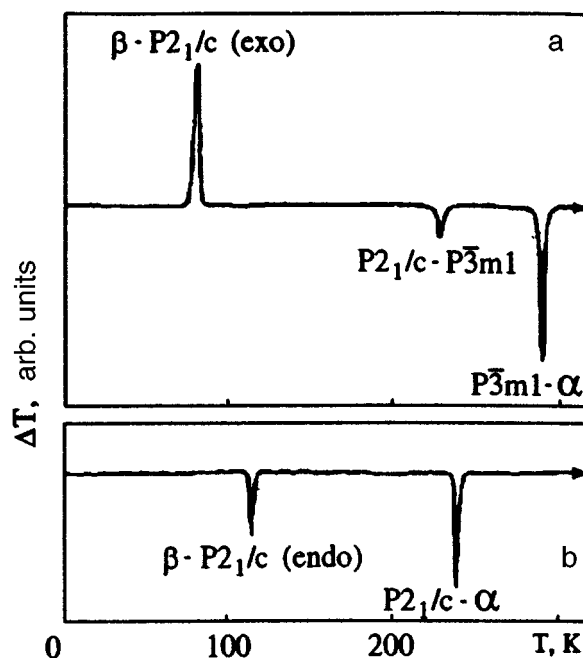
intersecting the $ab''dq$ curve on which a transition to the $P2_1/c$ state takes place (e.g., along the trajectory AD), at point D it will be in the $P2_1/c$ state with the monoclinic symmetry of the crystal lattice. If, however, we transform the sample from the point A to the same point D bypassing the boundary of the formation of the $P2_1/c$ phase (e.g., along the trajectory $ABCD$), the sample will experience a number of PT (the first-order PT $P\bar{3}m1 \rightarrow \alpha$ on the $bb'c'$ curve and the second-order PT $\alpha \rightarrow \beta$ on the dm curve) and will be at the point D in the state β with trigonal symmetry of the crystal lattice at the point D. Thus, below the $pnld'dfk$ curve, the states $P2_1/c$ and β are metastable and do not lose their relative stability down to helium temperatures.

It should also be noted that the sign of the thermal effect accompanying the corresponding first-order PT is reversed at various segments of the boundaries of formation and disappearance of the monoclinic state. For example, the disappearance of the $P2_1/c$ phase on the segment $b'd'l$ occurs with absorption of heat, while heat is liberated on the segment lnp. The formation of the ordered state through the PT $P\bar{3}m1 \rightarrow P2_1/c$ and $\alpha \rightarrow P2_1/c$ on the segments ab'' and $b''d$, respectively, is accompanied by liberation of heat. The phase transformation $\beta \rightarrow P2_1/c$ occurring as a result of heating is endothermal on the segment qf and exothermal on the segment fk. The difference in the type of thermal anomalies in the sample on these segments of the qfk curve are illustrated by thermograms typical of each region (Fig. 5). Irreversibility and the exothermal nature of the PT $\beta \rightarrow P2_1/c$ enable us to consider it as a relaxation process similar to crystallization of amorphous metals or a transition from a metastable state (at low temperatures) obtained by quench-hardening to an absolutely stable state as a result of annealing.
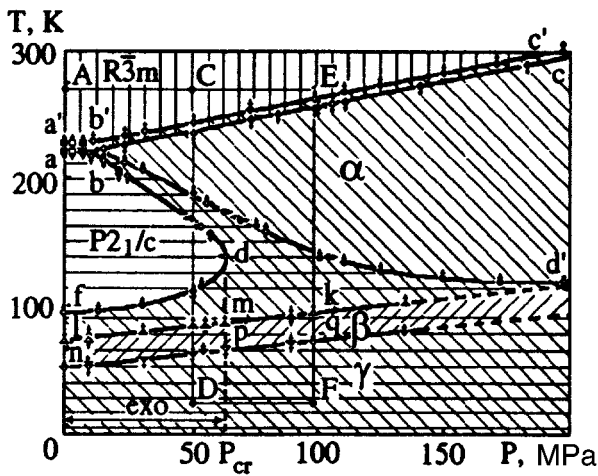
FIG. 6. P–T phase diagram for FeSiF$_6$6(H$_2$O).

FIG. 7. P–T phase diagram for CoSiF$_6$6(H$_2$O).

3.3. Peculiarities of *P–T* phase diagram for FeSiF$_6$6(H$_2$O) subsection

The P–T phase diagram for FeSiF$_6$6(H$_2$O) is shown in Fig. 6 and reflects the following features of the behavior of this compound under pressure.

(1) The familiar PT $R\bar{3}m \leftrightarrow P2_1/c$ is observed only up to the pressure 7.5 MPa (forward transition occurs along the ab curve and backward along the $a'b'$ curve). For $P > 7.5$ MPa, a first-order PT to a new state denoted by α on the P–T diagram is discovered. The invariability of the shape and intensity of the (440) peak in the course of the $R\bar{3}m \leftrightarrow \alpha$ transition suggests that the third-order symmetry axis is preserved in the state α.

(2) In addition to the above transformation $R\bar{3}m \rightarrow \alpha$, the first-order PT $\alpha \rightarrow P2_1/c$ is also observed in the pressure range 7.5 MPa $< P <$ 63 MPa upon cooling. After this transition, the monoclinic structure is preserved down to helium temperatures.

(3) The bc and bd curves corresponding to the direct PT $R\bar{3}m \rightarrow \alpha$ and $\alpha \rightarrow P2_1/c$ converge upon a decrease in the value of P, forming the triple point b together with the ab curve corresponding to the PT $R\bar{3}m \rightarrow P2_1/c$. The curves $b'c'$, $d'b'$, and $a'b'$ corresponding to reverse phase transitions also form the triple point b'.

(4) The state $P2_1/c$ is not formed if $P > P_{cr} = 63$ MPa. In this case, a change in T causes, in addition to the PT $R\bar{3}m \leftrightarrow \alpha$, two second-order PT $\alpha \leftrightarrow \beta$ and $\beta \leftrightarrow \gamma$. The invariability of the shape and intensity of the (440) peak in the course of these transformations indicates that the new phases β and γ possess the trigonal symmetry as well as the phase α. The regions of existence of the states β and γ on the P–T diagram for $P > P_{cr}$ are bounded by the curves mk and pq, respectively.

(5) In the given compound, as well as in Mn–FSH, the absolute stability region of the ordered state $P2_1/c$ is parabolic. The $abdf$ curve is the boundary of its formation, while the $a'b'd'$ is the boundary of its disappearance. These curves confine the region of metastable states, in which either the $P2_1/c$ phase, or the phases α, β, γ
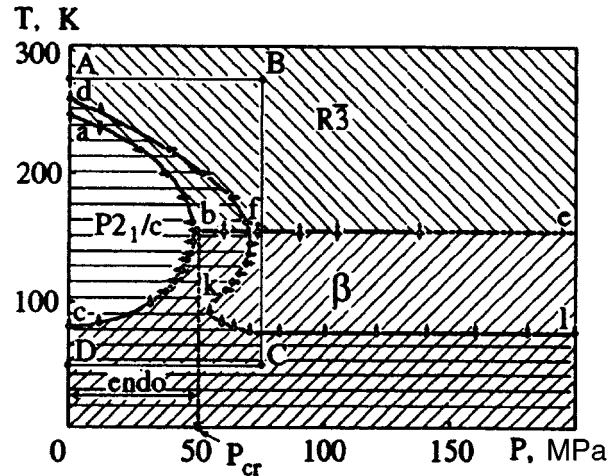
demarcated by the curves npq and lmk of the second-order PT can exist depending on the previous history of the sample. If the sample is compressed isothermally at T_r to pressures 7.5 MPa $< P <$ 63 MPa and then cooled isobarically (e.g., along the trajectory ACD on the P–T diagram), it will be transformed from the initial state $R\bar{3}m$ to the α phase upon the intersection of the bc curve and into the state $P2_1/c$ upon the intersection of the bd curve. In view of metastability of the states α, β, and γ, the curves fd, lmk, and npq will not be manifested, and the sample will remain in the phase $P2_1/c$ at the point D of the diagram. Subsequent heating along the trajectory DC leads to the reverse sequence of two PT $P2_1/c \rightarrow \alpha \rightarrow R\bar{3}m$. If, however, we transform the sample to the point D bypassing the boundary of the formation of the $P2_1/c$ phase, e.g., along the trajectory $AEFD$, the sample will be in the state γ at the point D as a result of the sequence of transitions $R\bar{3}m \rightarrow \alpha \rightarrow \beta \rightarrow \gamma$. If the sample is heated along the same trajectory DC, it experiences a cascade of five PT: $\gamma \rightarrow \beta \rightarrow \alpha \rightarrow P2_1/c \rightarrow \alpha \rightarrow R\bar{3}m$.

(6) In contrast to Mn–FSH, the sign of the thermal effect in Fe–FSH is not reversed at the boundaries of formation and disappearance of the monoclinic state. The PT $R\bar{3}m \rightarrow P2_1/c$ on the ab curve as well as the PT $\alpha \rightarrow P2_1/c$ on the bd curve are accompanied by liberation of heat, while the PT is exothermal along the entire df curve. The reverse transformations along the $a'b'd'$ and $b'c'$ curves occur with heat absorption. In addition, the boundary $b'd'$ of disappearance of the $P2_1/c$ phase has a less pronounced S-shaped curvature.

3.4. Phase transitions in CoSiF$_6$6(H$_2$O) under pressure

The P–T diagram for Co–FSH shown in Fig. 7 leads to the following conclusions.

(1) As the sample is cooled from T_r, the well-known first-order PT $R\bar{3} \rightarrow P2_1/c^1$ is observed only to the pressure

674   Low Temp. Phys. **23** (8), August 1997

Asadov *et al.*   674

$P_{cr} = 50$ MPa. The pressure dependence of temperature corresponding to this transformation forms the ab curve on the $P-T$ diagram.

(2) For $P > P_{cr}$, the $P2_1/c$ phase is not formed at all, but a second-order PT manifested in inflections on the isobaric dependence $d_{440}(T)$ occurs along the bfe curve. Since the shape and intensity of the (440) peak do not change in the vicinity of the temperature corresponding to the point of inflection, we can assume that the third-order symmetry axis is preserved in the new state β.

(3) The phase $P2_1/c$ can be obtained not only by cooling through the first-order PT $R\bar{3} \to P2_1/c$ along the ab curve, but also by heating through the first-order PT $\beta \to P2_1/c$ along the cb curve. For this purpose, the sample must be transformed to the state β without intersecting the boundary of formation of the $P2_1/c$ phase (e.g., to the point D along the trajectory $ABCD$). A further isobaric heating of the sample (e.g., along the trajectory DA) leads to two first-order PT $\beta \to P2_1/c \to R\bar{3}$ occurring at intersections of curves bc and df, respectively. The transformation $\beta \to P2_1/c$ is irreversible in the parameter T since the cb curve is not manifested upon cooling of the sample transformed to the monoclinic state down and the $P2_1/c$ phase is presented to helium temperatures. Thus, the region of formation of the ordered monoclinic state in this compound (abc curve) is parabolic as in manganese and iron fluosilicates.

(4) The boundary of disappearance of the $P2_1/c$ phase on the $P-T$ diagram is an S-shaped curve $dfkl$ typical of M–FSH. The region of metastable states (double hatching) in which either the $P2_1/c$ phase or the phases $R\bar{3}$ and β divided by the bf curve can be preserved depending on the past history of the sample lies between the curves corresponding to the formation and disappearance of the ordered phase.

(5) The sign of the thermal effect is reversed at the boundaries of formation and disappearance of the monoclinic state upon relevant PT. The PT $R\bar{3} \to P2_1/c$ is accompanied by liberation of heat on the entire segment ab of the boundary of formation of the $P2_1/c$ phase. The PT $\beta \to P2_1/c$ is also exothermal near the point of inflection b of the parabola abc, but the transformation becomes endothermal upon cooling by 20 K below the temperature corresponding to the point of inflection. The PT $P2_1/c \to \beta$ is accompanied with liberation of heat on the entire segment lkf. As the temperature T increases by 12 K above the temperature corresponding to the point of inflection f, the transformation $P2_1/c \to R\bar{3}$ changes from exothermal to endothermal.

3.5. Anomalies in the temperature behavior of crystal lattice of Ni and Zn fluosilicate hexahydrates under pressure

It was noted in Ref. 1 that Ni- and Zn–FSH under atmospheric pressure and at T_r have a rhombohedral crystal lattice with the symmetry $R\bar{3}$ which is also preserved upon cooling. At the same time, the results of our XD investiga-

tions of these single crystals indicate the presence of anomalies in the temperature behavior of the crystal lattice of both salts. Anomalies are identical and are manifested in a kink on the $d_{440}(T)$ dependences at $T = 220$ K for Ni–FSH and at $T = 200$ K for Zn–FSH. The emergence of anomalies is not accompanied by a change in the shape of diffraction peak which is sensitive to the crystal symmetry and cannot be detected on DTA thermograms. The observed changes in the slope of $d_{440}(T)$ curves actually indicate a continuous transition in Ni- and Zn–FSH from a high-temperature state with a smaller value of the thermal expansion coefficient of the crystal lattice to a low- temperature state with a larger value of this coefficient. Formally, we can assume that a second-order phase transition from the high-temperature $\alpha(R\bar{3})$ phase to the $\beta(R\bar{3})$ phase isostructural to it occurs at these temperatures (the space symmetry group of these phases is shown in the parentheses). The PT temperature for both compounds virtually does not depend on pressure to within the accuracy of its graphical determination from the $d_{440}(T)$ dependences obtained for various values of P and forms the lines parallel to the P-axis on the $P-T$ phase diagrams of Ni- and Zn–FSH.

4. GENERALIZED $P-T$ PHASE DIAGRAM OF CRYSTALLINE STATES OF FLUOSILICATE HEXAHYDRATES OF BIVALENT METALS

After the construction of $P-T$ phase diagrams for all the compounds under investigation, it became clear that we are dealing with fragments of a complicated but single pattern, viz., a generalized $P-T$ diagram. In spite of considerable differences in $P-T$ diagrams of the salts under investigation, there are several structural elements which can be used for constructing the $P-T$ diagram for each compound.

The first such element consists of the curves corresponding to the forward and backward first- order transitions between the high temperature state with the symmetry elements $\bar{3}m(R\bar{3}m$ or $P\bar{3}m1)$ and the low-temperature monoclinic $P2_1/c$ state. They reflect the fact that the temperature of realization of these PT remains virtually unchanged upon a variation of P, and hence are parallel to the pressure axis on the $P-T$ diagrams.

The second element is the triple point formed by the curves of three first-order PT.

The third element is the parabolic segment of the boundary of formation of the ordered monoclinic phase $P2_1/c$ and the S-shaped segment of its disappearance. The peculiarities of the shape of these boundaries in Mn-, Fe-, and Co–FSH determine the existence of critical pressures P_{cr} and the pressure-independence of the temperature corresponding to disappearance of the ordered phase.

Finally, the fourth element is the curve of the second-order PT between the states with the trigonal symmetry of the crystal lattice, which differ in the values of the thermal expansion coefficient.

The $P-T$ diagram formed by the above-listed elements in the form presented in Fig. 8 is essentially generalized phase diagram for M–FSH under investigation. The $P-T$ diagram for each compound can be presented as a segment of
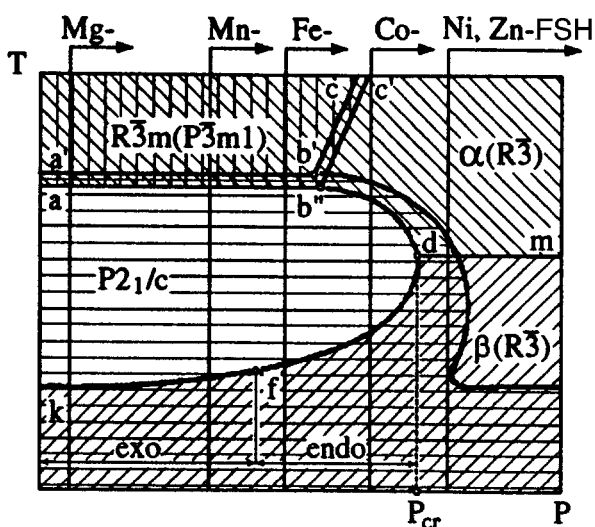
FIG. 8. Generalized P–T phase diagram of crystalline states of fluosilicate hexahydrates of bivalent metals.

the generalized P–T diagram on the right of the vertical line in Fig. 8, which corresponds to the given crystal. As we go over from one M–FSH to another from left to right, the curves are arranged in accordance with the experimentally observed decrease in the value of P corresponding to the triple point and the critical pressure P_{cr} of the formation of the $P2_1/c$ phase. In our experiments with Mg–FSH, neither the triple point nor the critical pressure P_{cr} have been attained in view of insufficient pressure generated by the gas compressor. The triple point for this salt was discovered by Gorev et al.[20] at $P = 210$ MPa, while the existence of critical pressure $P_{cr} \sim 360$ MPa follows from the results obtained by Krygin et al.[21] The pressure corresponding to the triple point is 90 MPa for Mn–FSH and 7.5 MPa for Fe–FSH. For Co–FSH, no triple point is observed, while $P_{cr} = 50$ MPa. For Ni- and Zn–FSH, a second- order phase transition between trigonal phases with different thermal expansion coefficients is observed even under the atmospheric pressure, while for the remaining M– FSH it is observed for $P > P_{cr}$.

It can be seen from Fig. 8 that the sequence of M–FSH formed as a result of such an arrangement repeats the arrangement of the corresponding bivalent metals in the Periodic Table. This means that the form of the P–T diagram for each M–FSH and the serial number N of the metal constituting it are connected through a relation according to which an increase in N is equivalent to a displacement of the origin of the coordinates of the relevant P–T diagram on the generalized P–T diagram towards higher pressures.

5. IDENTIFICATION OF HIGH-PRESSURE PHASES IN FLUOSILICATE HEXAHYDRATES OF BIVALENT METALS

With the help of experimental methods, only low-pressure phases (LPP) formed in the samples under the atmospheric pressure could be identified in M–FSH. The symmetry of phases existing only under a high pressure could not be determined directly in view of technical difficulties. The generalized P–T diagram shows, however, that the regions of existence of HPP of some M–FSH overlap with the

regions of existence of identified LPP of other M–FSH. The similarity of P–T diagrams for M–FSH with a large atomic number N of M and the region of the P–T diagram for a smaller number N, which follows from the structure of the generalized diagram, leads to the conclusion that the phases with coinciding regions of existence on the generalized P–T diagram must be crystallographically identical. For example, the phases α and β which are HPP for Mn-, Fe-, and Co–FSH (experiments for Mg–FSH under the pressure $P > 140$ MPa were not made) must have the same crystalline structure as the LPP in Ni- and Zn–FSH, i.e., the structure with $R\bar{3}$. This can be confirmed by the following arguments.

(1) Comparing the P–T diagrams for Co- and Ni–FSH and taking into account the identical behavior of the crystal lattices of these salts upon the intersection of the corresponding curves of the second-order PT, we note that the P–T diagrams of Ni– FSH and of Co–FSH compressed preliminarily to a pressure $P > P_{cr}$ are similar. According to the results of XD investigations,[1] the high temperature phases with $R\bar{3}$ in Co–FSH and the phase $\alpha(R\bar{3})$ in Ni–FSH are isostructural. This leads to the conclusion that the low-temperature HPP $\beta(R\bar{3})$ of Ni–FSH and the low-temperature phase β of Co–FSH are isostructural. Since the phases $\alpha(R\bar{3})$ and $\beta(R\bar{3})$ in Ni–FSH have identical symmetry and belong to the $R\bar{3}$ group, the low-temperature HPP β in Co–FSH also has the symmetry group $R\bar{3}$.

(2) The curves corresponding to the formation of the monoclinic phase $P2_1/c$ in Mn–FSH (see Fig. 1) and in Fe–FSH (see Fig. 6) can be divided into two segments. One of them lies at the boundary with the $R\bar{3}m(P\bar{3}m1)$ phase, while the other, starting from the triple point, serves as the boundary between the HPP α and β and forms a parabola closed by the T-axis. The same curvature is also typical of the curve corresponding to the formation of the $P2_1/c$ phase in Co–FSH at the boundary with the LPP $R\bar{3}$ and the HPP β belonging to the symmetry group $R\bar{3}$ (see Sec. 4). Such an analogy again leads to the conclusion that the HPP α and β in Mn- and Fe–FSH are identical to the phases $R\bar{3}$ and β in Co–FSH, and hence are two modifications of the structural type $R\bar{3}$ differing in the values of the thermal expansion coefficient of the crystal lattice.

6. CORRESPONDENCE OF P–T DIAGRAMS OF CRYSTALLINE STATES AND MAGNETIC P–T PHASE DIAGRAMS OF FLUOSILICATE HEXAHYDRATES OF MANGANESE, IRON, COBALT, AND NICKEL

The existence of the critical pressure P_{cr} on the P–T diagrams of the crystalline states of Mn–FSH (see Fig. 1), Fe–FSH (see Fig. 6), and Co–FSH (see Fig. 7) indicates that the sample cooled to ultralow temperatures under a pressure $P < P_{cr}$ has the monoclinic phase $P2_1/c$, while the sample cooled for $P > P_{cr}$ has a rhombohedral $R\bar{3}(P\bar{3}m1)$ crystal lattice. Obviously, the change in the type of ultralow-temperature magnetic ordering from AFM for a sample

676   Low Temp. Phys. **23** (8), August 1997

Asadov et al.   676

cooled under $P > P_{cr}$ to FM for cooling under $P < P_{cr}$[14] is in good agreement with the behavior of the crystalline structure under pressure (being a secondary effect relative to structural transformations) and indicates that the AFM ordering is typical of the $P2_1/c$ state, while the FM ordering is characteristic of the $R\bar{3}$ phase. Similarly, a spin state with zero effective magnetic moment is realized in the monoclinic phase $P2_1/c$ of Fe–FSH in a magnetic field parallel to the trigonal axis C_3 below $T = 10$ K under $P < P_{cr}$. Under the same conditions, for $P > P_{cr}$, iron fluosilicate in the disordered trigonal γ phase loses the properties of an easy-plane paramagnet.[17] According to the P–T diagram of crystalline states, Ni–FSH at ultralow temperatures has only one symmetry modification $R\bar{3}$, and the phase $P2_1/c$ is not formed at all. In conformity with what has been said above concerning the correspondence between the structural and magnetic properties of M–FSH, the crystal of this salt experiences only the ferromagnetic ordering at ultralow temperatures.[15]

7. COMPARISON WITH THEORETICAL MODELS

The first-order PT observed in M–FSH as well as in many other compounds occur, in all probability, not along the phase-equilibrium curves, but on lability boundaries. Possible reasons behind such a behavior can be complete blocking of the nucleation of a new phase due to jump in volume in the course of the first-order PT as well as other mechanisms of kinetic origin.[22]

Above a certain temperature T_z, the parabolic lability boundaries of the ordered and disordered phases on the P–T diagrams of the compounds under investigation are successfully described by the Landau theory.[23] At $T = T_z$, the lability boundary of the ordered phase is virtually independent of pressure. It was proposed in Ref. 23 that the emergence of an S-shaped lability boundary can be due to a strong cooperative interaction forming a metastable ordered state and preserving the attained degree of ordering up to $T = T_z$. The latter is equivalent to the statement that the entropy of the ordered subsystem is independent of the parameter P.

Breaner and Zavadskii[24] also attributed the emergence of an S-shaped boundary to the competing effect of the parameters T and P on the Landau coefficients.

Sukharevskii and Zavadskii[25] proposed a Landau model potential taking into account the existence of two ordering channels. This potential corresponds to the phase diagram with a triple point and with parabolic lability boundaries. It was proved that the interaction of two order parameters is responsible for a radical change in the thermodynamic parameter of TP: the sign of lability boundary curvature for the ordered and disordered phases and sign reversal of the thermal effect (single on the phase equilibrium curve and double on lability boundaries).

Thus, we can conclude that the main peculiarities of phase transitions in M–FSH as well as the shape of lability boundaries on the P–T diagrams can be explained satisfactorily in the above thermodynamic models.

8. CONCLUSION

This research completes the cycle of experiments devoted to an analysis of the behavior of M–FSH in wide ranges of pressures and temperatures. The results of measurements are presented in the form of P–T diagrams of crystalline state. The generalized P–T phase diagram makes it possible to systematize the properties of individual compounds and to identify high-pressure phases.

The correspondence between the P–T diagrams of crystalline states and the available P–T magnetic phase diagrams of fluosilicate hexahydrates of Mn, Fe, Co, and Ni is indicated.

Theoretical models allowing us to describe a phase diagram with a triple point and parabolic and S-shaped lability boundaries are considered.

[*]E-mail: kamenev@host.dipt.donetsk.ua

[1] S. Ray, A. Zalkin, and D. Templeton, Acta Cryst. **B29**, 24471 (1973).

[2] S. Ray, Indian J. Phys. **38**, 176 (1964).

[3] M. Majumdar and S. K. Data, J. Chem. Phys. **42**, 418 (1965).

[4] E. Kodera, A. Torii, K. Osaki, and T. Watnabe, J. Phys. Soc. Jpn. **32**, 863 (1972).

[5] P. Jehanno and F. Varret, Acta Cryst. **A31**, 857 (1975).

[6] W. Hamilton, Acta Cryst. **15**, 353 (1962).

[7] S. Syoyama and K. Osaki, Acta Cryst. **B28**, 2626 (1972).

[8] P. Chevrier and G. Jehanno, Acta Cryst. **A35**, 912 (1979).

[9] P. Chevrier, A. Hardy, and G. Jehanno, Acta Cryst. **A37**, 578 (1981).

[10] G. Rangarajan and J. Ramakrishna, J. Chem. Phys. **51**, 5290 (1969).

[11] K. Muthukrishna and J. Ramakrishna, J. Chem. Phys. **59**, 5571 (1973).

[12] S. Skjaeveland and I. Svare, Phys. Scripta **10**, 273 (1974).

[13] V. P. D'yakonov, È. E. Zubov, and I. M. Fita, *Abstracts of Papers to XXV All-Union Conf. on LTP*, part 2, Leningrad (1988).

[14] V. P. D'yakonov, È. E. Zubov, and I. M. Fita, Fiz. Tverd. Tela (Leningrad) **30**, 582 (1988) [Sov. Phys. Solid State **30**, 337 (1988)].

[15] V. G. Bar'yakhtar, I. M. Vitebskii, A. A. Galkin et al., Zh. Éksp. Teor. Fiz. **84**, 1083 (1983) [Sov. Phys. JETP **57**, 628 (1983)].

[16] È. A. Zavadskii, B. M. Todris, Yu. D. Zavorotnev, and S. K. Asadov, Fiz. Nizk. Temp. **11**, 82 (1985) [Sov. J. Low Temp. Phys. **11**, 44 (1985)].

[17] S. K. Asadov, E. A. Zavadskii, Yu. D. Zavorotnev, and B. M. Todris, Phys. Status Solidi **A109**, 307 (1988).

[18] N. G. Kabanova, S. N. Lukin, G. N. Neilo, and L. F. Chernysh, Kristallografiya **21**, 1235 (1976) [Sov. Phys. Crystallograph. **21**, 716 (1976)].

[19] È. A. Zavadskii, S. S. Zvada, V. I. Kamenev et al., Fiz. Tekh. Vys. Davl. **1**, 93 (1991).

[20] M. V. Gorev, I. N. Flerov, and K. S. Aleksandrov, Fiz. Tverd. Tela (Leningrad) **33**, 2210 (1991) [Sov. Phys. Solid State **33**, 1246 (1991)].

[21] I. M. Krygin, S. N. Lukin, G. N. Neilo, and A. D. Prokhorov, FTVD Fiz. Tekh. Vys. Davl., **4**, 12 (1994).

[22] V. G. Bar'yakhtar, I. M. Vitebskii, and D. A. Yablonskii, Fiz. Tverd. Tela (Leningrad) **19**, 347 (1977) [Sov. Phys. Solid State **19**, 200 (1977)].

[23] È. A. Zavadskii and B. Ya. Sukharevskii, Fiz. Nizk. Temp. **21**, 856 (1995) [Low Temp. Phys. **21**, 659 (1995)].

[24] K. Breaner, E. Zavadskii, and Ber Bunsenges, Phys. Chem **100**, 155 (1996).

[25] B. Ya. Sukharevskii and È. A.Zavadskii, Fiz. Nizk. Temp. **21**, 861 (1995) [Low Temp. Phys. **21**, 663 (1995)].

Translated by R. S. Wadhwa

LOW-TEMPERATURE PHYSICS OF PLASTICITY AND STRENGTH

Influence of oxygen content and structural defects on low-temperature mechanical properties of high-temperature superconducting single crystals and ceramics

S. V. Lubenets, V. D. Natsik, L. S. Fomenko, H.-J. Kaufmann, and V. S. Bobrov

B. Verkin Institute for Low Temperature Physics and Engineering of National Academy of Sciences of Ukraine, 47 Lenin Ave., Kharkov, 310164, Ukraine[*]

A. N. Izotov

Institute of Solid State Physics, Russian Academy of Sciences, Chernogolovka, Russia

The data for the microhardness and fracture toughness of Y–Ba–Cu–O and Bi-based single crystals and ceramics in the temperature range 77–293 K are presented and analyzed. Our study reveals that the microhardness of high temperature superconductors is very sensitive to the oxygen stoichiometry, the phase composition, the temperature, and to the microstructural defects such as impurities, intergranular boundaries, and voids. Attention is drawn to the anisotropy of the micromechanical properties and to the features of the fracture in the vicinity of the indentation. The data available on the plasticity of Y–Ba–Cu–O and Bi–Sr–Ca–Cu–O from micro- and macrotests are compared. © *1997 American Institute of Physics.* [S1063-777X(97)01608-3]

1. INTRODUCTION

Practical applications of Y–Ba–Cu–O and Bi–Sr–Ca–Cu–O superconducting compounds are often limited by their poor mechanical performance, i.e., extremely low ductility and elevated brittleness, especially at low and moderate temperatures. Plasticity and strength of high-temperature superconductors (HTSCs) are adversely affected by numerous defects: voids, surface and bulk microcracks, grain and twin boundaries, phase inhomogeneities, impurities, oxygen nonstoichiometry which result from the synthesis process at high temperature and from subsequent cooling to room temperature and mechanical treatment or loading.

A study of the mechanical properties of such complicated objects, whether they are ceramics (polycrystals) or single crystals, does not appear to be a simple task. Nevertheless, several procedures have been devised for this purposes. It is possible to suppress the intrinsic brittleness of superconducting oxides and reveal clear plastic flow with dislocation generation by deforming at elevated temperatures [1–5], at room temperature with the application of hydrostatic pressure [6] or by using shock-loading techniques [7]. However, most investigations have been made with the indentation techniques which can be used successfully over a wide range of temperatures [8–12].

The purpose of the present paper is to report new results and consider briefly some previous measurements of microhardness and fracture toughness of single crystals and ceramics of Y–Ba–Cu–O and Bi–Sr–Ca–Cu–O compounds in the temperature range 77–293 K. The behavior of the microhardness near the $N-S$ phase transition temperature T_c and the mechanism of microplasticity of HTSCs are of interest to us. We will discuss the dependence of micromechanical properties on temperature, oxygen and impurity concentra-

tions, density, and microstructural and phase inhomogeneities of ceramics, and we will estimate a difficult-to-measure property such as surface energy. Finally, we will compare the available data on the plasticity of these materials obtained from micro- and macrotests.

2. EXPERIMENTAL PROCEDURE

The Y–Ba–Cu–O and Bi–Sr–Ca–Cu–O compounds were prepared by high-temperature solid state reaction. Ceramic specimens were prepared first by cold pressing and then by sintering of synthesized powder. Variations in pressure (0.2–5 GPa) and annealing temperature (1073–1233 K) permitted different densities to be attained. The Y–Ba–Cu–O test samples had a density D between 2.1 and 5.85 g/cm^3 (0.33–0.92 of the x-ray density, D_R = 6.38 g/cm^3) and T_c = 85–92 K. Single crystals were grown in alundum or platinum crucibles (below referred to as Y–Al and Y–Pt, respectively) by a spontaneous crystallization technique. The crystals were flat with (001) faces dominating. The concentration of platinum in Y–Pt crystals and aluminum in Y–Al crystals was found to be 0.01 wt.% Pt and 0.25 wt.% Al. The investigation of the influence of the oxygen deficiency on microhardness was carried out on $YBa_2Cu_3O_{7-\delta}$ crystals with four concentrations of oxygen: δ = 0.1, 0.3, 0.4, and 0.9. The oxygen index in as-grown crystals was varied by further thermal treatment in oxygen or in argon. The microindentations were carried out at room temperature by using a PMT-3 standard diamond tester and at temperatures from 77 to 300 K they were made by using a special tester set described in Ref. 12. Hardness H_V and fracture toughness K_c (the critical stress intensity factor) were calculated by using the relations[9,13]
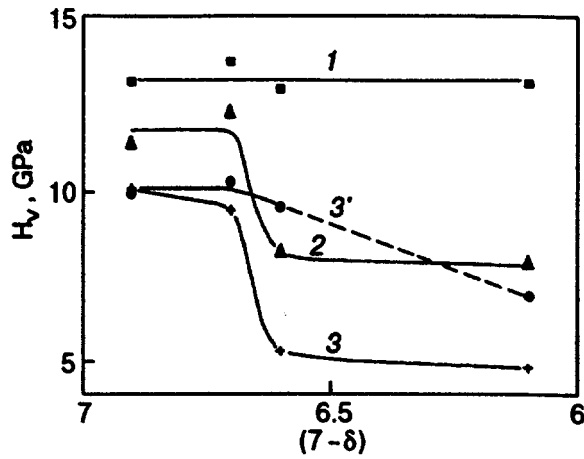
FIG. 1. Effect of oxygen concentration in Y–Ba–Cu–O single crystals on microhardness at temperatures 77 (*1*), 200 (*2*), and 293 K (*3* and *3'*). Curves *1*, *2*, and *3* correspond to crystals from the series Y–Pt, and curve *3'* corresponds to the Y–Al crystals.

$$H_V = 1.854(P - P_{th})/(2a)^2,$$

$$K_c = 0.016(E/H_V)^{1/2}(P - P_{th})/c^{3/2},$$

where $2a$ is the impression diagonal; P is the indentation load; P_{th} is the threshold load which does not result in an impression or a crack; E is the elastic constant (along the axes [100] and [010] $E_{11} = E_{22} = 156$ GPa and along the axis [001] $E_{33} = 89$ GPa for Y–Ba–Cu–O at room temperature[14]). The experimental data plotted in the coordinates $(2a)^2 - P$ and $c^{3/2} - P$ are well described by the linear relations giving the load-independent values of H_V and K_c.

3. RESULTS AND DISCUSSION

3.1. Y–Ba–Cu–O system. Single crystals

Effect of oxygen content on microhardness. The hardness of the Y–Ba–Cu–O system is highly sensitive to oxygen concentration.[12,15,16] The results of our measurements are shown in Fig. 1 for three temperatures. The strongest concentration dependence $H_V(\delta)$ for Y–Pt crystals is observed at room temperature: the hardness changes about 1.5 times in the δ interval from 0.3 to 0.4, i.e., in the range of orthorhombic-1→orthorhombic-2 phase transition, but it is not affected by orthorhombic-tetragonal phase transition ($\delta \simeq 0.5$). Thus, the sharp variation of H_V can apparently be associated with the variation in the properties of the lattice within the orthorhombic symmetry due to one-dimensional ordering of oxygen vacancies. The aluminum impurity in Y–Al crystals weakens the softening effect and extends the range of microhardness-oxygen concentration dependence toward higher values of δ.

The strong effect of oxygen stoichiometry on the plasticity of Y–Ba–Cu–O speaks in favor of shear in the BaO/CuO plane, since the main variations upon changing the oxygen index, occur just in the CuO plane.

The available data[17,18] show that the elastic moduli corresponding mainly to shear modes increase monotonically with oxygen concentration. The moduli corresponding to di-

latation modes increase up to the values ~ 6.7 of the oxygen index, after which they begin to decrease. Consequently, the considered behavior of $H_V(\delta)$ is due not to the variation of the elastic properties of crystals but to the effect of oxygen concentration and oxygen ordering on the core structure and mobility of dislocations.

The microhardness and fracture toughness of Y–Ba–Cu–O and some rare-earth cuprates Re–Ba–Cu–O (Re: Gd, Ho, Dy, Er, Yb) single crystals studied are shown to vary over wide ranges: at room temperature $H_V = 5 - 10$ GPa and $K_c = 0.4 - 1$ MPa·m$^{1/2}$.[8,9,12,19] This considerable spread of the measured values may be attributed to the variations in oxygen concentration which was not controlled.

Mechanical anisotropy of Y–Ba–Cu–O *crystals.* The hardness of Y–Ba–Cu–O crystals was found to be isotropic within an experimental error. However, the special measurements made on relatively large crystals with well-developed (100) and (001) faces have demonstrated that the hardness ratio of (100) to (001) surfaces is 1.2 for the orthorhombic phase and 1.8 for the tetragonal phase.[20]

The length of cracks and the direction of their propagation are very sensitive to indentation crystallography. Cleavage of these layered structures is easier along basal planes.[9,14] That is the reason why the hardness of aligned Y–Ba–Cu–O was found to be strongly anisotropic:[21] preferential cleavage of the basal planes results in much lower hardness for indentation on the (100)/(010) plane than on the (001) plane: 3.8 and 6.7 GPa, respectively.

Notice that the mechanical anisotropy may be affected by the presence of twin boundaries. Hardness was found to be insensitive to a twin structure, which arose during the tetragonal-orthorhombic phase transition; however, the fracture toughness for twinned crystals was different than that for untwinned crystals, according to Ref. 14.

Temperature dependence of microhardness. So far, only few results of an experimental study of the temperature dependence of the microhardness of Y–Ba–Cu–O single crystals have been reported. However, they cover a wide temperature range from the boiling point of liquid nitrogen to almost 1200 K and concern both phases of the Y–Ba–Cu–O compound, i.e., tetragonal and orthorhombic phases. We have summarized the basic data in Fig. 2.

Notice a linear increase in the hardness of the orthorhombic phase (Fig. 2, curve *1*) with decreasing temperature, without any anomalies near $T_c \simeq 93$ K.[12] The data obtained for softer crystals and at a higher temperature[22] (Fig. 2, curve *2*) show a similar temperature dependence. The increase of H_V at $T > 550$ K can be attributed to the changes in oxygen stoichiometry. Samples with the tetragonal structure exhibit lower hardness at room temperature, which increase rapidly, with decreasing temperature, and a sharp transition from ductile behavior to brittle fracture at about 200 K Ref. 12 (Fig. 2, curve *3*). Analogous H_V and their low-temperature dependences of normal brittle semiconductors (e.g., Si, Ge) and Y–Ba–Cu–O single crystals can indicate that in region I the similar thermally activated dislocation mechanisms control plastic deformation produced by indentation.[12] It may be suggested that strong covalent bonds (in the first case) and ionic bonds (in the second case) create high Peierls barriers,
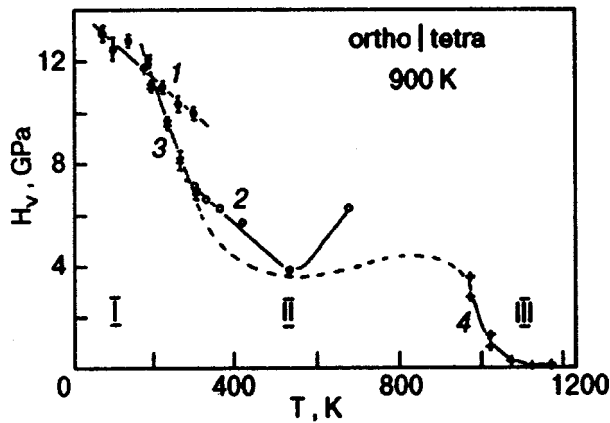
FIG. 2. Microhardness of Y–Ba–Cu–O single crystals as a function of temperature: the orthorhombic phase, $\delta = 0.1$ (*1*);[12] the orthorhombic phase, as-grown (*2*) (Ref. 20); the tetragonal phase, $\delta = 0.9$ (*3*) (Ref. 12); the tetragonal phase (*4*) (Ref. 10).

which constrain the dislocation mobility in these crystals.

The high-temperature deformation processes in the tetragonal phase (region III, Fig. 2, curve *4*; Ref. 10) are obviously diffusion assisted. In the intermediate region II the mixed dislocation-diffusion mechanisms are expected to control plastic flow (see, for example, Refs. 5 and 23 and the bibliography cited there).

Fracture toughness and surface energy. Measurements of the temperature dependence of the fracture toughness have been carried out with two series of Y–Ba–Cu–O single crystals: Y–Al and Y–Pt.[24] They are characterized by the same oxygen index $\delta \simeq 0.3$–0.4 and the same critical temperature $T_c \simeq 60$ K. For Y–Pt crystals, a decrease of H_V and K_c with increasing temperature arises from thermally activated dislocation glide. This provides evidence for a quasi-brittle type of fracture. In contrast, a weak rise of K_c of Y–Al crystals from 3.4 MPa·m$^{1/2}$ (at 77 K) to 3.5 MPa·m$^{1/2}$ (at 292 K) (and a weak drop of H_V from 9.3 GPa (at 77 K) to 8.5 GPa (at 292 K) with increasing temperature may point to an ideally brittle mode of fracture, without allowance for the glide dislocations or with their slight participation. In this situation, the calculated values of K_c are determined essentially by the material constants. Using the Griffith–Orovan relation $K^2 = 2\gamma E/(1 - v^2)$, where v is the Poisson ratio, we could estimate the surface energy γ of two surfaces $(100)/(010)$ and (001). The (001) face indentation gives an average K_c of about 0.35 MPa·m$^{1/2}$ and hence $\gamma_{100/010} \simeq 360$ erg/cm^2. An indentation of $(100)/(010)$ face showed a large anisotropy in crack length for crack directions perpendicular to and parallel to the basal plane (cf. Refs. 14–16, and 19): $K_c \simeq 0.7$ MPa·m$^{1/2}$ and $\gamma_{100/010} \simeq 1400$ erg/cm^2 in the first case and $K_c \simeq 0.2$ MPa·m$^{1/2}$ and $\gamma_{001} \simeq 160$ erg/cm^2 in the second case.

Ceramics

Indentation technique is very useful in estimating the density and homogeneity of samples because of the possibility of accurately locating the impressions on the surface and through the sensitivity of microhardness to the presence of structural and other defects. This is particularly evident in measurements on ceramics.

The influence of microstructure inhomogeneities on the hardness of Y–Ba–Cu–O ceramics is reflected very distinctly in histograms and in average values of hardness.[19] The hardness in the vicinity of grain boundaries is smaller and its dispersion is higher than they both measured within grains. The role of intergrain material in the formation of the ductility of ceramics can be demonstrated best of all by the example of fine-grain ceramics with the grain size $d \simeq 5 \mu$m. Its average hardness was found to be smaller by a factor of 3 as compared with that of ceramics of about the same density with $d \simeq 40 \mu$m, which indicates the determining influence of grain boundaries on the impression formation.

The temperature dependences of the microhardness of ceramics with an average grain size $d \simeq 5 \mu$m and different densities $D/D_R = 0.73$, 0.91, and 0.98 are plotted in Fig. 3.[25] Figures 3a and 3b show the data of H_V measurements at an indentor load $P_1 = 0.15$ N and $P_2 = 2$ N, respectively. At the P_1 load an impression area was very nearly equal to the grain area, whereas at the P_2 load it far exceeded the grain area. The measured values of H_V at P_2 characterize the hardness of given ceramics on average, as a whole, and then they are less than H_V values obtained at indentation with smaller load P_1. The smaller the load on the indentor, the closer are the measured values to the hardness of the grains. From Fig. 3 we see that the hardness is near-linear with temperature without any detectable features in the range from 77 to 293 K for all samples examined, but, what is more important in this context, it depends strongly on density.

Recently[19] we studied the dependence of the hardness on the density of Y–Ba–Cu–O ceramics in the interval of $D/D_R = 0.33$–0.92 at room temperature and deduced from the experiments that the hardness increases exponentially with increasing density (see also Ref. 26), as is usually observed for many structural ceramics:

$$H_V = H_{V0} \exp[-n(1 - D/D_R)].$$

This equation adequately describes the data in Fig. 3 at all temperatures (the plots for two fixed temperatures, 77 and 293 K, are presented in the insets in Figs. 3a and 3b). The H_{V0} value decreases with increasing temperature from 8.1 to 4.6 GPa at $P_2 = 2$ N and from 11.6 to 5.7 GPa at $P_t = 0.15$ N. The factor n in the exponent is equal to 4.6 at a load of 2 N independently of temperature. At a load of 0.15 N the n value increases from 2.6 at 293 K to 3.6 at 77 K. An increase in the value of n with decreasing temperature and an increase in the load is likely due to the crack formation along the grain boundaries. These microcracks enhance the dependence of hardness on density, which in the initial ceramics is determined by the intrinsic voids.

The maximum hardnesses of grains in ceramic samples and single crystals of the same oxygen concentration are in good agreement in the whole temperature range from 77 to 293 K.
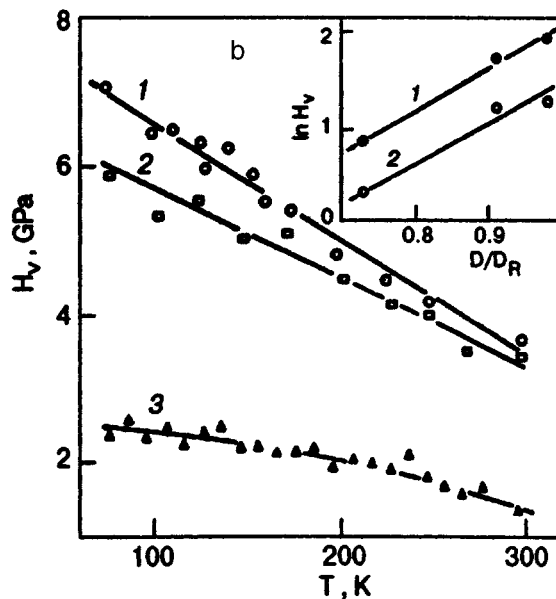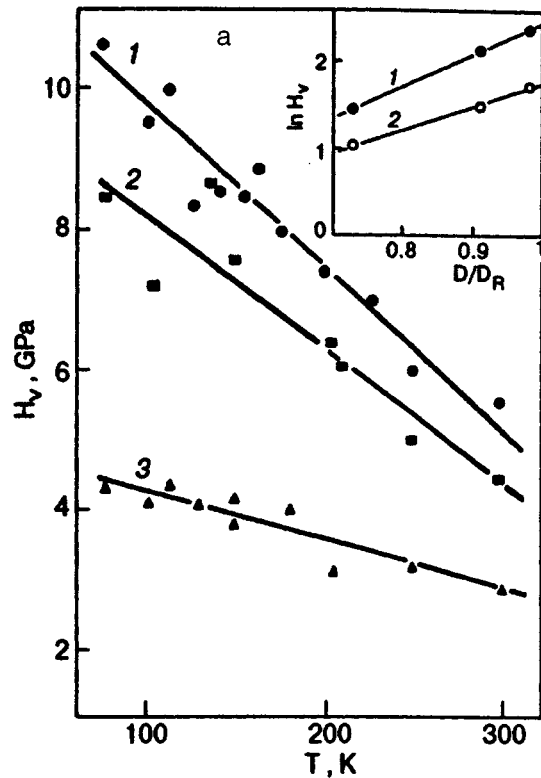
FIG. 3. Microhardness of Y–Ba–Cu–O ceramics as a function of temperature, at the loads on the indentor $P_1 = 0.15$ N (a) and $P_2 = 2$ N (b). Relative density $D/D_R = 0.98$ (1), 0.91 (2), and 0.73 (3). The insets show D/D_R dependences of $\ln H_V$ at two temperatures 77 (1) and 293 K (2).

3.2. Bi–Sr–Ca–Cu–O system

The Bi-containing HTSC ceramics and crystals exhibited highly nonuniform micromechanical properties.[27] The hardness of single crystals at room temperature was found to have three typical values: 0.5; 1.1, and 3.1 GPa. The data observed are close to those measured individually on two types of ceramic crystallites with different optical reflective capacities: 0.43 GPa and 1.08 GPa for "dark" crystallites
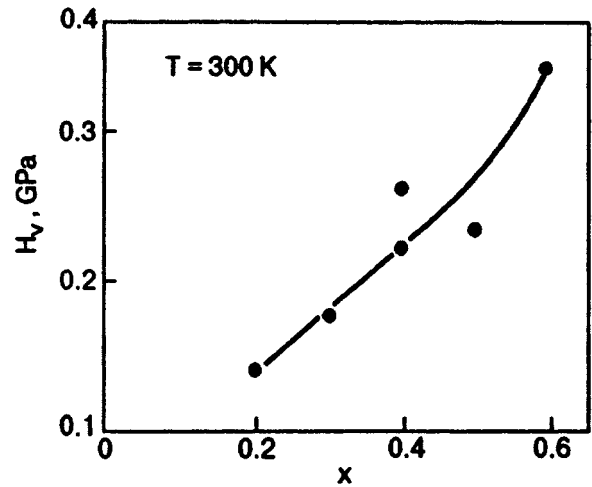
FIG. 4. Microhardness of $Bi_{2-x}Pb_xSr_2Ca_2Cu_3O_y$ ceramics as a function of Pb dopant concentration at room temperature.

and 3.8 GPa for "bright" crystallites. These values are considerably lower than the micro-hardness of a Y-Ba-Cu-O system.

Nonuniform mechanical properties of a Bi-Sr-Ca-Cu-O system apparently are attributable to their multiphase nature. Preparation of single-phase crystals of this system is seriously hindered by different causes. As was demonstrated, nearly single phase material (2212) can be obtained only by thoroughly controlling the processing parameters: the oxygen pressure, the maximum sintering temperature, the annealing time, and the cation stoichiometry.[28] The high quality (2223) phase samples were also prepared.[29,30]

Addition of Pb dopant to the Bi–Sr–Ca–Cu–O system stabilizes the 2223 phase and therefore hardens the $Bi_{2-x}Pb_xSr_2Ca_2Cu_3O_y$ ceramics.[31] Figure 4 shows the microhardness plotted as a function of Pb dopant concentration. Measurements were performed at room temperature by using six samples with different values of x but approximately the same density D/D_R, between 0.6 and 0.7. The microhardness increases almost 2.5 times with increasing x from 0.2 to 0.6. Near-linear rise of H_V with x is probably caused by solid-solution hardening. A deflection of $H_V(x)$ from the linear dependence at $x = 0.6$ may result from Ca_2PbO_4 particle formation, which leads to additional precipitate hardening.

The microhardness of the $Bi_{2-x}Pb_xSr_2Ca_2Cu_3O_y$ ceramics increases with decreasing temperature and, as with the Y–Ba–Cu–O system, has no anomalies in the range $T_c = 105–110$ K. Figure 5 shows the H_V values and their changes in the temperature interval from 77 to 293 K for a sample with $x = 0.4$.

Microhardness measurements with the Knoop indenter carried out on the (001) face of 2223 crystals showed polar hardness anisotropy between $H_{min} = 0.9$ GPa and $H_{max} = 1.33$ GPa for azimuth 45° [the short diagonal of the indenter was parallel to the (100) face] and 0° (or 90°), respectively.[32] The corresponding data for 2212 crystals[33] are $H_{min} = 0.8$ GPa and $H_{max} = 2.5$ GPa. Attention was drawn to a correlation between the H_{max} and T_c values for HTSC materials:[32,34,35] the higher the H_{max} the lower T_c (in
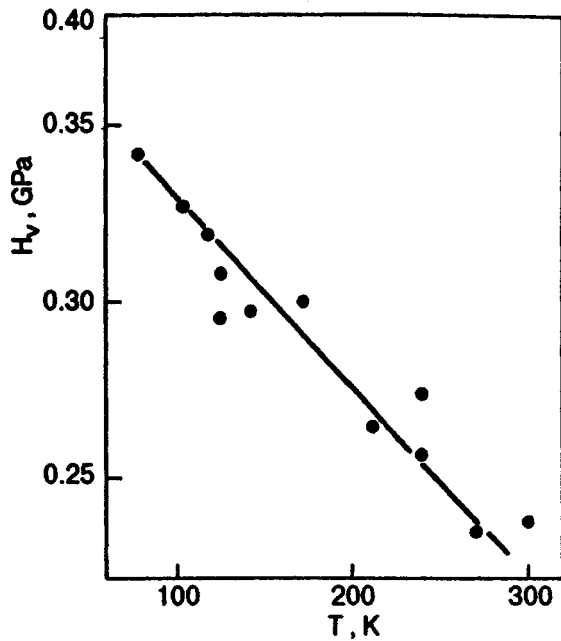
FIG. 5. Microhardness of $Bi_{2-x}Pb_xSr_2Ca_2Cu_3O_y$ ceramics as a function of temperature for $x = 0.4$.

particular, for the 2212 phase $T_c = 85$ K and for the 2223 phase $T_c = 100–110$ K). This correlation seems to support the notion that superconductors with higher T_c values have a more friable crystal structure.

The other feature of the Bi–Sr–Ca–Cu–O crystals is considerable lateral cracking or crushing as a result of indentation. As a result, well-developed radial cracks were rarely visible. An estimation of fracture toughness showed values as low as 0.11 MPa·m$^{1/2}$ (Ref. 27) and 0.22 MPa·m$^{1/2}$ (Ref. 36). Lateral cracking causes the formation of surface relief in the form of a ''roof.'' The residual strain of this blister is estimated to be no less than 1%.

4. COMPARISON OF MICRO- AND MACROCHARACTERISTICS

Some data on the plasticity of Y–Ba–Cu–O and Bi–Sr–Ca–Cu–O compounds obtained in micro- and macrotests can be compared. In the temperature range where the material is normally brittle, the empirical ratio of microhardness to yield stress is found to be about 3 (Ref. 37). In accordance with the available data for Y–Ba–Cu–O ceramics, the maximum $H_V = 4.3$ GPa (Ref. 19) and $\sigma_y = 1.25$ GPa (Ref. 6), hence $H_V/\sigma_y = 3.2$. It is of interest to compare the microhardness and the strength of the single crystals. At 77 K, $H_V = 13.2$ GPa (Ref. 12), and the strength $\sigma_T = 3.1–5.4$ GPa, as measured at the same temperature in a field-ion microscope,[38,39] therefore, $H_V/\sigma_T = 4.3 − 2.6$. We note that the σ_T values are close to the theoretical strength of a perfect crystal: $\sigma_T/E_{33} = 1/16 − 1/30$. A similar value of $\sigma_T \cong 4.3 \pm 0.7$ GPa at 78 K was found for $LuBa_2Cu_3O_{7-\delta}$ single crystals of diameter 74–245 nm in Ref. 40.

There are data on hardness of Bi–Sr–Ca–Cu–O (2212) crystals,[27,41] and tensile strength and elastic modulus of whiskers[42] at room temperature: the maximum $H_V = 3.1$ GPa (Ref. 27) and $H_V = 6.2$ GPa (Ref. 41), $\sigma_c = 0.94$ GPa and $E = 92$ GPa (Ref. 42); therefore, $H_V/\sigma_c = 3.3–6.6$ and $\sigma_c/E = 1/100$. In this case it is clear that, first, the yield point was not reached because of the brittle fracture of whiskers and, secondly, σ_c is less than σ_T because of the large cross section of whiskers more than 50 μm^2.

*E-mail: lubenets@ilt.kharkov.ua

[1] T. Yoshida, K. Kuroda, and H. Saka, Philos. Mag. **A62**, 573 (1990).
[2] V. N. Kuznetsov, V. I. Shalaev, V. V. Sagaradze, E. V. Dusje, V. L. Arbuzov, A. E. Davletshin, V. R. Poskrebyshev, and S. M. Cheshnitskii, Sverkhprovodimost' **5**, 1939 (1992).
[3] J. L. Routbort, D. J. Miller, E. J. Zamirovski, and K. C. Goretta, Supercond. Sci. Technol. **6**, 337 (1993).
[4] M. F. Imaev, F. F. Musin, R. O. Kaibyshev, and M. R. Shaglev, Doklady RAN **338**, 184 (1994).
[5] K. C. Goretta, E. J. Zamirovski, J. M. Calderon-Moreno, D. J. Miller, Nan Chen, T. G. Holesinger, and J. L. Routbort, J. Mater. Res. **9**, 541 (1994).
[6] J. Rabier and M. F. Denanot, J. Less Comm. Met. **164–165**, 223 (1990).
[7] M. Verwerft, D. K. Dijken, J. Tm. De Hosson, and A. C. Van Der Steen, Phys. Rev. **B50**, 3271 (1994).
[8] R. F. Cook, T. R. Dinger, and D. R. Clarke, Appl. Phys. Lett. **51**, 454 (1987).
[9] V. V. Demirskii, H.-J. Kaufmann, S. V. Lubenets, V. D. Natsik, and L. S. Fomenko, Sov. Phys. Solid State **31**, 1065 (1989).
[10] H. Saka, J. Inagaki, T. Joshida, T. Murase, and K. Kuroda, JJAP Ser. 2, Lattice Defects in Ceram., 143 (1989).
[11] V. S. Bobrov, I. I. Zwerkova, A. P. Ivanov, A. N. Izotov, A. A. Novomlinskii, R. K. Nikolaev, Yu. A. Osipyan, N. S. Sidorov, and V. Sh. Shekhtman, Fiz. Tverd. Tela **32**, 826 (1990).
[12] B. Ya. Farber, N. S. Sidorov, V. I. Kulakov, Yu. A. Iunin, A. N. Izotov, G. A. Emelchenko, V. S. Bobrov, L. S. Fomenko, V. D. Natsik, and S. V. Lubenets, Sverkhprovodimost' **4**, 2394 (1991).
[13] G. R. Anstis, P. Chanticul, R. P. Lawn, and D. B. Marshall, J. Amer. Ceram. Soc. **64**, 533 (1981).
[14] A. S. Raynes, S. W. Freiman, F. W. Gayle, and D. L. Kaiser, J. Appl. Phys. **70**, 5254 (1991).
[15] T. Graf, G. Triscone, and J. Muller, J. Less Comm. Met. **159**, 349 (1990).
[16] S. V. Lubenets, V. D. Natsik, L. S. Fomenko, V. S. Bobrov, and A. N. Izotov, Low Temp. Phys. **21**, 247 (1995).
[17] H. Ledbetter, J. Mater. Res. **7**, 2905 (1992).
[18] S. Lin, M. Lei, and H. Ledbetter, Mater. Lett. **16**, 165 (1993).
[19] V. V. Demirskii, S. V. Lubenets, V. D. Natsik, M. N. Sorin, L. S. Fomenko, and N. M. Chaykovskaya, Sverkhpropodimost' **3**, 84 (1990).
[20] E. Cruceanu, J. Deutz, H. Klein, W. Schmitz, and H. Ullmaier, Mater. Sci. Engn. **A160**, L9 (1993).
[21] A. Goyal, P. D. Funkenbusch, D. M. Kroeger, and S. J. Burns, J. Appl. Phys. **71**, 2363 (1992).
[22] V. S. Bobrov, V. K. Vlasko-Vlasov, G. A. Emelchenko, M. L. Indenbom, M. A. Lebedkin, Yu. A. Osipyan, V. A. Tatarchenko, and B. Ya. Farber, Fiz. Tverd. Tela **31**, 93 (1989).
[23] M. Jimenez-Melendo, A. R. De Arellano-Lopez, A. Dominguez-Rodriguez, K. C. Goretta, and J. L. Routbort. Acta Metall. Mater. **43**, 2429 (1995).
[24] S. V. Lubenets, V. D. Natsik, L. S. Fomenko, M. N. Sorin, N. M. Chaykovskaya, V. S. Bobrov, A. N. Izotov, and A. A. Zhokhov, Sverkhprovodimost' **6**, 1406 (1993).
[25] S. V. Lubenets, V. D. Natsik, L. S. Fomenko, I. A. Lyashenko, and I. T. Ostapenko, III Vsesojuzn. Sovesch. VTSP (Thezisy), Kharkov (1991), p. 76.
[26] W. H. Tuan and J. M. Wu, J. Mater. Sci. **28**, 1415 (1993).

[27] S. V. Lubenets, V. D. Natsik, M. N. Sorin, L. S. Fomenko, N. M. Chaykovskaya, H.-J. Kaufmann, and K. Fischer, Sverkhprovodimost' **3**, 1857 (1990).

[28] B. Hebb, L. J. Gauckler, H. Heinrich, and G. Kostorz, J. Electric Mater. **22**, 1279 (1993).

[29] H. Zhang, F. Ritter, T. Frieling, B. Kindler, and W. Assmus, J. Appl. Phys. **77**, 3704 (1995).

[30] I. F. Kononyuk, V. V. Washuk, L. V. Makhnach, and Yu. G. Zonov, Sverkhprovodimost' **3**, 298 (1990).

[31] I. F. Kononyuk, L. D. Makhnach, S. V. Lubenets, V. D. Natsik, and L. S. Fomenko, III Vsesojuzn. Sovesch. VTSP (Thezisy), Kharkov (1991), p. 75.

[32] V. N. Osipov, L. I. Derkachenko, Yu. G. Nosov, V. N. Gurin, W. Jung, and R. Muller, Solid State Commun. **97**, 377 (1996).

[33] Tong B. Tang and S. C. Fung, Solid State Commun. **87**, 325 (1993).

[34] V. N. Osipov, Yu. G. Nosov, V. N. Gurin, I. N. Zimkin, N. F. Kartenko, and S. P. Nikanorov, Sov. Phys. Solid State **36**, 2451 (1994).

[35] T. S. Orlova, B. I. Smirnov, and V. V. Shpeizman, Sov. Phys. Solid State **32**, 1838 (1990).

[36] J. H. Jia and Q. P. Kong, Phys. Status Solidi **A145**, K51 (1994).

[37] D. Tabor, *The Hardness of Metals,* Oxford, Clarendon Press (1951).

[38] E. F. Talantsev, V. A. Ivchenko, and N. N. Syutkin, Sverkhprovodimost' **3**, 2017 (1990).

[39] I. M. Mikhailovskii, E. V. Sadanov, V. A. Ksenofontov, and O. A. Velikodnaya, Sverkhprovodimost' **5**, 1453 (1992).

[40] E. F. Talantsev, Supercond. Sci. Techn. **7**, 491 (1994).

[41] M. Muralidhar, Reddy K. Narasimha, and V. Hari Babu, Phys. Status Solidi (a) **126**, 115 (1991).

[42] I. Matsubara, J. Hashimoto, K. Atago, H. Yamashita, M. Kinoshita, and T. Kawai, J. Appl. Phys. **31**, Part 2, No 1 A/B. L14 (1992).

This article was published in English in the original Russian journal. It was edited by S. J. Amoretty.

683   Low Temp. Phys. **23** (8), August 1997

Lubenets *et al.*   683